DOCTOR OF PHILOSOPHY

Development of improved predictive tools for mechanical soil root interaction

Duckett, Natasha-Rass

Award date:
2014

DOCTOR OF PHILOSOPHY

Development of improved predictive tools for mechanical soil root interaction

Natasha-Rass Duckett

2014

University of Dundee

College of Art Science and Engineering
School of Engineering and Physical Sciences
Department of Civil Engineering

Development of improved predictive tools for mechanical soil root interaction

Natasha-Rass Duckett

A dissertation submitted for the degree of Doctor of Philosophy to the University of Dundee.

August 2013

i. Declaration

This is to certify that, except where specific reference to other investigation is made, the work described in this dissertation is the result of the investigation of the candidate. Neither this dissertation, nor any part of it, has been presented or is currently submitted in candidature for any degree at any other university.

Miss Natasha-Rass Duckett (Candidate), Dundee 30/August/2013

Dr. Jonathan Knappett (Supervisor), Dundee 30/August/2013

ii. Acknowledgements

This research was carried out as a collaborative study between the University of Dundee and the James Hutton Institute, Invergowrie.

I would like to thank: My supervisors, Jonathan Knappett, Paul Hallett and Glyn Bengough, for their invaluable support, advice, constructive comments and patience; Fraser Bransby, for his input and guidance during the early stages of the project; Kenneth Loades, for introducing me to the laboratory and showing me how everything works; The technical staff at both the University of Dundee and the James Hutton Institute, for helping me to modify equipment; Slobodan Mickovski, for giving me access to his detailed and well-recorded laboratory test output, which was so fundamental to this project; Jonathan Kobine, Andrew Brennan, Ian Mackie and Fraser Smith, for giving me the opportunity to teach and tutor undergraduates; The remaining staff at the University of Dundee and the James Hutton Institute for always making me feel welcome!; Last, but not least, my support group, Michael Yule, Gary Duckett, Nonie Duckett, Aimée-Jo Stevenson and Bruce Stevenson, for their love, support and encouragement.

iii. Abstract

Plant roots can stabilise a soil through two key mechanisms, namely: mechanical interaction and suction (drawing water from the soil). As a result, they offer a sustainable alternative to traditional soil stabilisation techniques, such as soil nailing or piling, and are becoming increasingly sought after as concerns for global climate change increase. In practise, however, use of vegetation in infrastructure (termed bioengineering) is little used due to a lack of understanding of root functions and, therefore, a lack of confidence from engineers. Predicting the response of soil root systems to mechanical loading is therefore of significant importance in the development and improved use of bioengineering techniques. Previous research has primarily focused on predicting a root cohesion factor, which can be used to estimate the ultimate limit state but not pre-failure behaviour (e.g *Wu et al., 1974*).

This Thesis reports an extensive series of laboratory uprooting[1] and shear box tests, which were carried out to quantify soil root interactions, and to provide a database of results to develop and test predictive numerical models. The laboratory tests used root analogues made from either rubber or wood, to span a wide range of root stiffness, whilst avoiding the natural variability associated with plant roots. These included full section-centre tests, where the roots were located in the centre of the soil sample, and novel cross section-front tests, where the roots were halved along their length and placed at the edge of the soil sample to provide a window into the system during loading. The latter allowed the soil and root deformation to be digitally photographed during loading and thus the displacement fields to be measured using GeoPIV analysis, a computer program designed to trace the movement of pixels through a series of digital images. With such data, the forces acting within the roots could be assessed during loading and the interface friction between the root and the soil could be quantified for input into the numerical models (using *t-z* and *p-y* pile analysis theory). The full section-centre direct shear box tests considered the impact of the following factors on the reinforcing potential of roots: root area ratio (the ratio of root area to soil sample area), root length, root diameter, root stiffness and root spacing/distribution.

[1] Uprooting tests were carried out by S. B Mickovski, formerly of the James Hutton Institute, Invergowrie, and the output reanalysed in this Thesis.

The numerical models were developed in line with the *p-y* and *t-z* pile analysis techniques, used to model lateral and axial loading, respectively, and were constructed in Abaqus/CAE. They consider the root as a beam-column and the mechanical soil root interaction as a series of discrete non-linear springs. The properties of the springs were back calculated from the cross section-front laboratory shear box and uprooting tests, as well as being determined theoretically (using standard pile design codes). The results of the numerical models show that the *p-y* and *t-z* analysis techniques can be successfully applied to the study of soil root interaction, provided appropriate springs and root properties can be defined. Moreover, they show that the proposed tools improve substantially upon existing root analysis models by accurately predicting the uprooting force (axial) or shearing contribution (lateral) as a function of applied axial or lateral displacement of the soil root system during deformation. Standard pile design codes, however, were shown to require adjustment for the application of soil root interaction.

The output of the laboratory and numerical testing revealed a number of interesting findings, including: (i) A stress related parameter, such as dilation, provides a better representation of a roots contribution to soil shear strength than a root cohesion factor, which is currently used. (ii) The root area ratio, often used to define a root cohesion factor, is not directly related to root contribution (e.g. two samples with the same root area ratio, but different root lengths, stiffness's or diameters, will not necessarily have the same shear strength) (iii) Root bending capacity is significant in defining its reinforcing potential.

Overall, the predictive tools developed in this Thesis have advanced their predecessors by: incorporating the effects of root bending; modelling the progressive contribution of roots during soil deformation, and; utilising an analysis technique that is already well established in industry. At present, however, they are in the early stages of development and require considerable improvement (such as the development of theoretical design codes for estimating *t-z* and *p-y* springs suitable for plant root soil interaction) before they can be considered a useful tool in practice.

iv. Glossary

a	Length of root branches
A	Cross sectional area
A'_s	Constant
AD	Applied displacement
A_{FS}	Area of failure surface / shear plane
API	American Petroleum Institute
A_{pile}	Cross sectional area of pile
A_{plate}	Surface area of soil at edge of soil root plate
$A_{r,half}$	Cross sectional area of half root
A_{root}	Cross sectional area of (full) root
$A_{root\text{-}FS}$	The total cross sectional area of roots crossing a failure surface / shear plane
A_{RS}	Surface area of root / soil root contact area
BR_{max}	Maximum bending resistance
B_s	Constant
C	Constant
c.t.c.	Centre to centre
c'	Apparent soil cohesion
CIS	Constant Image Scale
c_R'	Additional apparent cohesion provided by roots
c_u	Undrained shear strength of soil
D_{50}	Average soil particle size
D_{av}	Average diameter
D_{bar}	Diameter of reinforcement bar
D_{pile}	Diameter of pile
D_{root}	Diameter of root
E	Young's modulus
E_B	Bending modulus
E_{lin}	Young's modulus of Linden wood
E_{pile}	Young's modulus of pile material
$E_{r,half}$	Young's modulus of half root
E_{root}	Young's modulus of (full) root
E_{vit}	Young's modulus of Viton rubber

E_{will}	Young's modulus of Willow root
f	Skin friction at the soil pile interface
F	Force required to pull a single root from a soil mass
$F_{bar\text{-}d}$	Force required to pull a reinforcement bar from drained soil
$F_{bar\text{-}u}$	Force required to pull a reinforcement bar from undrained soil
FBM	Fibre Bundle Model
FE	Finite Element
FEA	Finite Element Analysis
FEM	Finite Element Model
F_{fallow}	Force required to shear a fallow soil sample
F_{fib}	Force required to pull a fibrous root system from a soil mass
FOS	Factor of Safety
FOS_{pile}	Factor of safety of a pile reinforced slope
F_{pk}	Peak pull out force
F_R	Force resisting soil shearing
F_{root}	Additional shear force provided by a single root
F_{rooted}	Force required to shear a root reinforced soil sample
$F_{root\text{-}group}$	Additional shear force provided by root group
F_{wind}	Overturning force created by wind
GLS	Global Load Sharing
h	Width/depth of shear zone
h_d	Horizontal pile displacement
h_p	differential horizontal displacement between 2 patches
h_s	Height of soil
h_{soil}	Horizontal soil displacement
h_w	Height of water
I_D	Relative soil density
I_{pile}	Second moment of area of pile
I_R	Relative density index
$I_{r,full}$	Second moment of area of (full) root
$I_{r,half}$	Second moment of area of half root
I_s	Second moment of area of sample
K	Lateral earth pressure coefficient
k	Modulus of subgrade reaction

k_a	Active lateral earth pressure
L_{anc}	Anchor length
L_{bar}	Anchor length of reinforcement bar
L_E	Effective root length
L_e	Element length
$L_{e,sub}$	Length of element submerged in the soil
LEA	Limit Equilibrium Analysis
LLS	Local Load Sharing
L_n	Length along base of soil slice
L_o	Original length
L_{pile}	Length of pile
L_{root}	Length of root
L_s	Length of sample
LVDT	Linear Variable Differential Transformer
M_{cr}	Bending moment in pile at the point where it crosses the failure surface / shear plane
M_D	Driving moment
M_{max}	Maximum bending moment
M_{pile}	Bending moment in pile
M_R	Resisting moment
M_{root}	Bending moment in root
N	Nitrate
n_a	Constant
NI	Number of images
N_R	Number of roots
N_x	Number of roots in x direction
N_y	Number of roots in y direction
O	Centroid
P	Phosphate
p	Soil reaction to loading
p_e	Average soil reaction acting along an element
P_f	Applied transverse load
p_{full}	Soil reaction to loading from a full root
p_{half}	Soil reaction to loading from a half root
PIV	Particle Image Velocimetry

p_k	Value of p at data point k
p_m	P-multiplier
$p_{m\text{-}T}$	Total p-multiplier
p_o'	Effective overburden pressure
P_{pen}	Maximum pressure exerted by root to penetrate soil
p_{pile}	Soil reaction to loading from a pile
p_{pm}	Value of p at data point m
P_s	Force in spring
P_t	Applied tensile load
p_u	Ultimate soil reaction to loading
p_u	Value of p at data point u
p_{ud}	Ultimate soil reaction to loading at deep depths
p_{us}	Ultimate soil reaction to loading at shallow depths
P_V	Vertical loading
R	Radius
RAR	Root Area Ratio
RF	Reaction force in beam
R_{po}	Pull out rate
S	Sulphate
s	spacing
s_{root}	Root tortuosity
s_x	Spacing in x direction
s_y	Spacing in y direction
t	Vertical shear force between inclusion and soil
$t_{0.005}$	Value of t after 0.005m of applied displacement
T_1	Factor to account for root stretching
T_2	Factor to account for root slippage
t_{ic}	Image capture interval
t_{max}	Maximum interface shear force between inclusion and soil
t_{pile}	Vertical shear force between pile and soil
T_{root}	Tensile strength of root
$t_{z,top}$	Value of t when the top of an element reaches the soil surface
u	Pore water pressure
$UR3$	Rotation of inclusion

V_{cr}	Shear force at failure surface
V_{head}	Shear force at pile head
V_{max}	Maximum shear force
v_p	Differential vertical displacement between 2 patches
V_{pile}	Shear force in pile
V_{root}	Shear force in root
W_n	Weight of soil slice
W_{soil}	Weight of unstable soil mass
W_{trees}	Weight of above ground tree/plant mass
X	Lateral displacement of shear box
x	Depth from soil surface / strain gauge position
$x_{0.001}$	Average number of pixels between 1mm markers
$x_{elem,base}$	Distance between soil surface and base of element
$x_{elem,top}$	Distance between soil surface and top of element
y	Relative movement between inclusion and soil
Y_{head}	Vertical distance between pile head and centre of rotation of unstable soil mass
y_k	Value of y at data point k
y_m	Value of y at data point m
y_u	Value of y at data point u
z	Vertical movement of inclusion
α	Angle between root branch and primary root
α_1	Dimensionless factor
α_a	Adhesion factor
α_n	Angle between vertical and centre of soil slice
α_R	Parameter to account for root inclination
β	Angle of slope
β_f	Deflection of sample at failure
γ	Soil density
γ_{max}	Maximum soil density
γ_{min}	Minimum soil density
γ_s	Unit weight of soil
γ_w	Unit weight of water
δ	Angle of interface friction
$\Delta c'$	Change in apparent cohesion

ΔFOS	Additional Factor of Safety as a result of reinforcement
ΔL	Change in length
$\Delta\phi'$	Change in angle of friction
ε	Strain
ε_f	Strain at failure
ζ	Correction factor to account for root inclination, distortion and slope angle
η_g	Efficiency of pile group
η_i	Efficiency of individual pile
θ	Slope of failure surface / shear plane as it crosses pile
θ_w	Inclination of water flow
θ_R	Angle of root crossing shear plane
θ_γ	Angle of root distortion
λ_α	Angle used to define soil wedge
λ_β	Angle used to define soil wedge
μ	Coefficient of friction between root and soil
ν	Poissons ratio
ϖ_R	Additional friction angle provided by roots
σ	Stress
σ_n'	Normal effective stress
σ_{root}	Tensile breaking stress of root
σ_v'	Effective vertical stress
τ_{pers}	Friction between root and Perspex surface
τ_{pk}	Peak shear strength of soil
τ_{root}	Friction between root and soil
τ_S	Shear strength of soil
τ_{S+R}	Shear strength of root reinforced soil
φ	90-β
ϕ'	Angle of soil friction
ϕ_{cr}'	Critical angle of soil friction
ϕ_{pk}'	Peak angle of soil friction
ϕ_{sec}'	Secant angle of soil friction
χ	Slope of pile
ψ	Angle of dilation

v. Table of Contents

Chapter 1 Introduction

1.1 Background

Slope instability is a major geotechnical hazard worldwide and is predicted to intensify as a result of the changes in rainfall patterns that are brought about by global climate change (*Buma and Dehn, 1998; Dupuy et al., 2005*). It is in the interest of the engineer, therefore, to provide stabilisation techniques that not only improve the safety of slopes but endorse environmentally friendly and sustainable practice in construction (*Danjon et al., 2008*). Decades of research has shown that vegetation is an ideal medium for achieving this as it has the capacity to increase soil strength, protect surface soil from erosion, improve slope ecology and restore a natural environment (*Collison et al., 1995; Norris and Greenwood, 2006*). The latter two of these are not features of traditional stabilisation techniques and, moreover, vegetation can offer economic benefits through its low cost and ability to utilise local skills and materials (*Collison et al., 1995*).

Over the past few decades, as sustainability has become an increasing concern, there has been a surge of interest in the study of root functions. This interest lies not only in the area of using vegetation in infrastructure (termed bioengineering) but also in combating agricultural and forestry issues, such as: how to continue providing affordable food for an increasing population, how climate change influences crop yields (*e.g. Schlenker and Roberts, 2008*) and how to protect trees from toppling in extreme wind conditions (*e.g. Fourcaud et al., 2007*). This diverse research base has revolutionised the understanding of plant root functions and has resulted in the development of a number of analytical tools that measure the effects of vegetation. In terms of bioengineering, a number of calculation models that account for the effects of vegetation in slope stability have been developed (*e.g. Waldren, 1977; O'Loughlin and Ziemer, 1982; Schwarz et al., 2009*). Understanding and accurately quantifying soil root interaction, however, remains an unresolved problem (*Sonnenberg, 2008; Schwarz et al., 2009*) and this has resulted in slope stability models that over simplify both the soil root system and the properties of the roots. In their current state, therefore, these models fail to account for the full, or relevant, effects of vegetation (*Danjon et al., 2008; Sonnenberg, 2008; Stokes et al., 2009; Schwarz et al., 2009*).

The continual improvement and increasing availability of technology has seen the development of a number of procedures that allow non-invasive analysis of soil root systems under various loading conditions. For example: the use of transparent materials, X-ray transmission and particle image

velocimetry (GeoPIV). GeoPIV is an analysis tool, developed by White *et al.* (2003), that measures displacement fields by evaluating sets of digital images that capture soil deformation processes. It is becoming increasingly popular in the study of soil root interaction, and has developed a successful track record thus far. Of particular interest in this study is the work of Mickovski *et al.*(2007), Sonnenberg (2008) and Loades *et al.* (2009) who established effective techniques for excecuting laboratory tests in which roots are visible during loading. Using these tests, they were able to capture (using a digital camera) and analyse (using GeoPIV analysis) root and soil deformation during uprooting, slope failure and shearing processes with ease. Such a method radically reduces the problems associated with observing a root underground and therefore opens the door to increasing the understanding of soil root interaction, a key step in the development of a technique for accurately quantifying soil root interaction.

Current studies that focus on mechanical soil root interaction (e.g. *Gregory, 2006; Schwarz et al., 2010; Mickovski et al. 2010*) suggest that plant roots respond in a similar way to inert soil inclusions, such as soil nails or pile foundations, when subjected to loading. Despite this, very few attempts have been made to utilise existing soil nail or pile analysis techniques (which are detailed, well-researched and well-used in the field of geotechnical engineering) in the development of analytical tools. Figure 1.1 highlights and compares the properties of plant root and pile foundation systems. In this figure, the scale, material and architectural properties of the two systems are, unsurprisingly, shown to vary. Plant roots are small, complex systems whose properties are governed by an intricate matrix of factors (including local environment, species and age). This makes them difficult to accurately define. This contrasts to pile foundations, which are designed and manufactured to have a specific strength, scale and architecture. If, however, a plant root is considered, in its simplest form, as a beam-column with lateral supports then these two systems become comparable from an architectural perspective. Both consist of a key axial element that penetrates the soil and provides a column of material that compliments soil properties. In particular, both systems provide a degree of tensile strength and bending capacity to the soil, which is otherwise lacking in these areas.

With a focus on pile analysis techniques (which can be used to study both tensile loading and bending), this Thesis examines the suitability of existing engineering analysis models to the application of plant roots and assesses whether or not they can predict the response of a plant root to loading more accurately than the current plant root analysis models.

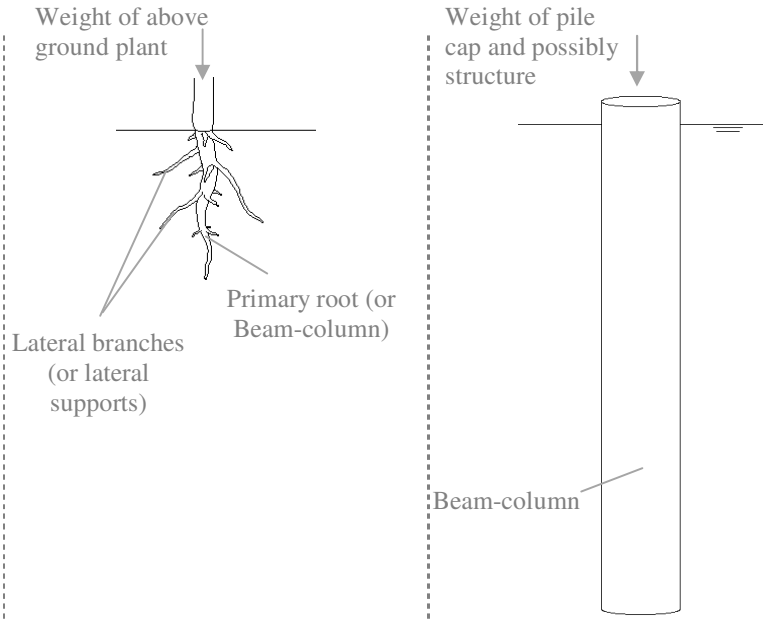

Property	Plant root system	Pile Foundation
Typical length:	< 2 m[1]	> 3 m
Typical diameter:	< 10 mm[2]	> 150 mm
Material:	Organic Non-uniform Dependant on age, species, environmental conditions[3]	Inert Approx. uniform Controlled during manufacture
Architecture:	Non-uniform Lateral branches/supports Tortuous, depending on species and environmental conditions[3, 4]	Approx. uniform along length No lateral support No tortuosity

References: 1. Kleidon (2004), 2. Operstein and Frydman (2000), 3. Fitter and Stickland (1991), 4. Lopez-Bucio *et al.* (2003)

Figure 1.1: Comparison of plant roots and pile foundations.

1.2 Aims and objectives

The aim of this Thesis is to develop a numerical tool that can be used to accurately predict the mechanical response of a plant root to imposed loading conditions and, in doing so, improve upon existing root analysis models. The numerical model will utilise existing pile analysis techniques. This will be met through the following key objectives:

i. Generate test data that can be used to analyse the effects of soil root interaction and verify the numerical modelling techniques that will be developed later: Perform a series of laboratory uprooting and direct shear box tests, which respectively expose the root to axial

and lateral loading (the two key loading mechanisms experienced by plant roots). For simplicity, and to reduce the variables between plant roots and pile foundations, consider inert analogue root systems within a silica sand sample. Use the test results to analyse: (a) the force required to pull a root from the soil mass (uprooting tests) and (b) the change in soil shear strength as a result of root inclusions (direct shear box tests).

ii. Observe and quantify the movement of a soil root system during loading: Using the same soil root systems as before, perform a series of laboratory tests in which the roots are clearly visible during uprooting and direct shear (in line with the established techniques developed by Mickovski *et al.* (2007), Sonnenberg (2008) and Loades *et al.* (2009)). Photograph the root at even time intervals throughout loading and then, using GeoPIV analysis, measure the movement of the root and soil during loading.

iii. Using the measurements gathered in Objective (ii), and a pile foundation design model, empirically estimate soil root interaction: The *t-z* and *p-y* modelling techniques are well used in industry to respectively estimate the axial and lateral response of a soil pile system to loading. In these techniques, the pile is considered as a beam-column and the soil as a series of discrete non-linear springs. The aim of this objective is to use the measurements gathered from the GeoPIV analysis to empirically calculate the properties of such springs for the soil root systems under consideration.

iv. Using standard engineering design codes, theoretically estimate the soil root interaction: Continuing with *t*-z and *p-y* theory, theoretically calculate the properties of the non-linear springs (i.e. soil root interaction) using standard engineering design codes for the soil root systems under consideration. Compare these springs with those calculated in Objective (iii) to assess the applicability of existing design codes.

v. Develop a numerical model, which utilises the quantification of soil root interaction, to predict the laboratory tests in Objective (i): Using the finite element programme Abaqus CAE, develop a simple, 2D numerical model that considers the root as a beam-column and the soil as a series of discrete non-linear springs. Define the spring properties using those calculated in Objectives (iii) and (iv). Use the model to predict the laboratory tests in Objective (i).

1.3 Thesis outline

Chapter 2 of this Thesis reports an extensive literature review that investigates: the properties and functions of plant root systems; current analytical models; slope stability, and; traditional stabilisation techniques.

Chapter 3 describes and discusses laboratory uprooting tests, including the selection of root analogues, testing techniques and test output data. The chapter then moves on to apply GeoPIV analysis to the digital photographs of visible root analogues and measures their displacement during loading.

Chapter 4 reports on the use of *t*-z modelling to (i) quantify axial soil root interaction, and (ii) develop a numerical model that predicts a roots response to uprooting. The suitability of standard pile design codes is discussed and modifications are suggested for their use in this application.

Chapter's 5 and 6 repeat Chapter's 3 and 4, but report on the direct shear box testing and the consequent numerical modelling of roots subjected to lateral loading, using *p*-*y* theory.

Chapter 7 concludes the research and offers suggestions for its future development.

Chapter 2 Literature review

2.1 Introduction

It is well established that vegetation can bring important engineering functions to a slope and that these directly influence both its surface and deep soil properties (*Norris and Greenwood, 2006*). To understand these functions, knowledge of the root system is required. This is a complex biological structure that is little known to the engineer.

In recent years, a number of computer models have been developed and used to improve the current understanding of root systems. These models cover an array of root functions, and have many applications, from looking at the hydrological cycle of a root reinforced slope (*e.g. Briggs, 2010*) to modelling the root growth patterns of different plant species (*e.g. SimRoot - Lynch et al., 1997*). Whilst promising, the majority of these models are either relatively basic (excluding important root characteristics) or extremely complex (difficult to replicate or adapt to slope stability applications). An additional area of study that is currently advancing is mechanical soil root interaction and its connection to increased soil strength (e.g. *Schwarz et al., 2010*). This has major applications in the development of a design standard for root reinforced slopes, as well as in the improvement of forest and crop management.

This Chapter presents a literature review covering (i) root physiology and key engineering parameters, and (ii) slope instability, traditional remedial techniques and the reinforcing potential of vegetation.

2.2 Root Physiology and key engineering parameters

2.2.1 Root Physiology

The root system is the plant's organ of absorption, transportation and attachment, typically sitting underground. It comprises primary roots, lateral roots, root caps and root hairs (Figure 2.1) and requires full collaboration of these in order to (i) acquire nutrients, minerals and water, (ii) transport these through the plant, and (iii) anchor the plant into the soil (*Pratt et al., 2007*). The material and architectural properties of the root system are driven by a combination of genetic control and local environmental conditions, which results in a wide variation of properties both within and between plant species (*Fitter and Stickland, 1991*).

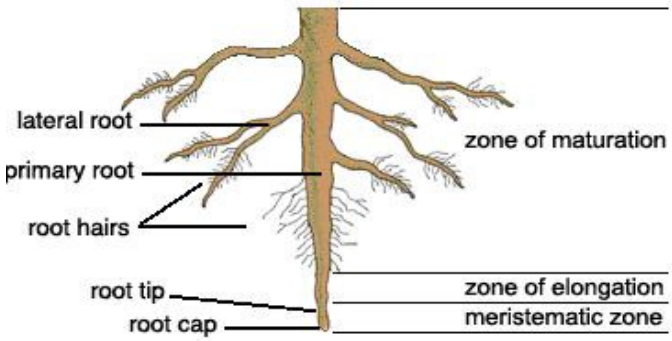

Figure 2.1: Overview of root physiology: A typical arrangement of primary roots, lateral roots, root caps and root hairs within a root system (*http://extension.oregonstate.edu/mg/botany/roots.html*)

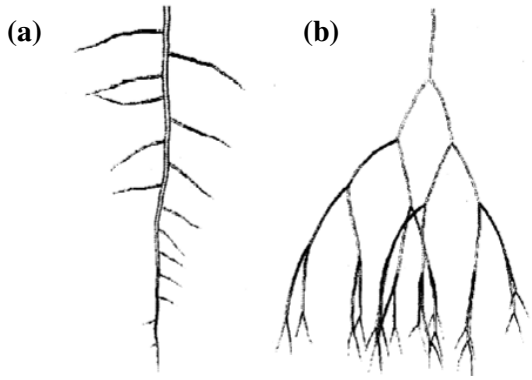

Figure 2.2: Examples of root architecture. (a) Lateral roots - grow from a primary root, (b) Dichotomous branching - each root terminates and initiates two new roots (*Lynch et al., 1997*).

In an attempt to generalise material and architectural properties, vegetation is commonly grouped into two categories. These are named herbaceous and woody. Herbaceous describes plants with thin, supple roots that die at the end of each growing season and woody describes plants with thick roots that are coated in layers of cork and live through all seasons (*Fogiel, 2004*). Herbaceous plants include herbs and most grasses and are generally smaller than woody plants, which include trees, shrubs and vines. Root branching pattern can also be generalised into two categories, namely lateral and dichotomous (see Figure 2.2). Lateral describes a branching system in which secondary roots grow from a primary root and dichotomous describes a system in which each root terminates to form two new roots. These branching patterns are indigenous to both woody and herbaceous vegetation.

2.2.2 Material Properties and Complexity in Root Microstructure

In order to accommodate its key functions, the cellular structure of a root varies along its length. This creates three distinct zones of unique material properties, known as: the zone of maturation, the zone of elongation and the meristematic zone (see Figure 2.1). The elongation and meristematic zones

control root growth and penetration, respectively, with the very tip of the root (meristematic zone) possessing flat hard cells that allow it to push through the soil (*Lijima et al., 2003*). The zone of maturation, on the other hand, dominates the length of the root and provides it with its overall structural integrity. As the main structural element, this Thesis focuses on the cellular structure, and consequent material properties, of the zone of maturation only.

The maturation zone comprises a number of layers of tissue, named: epidermis, cortex, endodermus, pericycle, cambium, phloem and xylem, as shown in Figures 2.3(a) and (b). Each of these layers plays a unique role in regulating the survival of the plant and, as such, has unique material properties. In terms of engineering properties, the xylem and cambium layers are the most significant as they drive the characterisation of tensile strength and stiffness, respectively (*Karam, 2005; Pratt et al., 2007*). The xylem tissue runs through the core of the root and is composed of long, cylindrical cells that are joined from end to end and provide unidirectional fibre orientation (*Karam, 2005*). Its purpose is to transport minerals, nutrients and water throughout the plant. This requires strong walled cells and thus large quantities of cellulose, the structural material from which cell walls are built (*Karam, 2005; De Micco et al., 2008*). Xylem tissue is therefore very strong. The cambium layer sits between the xylem and phloem tissues and generates layers of cork by separating secondary and primary xylem and phloem as the plant ages. It stands, therefore, that the cambium layer is not

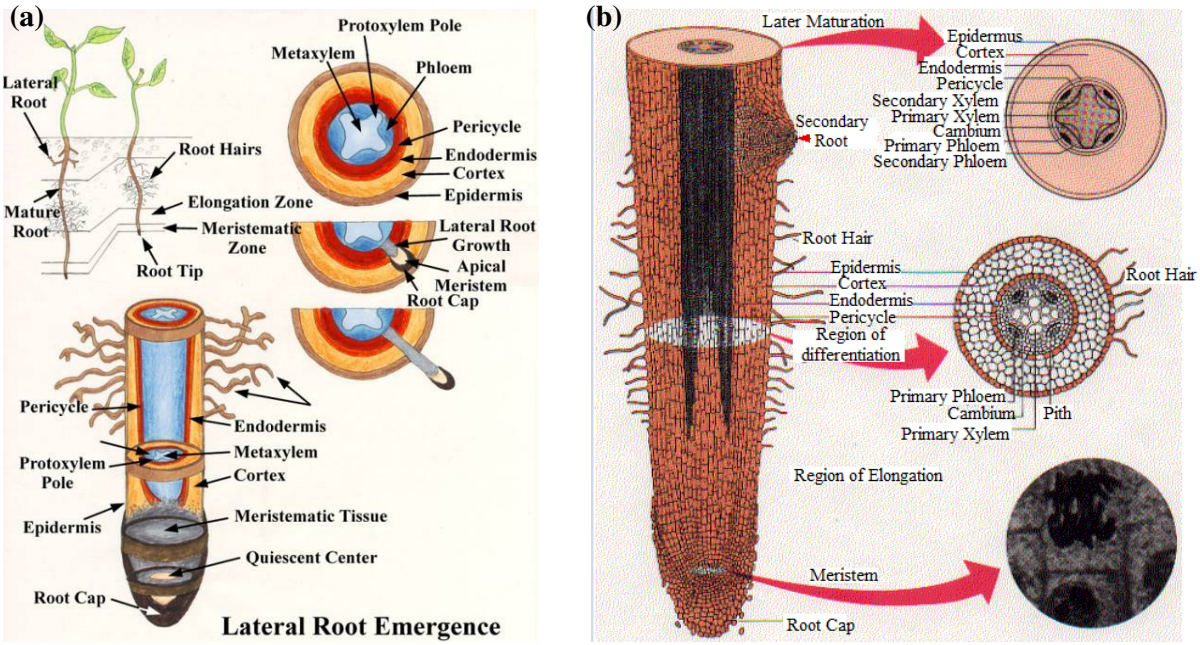

Figure 2.3: Layers of tissue that form (a) herbaceous (non-woody) roots (*www2.puc.edu/Faculty/Gilbert_Muth/art0060.jpg*), and (b) woody roots (*http://siera104.com/bio/planttissues.html*).

present in herbaceous species (see Figure 2.3). It also stands that during the early growth of a plant (i.e. before cork is generated) there is little difference in mechanical properties between roots belonging to herbaceous vegetation and those belonging to woody vegetation. Moreover, woody vegetation has seasonal non-woody roots that die over winter and regenerate over summer. The material properties of roots hereon will therefore be categorised as woody and non-woody, where non-woody describes both herbaceous and young woody roots.

2.2.2.1 Root Stiffness

The cork layers that are present in woody roots provide a stiff outer shell, which improves their resistance to lateral loading. As a result, the Young's modulus of a woody root can be significantly greater than that of an equivalent non-woody root. As cork layers are a product of the root aging process, it is fair to assume that Young's modulus increases with plant age. A difference in Young's modulus also exists, however, between different non-woody roots and different woody roots, albeit considerably lesser (*Operstein and Frydman, 2000*). This suggests that cork is not the only significant factor in defining Young's modulus. This is confirmed in Figure 2.4, which shows a relationship between root diameter and root stiffness. In particular, root stiffness increases exponentially with decreasing root diameter. Such a relationship can be represented mathematically as shown in the equation below (*e.g. Waldren and Dakessian, 1981; Operstein and Frydman, 2000; van Beek et al., 2005; Mickovski and van Beek, 2009*):

$$E_{root} = A \cdot e^{(B \cdot D_{root})} \qquad \text{Eq 2.1 (a)}$$

Where: $\boldsymbol{E_{root}}$ is the value of Young's modulus for the root; $\boldsymbol{D_{root}}$ is the root diameter, and; $\boldsymbol{A}$ and $\boldsymbol{B}$ are constants, which have unique values for each plant series.

An alternative method of describing the relationship between E_{root} and D_{root} is to consider a power equation, as shown in Equation 2.1 (b) (*e.g. Operstein and Frydman, 2000*).

$$E_{root} = A \cdot D_{root}^{\ B} \qquad \text{Eq 2.1 (b)}$$

As demonstrated in Figure 2.4 (which fits two trend lines to measured data, one using an exponential equation and the other using a power equation), Equation 2.1 (b) underestimates the general data trend when the root diameter is small ($D_{root} < 2$mm, in this case). Equation 2.1 (a), on the other hand, provides an improved, but less conservative, fit to the data. Both equation forms are reported in literature.

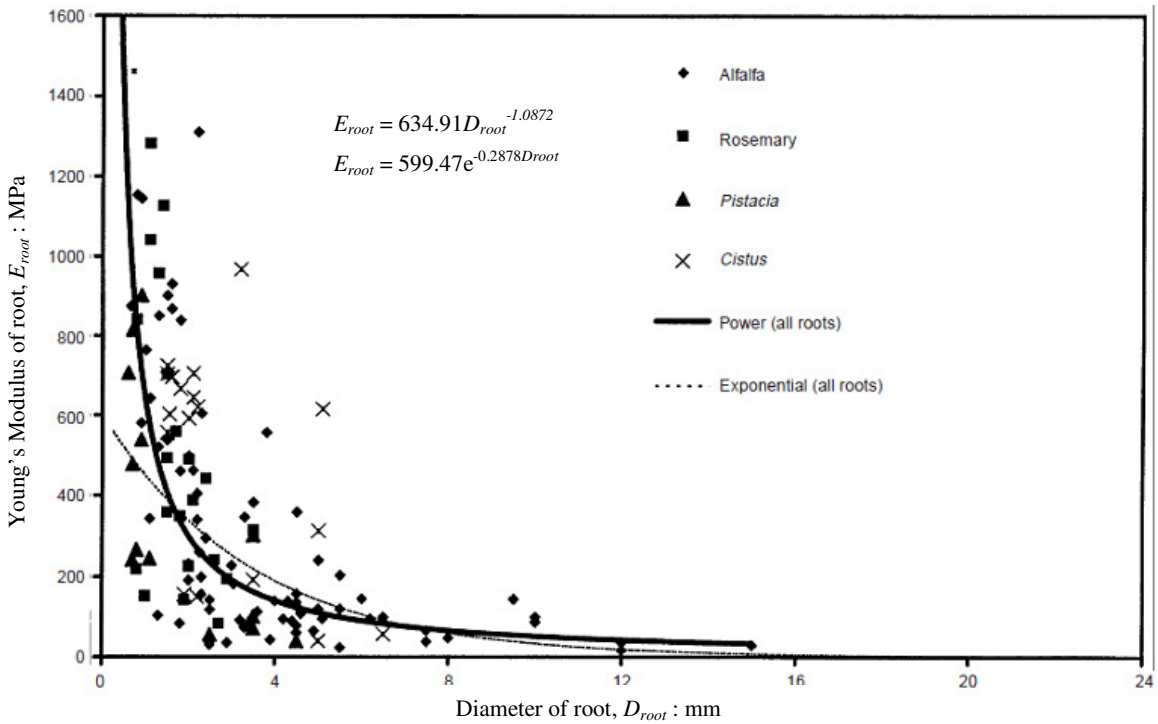

Figure 2.4: Effect of root diameter on Young's modulus (*Operstein and Frydman, 2000*)

Equations 2.1 (a) and (b) employ root diameter and some constants, which are distinct for each plant species, to determine E_{root}. It should be noted, however, that these constants may also vary between plants of the same species if they are grown in different local environments. In particular, vegetation grown in an environment with low to moderate dynamic loading is known to be significantly less stiff than vegetation grown in an environment with high levels of dynamic loading (*Read and Stokes, 2006*). Unlike traditional engineering materials, therefore, the stiffness of a root will improve with age (*Hamza et al., 2006*) and under adverse loading conditions. Cork remains, however, the most significant factor influencing root stiffness.

2.2.2.2 Root Tensile Strength

In tension, roots display an initial elastic response to loading and can stretch by up to 10% until a maximum strain is reached and the root fails (*Hamza et al., 2006; Gregory, 2006*). Such failure typically follows two stages, (i) breakage of the stiffer outer root structure followed by (ii) breakage of the inner root structure (*Hamza et al., 2006*). The tensile force required to cause total failure of a root is influenced primarily by: root geometry, plant species and root age.

Past research (*e.g. Waldren and Dakessian, 1981; Operstein and Frydman, 2000; van Beek et al., 2005; Mickovski and van Beek, 2009*) has revealed a strong relationship between root diameter and root tensile strength, which is similar to the relationship between root diameter and stiffness if tensile strength is considered as a stress. In particular, root tensile stress decreases exponentially with increasing root diameter, as shown in Figure 2.5 (a) and expressed in Equation 2.2 (a);

$$T_{root} = C \cdot e^{(D \cdot D_{root})} \qquad \text{Eq 2.2 (a)}$$

Where; $\boldsymbol{T_{root}}$ is the root tensile stress; $\boldsymbol{D_{root}}$ is the root diameter, and; $\boldsymbol{C}$ and $\boldsymbol{D}$ are constants, which are unique to the plant species under consideration (and different from the constants used to define $\boldsymbol{E_{root}}$).

Past literature also reports the more conservative use of a power equation, in the form shown below (*e.g. Operstein and Frydman, 2000*):

$$T_{root} = C \cdot D_{root}{}^{D} \qquad \text{Eq 2.2 (b)}$$

Using the data in Figure 2.5 (a), an alternative relationship between tensile strength and root diameter was calculated, where tensile strength is considered as a breaking load rather than a breaking stress (Breaking load = $T_{root} \cdot A_{root}$). This relationship is shown in Figure 2.5 (b). As demonstrated, while the strength of the root per unit area decreases with increasing diameter (Figure 2.5 (a)), the overall strength of a larger diameter root is generally greater than that of a smaller diameter root (Figure 2.5 (b)). That is, the larger the cross sectional area of the root, the larger the force required to break it.

The presence of factors *C* and *D* in Equations 2.2 (a) and (b) shows that plant species plays a role in determining T_{root}. Despite variation in root tensile strength between plant species, however, there is no clear difference between woody and non-woody roots (*De Beats et al., 2008*). A woody root can be stronger in tension than a non-woody root and vice versa. Testing the relationship between tensile strength and other geometrical features, such as length and number of lateral roots, has received very little attention. It is likely that this is because the few tests that have been carried out have indicated no correlation (*e.g. Ali, 2010*).

As a root ages, its cell walls develop reinforcement, which increases its cellulose content (*Karam, 2005*). This indicates an increase in tensile capacity over time (*Karam, 2005; Genet et al., 2005*). Little test data exists in this area, however, and that which does exists does not provide a conclusive outcome. For example, Sonnenberg *et al.* (2010) conducted a series of tensile tests on the roots of plants aged between 135 and 290 days, finding an increase in tensile strength over time (as shown in

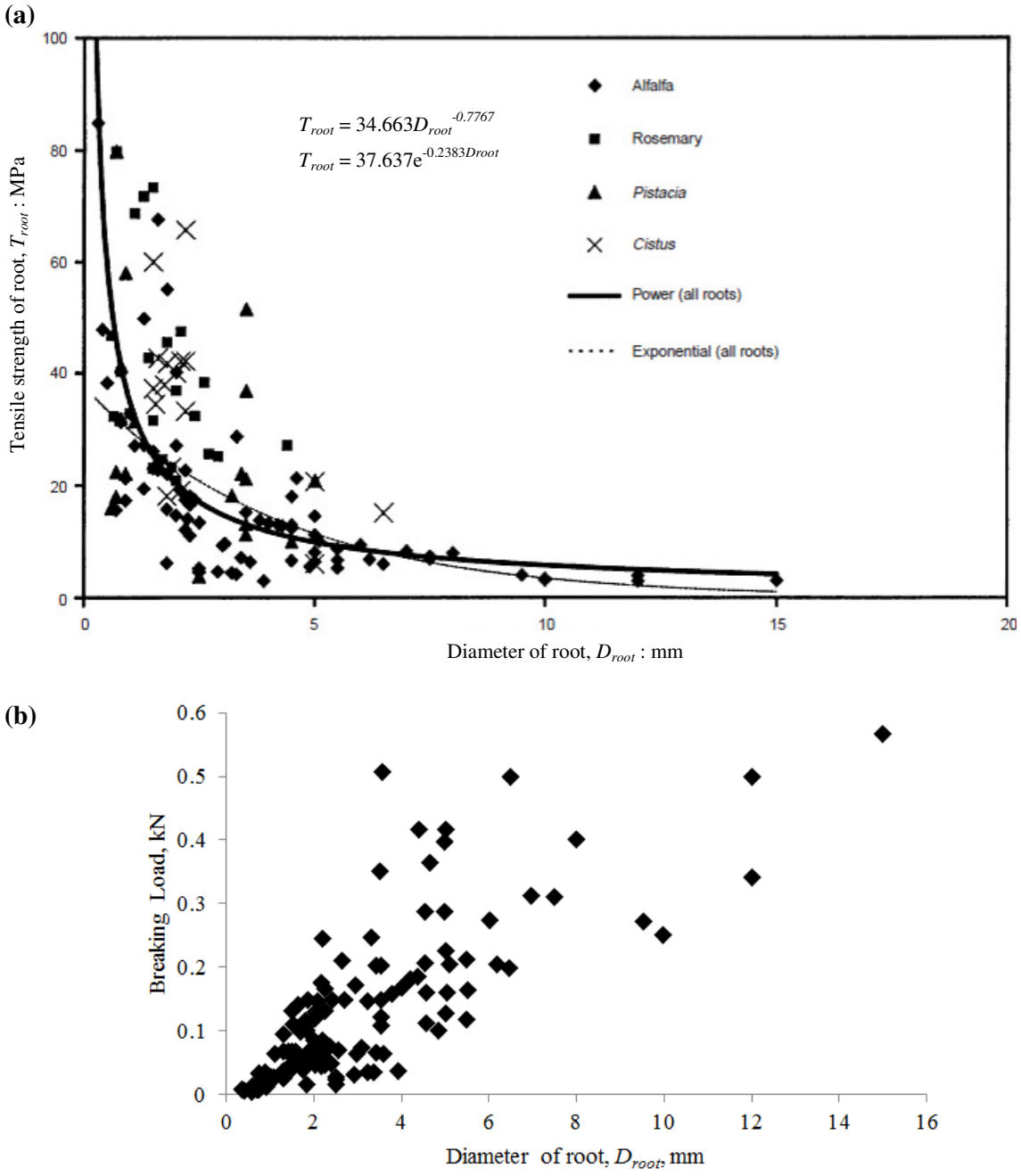

Figure 2.5: Effect of root diameter on tensile strength (a) where tensile strength is considered as a stress (*Operstein and Frydman, 2000*) (b) where tensile strength is considered as a breaking load (*Adapted from Operstein and Frydman, 2000*)

Figure 2.6(a)). This finding confirms testing carried out by Loades *et al.* (2009). Operstein and Frydman (2000), however, carried out a series of tensile tests on roots of similarly aged plants, finding that overall tensile strength is relatively insensitive to age (as shown in Figure 2.6(b)). All of these tests, however, consider the roots of relatively young plants only (< 290 days), which may be

influencing the results. Moreover, the age of a root is not necessarily the same as the age of its plant. A discrepancy in the age of the roots may therefore also be influencing the results. The only conclusive outcome, therefore, is that root strength either increases or remains consistent over time and that this holds true provided that the above ground portion of plant isn't destroyed, in which case tensile strength decreases significantly with age (*Gray and Sotir, 1996*).

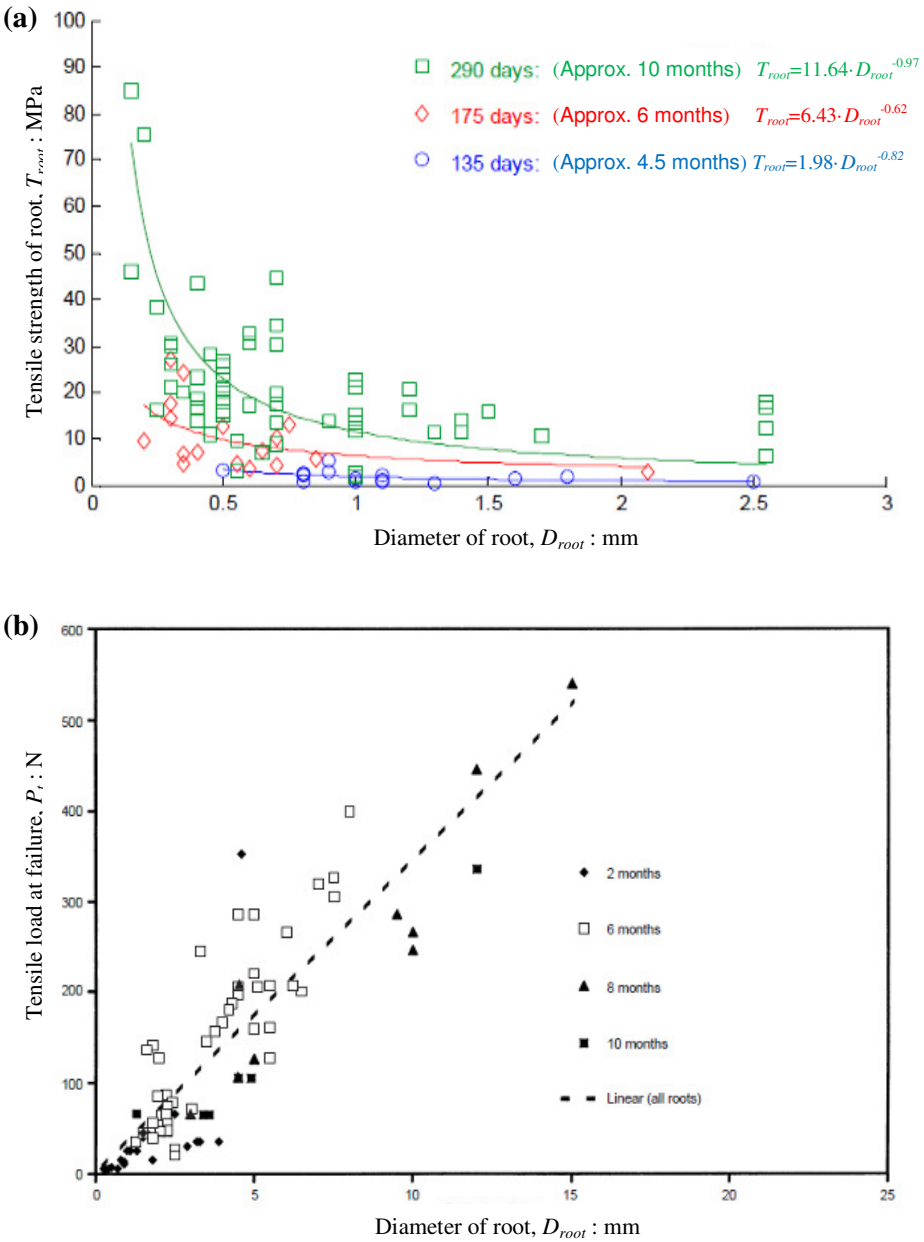

Figure 2.6: (a) Relationship between tensile strength and diameter for roots of different ages (*Sonnenberg et al., 2010*), (b) Relationship between failure load and diameter for roots of different ages (*Operstein and Frydman, 2000*).

In contrast to their strong tensile capacity, roots are very weak in compression (*Ali, 2010*). Windsor-Collins *et al.* (2008) suggest that, when considering woody plants, the compressive strength of a root is around 50% of its tensile strength (although this may vary depending on plant species). Soil, however, is very strong in compression and weak in tension. Through combining these materials, a fibre reinforced composite that is much stronger than its counterparts can be created.

2.2.3 Root Architecture

In order to ensure sufficient anchorage and absorption, roots readily adapt to changes in their environment (*Fitter and Stickland, 1991*). In the past, it was thought that absorption dominated the environmental development of a root's architecture, with sufficient anchorage being provided through the high tensile capacity of individual roots (*Gregory, 2006*). Anchorage, however, has since been shown to play a significant, if not larger, role in root morphology (*Gregory, 2006*). This Section provides a brief overview of the links between root genetics, anchorage requirements, absorption requirements and root architecture.

2.2.3.1 Plant Genetics

Controlled laboratory experiments have shown that selected genes within a plant largely influence the size, plasticity and branching pattern of its root system (*e.g. Saleeba et al., 2009*; *Silva et al., 2003; Norris et al., 2008*). For example, herbaceous plants have highly flexible stems, which transmit mainly tensile forces to their roots. As a result, they produce shallow, fine, fibrous root systems (Figure 2.7(a)) (*Ennos, 1993*). Shrubs and trees, on the other hand, have stiff stems that translate both tensile and overturning forces to their root systems, which are consequently stiffer, deeper and more favourable for slope stability applications.

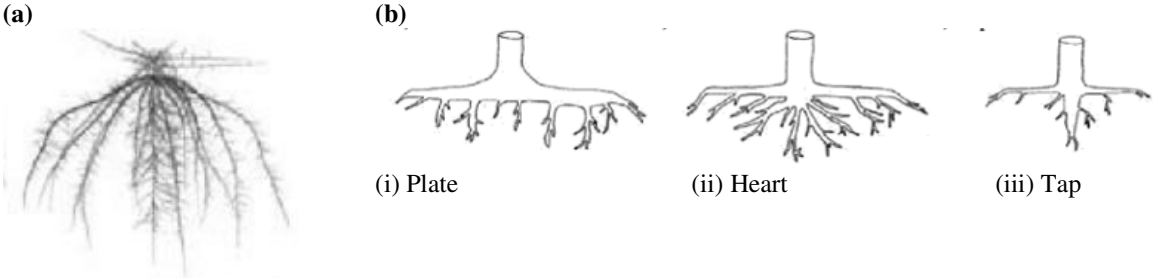

Figure 2.7: (a) Fibrous herbaceous root formation (*Walk et al., 2004*), (b) Architectural forms of woody roots (*Norris et al., 2008*).

The general architecture of woody roots can be categorised into plate, heart and tap (Figure 2.7 (b)). Plate and heart are examples of fibrous root systems, but are significantly less fine than the fibrous systems found in herbaceous plants. Plate root systems are relatively shallow and have large, approximately horizontal, lateral roots off which vertical sinkers grow. Heart root systems comprise a number of oblique, horizontal and vertical roots that emerge from the base of the stem (*Norris et al., 2008*). Tap root systems have a single, approximately vertical root off which branches grow and are not uncommon in herbaceous species that have stiffer stems. The form of root architecture adopted by each plant species is dependent on genetic control. As suggested in Figure 2.7, the natural development of a root system is approximately symmetrical.

2.2.3.2 Soil Properties and Absorption Requirements

The majority of roots within a root system are found in the top layers of a soil, where the best nutrient, water, penetration and aeration conditions are found (*e.g. Mafian et al., 2009*). Root biomass, therefore, decreases with increasing soil depth (*De Beats et al., 2007*). In general, 50% of a roots biomass can be found in the top 500mm of a soil and 95% in the top 2m (*Schenk and Jackson, 2002*). A minority of roots, however, can grow to great depths. This is shown by Kleidon (2004), who compiled a database of the maximum hydraulically active rooting depth of various species (see Figure 2.8). This highlights the large variation in root properties as a result of species and environmental conditions.

To penetrate a soil, roots can exert a maximum pressure in the region of 0.8 - 1.5 MPa (*Schwarz et al., 2010*) or more specifically through the following equation (*Materechera et al., 1991*):

$$P_{pen} = 242 \cdot D_{root}^{0.94} \qquad \text{Eq 2.3}$$

Where; $\boldsymbol{P_{pen}}$ is the maximum pressure a root can apply to penetrate the soil (measured in kPa), and; $\boldsymbol{D_{root}}$ is the roots diameter (measured in mm).

If the soil strength exceeds P_{pen}, roots can accommodate growth by either exploiting large cracks and pores or displacing soil particles to increase the size of voids (*Clark et al,. 2003*). These actions result in stunted root length, increased root diameter and a clumped spatial distribution (*Materechera et al., 1991; Tardieu, 1994; Clark et al., 2003*). Materechera *et al.* (1991) compared the root lengths of 22 plant species grown in a strong soil (penetration resistance of 4.2 MPa) against those grown in a control soil (vermiculite, penetration resistance of 0 MPa). In these tests, penetration resistance was measured by driving a small steel cone (diameter of 2.0mm and side slope of 30°) to a depth of 32mm

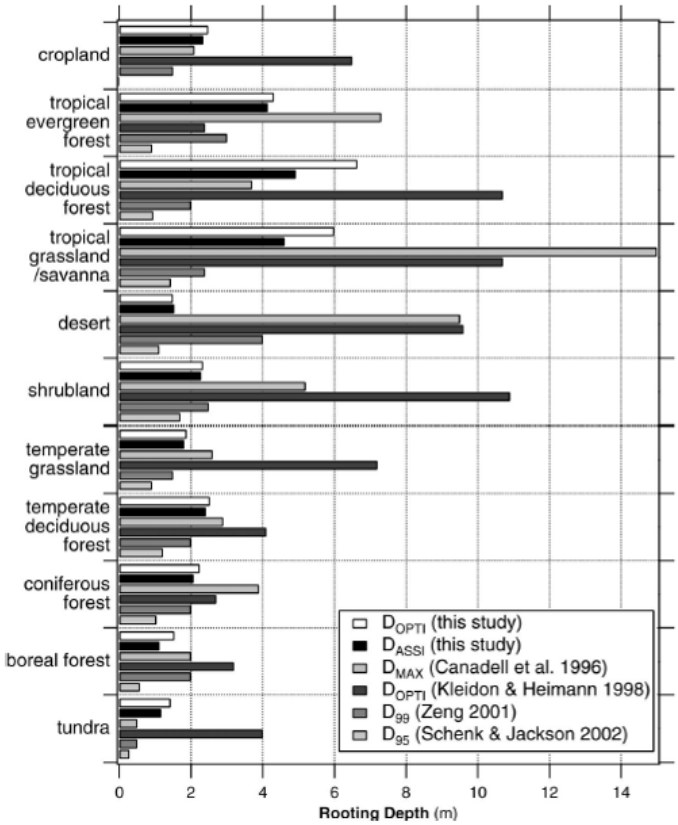

Figure 2.8: Maximum rooting depth compiled from various authors (*Kleidon, 2004*). Note: D_{OPTI} = Rooting depth inferred assuming vegetation is optimally adapted to its environment (maximisation of net carbon uptake); D_{ASSI} = Rooting depth inferred assuming water availability affects rooting depth (assimilation); D_{MAX} = Observed maximum rooting depth; D_{99} = Inferred using maximisation of root profiles at a depth containing 99% of root biomass; D_{95} = Inferred using maximisation of root profiles at a depth containing 95% of root biomass.

(approx. depth of root elongation considered in the experiment) through holes in the plant growth apparatus (apparatus used for growing the seedlings/roots). The force at the tip of the cone was measured using a proving ring and converted to a penetration resistance using the area of the cone. A 90% decrease in root length was found in the strong soil when compared to the roots grown in the control soil. This was found to relate to an increase in root diameter, due to the requirement of a root to generate a reasonable surface area for nutrient absorption and anchorage. Conversely, roots have also been found to narrow their diameter in order to grow through solid pores in impenetrable soil (*Bengough et al., 1997*). These phenomena contribute to the dense root distributions in the upper soil layers, where soil is generally less compact.

The patchy, and sometimes scarce, occurrence of nutrients and water also impact root morphology. Roots tend towards patches of nutrient, and/or, water rich soil and this can result in skewed root

distributions with areas of high root intensity (*Oriens et al., 2002*). Figure 2.9 compares the effects of nutrient scarcity and nutrient availability on root development, showing large variations in the number, length and distribution of lateral roots. In particular, roots tend to increase their surface area when nutrients are scarce, thus increasing absorption (*Mickovski and Ennos, 2003*). Possibly the most notable alteration in architecture, however, occurs with reduced phosphate levels. This creates a phenomenon known as cluster roots, where a large number of small rootlets are produced within a small area along a primary or lateral root such as to mobilise nutrients and increase uptake (*Lopez-Bucio et al., 2003*). In addition, the overall depth of the root system is stunted. The hairs present on these rootlets adhere strongly to soil particles and organic matter, providing improved bonds between the soil and the root (*Skene, 1998*).

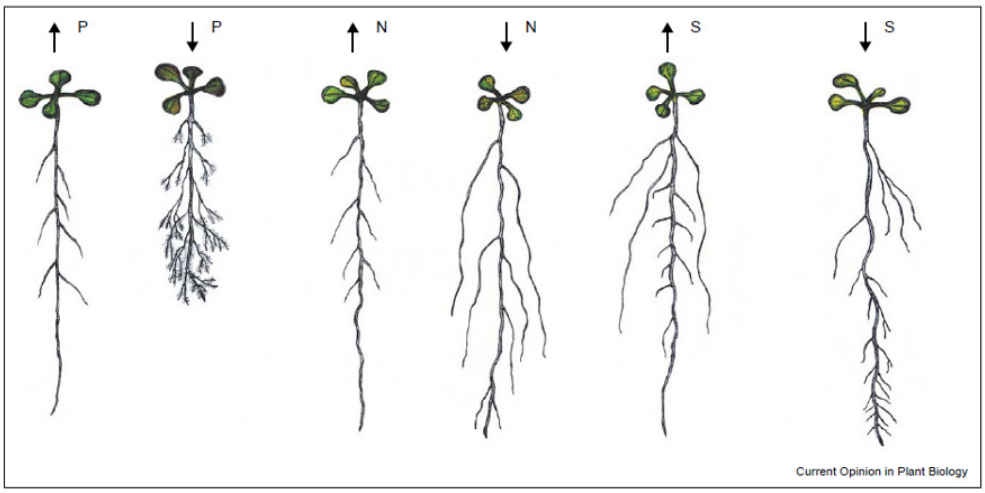

Figure 2.9: Response of root architecture to nutrients in the soil. P = Phosphate, N = Nitrate and S = Sulphate (*Lopez-Bucio et al., 2003*).

The properties of a soil (in particular its strength and nutrient content), therefore, have a significant impact on root morphology. This will impact the mechanical soil root interaction that occurs when the root or upper plant is subjected to loading.

2.2.3.3 Anchorage Requirements

When the above ground portion of a plant is subjected to loading, particularly from strong wind events or animal grazing, various axial and lateral forces are translated to the root system. As such, the root requires a combination of fibrous and rigid elements to resist uprooting and overturning, respectively (*Ennos, 1993; Dupuy et al., 2007*). The location, scale and quantity of these elements are related to the magnitude and frequency of loading during root growth as well as genetic factors.

Due to their supple nature, herbaceous plants are more likely to either be uprooted from the soil or incur stem breakage, while stiffer woody plants are more likely to overturn, pull out or break.

Yen (1987) proposed a system for classifying different root architectures based on their branching pattern and general form. This is shown in Figure 2.10. Of these root patterns, the VH- and H-types were reported to be superior in slope stability applications, while the H- and M-types were reported to be superior for use in soil restoration and soil reinforcement (*Fan and Chen, 2010*).

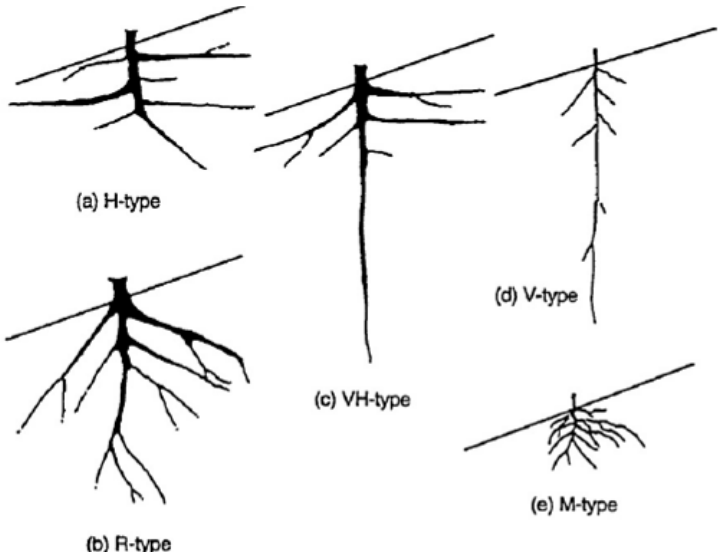

Figure 2.10: Classification of different architectural patterns, as proposed by Yen (1987).

2.2.3.3.1 Uprooting

There are three key factors that influence the resistance of a single root to uprooting. These are: the strength of the root, the strength of the soil and the soil root contact area. Using these factors alone, the force required to either dislodge a root from the soil (*Ennos, 1993; Gregory, 2006*) (Equation 2.4) or induce tensile failure (*Wu et al., 1979*) (Equation 2.5) can be estimated:

$$F = A_{RS} \cdot \tau_S \qquad \left[A_{RS} = \pi \cdot D_{root} \cdot L_{anc}\right] \qquad \text{Eq 2.4}$$

$$T_{root} = \frac{4 \cdot \sigma_{root}}{\pi \cdot D_{root}^{\ 2}} \qquad \text{Eq 2.5}$$

Where; $\boldsymbol{F}$ is the force required to dislodge a root from the soil; $\boldsymbol{A_{RS}}$ is the root surface area (or the root soil contact area); $\boldsymbol{\tau_S}$ is the shear strength of the soil; $\boldsymbol{D_{root}}$ is the root diameter, $\boldsymbol{L_{anc}}$ is the root anchor length, $\boldsymbol{T_{root}}$ is the root tensile strength, and; $\boldsymbol{\sigma_{root}}$ is the tensile breaking stress of the root.

The failure mechanism of the soil root system during uprooting (dislodging or root breaking) is governed by that which requires a lesser force (i.e. the lesser of F and T_{root}). Equation 2.4 suggests that a soil root system composed of a higher strength soil and a larger root surface area will have a superior resistance to failure (*Gregory, 2006*). Undeniably, a larger surface area allows a quicker transfer of tension from the root to the soil (*Stokes et al., 1996*), which if strong will provide a high resistance to the resulting shear force. In such a system, it is likely that root breakage will govern failure. A positive linear correlation between uprooting and surface area has been confirmed through a number of studies (*e.g. Ennos, 1993; Operstein and Frydman, 2000*). Similarly, the improvement of root pull out resistance in stronger soils has been confirmed (*e.g. Norris, 2005; Mickovski et al., 2007*).

Ennos (1993) expands on Equations 2.4 and 2.5 to consider the pull out capacity of an entire fibrous root system. This is achieved by multiplying both equations by the number of roots present, N_R, and assuming that: the root system is symmetrical; branching is insignificant, and; each root has the same diameter and length (as shown in Figure 2.11). Considering a collection of, rather than single, roots introduces the additional failure mechanism of shearing at the edge of the soil root plate, rather than around the perimeter of the root (i.e. the rooted soil mass failing as a block). Using the same parameters as before, Ennos (1993) suggests that this failure can be described as follows;

$$F_{fib} = A_{plate} \cdot \tau_S \qquad \left[A_{plate} = 2 \cdot \pi \cdot L_{anc}{}^2\right] \qquad \text{Eq 2.6}$$

Where; $\boldsymbol{F_{fib}}$ is the required pull out force for a fibrous root system; $\boldsymbol{A_{plate}}$ is the surface area of the soil at the edge of the soil root plate (assuming a hemisphere with a radius of $\boldsymbol{L_{anc}}$), and; $\boldsymbol{\tau_S}$ is the shear strength of the soil.

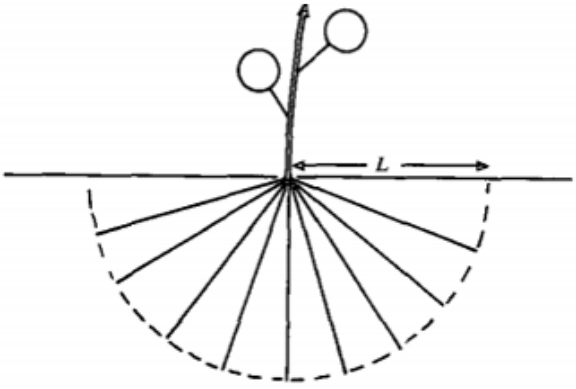

Figure 2.11: Simplified model of a fibrous root system used to ascertain pull out resistance (*Ennos, 1993*)

Despite reasonable success, Equations 2.4 to 2.6 fail to account for the intricacies of root architecture, such as asymmetrical spatial distribution and lateral root patterns. These properties can significantly alter the distribution of plastic strains and stresses within a soil (*Fan and Chen, 2010*) and are reported to have a significant impact on pull out resistance (*e.g. Dupuy et al., 2007; Mickovski et al., 2007*). Additionally, these equations do not account for the properties of a root system that influence soil root friction, such as root hairs and root exudate. Equations 2.4 to 2.6, therefore, oversimplify the complex relationship between soil and roots and, as a result, provide a crude representation of the relationship between applied displacement and root dislodging.

The number of lateral branches influences the pull out resistance of a root. Ali (2010), who conducted *in situ* pull out tests of three different species of tropical plant, found this relationship to be positive and linear, as shown in Figure 2.12. This positive relationship is likely to result from a combination of increased root surface area and changes in the mechanical response of the soil root system. Mickovski *et al.* (*2007*) used GeoPIV analysis (described in detail in Section 3.5) to study the uprooting behaviour of single roots in both different soil conditions and with different branching patterns. They found that the movement of soil surrounding roots with lateral branches is much more complex than the movement of soil surrounding simple tap roots and that this increased work results in an increase in the system's resistance to axial loading. In addition, they found that the location of lateral branches on the root is critical, as shown in Figure 2.13. In particular, lateral branches that are located deeper along the primary root, where the stresses in the soil are higher, were found to provide improved uprooting resistance (*Mickovski et al., 2007*). The dichotomous branching pattern is therefore considered to be the most efficient in providing resistance to pull out (*Stokes et al., 1996; Mickovski et al., 2007*).

The orientation of a primary root has a significant impact on its uprooting capacity, as it influences the magnitude of the axial force within the root. The axial forces will reduce as the angle between the roots axis and the direction of pull out increases. Such loading also induces bending. The orientation of lateral branches, however, does not impact uprooting capacity, as their orientation continually changes during loading (*Schwarz et al., 2010*). Applying this theory to an entire root structure, it is apparent that a system with a high number of small diameter, randomly orientated roots will be more efficient in resisting uprooting than a system with a small number of large diameter roots (*e.g. Ennos, 1993; Bailey et al., 2002*). This is the result of: (i) increased surface area, (ii) uneven load distributions and (iii) complications in load distributions caused by the interaction between roots

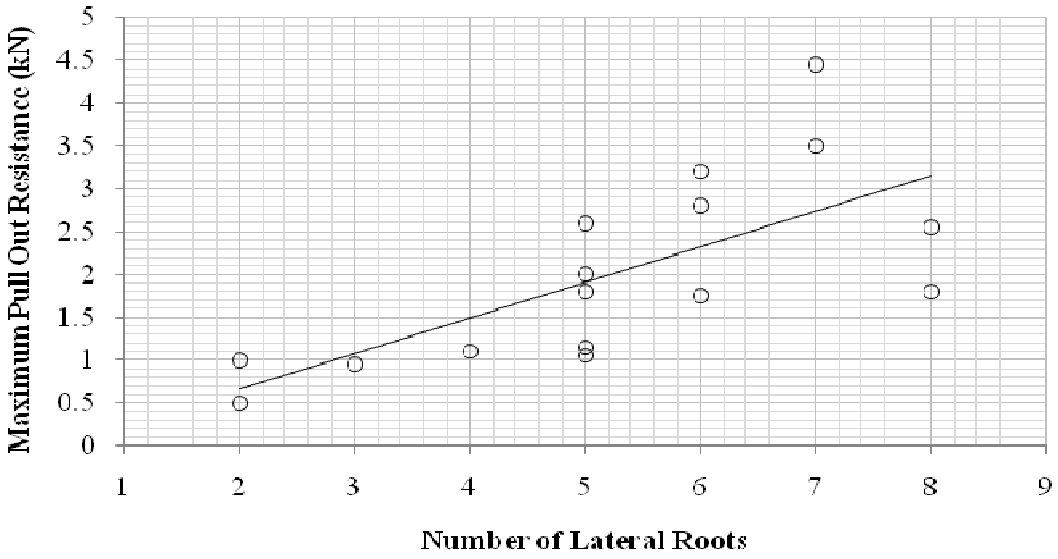

Figure 2.12: Effect of lateral roots on pull out resistance (*Ali, 2010*)

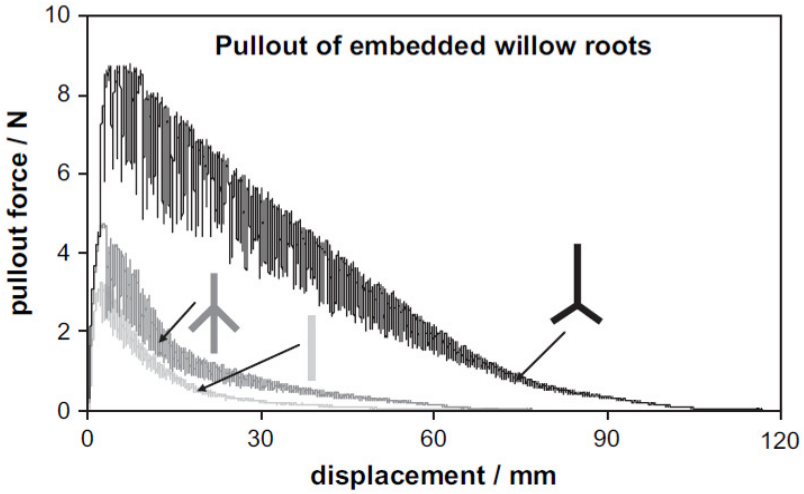

Figure 2.13: Comparison of uprooting force required to pull roots with different branching patterns from the soil (*Mickovski et al., 2007*).

(*Bailey et al., 2002*). In weak soils, where *F* governs failure (*Norris, 2005*), fibrous root systems are very favourable. Such a system is less favourable in strong soils, however, as they typically have slender roots that break in tension before their tips can contribute to their resistance (*Ennos, 1993; Mickovski and Ennos, 2003*).

The manner in which roots weave through soil creates tortuosity, see Figure 2.14. This results in an effective root length that under tensile loading takes time to straighten. It is not until the root is straight that its tissue goes into stress. This results in the first part of a root's strain curve displaying

an E_{root} value that can be underestimated by up to 60% (*Schwarz et al., 2010*). Tortuosity is typically described as a ratio of effective length to actual length as shown below;

$$s_{root} = L_{root} / L_E \quad \text{Eq 2.7}$$

Where; s_{root} is the root tortuosity; L_E is the effective length of the root, and; L_{root} is the root length.

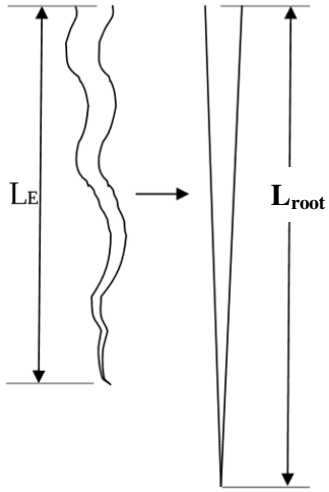

Figure 2.14: Explanation of root tortuosity, showing the root as it grows in the soil, and the root straightened to reveal its true length.

2.2.3.3.2 Overturning

Overturning is a failure mechanism most common to woody plants and is generally the result of strong winds applying a lateral load to the above ground plant. Resistance to overturning is a function of root stiffness, soil compressive resistance and root pull out resistance (or soil root interaction) (*Gregory, 2006*). It is also influenced by the point about which the system rotates, which is driven by the properties of the soil root composite (or soil root plate). Figure 2.15 shows the likely overturning mechanisms of plate, heart and tap root systems.

Fourcaud *et al.* (2007) used finite element analysis to study the relationship between root morphology in fibrous root systems and overturning, finding that small changes in architecture result in large changes in the shape and scale of the soil root plate and the location of its rotation axis (Figure 2.16). The properties of the soil were also reported to be significant, with stronger soils developing a rotation axis towards the centre of the soil root plate and weaker soils developing a rotation axis towards the edge of the soil root plate. In the latter, failure of the roots and/or the soil root bond was shown to dominate the overall failure of the system (i.e. individual root breakage or pull out) (Figure

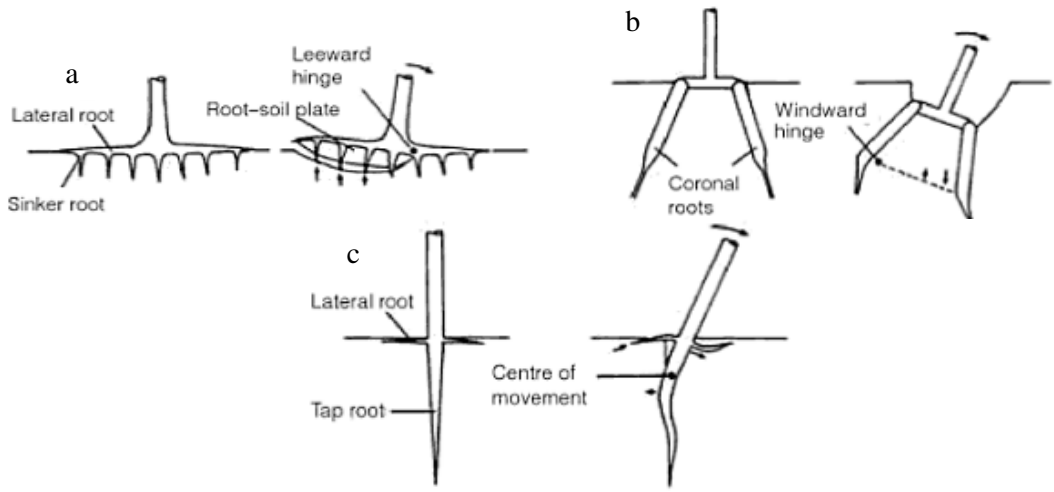

Figure 2.15: (a) Rotation of plate root system, (b) rotation of a lateral root system and (c) rotation of a tap root system. Gregory (2006).

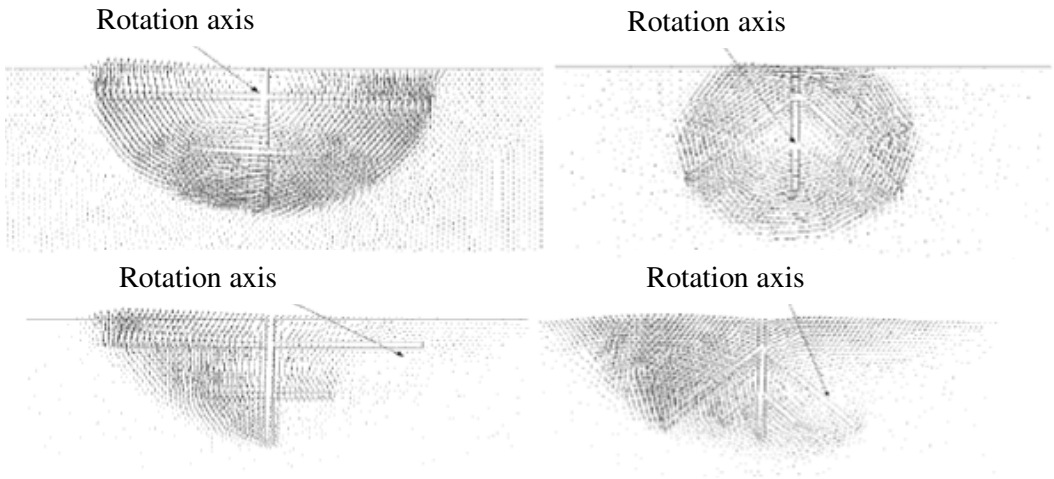

Figure 2.16: Change in position of rotation axis and soil root plate depending on root morphology and soil properties [upper images: stiff soil; lower images: loose soil] Displacement vectors shown on image. (*Fourcaud et al., 2007*).

2.16). In the former, however, failure was dominated by the soil shearing along the plate's perimeter as the whole system rotated. These mechanisms have a significant influence on the development of root growth. For example, it has been demonstrated that if unidirectional lateral loading is consistently applied to a plant, the root system generates an increase in root mass on its leeward side (that which sits opposite the point of applied load) through increasing the number and scale (i.e. the length and diameter) of roots, and a change in root angles (*Sun et al., 2007; Burylo et al., 2009*). Similarly, roots on the windward side (that which houses the applied load) develop a higher number of lateral branches per unit length, increasing soil root friction and thus pull out resistance (*Read and Stokes, 2006*). This increases the rigidity of the soil root plate against loading in that direction

(*Gregory, 2006*) and thus reduces the ability of the system to rotate. More realistically, however, a plant will be subjected to wind loading from a number of directions and it is difficult, therefore, to predict where the mechanical stresses, and thus excess material, will develop (*Fourcaud et al., 2007*). Furthermore, plants grown on a slope consistently develop longer upslope roots and shorter down slope roots, regardless of wind direction (*Nicoll et al., 2006*).

In recent years, the ability of a tap root system to resist lateral loading has been compared to pile foundations (*e.g: Ennos, 1993; Gregory, 2006*). Both soil pile and soil tap root systems consider a key rigid element that undergoes bending when subjected to lateral loading (*Gregory, 2006*), as shown in Figure 2.15 (c).

2.2.3.4 Planting Technique

The relationship between the method of plantation and the development of root architecture has been reported through a number of studies (*e.g. Mulatya et al., 2002*). There are four methods of planting available, namely: direct seeding on site, transplanting seedlings that have been grown in containers, planting bare root seedlings and planting cuttings (*Preti and Giadrorossich, 2009*). Mulatya *et al.* (2002) found that the cuttings of a particular species (namely, *Melia volkensii*) consistently grew shallower root systems than seedlings. Moreover, they found that the orientation of the seed or cutting further impacted the consequent architecture.

2.2.4 Permeability and Transpiration

The pore water pressure within, and thus strength of, a soil is a function of its permeability and climatic conditions, both of which are influenced by the presence of vegetation (*Scott et al., 2007*). As a plant grows, its roots penetrate the soil and create a network of channels. They also introduce macropores and increase the roughness of surface soil (*Reubens et al., 2007*). These changes in soil properties increase the system's capacity for water infiltration and this can result in a large increase in moisture content during adverse weather conditions. In growing seasons, however, this is often limited by the rainfall interception provided by the above ground canopy (leaves) as well as through transpiration and suction effects (*e.g. O'Brien, 2007*).

Absorption is one of the key functions of a root and is facilitated through creating suction within the soil. This leads to a negative pore water pressure, which encourages the flow of fluid. Suction is effective to a depth of up to 3 times the depth of the roots and has a magnitude that is dependent on

plant species (*Tarantino et al., 2002*). Perry *et al.* (2003) reported suction effects up to 1 MPa for the near surface roots of deciduous trees (those that lose their leaves after growing season) and 0.1 MPa for grass roots. O'Brien (2007) further found that the effects of suction can last a long time in soils with low permeability. Outside growing season, however, water uptake is either significantly reduced or stopped and this coincides with a reduction or absence of the plants canopy. This seasonal dormant period corresponds with seasonal increases in extreme weather conditions and, therefore, during this period the soil conditions may be worsened by the presence of vegetation. The strengthening hydrological effects of vegetation, therefore, vary with season, as well as with plant species.

2.2.5 Rhizosphere

The rhizosphere is a narrow band of soil, with no distinct edge, that surrounds the root and is directly influenced by its exudate and associated micro-organisms (*McNear, 2013*). It performs a multitude of roles such as to provide a suitable environment for the root and maintain a moist surrounding to protect it from pathogenic organisms (*Hinsinger et al., 2009*). The change in chemical properties (induced by the root exudate) and apparent cohesion (induced by the root hairs and moisture content) in this zone of soil will impact its mechanical properties, making it differ from the global soil mass and altering local mechanical soil root interaction (*Hinsinger et al., 2009*). These changes in property are important factors in determining the erodability of soil (*Reubens et al., 2007*), as well as other properties. Research in this area of study, however, is limited and the implications of the rhizosphere to the mechanical interaction between the soil and the root are currently unknown.

2.2.6 Summary

The structural form of a plant root system, including architectural and material properties, is developed in a way that provides an optimum balance of stability and health for the plant. Root systems are therefore very sensitive to local environmental conditions, such as soil strength, nutrient availability and weather conditions, as well as to their genetic form. The key points arising from the literature review on root physiology and key engineering parameters are:

(a) There are two key forms of plant, namely woody and herbaceous. Woody plants have stiff roots that grow to a large depth, while herbaceous plants have a dense, shallow root system composed of flexible roots. The roots of both plant groups have comparable tensile strengths.

(b) The diameter, age and geometry of a root affect both its material properties and anchorage ability. A reduction in root diameter results in an increase in both tensile strength and stiffness, as does an increase in age. Anchorage is additionally aided by strong soil, a strong soil root bond and an increase in the soil root contact area.

(c) Anchorage is categorised into two mechanisms, namely uprooting and overturning. The most likely of these is overturning although uprooting is common in grasses and small herbaceous plants, due to animal grazing.

(d) Root systems are able to overcome both mechanical impedances and changes in their environmental conditions through adapting their cell development (*Degenhardt and Gimmler, 2000*). This impacts both architecture and material properties.

Unlike traditional materials used for soil reinforcement, therefore, the characteristics and mechanical properties of a root are very volatile and dependant on circumstance.

2.3 Slope instability, traditional remedial techniques and reinforcing potential of vegetation

2.3.1 Traditional Slope Design

The stability of a slope is subject to a balance of driving and resisting moments, where driving moments act to destabilise and resisting moments act to stabilise. This is generally represented as a ratio, as shown below:

$$FOS = \frac{\sum M_R}{\sum M_D} \qquad \text{Eq. 2.8}$$

Where; $\boldsymbol{FOS}$ is the factor of safety; $\boldsymbol{M_R}$ is the resisting moment (which is beneficial), and; $\boldsymbol{M_D}$ is the driving moment (which is adverse).

Driving and resisting moments are generated by both slope properties and local environmental conditions, such as: geometry, material, climate, cover and slope age. Their combination results in slope instability when driving moments become greater than resisting moments (i.e when *FOS* falls below 1.0, Equation 2.8). This will manifest within the slope as a surface erosion or an internal weakness. Surface erosion occurs when the surface layer of a soil is weakened and can lead to further failures, such as gullying, that can destabilise a slope if not controlled. Internal weaknesses, on the

other hand, occur at depth and cause soil movements that can lead to landslides. Landslides can have a devastating impact on infrastructure and safety, causing loss of life in extreme cases. The possible severity of slope instability has resulted in extensive research and the development of a number of analysis techniques and remedial measures.

Figure 2.17 depicts the most common deep failure mechanisms for soil slopes, explaining the conditions in which they are most likely to occur (*Craig, 2004*). As demonstrated, each mechanism experiences a unique soil movement. This requires a variety of analysis techniques. For rotational failure, an analysis model known as the limit equilibrium method is commonly used. This model produces sufficiently accurate results and is well established in both standards (e,g. Eurocode 7) and commercial computer programs (e.g. Geo-Slope International "SLOPE/W"). For the more complex compound and translational failures, infinite slope analysis and numerical modelling techniques are commonly used. Typically, all of these approaches use the Mohr-Coulomb failure criterion to describe the shear strength of the soil *(Aryal, 2006)*. This criterion is shown in Equation 2.9.

$$\tau_S = \sigma_v' \cdot \tan \phi' + c' \qquad \text{Eq. 2.9}$$

Where; τ_S is the mobilised shear strength; σ_v' is the effective vertical stress; ϕ' is the effective angle of internal friction, and; c' is the apparent soil cohesion.

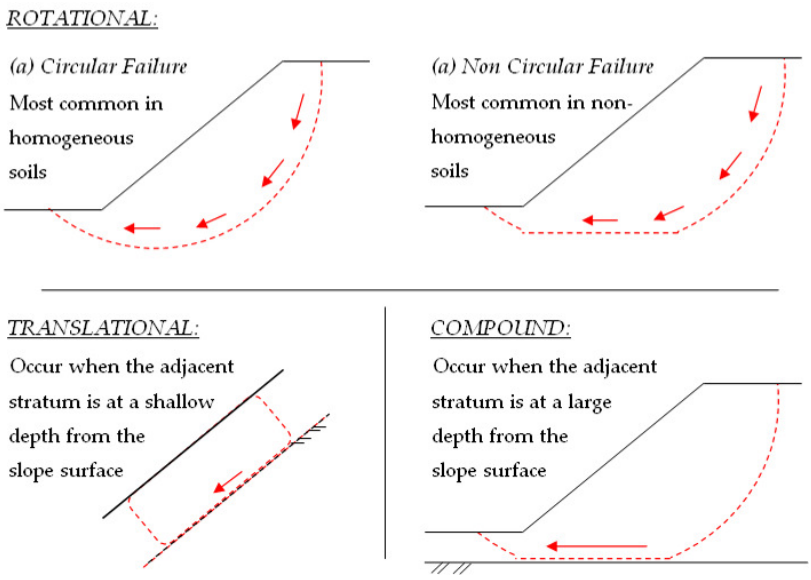

Figure 2.17: Most likely manifestations of mass movement (*Adapted from Craig, 2004*)

In actuality, the failure envelope of a soil is a lot more complicated than suggested by the Mohr-Coulomb failure criterion. This criterion fits a straight line to soil strength data and, through this

simplification, estimates soil strength using only a few parameters. It therefore provides a user friendly analysis technique that is sufficiently accurate.

2.3.1.1 Limit Equilibrium Analysis (LEA)

The limit equilibrium method investigates the equilibrium of a mass of soil sliding over a trial failure surface by considering the mass as a series of theoretical vertical slices (see Figure 2.18). To calculate the forces acting on each slice, the properties of both the failure surface (i.e. radius, R, and centroid, O) and each slice (i.e. weight, W_n; length along base, L_n; and position on slope, α_n) must be known or assumed. For simplicity, the model recommends that the slices have the same *FOS* and move simultaneously under failure. This, however, introduces the issue of inter slice forces (*Knappett and Craig, 2012*), which have to be accounted for in the calculation model. Accurately determining these theoretical forces, however, is complicated and research in this area has therefore received lots of attention. The result is a number of alternative calculation models, each using different assumptions and producing slightly different *FOS* values (*Aryal, 2006*). Despite their differences, however, they all compare well with experimental results, demonstrating the approximate nature of limit equilibrium analysis. The most popular LEA models are Bishops, Janbus and Spencers as they can be used to model both circular and non-circular failure surfaces to a sufficient accuracy (*Aryal, 2006*).

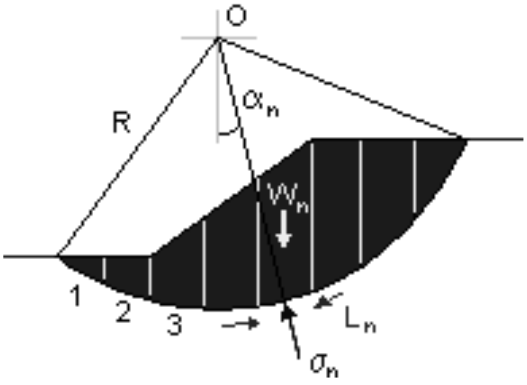

Figure 2.18: Slope model used in limit equilibrium analysis, highlighting key parameters to be considered in calculations. [*http://environment.uwe.ac.uk/geocal/SLOPES/SLOPSLID.HTM*]

The key success of limit equilibrium analysis is that it balances a simple and quick calculation technique with the modelling of complex soil profiles, seepage and a number of loading conditions (*Yu et al., 1998*). It is, however, an approximate method that neglects the plastic flow rule for soil and investigates global stability only. Whilst this raises concern about the accuracy of the method

(*Yu et al., 1998*), comparisons against more thorough techniques *(e.g. finite element analysis - Yu et al., 1998 and the shear reduction method – Cheng et al., 2007)* have shown that the limit equilibrium method provides satisfactory results, particularly when considering a simple slope composed of homogeneous soil. In addition to this, Cheng *et al.* (2007) found that the LEA method is relatively insensitive to the flow rule and therefore elimination of this property is insignificant. This method will, however, produce inaccurate results if used inappropriately, for example, when a non-homogenous soil is considered *(Yu et al., 1998; Cheng et al., 2007)* or when a soil has both high cohesion and a low angle of friction or both a high angle of friction and low cohesion *(Cheng et al., 2007)*. It is important, therefore, that an engineer using this method is aware of the slope conditions appropriate for this calculation technique.

A number of commercially available computer programs have been developed to model a slope using the limit equilibrium method, such as SLOPE/W by Geo-Slope International Ltd., Canada. These programs are widely used in practise.

2.3.1.1.1 Infinite Slope Analysis

The infinite slope analysis method considers an unstable mass of soil sliding along a failure plane that sits approximately parallel to the surface of the slope (as demonstrated in Figure 2.19). The *FOS* of such a slope may be determined using the equation below (*Powrie, 2004*):

$$\begin{aligned} FOS &= \tan\phi'_{cr} / \tan\phi'_{mob} \\ &= \left[1 - (u / \gamma_s Z \cos^2 \beta)\right] \cdot \left[\tan\phi_{crit}' / \tan\beta\right] \end{aligned} \qquad \text{Eq. 2.10}$$

Where; ϕ'_{cr} is the critical state angle of friction; ϕ'_{mob} is the mobilised soil strength (required to maintain the stability of the slope); u is the pore water pressure; γ_s is the unit weight of the soil; Z is the depth from the soil surface to the failure plane, and; β is the slope angle.

The definition of pore water pressure, u, considers the inclination of water flow (θ_w).

$$u = \gamma_w Z /(1 + \tan\theta_w \tan\beta) \qquad \text{Eq. 2.11}$$

Where; γ_w is the unit weight of water, and; θ_w is the inclination of water flow

This technique is well established, produces results that are sufficiently accurate and generally agrees with field observations. As with the limit equilibrium technique, however, inaccurate results will be

produced if this method is applied to the wrong situation. For example, if the ratio of failure length to depth falls below 20 (*Gray and Sortir, 1996*).

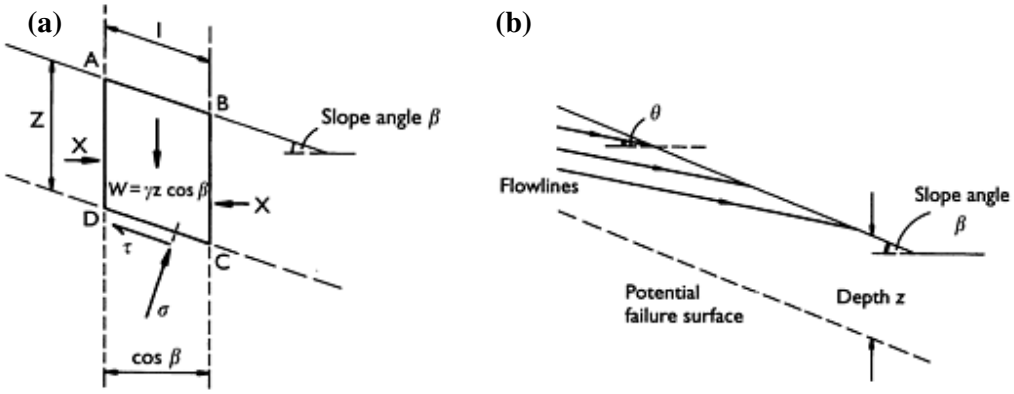

Figure 2.19: Infinite slope analysis model, highlighting key parameters to be used in calculations. (a) general parameters, (b) inclination of water flow, θ_w. (*Powrie, 2004*).

2.3.2 Traditional Remedial Techniques (focussing on inert inclusions)

The purpose of slope reinforcement is to increase the resisting forces and/or reduce the disturbing forces within a slope, so that the *FOS* is increased to an acceptable and safe level. Traditional remedial techniques, in the form of inert inclusions, penetrate the soil and favourably influence its mechanical behaviour. This is not unlike plant roots. In order to study roots as a reinforcing material, therefore, it is important to recognise the mechanical behaviour and requirements of inert inclusions, in particular soil nails, dowels and piles.

A slope may be considered as two separate masses, one being stable and the other tending to move. Inclusions act to secure the moving soil mass by extending from the slope's surface, through the failure plane, to the stable soil. The consequent improvement in slope strength is a function of the soil inclusion interaction, of which there are typically two modes; (i) bearing, which leads to shear forces and bending moments, and (ii) friction, which leads to axial tension and compression (*Pedley, 1990*), see Figure 2.20. Through these mechanisms, stresses are transferred from the moving soil mass to the reinforcement and, therefore, to the stable soil. This acts to both minimise deformation and relieve stresses within the unstable soil. Inadequate interaction can result in the redistribution of stress back into the moving soil mass, which can lead to gradual deformation of the soil structure and ultimately slope failure (*Knappett and Craig, 2012*).

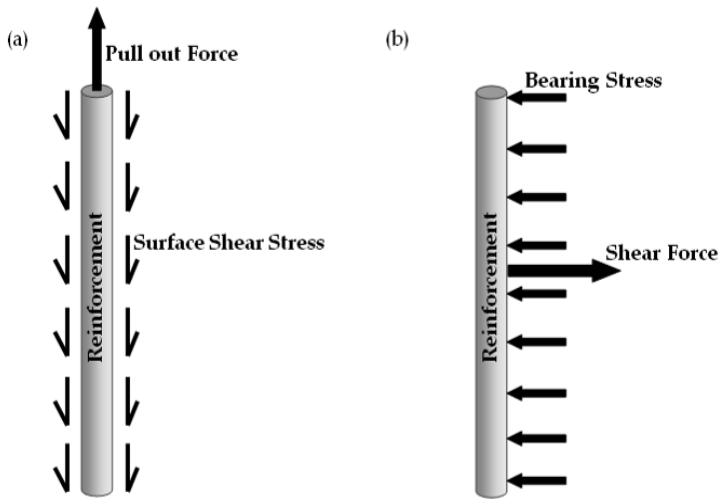

Figure 2.20: Mechanisms of soil inclusion interaction. (a) Friction, and (b) bearing. (*Adapted from Pedley, 1990).*

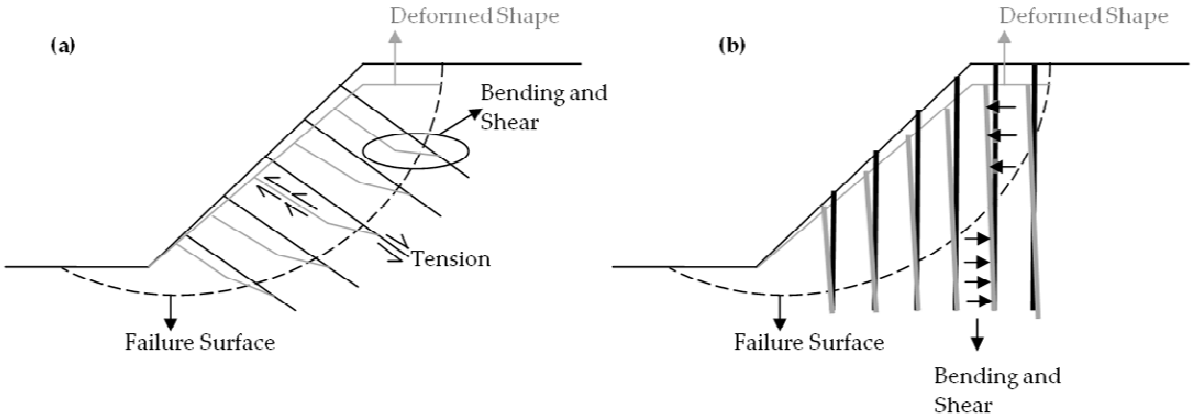

Figure 2.21: Mechanisms of soil-reinforcement interaction used by different reinforcing techniques. (a) Soil nailing reinforcement, (b) Dowelling and piling reinforcement.

Dowelling and piling techniques predominantly interact with the soil through the bearing mechanism, while soil nails use friction (see Figure 2.21). The orientation and cross section of reinforcement play a large role in defining its reinforcing mechanism (*Pedley 1990*). Soil nails are installed approximately perpendicular to the shear plane and have small cross sections in relation to their length, making them slender. These factors combine to create an element that is typically orientated in the direction of tensile strain (*Geotechnical Engineering Office, 2008*) and provides little resistance to bending and shearing forces (i.e is easily deformed, see Figure 2.21(a)). Soil piles and dowels, however, have larger cross sections and are typically orientated vertically. They are therefore stiffer elements than soil nails with very little tensile loading and a much greater ability to resist bending and shearing forces. With knowledge of the interaction mechanism, it is possible to utilise limit equilibrium analysis to analyse a slope that is reinforced with inert inclusions.

2.3.2.1 Soil Nailing

Soil nails are typically solid, high yield deformed steel bars with a diameter of 20 – 30 mm, although other materials and sections can be used (*Pedley, 1990*). Installation involves placing each nail into a drill hole and either grouting it along its length or driving it into the ground (*Mittal and Biswas, 2006*). To increase soil inclusion interaction (i.e. friction), the nails are installed at close spacing and are best suited to slopes composed of cohesive soils or rock, due to their high frictional resistance (*Tei, 1993*). To prevent the nails from pulling into the soil under deformation, an anchor is provided at the soil nail head. This is typically composed of a concrete pad, a steel bearing plate and bolts, and provides the reaction required to mobilise a tensile force in the nail and thus prevent it from pulling into the soil mass (*Geotechnical Engineering Office, 2008*). The slope surface is locally stabilised by a facing element, which can be either structural or non-structural. Its principle purpose is to provide protection against erosion but, where a structural facing is used, it can also act to redistribute forces and thus enhance the efficiency of the soil nail system. The most common non-structural facing is vegetation, while the most common structural facings are walls or shotcrete surfaces (*Geotechnical Engineering Office, 2008*).

Soil nailing is a passive system that requires mobilisation to generate a reinforcing action (*e.g. Geotechnical Engineering Office, 2008*). This is provided through the interactions that occur between the soil and nail as the ground deforms during and after construction (*Tan and Chow, 2004*). This is demonstrated in Figure 2.22, which shows the general tensile stress distribution on each soil nail under different deformations. The line of maximum tensile force reflects the interaction between nail and soil rather than the failure surface of the slope (*Wei and Cheng, 2010*). As the principle mechanism used by soil nails is friction, it is common practise to consider only axial forces in the design of a soil nailed slope.

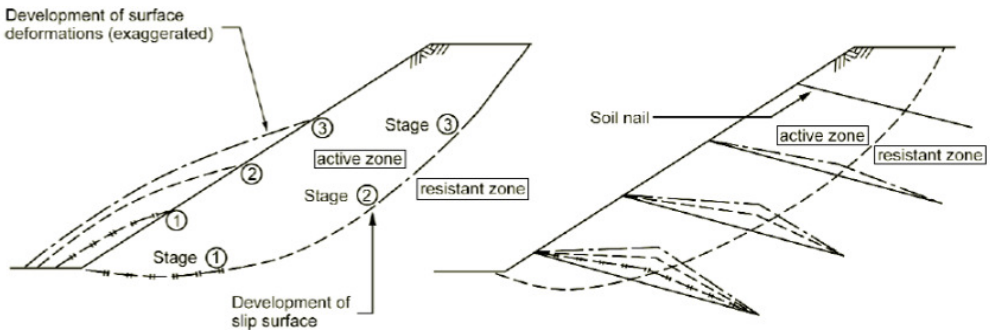

Figure 2.22: Example of slope deformation mobilising a reinforcing action in the soil nails (*Phear et al., 2005*).

The orientation of the soil nail greatly impacts its contribution to the shear resistance of a slope as it defines the loading conditions to which the nail will be subjected (*Jones, 1990*), much like plant roots (see Section 2.2.3.3.1). If the nail sits perpendicular to the direction of soil movement then it will not be subjected to axial loading and will provide reinforcement through the bearing mechanism. This is not ideal as soil nails are weak in bending and shear. If, however, the nail sits at an angle clockwise or counter clockwise to the perpendicular orientation then compressive and tensile axial loading, respectively, will be mobilised. In practise, it is common to place soil nails either horizontally or perpendicular to the slope face, with all soil nails sitting parallel to each other (*Patra and Basudhar, 2005*). The nails sitting at the slope crest will therefore be in compression, while those at the foot will be in tension (*Jones, 1990*), see Figure 2.23. Johnson (2002) suggest that the optimum angle between the vertical and the nail is 55°, with efficiency reducing to 0% as the nail inclination tends towards 125°. This is supported by Jewell and Wroth (1987) who carried out a series of shear box tests with inclusions sitting at various angles to find that fibres exposed to compression are inefficient (Figure 2.24). The efficiency of a soil nail system, particularly at the crest, could therefore be improved by installing soil nails with a negative inclination. This, however, is not practically possible from a construction sense (*Johnson, 2002*). Moreover, studies carried out by Stocker *et al.* (1979) and Clouterre (1991) show that when mass movements occur in a slope, the majority of the consequent forces and moments are taken by the lower rows of soil nails, with little contribution coming from the top row (as suggested in Figure 2.22). It is not imperative, therefore, that soil nails in the upper portion of the slope are as efficient as those in the lower portion.

There are a number of mechanisms through which a soil nail system can fail, namely: local failure of materials (e.g. breakage of nail, cracking/spalling of surfacing and disintegration of soil), failure of bonds (e.g. nail pull out and failure of head nail connection) and development of external failures (e.g slope failure surface develops outside the reinforced zone) (*Chen, 2004*). The careful detailing of current design procedures along with development of finite element programs almost rules out failure of materials and development of external failures. The most significant failure mechanism is therefore failure of bonds; of which nail pull out is the most likely (*Phear et al., 2005*). For this failure to occur, the line of maximum tensile strength in the soil nail structure must sit before the failure plane in the moving portion of the soil mass (*Wei and Cheng, 2010*). Calculating the pull out force of a soil nail (i.e. the maximum allowable tensile force) is therefore of critical importance and can be achieved through the following equations, which account for drained and un-drained soil conditions, respectively (*Phear et al., 2005*):

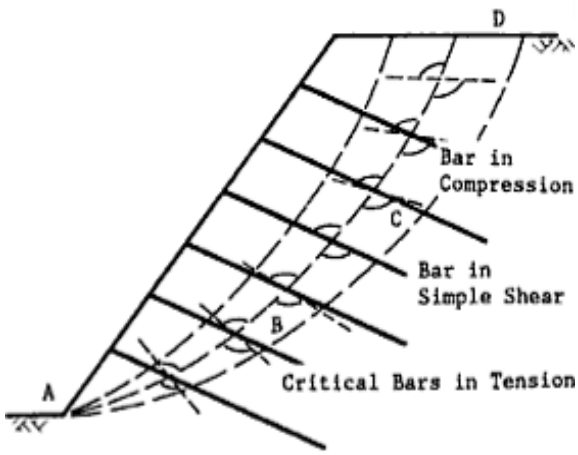

Figure 2.23: Effect of maintaining an inclination angle through the slope (*Jones, 1990*).

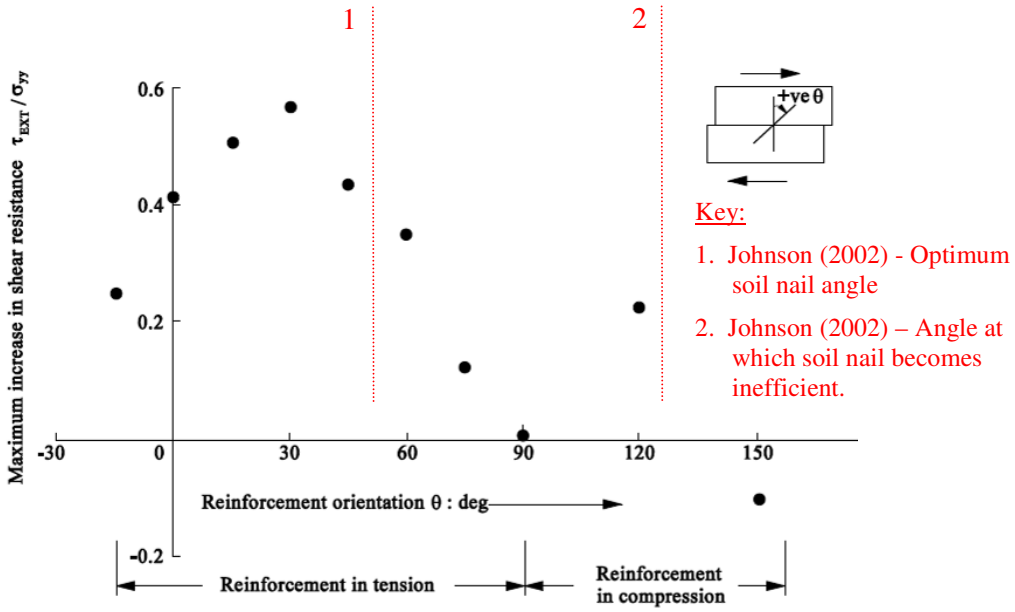

Figure 2.24: Effect of inclination angle to an inclusions contribution to shear resistance (*Adapted from Jewell and Wroth, 1987*).

$$F_{bar-d} = \pi \cdot D_{bar} \cdot L_{bar} \cdot \alpha_a \cdot c_u \qquad \text{Eq 2.12}$$

$$F_{bar-u} = \pi \cdot D_{bar} \cdot L_{bar} \cdot \left(K \cdot \sigma_n' \cdot \tan\delta + c'\right) \qquad \text{Eq 2.13}$$

Where; F_{bar-d}/ F_{bar-u} are the forces required to pull a reinforcement bar from drained (d) and un-drained (u) soil; D_{bar} is the diameter of reinforcement bar; L_{bar} is the anchorage length of the reinforcement bar; α_a is an adhesion factor; c_u is the un-drained shear strength of soil; K is the earth pressure coefficient [reported to be 1.4-2.3 for dense to medium dense sands; 1.4 for dense sands; 1.0 for fine sands and silts (high density); 0.5 for fine sands and silts (low density)]; σ_n' is the normal effective stress at the slip plane, and; δ is the angle of interface friction.

These pull out equations are comparable to the uprooting equation that was developed for plant roots (see Equation 2.4). The soil nail equations, however, account for the interaction between the nail and the reinforcement through some factors (α_a in Equation 2.12 and K in Equation 2.13), which requires an understanding of the soil nail interaction. In addition, Equations 2.12 and 2.13 provide a more comprehensive inclusion of soil properties. With better knowledge of soil root interaction, therefore, it may be possible to improve upon the predictions of root pull out (Equation 2.4) by considering equations akin to Equations 2.12 and 2.13. It should be noted, however, that the proposed values of K in Equation 2.13 are loosely defined in terms of soil density and fines content, which is inconsistent with the method in which K values are normally derived. In pile analysis, for example, K is normally taken as a function of either the installation method (*e.g. Fleming et al., 2009*), the peak friction angle (*e.g. Mitsch and Clemence, 1985*) or the lateral earth pressure coefficient (*e.g. Bransby et al., 2011*). The 'design' values of K in Equation 2.13 should therefore be used with caution, as they could result in the over- or under-estimation of pull out capacity. Adopting a more general approach to define K would therefore be more suitable than applying the values stated by Phear *et al.* (2005).

2.3.2.2 Piling

Pile systems are employed on slopes to transfer loads either laterally or by a combination of lateral and axial interaction (*Gunaratne, 2006*). They are stiff elements composed of either treated timber, steel, concrete or a combination of these materials. Piles sit vertically or slightly inclined in the soil and have a cap sitting at their head, usually composed of concrete. The purpose of the cap is to evenly distribute any axial loading among the piles, maintain pile spacing and ensure the piles are working together. Its detailing depends on the predicted loading conditions of the piles and on whether free or restrained heads are required. Installation involves driving a prefabricated pile into the ground or drilling a hole into which fresh concrete is poured (*Gunaratne, 2006*). The response of a pile to lateral loading is provided by the properties of the pile, the soil and the interaction between the two (*Kramer and Heavey, 1988*). It stands, therefore, that pile soil interaction is a key factor in determining the reinforcing capacity of a pile system.

The length of a pile in relation to the depth of the failure surface significantly impacts its reinforcing capacity. A pile that extends far beyond the failure surface provides anchorage into the stable soil and has only a small fraction of length undergoing lateral loading. As pile length decreases, this fraction increases, as demonstrated in Figure 2.25, and this has a significant effect on the failure

mechanism of the system. Short piles displace along their entire length, with the upper pile moving in step with the soil movement. Eventually, its tip displacements become significant and provoke the soil to yield, resulting in failure of soil pile interaction and ultimately failure of the system (*Ang, 2005*). Intermediate length piles, on the other hand, are anchored by their additional length, which acts to stiffen the pile soil system and reduce tip displacements (*Ang, 2005*). In this case, soil pile interaction remains throughout loading and it is likely that failure will take place in the pile itself through the formation of a plastic hinge (*Phanikanth et al., 2010*). Increasing pile length further to consider long piles induces plastic behaviour in the soil surrounding the upper section of pile (*Poulos, 1995*). Soil pile interaction is therefore lost in this zone and the soil flows around the pile, which moves very little. Short and long piles are therefore not ideal for slope stabilisation. Increasing pile diameter results in the increase of both lateral strength and stiffness of a pile soil system (*Phanikanth et al., 2010*). It is likely that the same is not true of a plant root, as strength per unit area decreases with increasing diameter (e.g. *Operstein and Frydman, 2000*) unlike a pile whose unit strength properties remain constant as more material is added.

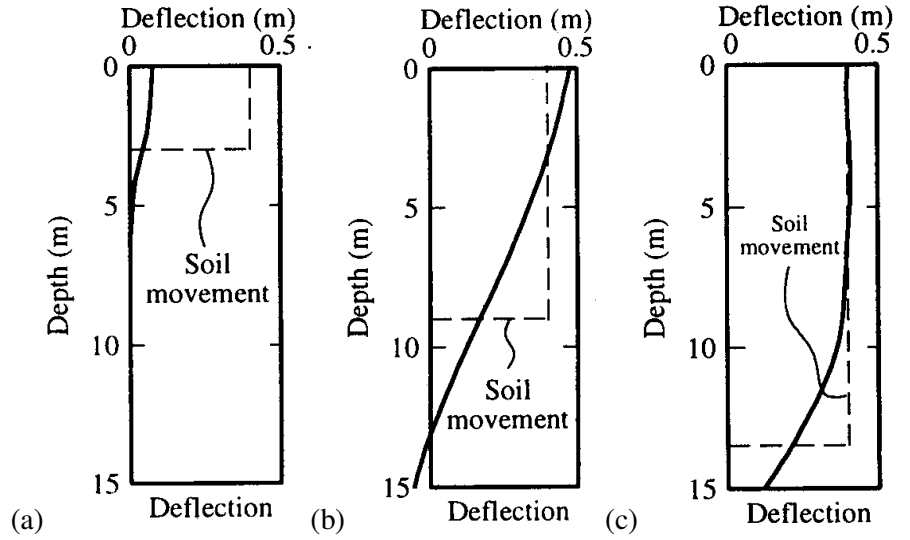

Figure 2.25: Pile deflection and soil movement in a (a) long pile system, (b) intermediate pile system and (c) short pile system. (*Poulos, 1995*)

As a general rule, it is possible to classify piles into short, intermediate or long by considering their stiffness, length and surrounding soil, as shown below (*e.g. Ashour et al., 2008*);

$$\textit{Short rigid pile};\quad \frac{L_{pile}}{\left(\left(EI\right)_{pile}/k\right)^{1/5}} < 2 \qquad \text{Eq 2.14 (a)}$$

$$\textit{Intermediate pile};\quad 2 \le \frac{L_{pile}}{\left(\left(EI\right)_{pile}/k\right)^{1/5}} \le 4 \qquad \text{Eq 2.14 (b)}$$

$$\textit{Long flexible pile};\quad \frac{L_{pile}}{\left(\left(EI\right)_{pile}/k\right)^{1/5}} > 4 \qquad \text{Eq 2.14 (c)}$$

Where; $\boldsymbol{L_{pile}}$ is the length of the pile; $\boldsymbol{E_{pile}}$ is the young's modulus of the pile; $\boldsymbol{I_{pile}}$ is the moment of inertia of the pile, and; $\boldsymbol{k}$ is the modulus of sub-grade reaction for the soil (typically ranging between 27-109 MPa/m for sand) (*Ashour et al., 2008*).

The spacing and number of piles are also extremely important factors to consider in pile analysis. Under loading, a pile translates stress into its surrounding soil. This is known as the stressed zone and its magnitude is related to the magnitude of loading. Under certain conditions, the stress zones surrounding a pile can overlap with those surrounding its neighbouring piles (an effect known as shadowing) and this has a significant impact on the load distribution between piles (see Figure 2.26). As such, the response of a pile group to lateral loading is not the sum of the individual pile responses, except where the piles are widely spaced.

A number of methods have been developed for the analysis of laterally loaded piles, ranging from simple to complex. Of these, the most widely used is the *p-y* method as it has intermediate complexity and reasonable accuracy (*Kramer and Heavey, 1988*). This method describes the response of the system to loading by considering the pile to be an elasto-plastic beam loaded through a series of springs that sit along its length (see Figure 2.27). Displacement of the far end of the spring represents soil movement in the free-field; the springs are given appropriate properties to model the soil pile interaction close to the pile (near-field). The beam-on-Winkler foundation theory states that the behaviour of each spring can be calculated from load deflection data, which in turn, can be obtained through the use of remote strain gauges, or similar measuring devices that can observe a pile movement under lateral loading. Taking h_d to represent the horizontal deflection of a pile and x to represent strain gauge (or measurement) location, a function can be applied to the data such as to relate h_d and x and thus describe the distribution of deflection along the length of the pile. This

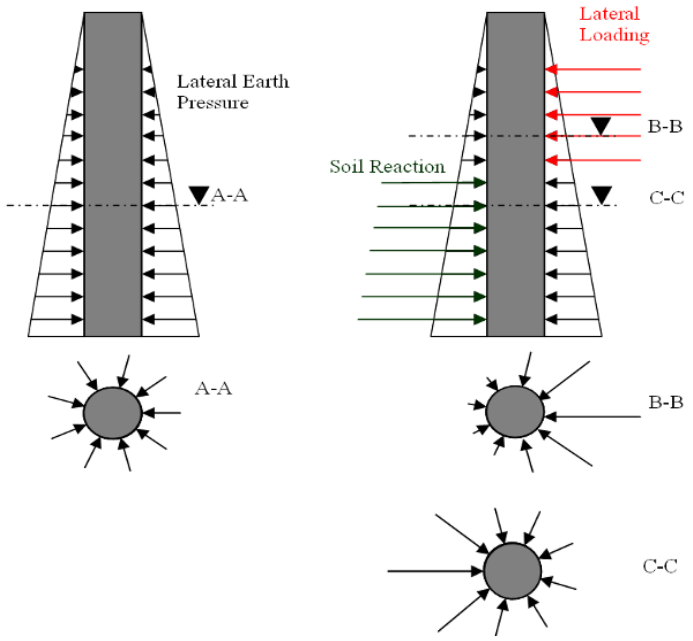

Figure 2.26: (a) Stress zones surrounding pile subjected to lateral earth pressure only, (b) Stress zones surrounding a pile subjected to lateral earth pressure and external lateral loading (*adapted from Jeong et al., 2003*).

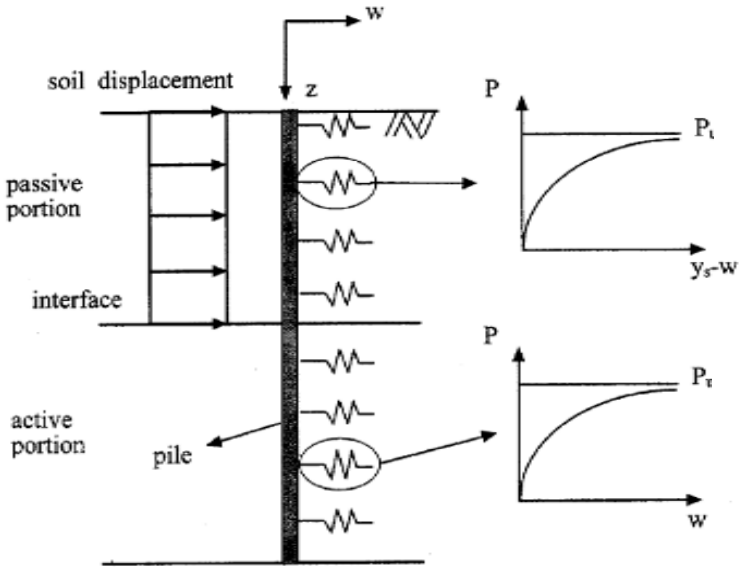

Figure 2.27: Simplification of soil pile system used in *p-y* analysis (*Jeong et al., 2003*).

function, usually in the form of a polynomial equation, can be used to find the moment, shear and soil reaction distributions along the length of the pile. This is achieved through differentiation, as follows:

$$M_{pile} = (EI)_{pile} \cdot \frac{d^2 h_d}{dx^2} + P_v \cdot h_d \quad \text{Eq 2.15}$$

$$V_{pile} = (EI)_{pile} \cdot \frac{d^3 h_d}{dx^3} + P_v \cdot \frac{dh_d}{dx} \quad \text{Eq 2.16}$$

$$p_{pile} = (EI)_{pile} \cdot \frac{d^4 h_d}{dx^4} + P_v \cdot \frac{d^2 h_d}{dx^2} \quad \text{Eq 2.17}$$

Where; $\boldsymbol{M_{pile}}$ is the bending moment in pile; $\boldsymbol{V_{pile}}$ is the shear force in pile; $\boldsymbol{p_{pile}}$ is the soil reaction; $\boldsymbol{(EI)_{pile}}$ is the flexural stiffness of pile, $\boldsymbol{P_v}$ is the vertical loading on the pile, $\boldsymbol{x}$ is the strain gauge or measurement location, and; $\boldsymbol{h_d}$ is the horizontal deflection of the pile.

Soil reaction is a measure of the resisting stresses that are mobilised in the soil as a result of lateral loading. It stands, therefore, that this property varies with the relative displacement between a pile and its surrounding soil, *y*. This can be graphically represented by plotting *p* against *y*, which is where the *p-y* method gets its name. The accuracy of this method is highly dependent on the accuracy of both the initial h_d and *x* data and the function used to describe their relationship.

Similarly, the response of a pile to vertical loading can be determined through analysing vertical displacements, *z*, against their location on the pile, *x*. This method is known as the *t-z* method, where *t* is the vertical (shear) force and is represented by the first differential of the best fit curve between vertical displacement, *z*, and strain gauge location, *x*. This is shown in Equation 2.18:

$$t_{pile} = (EA)_{pile} \cdot \frac{dz}{dx} + P_v \cdot z \quad \text{Eq 2.18}$$

Where; $\boldsymbol{t_{pile}}$ is the vertical shear force between a pile and its surrounding soil; $\boldsymbol{(EA)_{pile}}$ is the axial stiffness of the pile, and; $\boldsymbol{z}$ is the vertical movement of the pile.

The limit equilibrium method is widely used for determining the safety of a slope that is reinforced with piles (*Ausilio et al., 2001*). Jeong *et al.* (2003) report on the suitability of the Bishop simplified method, when considering a circular failure surface (see Figure 2.28). This utilises the bending moments (M_{cr}) and shear forces (V_{cr}) that develop at the failure plane, as calculated through the *p-y* method, to determine the additional *FOS* provided by a pile, as follows;

$$\Delta FOS = \frac{V_{cr} \cdot R \cdot \cos\theta - M_{cr} + V_{head} \cdot Y_{head}}{M_D} \quad \text{Eq 2.19}$$

Where; ***ΔFOS*** is the additional FOS as a result of reinforcement; V_{cr} is the shear force at failure surface; R is the radius of failure surface; θ is the slope of the failure surface at the pile location, M_{cr} is the bending moment at failure plane; V_{head} is the shear force at pile head; Y_{head} is the vertical distance from pile head to centre of rotation, and; M_D is the driving moment.

The resulting *ΔFOS* value can be added to Equation 2.8 to calculate the stability of a pile reinforced slope, as shown below;

$$FOS_{pile} = FOS + \Delta FOS \quad \text{Eq 2.20}$$

Where; FOS_{pile} is the FOS of a pile reinforced slope.

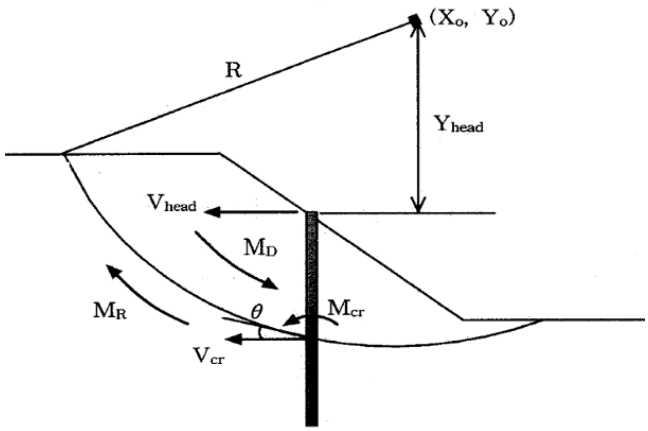

Figure 2.28: Limit equilibrium method including pile system (*Jeong et al., 2003*).

2.3.3 Slope Reinforcement using Plant Roots

Vegetation will naturally establish over time, even on slopes composed of quite barren soils (*Greenwood et al., 2004*). The inclusion of roots in slope stability calculations is therefore necessary for establishing the stability of existing slopes. It is increasingly desired, however, in initial design and remediation (*Sonnenberg, 2008*).

The reinforcement provided by vegetation is offered through two key mechanisms. These are: (i) increasing soil shear strength through mechanical soil root interaction and (ii) reducing pore water pressure through suction and rainfall interception (*Chok et al., 2004*). The dominant mechanism provided is a function of the root depth in relation to the depth of the failure plane (*Gray and Sotir,*

1996), as summarised in Table 2.1. Further to this, the above ground canopy and the concentrated root mass in the upper soil strata can provide protection against the degrading effects of weather exposure. Not all of the mechanisms provided by plants, however, are beneficial. Trees and shrubs, for example, extract high levels of moisture from a soil and this can cause the seasonal swelling and shrinking of a slope (*Norris and Greenwood, 2006*). This, in turn, can damage local infrastructure and create a reduction in slope stability. Greenway (1987) provides a comprehensive overview of both the adverse and beneficial hydrological and mechanical mechanisms provided by vegetation, which are summarised in Table 2.2. Such mechanisms are well described for simple processes, such as sheet erosion, but research has failed to develop an understanding of these actions during more complex processes, such as gully erosion (*Ruebens et al., 2007*). Their full capacity is therefore unknown. The impact that vegetation has on a slope is related to a number of properties, including: plant species; installation method; placement of vegetation on slope, and; local environmental conditions (*Mafian et al., 2009*).

Table 2.1: Link between slope failure type and the reinforcing action of roots. Adapted from Sonnenberg (2008).

<table>
<tr><td rowspan="3">SLOPE FAILURE TYPE</td><td colspan="2">DEEP FAILURE
(Rotational, circular)</td><td rowspan="2">Vegetation impacts the slopes water regime (groundwater and precipitation)</td></tr>
<tr><td rowspan="2">SHALLOW FAILURE
(Translational)</td><td rowspan="2">Suspected or pre-failure between layers that are interweaved by roots?</td><td>NO</td></tr>
<tr><td>YES</td><td>Vegetation reinforces across potential failure planes and impacts the slopes water regime.</td></tr>
</table>

Table 2.2: Hydrological and mechanical mechanisms of vegetation, adapted from Greenway (1987).

Hydrological Mechanisms	**Impact**	**Mechanical Mechanisms**	**Impact**
Canopy interception	Beneficial	Increased surcharge	Adverse/Beneficial
Canopy runoff	Beneficial	Canopy transmitting wind dynamic forces into the soil	Adverse
Transpiration	Beneficial	Surface binding	Beneficial
Infiltration	Adverse	Root reinforcement	Beneficial
Increased soil permeability	Adverse	Root buttressing	Beneficial

2.3.3.1 Key Design Considerations

2.3.3.1.1 Time dependant FOS

Unlike an inert stabilisation system, which reaches its peak capacity just after construction and slowly degrades over time, a bioengineered system can initially reduce the stability of a slope before slowly

increasing it to a peak capacity, which if maintained will not degrade (*Collison et al., 1995*). This is illustrated in Figure 2.29, where the time scale for reaching the peak capacity of an ecosystem can be up to 10 + years. Collison *et al.* (1995) used finite element analysis to study the effects of initial soil permeability on the development of stability in a bioengineered slope system. They found that the increase in permeability supplied by vegetation is insignificant in a high permeability soil ($1x10^{-5}$m/s) and, as such, the *FOS* slowly increases with time with no initial loss. In this case, the capacity of the system is defined by the mechanical soil root interaction. A slope with a low permeability soil ($1x10^{-6}$ m/s), however, will have a steady decrease in *FOS* before increasing to a maximum safety (as indicated in Figure 2.29). This initial decrease is caused by the high conductivity differential that develops at the edge of the root system, causing high pore-water pressures, reduction in suction and therefore a decrease in soil shear strength (*Collison et al., 1995*). This effect encourages the slope's failure surface to develop at the edge of the root system. Over time, however, this effect reduces and the shear zone moves to pass through the roots, thus allowing mechanical soil root interaction to take hold. This, in turn, increases the shear strength of the material in this zone. The long time period leading up to a maximum *FOS* value, coupled with a potential initial loss of stability, may indicate a need to integrate traditional methods, such as geotextiles, into the initial stages of bioengineering. Through doing this, it may be possible to cancel out the negative hydrological effects of young vegetation and thus increase and maintain the stability of a slope to an acceptable level until the mechanical reinforcement provided by the roots is established.

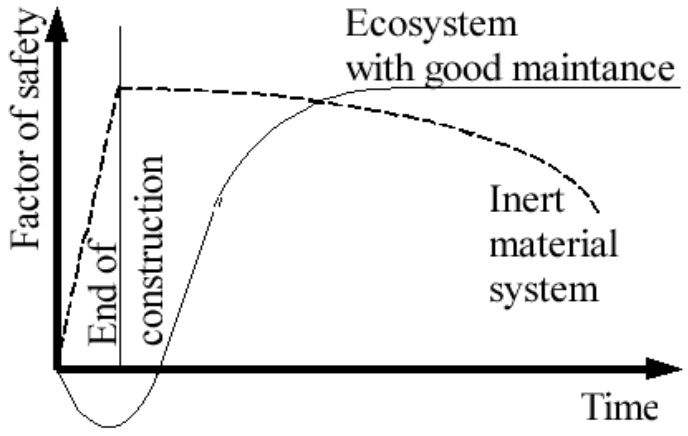

Figure 2.29: Comparison in the safety over time of bio- and traditionally engineered slopes (*Fröhlich 1990, as cited by Sonnenberg, 2008*)

2.3.3.1.2 Planting Techniques

In an attempt to accelerate the development of vegetation's favourable contribution to slope stability, a number of installation techniques have been developed. Figure 2.30 illustrates the pole and bush layering methods. The pole method involves driving poles, composed of live tree branches, into the ground either horizontally or perpendicular to the slopes surface (*Mafian et al., 2009*). These poles are typically in the region of 1 – 2 m long, with a diameter of 40 – 100 mm (*Steele et al., 2004*). As such, this technique is comparable to soil nailing, increasing initial stability through anchoring the poles into the stable soil. The poles, however, are stiff and therefore have significant bending capacity. As the plant ages, lateral roots develop and act to increase the surface area of the system, the soil root interaction and, ultimately, the ability of the system to resist lateral loading. The bush layering technique, on the other hand, involves either digging trenches into which layers of live branches are placed or inserting live branches between layers of compacted soil (*Mafian et al., 2009*). This system is best suited to protect a slope against surface erosion but, when inserted deep enough, is ideal for increasing stability against shallow slope failures. As with the pole technique, the branches will develop lateral roots through time (see Figure 2.30 (b)) and thus the efficiency of the system will increase. Additional techniques, such as seeding on site and transplanting seedlings, are also available but require a longer lead time for the reinforcement properties to become established.

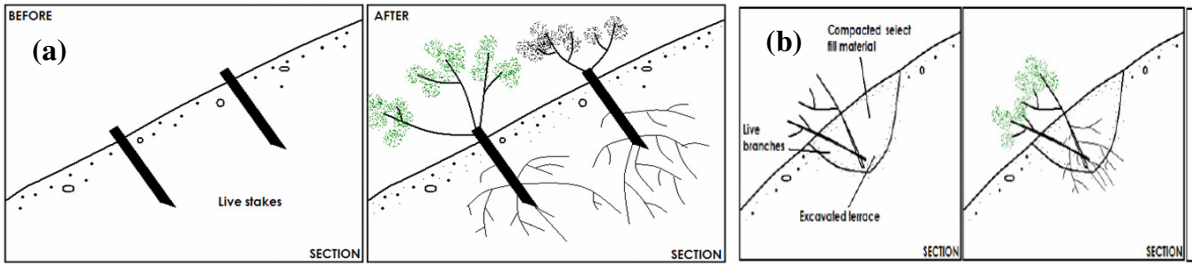

Figure 2.30: Illustration of root installation techniques (a) 'stake' or 'pole' method, (b) 'bush layering' method (*Mafian et al., 2009*)

Growing a plant on site, particularly an engineering site, is however complex. Root morphology is dependent on an array of factors and small fluctuations in properties can lead to large variations in root systems even between plants of the same species (Section 2.2.3). Moreover, the often barren nature of soils used in engineering sites and the tendency to increase strength through compaction, can lead to problems with establishment (*Bengough, 2003*). Careful selection of suitable vegetation for the soil at hand is therefore essential, along with appropriate planning and supervision.

2.3.3.1.3 Placement of Vegetation on Site

The location of vegetation on a slope, along with its above ground mass, has a significant impact on stability and should be carefully accounted for in design (*Chok et al., 2004*). Shrubs and trees have very comparable root properties (i.e. strength and depth) but the larger above ground height of a tree increases its susceptibility to wind-throw (i.e overturning). This could pose danger to surrounding infrastructure and/or transport operations (*Greenwood et al., 2004*), making it a less favourable solution. Collison *et al.* (1995) developed a computer model that assesses the impact of vegetation on slope stability as a result of the dynamic mechanical and hydrological response of a vegetated slope to rain events. Using this model, they report the effects of changing the location, quantity and distribution of woody vegetation to the location and size of a slope's failure plane and to the slope's *FOS* (as shown in Figure 2.31). As demonstrated, they found that slopes with vegetation concentrated either (i) at the toe only or (ii) evenly across the entire slope are superior at increasing slope stability. Heavy concentrations of vegetation at either (i) the crest, (ii) the face only or (iii) at the crest and the toe only, however, decrease slope stability. Collison *et al.* (1995) also found that planting trees at the foot of a slope reduces the hydrological impact of vegetation whilst allowing

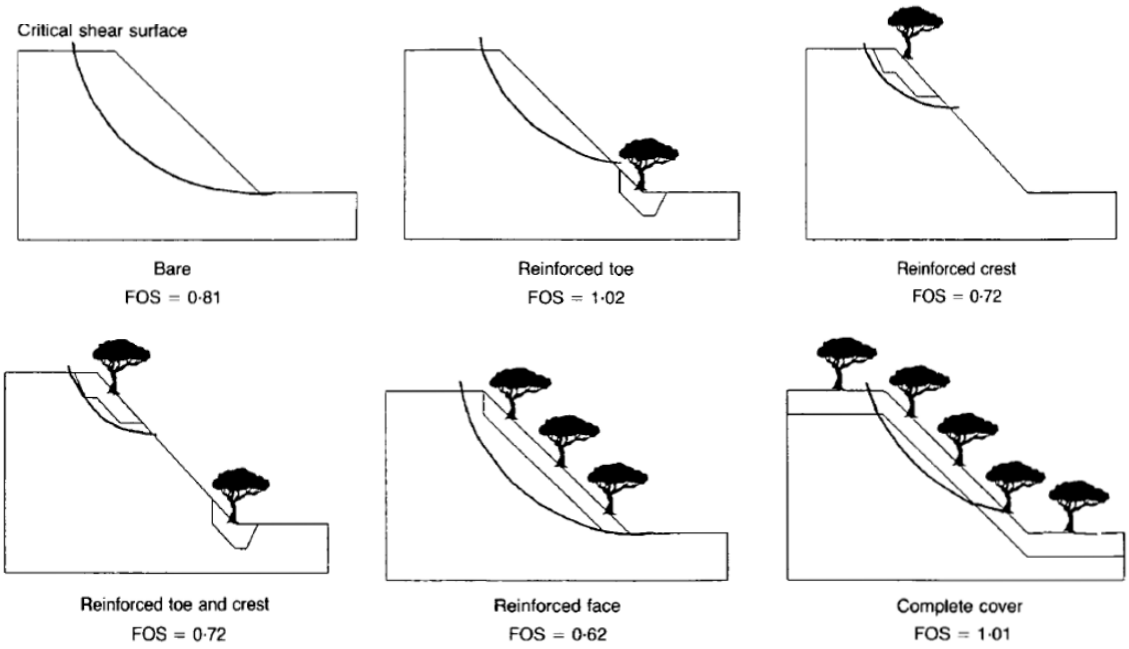

Figure 2.31: Effect of vegetation location on the stability of a slope, showing change in failure plane and FOS value with changing number and location of plants (*Collison et al., 1995*)

optimum mechanical interaction. Fan and Chen (2010) further report that the increased lateral distribution and deep anchorage of a heart root system makes it ideal for use in this location. This can be combined with planting grasses on the slope face to reduce erosion (*Mafian et al., 2009*). Such properties are in line with soil nailing, where the beneficial effects of soil nails are best at the foot of the slope. Schwarz *et al.* (2009) further found that the contribution of vegetation to slope stability reduces when the area of the failure surface increases. As such, vegetation is best suited to slopes of a moderate grade, where the grade of a slope is typically described as a percentage of rise over run. For example, a slope with a rise of 1 metre and a run of 10 metres would be described as having a grade of 10%. As a general guide, grades can be categorised into shallow (0-14%), moderate to moderately steep (15 - 24%), and steep to prohibitively steep (≥ 25%), although this scale is flexible depending on land use (*conservationtools.org*).

2.3.3.1.4 Maintenance

The beneficial impacts of a well-designed bioengineered slope significantly reduce if not properly maintained. Vegetation, if left, can: (i) cause amassing of fallen leaves and debris, and thus blockage of drainage channels and potential flooding (*Greenwood et al., 2004; Norris and Greenwood, 2006*), and (ii) incur damage to the above ground plant, which will significantly reduce the strength of its roots. These will act to reduce the mechanical and hydrological benefits of vegetation. Links between reduced root strength, increased moisture content and increased landslide potential are well documented (*e.g. Wu et al., 1979; O'Brien, 2007*).

2.3.3.2 Mechanical Mechanisms

The uprooting and overturning resistance provided by a plant to maintain anchorage against above ground loading (see Section 2.2.3.3) is the same as that provided to maintain anchorage against lateral loading on the upper root, caused by landslides. Such reinforcement, however, can only be provided by roots that cross the failure plane (e.g. *Coppin and Richards, 2007*). Once established, the root systems of woody vegetation are typically deep enough to cross shallow to moderate failure surfaces (< 1.5m) within a slope (*Greenwood et al., 2004; Comino and Druetta, 2009*). These systems comprise a number of stiff, long and randomly orientated roots that can provide single points of anchorage and thus develop bending, shearing and tensile stresses under lateral loading (*Comino and Druetta, 2009*). The roots within these systems can therefore stabilise a soil through a combination of the bearing and friction mechanisms. They typically, however, undergo pull out without breaking

and thus only ever mobilise a small portion of their tensile strength. Conversely, herbaceous vegetation typically has shallow roots (< 500mm) that are unlikely to cross any failure plane (*Comino and Druetta, 2009*). The mechanical reinforcement of such roots is provided through a membrane strength effect, where the binding action of the roots creates a blanket of strength in the upper layers of soil, which holds the lower soil layers in place (*O'Loughlin and Ziemer, 1982*). Such reinforcement is much less successful in resisting landslides (*Chok et al., 2004*) and, as such, most researchers consider only roots that cross the failure surface in their studies.

It is common practise to simulate soil and root behaviour during landslides through *in situ* or laboratory shearing tests (*e.g. Operstein and Frydman, 2000*). Shear tests involve forcing a mass of soil over a known failure plane and are typically used to measure the shear strength of a fallow or rooted soil sample. Tobias (1994) and Lawrence *et al.* (1996) carried out shear box tests on root permeated soil samples to estimate the change in slope stability that occurs as a result of root inclusions. Each using different plant species, they found slope stability to alter between -2 and 55%, and between -48 and 56% of their initial stability, respectively. Gray and Sotir (1996) and Reubens *et al.* (2007) found such changes in soil strength to be a function of root strength, soil root interaction and the concentration, branching pattern and spatial distribution of the root system. The size and location of the shear band was also found to be significant. Kassif and Kopelovitz (1968) used shear box testing to determine the mechanical failure mechanism of a fibre reinforced soil block, finding three key deformation stages. These are (i) elastic deformation of the soil and its reinforcing fibres, (ii) continued elastic deformation of fibres and plastic deformation of the soil, and (iii) plastic deformation of both the soil and the fibres and thus failure of the entire system. It is during the second stage that the maximum shear strength of the fibre reinforced soil exceeds that of a corresponding fallow soil. Fibre reinforced soils are, therefore, ductile as they can take loads even after large displacements (*e.g. Mickovski et al., 2007i*). In more recent years, and in collaboration with GeoPIV analysis (see Section 3.5), shear box tests have also been used to visually examine the interaction between roots and soils during lateral loading (*e.g. Mickovski et al., 2007; Loades et al., 2009*). The information that can be gained from shear box testing is, therefore, vast and has played a significant role in advancing the knowledge of soil root interaction.

2.3.3.3 Hydrological Mechanisms

The hydrological mechanisms of vegetation play a significant role in altering the water content within a soil (see Figure 2.32). The out of step occurrence of opposing processes (described in Section 2.2.4), however, makes assessing their overall balance, and thus the hydrological contribution of vegetation to slope stability, difficult (*Reubens et al., 2007*).

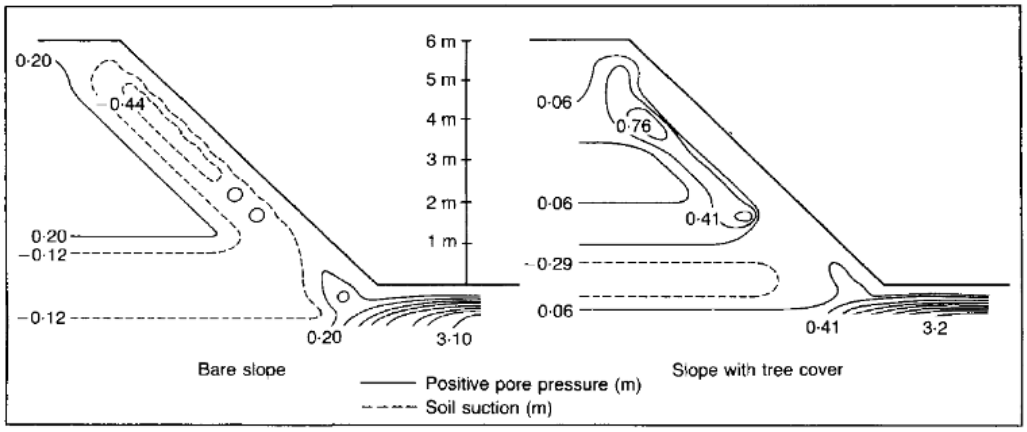

Figure 2.32: Difference in pore water pressure distributions between a bare and vegetated slope (*permeability = 1x10^{-6} ms^{-1}*) (*Collison et al., 1995*).

The impact of the seasonal reductions in beneficial hydrological effects combined with the seasonal increases in extreme weather conditions has received much attention and a number of hydrological models of bioengineered slopes have been developed (*e.g. Scott et al., 2007; Briggs, 2010*). These models have shown that the shrinking and swelling cycles of clay slopes are significant and that the rate of development of a progressive failure within a slope can be directly linked to seasonal suction effects (*Scott et al., 2007*). Such modelling has further demonstrated that tree covered slopes are more stable than grass covered slopes (*Scott et al., 2007*).

Suction is, generally, not considered in engineering design due to its unreliable contribution to an unstable soil (*e.g. Greenwood et al., 2004*). Some researchers (*e.g. Collison et al., 1995; Zhang et al., 2004*), however, insist that hydrology plays an important role and only a model that accounts for both hydrological and mechanical mechanisms can provide a sufficiently accurate account of the effects of vegetation on slope stability.

2.3.4 Assessing the Stability of a Bioengineered Slope

A growing number of calculation and computer models are being developed to provide a quantitative measure of the stability of a bioengineered slope. Such models must account for the non-linear behaviour and asymmetrical shape of a plant root system and to achieve this many assumptions and simplifications have to be made (*Sonnenberg, 2008*). As such, the present methods available for assessing bioengineering schemes fail to account for the full range of dynamic hydrological and mechanical processes (*Collison et al., 1995*) and typically include hydrological mechanisms through lowering the water table within the soil. In addition, models typically consider fully developed root systems and therefore fail to encompass the possible medium term decline in stability as vegetation becomes established (*Collison et al., 1995*). As a result, calculation and computer models do not compare fully to real life slopes (*Schwarz et al., 2009*).

Over the last few decades, the theories of foundation design and composite materials have been applied to the study of roots as a reinforcing material. Fibrous root systems are comparable to composite materials, such as fibreglass, where the low tensile strength of the soil is reinforced by a high density of randomly orientated roots (or fibres) that have a high tensile strength (*e.g. Mickovski et al., 2009*). In such models, roots are considered to stabilise a slope through increasing the apparent cohesion of the soil mass (*Schwarz et al., 2009*). Large single roots that provide a single point of anchorage, on the other hand, are comparable to foundations and inert stabilisation techniques, such as soil nails and piles (*e.g. Coppin and Richards, 2007*). As such, different models exist for different sized roots. In line with inert stabilisation techniques, these models typically consider a 2D cross section of slope and roots crossing the failure plane only (*Schwarz et al., 2009*).

2.3.4.1 Calculation Models

2.3.4.1.1 Modelling Fibrous Root Systems

When accounting for fibrous and/or short root systems in slope stability, soil root interaction is commonly expressed in its simplest form as a ratio of the area of roots crossing the failure plane to the area of the failure surface (*e.g. Bischetti et al., 2005*), as shown below:

$$RAR = \frac{A_{root-FS}}{A_{FS}} = \frac{\sum_{i=1}^{d} n_i \cdot A_{root-i}}{A_{FS}} \quad \text{Eq 2.21}$$

Where; ***RAR*** is the root area ratio; $\boldsymbol{A_{root\text{-}FS}}$ is the area of roots crossing the failure surface; $\boldsymbol{A_{FS}}$ is the area of the failure surface; ***d*** is the total number of diameter categories; $\boldsymbol{n_i}$ is the number of roots in diameter category *i*, and; $\boldsymbol{A_{root\text{-}i}}$ is the average cross sectional area of roots in diameter category *i*.

Wu *et al.* (1979) developed a model that calculates apparent root cohesion through combining the *RAR* value, root tensile strength and the inclination of a root to the shear plane, as shown in Equation 2.22;

$$c_R' = \zeta \cdot \frac{\sum_{i=1}^{d} (T_{root-i} \cdot n_i \cdot A_{root-i})}{A_{FS}} = \zeta \cdot \sum_{i=1}^{n} T_{root-i} \cdot RAR \quad \text{Eq 2.22}$$

$$\zeta = \cos(\varphi) \cdot \tan(\theta_\gamma') + \sin(\varphi) \quad \text{Eq 2.22 (a)}$$

Where; $\boldsymbol{c_R'}$ is the apparent cohesion provided by vegetation; $\boldsymbol{\zeta}$ is a correction factor that considers the inclination of roots, root distortion and slope angle, typically varying between 1.0-1.2; $\boldsymbol{\varphi}$ is equal to 90°-β, where β denotes slope inclination; $\boldsymbol{\theta\gamma}$ is the angle of root distortion, and; $\boldsymbol{T_{root\text{-}i}}$ is the maximum tensile strength of roots in diameter class *i*.

Once calculated, the root cohesion factor can be added to the apparent cohesion factor, *c'*, in the Mohr-Coulomb equation (Equation 2.9), to calculate soil shear strength as follows:

$$\tau_{S+R} = \sigma_V' \cdot \tan\phi' + (c' + c_R') \quad \text{Eq 2.23}$$

Where; $\boldsymbol{\tau_{S+R}}$ is the shear strength of root reinforced soil

The contribution of such a root system to the stability of a slope can therefore be described through a simple *FOS* formula (*O'Loughlin and Zeimer, 1982*), which combines the beneficial impact of apparent root cohesion with the adverse impact of both the above ground plant mass and loading on the upper plant (Figure 2.33), as shown below:

$$FOS = \frac{[\sigma_v' \cdot \tan\phi' + (c' + c_R')]}{(W_{trees} + W_{soil}) \cdot \sin\beta + F_{wind}} \quad \text{Eq 2.24}$$

Where; $\boldsymbol{W_{trees}}$ is the weight of tree/plant mass; $\boldsymbol{W_{soil}}$ is the weight of soil mass; $\boldsymbol{\beta}$ is the angle of slope, and; $\boldsymbol{F_{wind}}$ is the magnitude of wind loading.

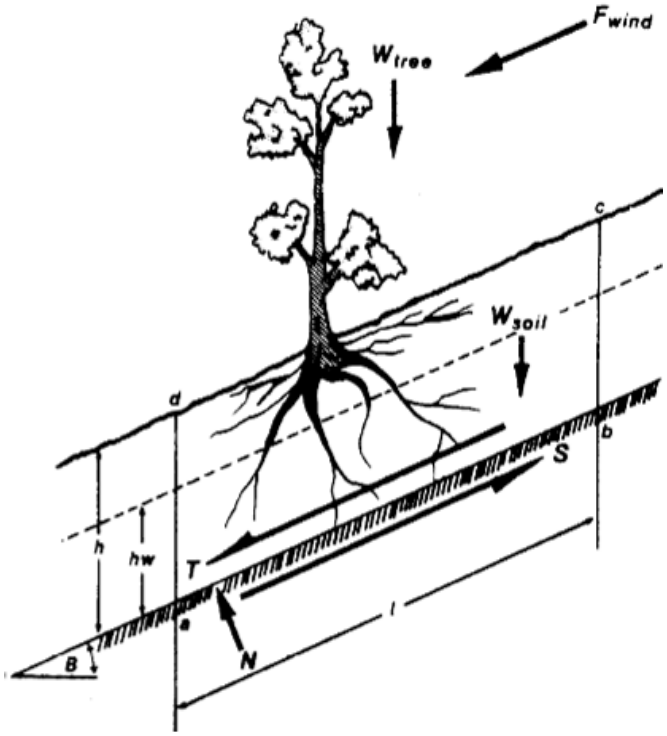

Figure 2.33: Explanation of forces acting on a slope for *FOS* calculations (*O'Loughlin and Ziemer, 1982*).

It should be noted, however, that calculation of τ_{S+R} considers root cohesion at the failure plane only and applies it to the whole slope. In actuality, apparent root cohesion reduces with reducing *RAR* to a value of zero, which typically occurs at a depth of about 1m (*Danjon et al., 2008*). For a more thorough investigation into the effects of apparent root cohesion, it is therefore advised to complete the calculation at various depths.

The Wu *et al.* (1979) model attempts to account for the variation in root strength as a function of root diameter, root inclination and a mix of different diameter roots. It inaccurately assumes, however, that (i) all roots, regardless of diameter, orientation or strength, are fully mobilised in tension at the same point and thus break simultaneously (*Preti and Giadrossich, 2009*); (ii) roots are cylindrical and have an even diameter along their length, thus developing an even tensile stress (*Sonnenberg, 2008; Comino and Druetta, 2009*); (iii) soil root behaviour is homogenous, without local variations or complex root distributions (*Schwarz et al., 2010*); and (iv) the angle of shear resistance is not impacted by root presence (*Comino and Druetta, 2009*). In addition, the usual use of a value between 1.0 and 1.2 for the factor accounting for root angle, deformation and orientation, ζ, has questionable accuracy (*Thomas and Pollen-Bankhead, 2010*). Thomas and Pollen-Bankhead (2010), among others, have found that a value of ζ in this range is generally too large and is only applicable when

soil friction angles are greater than 35°. Wu (2007) found that only 20-33% of roots fail at any one time during shearing, as the random orientation of roots means that some will fully mobilise their tensile strength while others will take no load. The success of this model in accurately measuring root reinforcement is, therefore, somewhat limited and introducing c_R' into slope stability calculations significantly over estimates the contribution of vegetation (*Schwarz et al., 2009*). A number of studies (*e.g. Shewbridge and Sitar, 1990; Pollen et al., 2004; Pollen, 2007*) have assessed the discrepancy between measured and calculated values of c_R', concluding that the Wu *et al.* (1979) model has an average overestimation of 150%, although much higher overestimations have been found. This is commonly incorporated into Equation 2.22 through multiplication by a factor of 0.4 (*Schwarz et al., 2009*).

Roots undergoing uprooting do not mobilise their full tensile strength upon system failure, while roots that break do. The assumption that the same contribution to soil strength will be incurred if a root breaks or uproots is therefore an additional oversimplification of root soil behaviour. Waldren and Dakessian (1981) introduced two new parameters to account for these effects. These are shown below.

$$T_{root} \cdot RAR = T_1 \cdot RAR_1 + T_2 \cdot RAR_2 \qquad \text{Eq 2.25}$$

$$T_1 = \sqrt{E_{root} \cdot h \cdot \frac{4 \cdot \tau_{root}}{D_{root}}} \cdot \sqrt{\cos(\varphi) - 1} \ \{\text{for root stretching}\} \qquad \text{Eq2.25(a)}$$

$$T_2 = \frac{4 \cdot \tau_{root} \cdot L_{root}}{D_{root}} \ \{\text{for root slippage}\} \qquad \text{Eq 2.25(b)}$$

$$\tau_{root} = \mu \cdot \sigma_n' \qquad \text{Eq 2.25(c)}$$

Where; $\boldsymbol{T_{root}}$ is the tensile stress of contributing roots; $\boldsymbol{RAR_1}$ is the RAR of roots that stretch; $\boldsymbol{RAR_2}$ is the RAR of roots that slip; $\boldsymbol{E_{root}}$ is the root's Young's modulus; $\boldsymbol{h}$ is the width of shearing zone; $\boldsymbol{\tau_{root}}$ is the soil root friction; $\boldsymbol{D_{root}}$ is the root diameter; $\boldsymbol{\varphi}$ is equal to 90°-β, where β denotes slope inclination; $\boldsymbol{\mu}$ is the coefficient of soil root friction, and; $\boldsymbol{\sigma_n'}$ is the stress normal to root.

Assessing which roots will uproot and which roots will break prior to loading is, however, difficult. Operstein and Frydman (2000) suggest that roots with a diameter greater than 2 mm do not break and instead undergo uprooting. Additionally, the length of roots can be used to assess their failure

mechanism, with sufficient anchorage length being a key element in a roots ability to resist uprooting. The minimum anchorage length required to mobilise a full tensile strength is (*Gray and Sotir, 1996*):

$$L_{root} = \frac{T_{root} \cdot D_{root}}{4 \cdot \tau_{root}} \qquad \text{Eq 2.26}$$

The key strength of the Wu *et al.* (1979) model is that it considers the properties of individual roots in order to assess the average strength of the root system. Its key failing, however, is that it assumes all roots will fail at the same time. Additionally, it fails to link root tensile strength to soil moisture content, density and type (*Pollen, 2007*). A more logical approach is to take the percentage of roots that are weaker than the tensile stress induced by loading and assume these to be the only failing roots under that particular load. The fibre bundle model (FBM) uses this idea and therefore provides a better overview of how a bundle of roots, with varying properties, break in tension (*Schwarz et al., 2009*). To achieve this, the FBM assumes that, at a particular strain, ε, roots in diameter group i with a strength, T_{root}, that is less than $E_{root\text{-}i} \cdot \varepsilon$ break, while the remaining roots carry a load of magnitude $E_{root\text{-}i} \cdot \varepsilon$. This is expressed in the following equation:

$$T_{root}(\varepsilon) = \sum_{i=1}^{m} E_{root-i} \cdot \varepsilon \qquad \text{Eq 2.27}$$

Where: $\boldsymbol{E_{root\text{-}i}}$ is the Young's modulus of roots in diameter group $\boldsymbol{i}$.

The FBM doesn't differentiate between uprooting and breakage when considering root failure, as interest lies only in whether or not the fibre can continue to bear tensile load (*Thomas and Pollen-Bankhead, 2010*). Once a root has failed, its loading is redistributed among the remaining roots, which increases their loading and makes them more likely to fail. In its simplest form, redistribution can be considered as an even load share throughout the intact system. This is known as global load sharing or GLS (*Thomas and Pollen-Bankhead, 2010*). In actuality load distributions are based on the proximity of the intact fibres to the broken fibre, with only a small element of loading being redistributed globally (*Thomas and Pollen-Bankhead, 2010*). Local load sharing, or LLS, can therefore be considered as an alternative. Realistically, however, LLS is difficult to define as root mapping in the field is invasive and thus the local distribution of roots is generally unknown (*Thomas and Pollen-Bankhead, 2010*). GLS FBM's are therefore most commonly used. The FBM does not account for root orientation.

In conclusion, the c_R' method considers the key elements of fibre reinforcement only and thus simplifies the soil root system to create a straight forward and quick calculation model, the results of which correspond reasonably well to field and lab experiments (*Abernethy and Rutherford, 2001*). Developing a more in depth and accurate analysis model is complex, due to the high number of significant variables in a root system, and will be undesirable to the engineer unless it is reasonably quick to use and possible to implement in current design techniques, e.g. finite element modelling (*Sonnenberg, 2008*).

2.3.4.1.2 Modelling Anchor Roots

Roots that are large enough to provide sufficient anchorage into the stable soil mass are modelled using the well-established pile and soil nail analysis techniques. In particular, pile foundation theory is applied to roots in compression, while soil nail theory is applied to roots in tension. When these roots have a diameter that is smaller than 50 mm, however, Wu and Watson (1998) suggest an approach that is similar to the modelling of fibrous root systems. In this case, root cohesion is evaluated based on root orientation, is assumed to be fixed at the soil surface and has a value that is consistently greater than $0.3 \cdot T_{root} \cdot RAR$ (*Wu and Watson, 1998*). Alternative models to analyse the behaviour of roots that sit between the fibrous and anchor categories are scarce, as is the experimental data to support the model suggested by Wu and Watson (1998). Further research is therefore required to understand the behaviour of such roots.

Using the pole installation method, the complex properties of root architecture are simplified to a simple, straight tap root, which can be further simplified to have an approximately even diameter along its length. This makes the consideration of lateral branches in initial design redundant (*Schuppener, 2001*). Figure 2.34 shows the failure mechanisms of such a system, namely breakage and uprooting. This is comparable to a soil nail system, indicating that the strength of bond between root and soil is likely to be of key importance, along with root material properties. The bond strength between a root and its surrounding soil is a function of the soil's density and will increase as the root grows and develops lateral branches (*Schuppener, 2001*). Counter-intuitively, normal stress is not considered to be a good indicator of bond strength, due to irregularities along the root's length (*Schuppener, 2001*). Schnuppener (2001) reported that the average shear strength at the interface of a 2m long pole that sits on a slope with a 45° incline is around 15 kNm^{-2}, provided that the normal stress does not exceed 25 kNm^{-2}. As well as soil nails, however, this root system is also akin to that of a group of flexible piles that are subjected to a lateral load. Considering this system, it has been

suggested that root stiffness and deformation are significant factors in defining shear strength (*Sonnenberg, 2008*). The increase in mechanical interaction, and therefore system strength, as a root develops lateral branches eliminates any concern about not accounting for branches in bioengineering design, as the system will be stronger than anticipated.

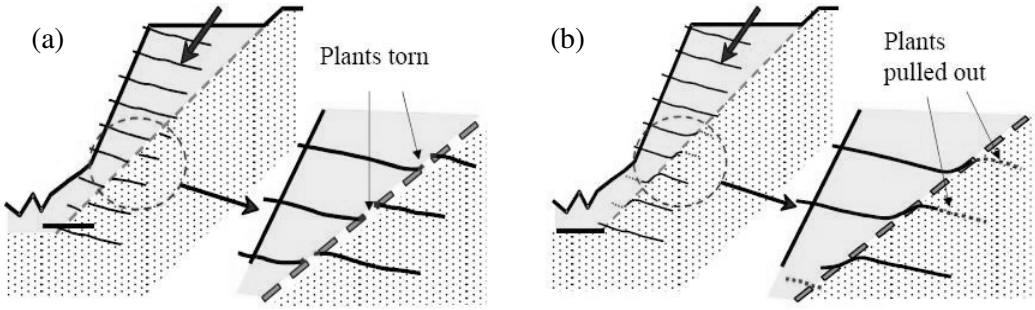

Figure 2.34: Likely root failure mechanisms when considering the pole installation technique on a slope (a) breakage and (b) root pull out (*Schuppener, 2001, as sited by Sonnenberg, 2008*).

Defining the stability of pre-vegetated slopes is more complex due to random root patterns coupled with the difficulty in mapping them. They, perhaps, call for a more thorough investigation into root architecture.

2.3.4.2 Computer Modelling

Computer modelling of root reinforced slopes, particularly finite element modelling, is becoming increasingly sought after. Such models have the capacity to maintain a reasonable time frame for assessing stability whilst encompassing a larger range of parameters than hand calculations, accounting for the 3D effects of vegetation, and providing a visual representation of soil root behaviour. The development of computer models in this field has been explored from three different perspectives. The first is interested in simulating root growth, development and architecture as a function of its local environment and species (*e.g. SimRoot - Lynch et al., 1997; Zhang et al., 2013*), and often includes complex hydrological and mechanical processes. The second simulates uprooting and overturning as a function of loading, root architecture, and root and soil material properties (*e.g Fourcaud et al., 2007*). Such models typically assess mature roots only and often consider simplified root systems. The third looks into whole slope modelling, accounting for the effects of vegetation with a change in moisture content and/or apparent cohesion (*e.g. Collison et al., 1995; Chok et al., 2004; Briggs, 2010*). These models can also account for more complex interactions (*e.g. Danjon et*

al., 2008). The first modelling technique accounts for local behaviour, the third accounts for global behaviour and the second modelling technique sits somewhere in between.

On a global scale, Chok *et al.* (2004) report on the suitability of finite element (FE) analysis in modelling a root reinforced slope. Their FE analysis involved sectioning a slope into a series of small elements and accounting for the effects of vegetation, in their simplest form, by changing the parameters of the individual elements affected by vegetation (see Figure 2.35). This method can be used in two or three dimensions and accounts for the variable and random nature of vegetation through providing flexibility in both locating the relevant soil elements and assigning representative mechanical properties (*Chok et al., 2004*). Unlike hand calculations, this form of FE analysis allows local variance to be easily accounted for in the calculation of mass stability, which is very favourable. Increased accuracy can be gained through increasing the number of elements; however, this also increases the time taken for the model to reach a solution.

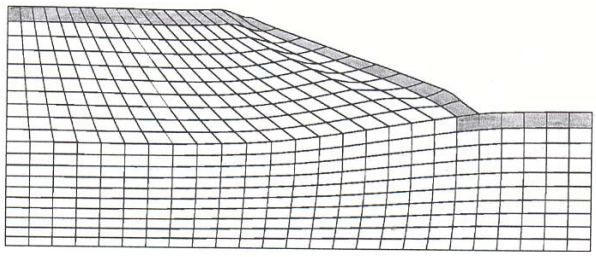

Figure 2.35: Finite element modelling of a bioengineered slope, showing slope sectioned into elements. Shaded elements have been altered to account for vegetation (*Chok et al., 2004*).

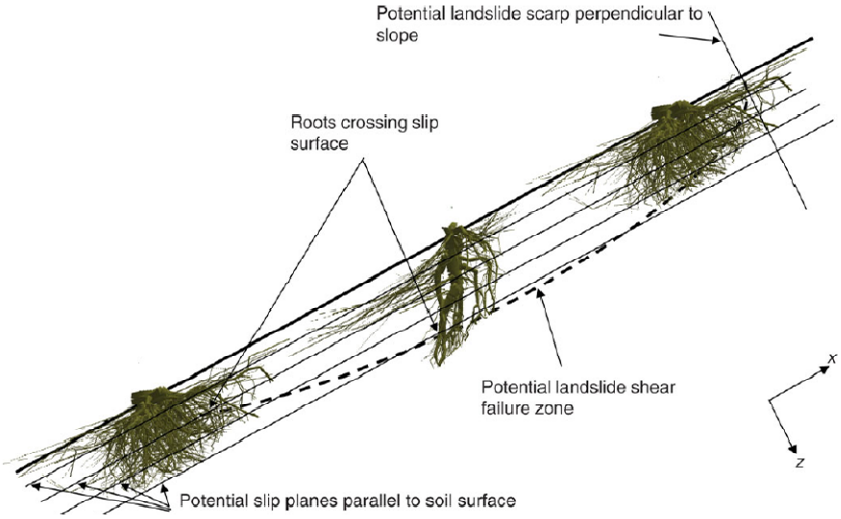

Figure 2.36: Inclusion of complex root architecture in a shallow slope stability model (*Danjon et al., 2008*)

Specialised bioengineered slope models, which account for small aspects of either purely mechanical or purely hydrological mechanisms, are becoming increasingly popular. Briggs (2010), for example, looked into the hydrological cycle of a clay embankment that is permeated with vegetation. In this model, vegetation is accounted for through transpiration, starting at a depth of 3 m for trees and 0.9 m for grasses, and infiltration only. The output of this model compared well to field data. Danjon *et al.* (2008), on the other hand, modelled the effects of spatial root distribution on the value of apparent root cohesion within a shallow slope. To achieve this, very complex three-dimensional root architecture was considered (see Figure 2.36) along with root material properties. The effects of spatial distribution were found to be significant. Modelling local soil root interaction furthers the understanding of key parameters and can be used to develop simplified descriptions that can be included in whole slope modelling. A number of models have been developed to look into the mechanical impact of lateral and/or axial loading to a root sitting in a soil. Fourcaud *et al.* (2007), for example, developed a continuum FE model that simulates the uprooting of a whole root system in different types of soil. This has been validated against winch tests and can be used in either 2D or 3D. Using this model, the mechanical stresses within any part of the soil root system can be visualised and how these are affected by root morphology and root loss can be calculated.

2.4 Research requirement

Understanding the functions of plant roots and their influence on soil (and slope) properties is of extreme importance in improving bioengineering techniques and thus moving the construction industry towards a more environmentally friendly and sustainable future. It would also allow for the improved management of naturally vegetated slopes, crops and forests.

Plant root functions can be categorised into mechanical and hydrological (*Greenway, 1987*). There is disagreement in current research, however, as to which is the most critical in terms of influencing soil (and slope) stability, but mechanical soil root interaction is more commonly accepted (*e.g. O'Loughlin and Ziemer, 1982; Mickovki et al., 2007*). This is because, while the hydrological functions alter the strength of soil through influencing its pore water pressure, it is ultimately the mechanical functions that will decide whether or not the slope will fail when weaknesses arise in the system. For this reason, this Thesis will focus on mechanical soil root interaction hereon.

The literature review revealed a number of key shortcomings in the current calculation models, which have been designed to estimate the mechanical contribution of a plant root to soil strength. Most

notably, they do not provide a consistently reliable output and, in some cases, require arbitrary factors in order to force them to match measured data (e.g. the Wu *et al.* (1979) model is commonly multiplied by a factor of 0.4). This could be the result of an over simplification of the roots mechanical response to loading. In particular, most models consider roots to contribute to soil strength through their tensile capacity only (e.g. the FBM and application of soil nail design techniques) yet roots are known to have a stiffness that is significant in comparison to their tensile strength (e.g. *Operstein and Frydman, 2000*). This lack of understanding in the fundamentals of mechanical root functions has been carried through to the development of finite element models that study the effects of vegetation in slope stability. In many cases, these models rely on existing calculation techniques to estimate the change in soil properties as a result of vegetation (e.g. *Chok et al., 2004*). The change in soil properties is commonly summarised by an apparent root cohesion, c_R' factor. This, however, is a stress independent parameter and it has therefore been suggested that an apparent root dilation would provide a more reliable account of root contribution (*Graf et al., 2009; Diambra et al., 2010*).

Chapter 3 Root pull out testing

3.1 Introduction

Testing the pull out capacity of a root system, both in the laboratory and *in situ*, has received considerable attention over the last couple of decades (*e.g. Operstein and Frydman, 2000; Hamza et al., 2006; Mickovski et al., 2007; Loades et al., 2009*). The standard testing procedure involves clamping a plant at ground level and applying an upwards force until the root system becomes dislodged from its surrounding soil. Such tests (known as uprooting or pull out tests) are simple to perform and measure root anchorage capacity as the force that resists root pull out. Post-testing, the properties of the root system (for example, the length of the primary and lateral roots, the branching pattern, the root tensile strength and the location and scale of any root failures/breakages) can be measured and used to link system features to anchorage capacity. As such, uprooting tests measure global, rather than local, soil root interaction.

Mickovski *et al.* (2007) performed a considerable number of laboratory uprooting tests on both real and analogue root systems. The purpose of their project was: (i) to study the global impact of system changes to system anchorage capacity; and (ii) to develop a novel technique for visualising and thus measuring local soil and root movement during loading (along a cross section through the model). In addition to performing pull out tests in their traditional form, therefore, they performed a series of 'cross section' uprooting tests (see Figure 3.1). In traditional (or full section-centre) tests, the roots had a full cross section, sat in the centre of the soil sample and were surrounded entirely by soil. In cross section (or half section-front) tests, the roots had a half cross section, sat at the boundary of the soil sample and were surrounded by both soil and a transparent containing wall, made of Perspex. This set up modelled the cross section of the soil root system and, assuming that the effect of the boundary condition is negligible, was used to visualise local soil root interaction during loading.

Through capturing digital images of a soil root system at even time intervals during a cross section-front test, and applying GeoPIV analysis (*White and Take, 2002*, see Section 3.5), the displacement fields within the system can be measured, from which strains can be calculated. This procedure has been used by Mickovski *et al.* (2007), *Sonnenberg* (2008) and Loades *et al.* (2009) and has proved to be a useful tool for measuring local soil and root movements during a range of geotechnical soil root processes, including: whole slope modelling, uprooting tests and shear box tests. In these studies, the data collected from the GeoPIV analysis (i.e. displacement fields) formed the end of the investigation

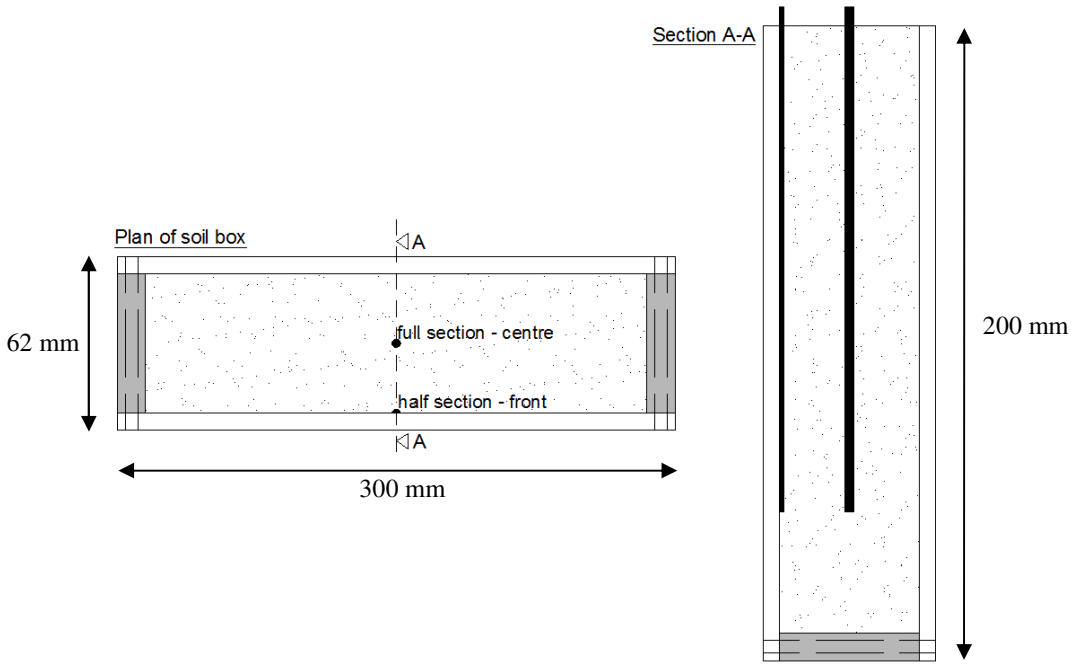

Figure 3.1: Plan of and section through a soil box, showing the position of a root in a full section-centre and half section-front pull out test. In the cross section-front approach, the root is in contact with the front face so that the deformation of the root and surrounding soil can be visualised.

into soil root interaction. Through assuming similarity between the root soil system and a pile soil system (see Figure 1.1) and thus applying the beam-on-Winkler foundation theory to the measured root movements (see Section 2.3.2.2), however, it is possible to use these digital images to quantify the mechanical behaviour of the root, the soil and the detailed soil root interaction during loading. Furthermore, if this quantified behaviour can be theoretically replicated using foundation design codes, then it is possible to develop a numerical model that can predict the response of a root to loading. This will be covered in Chapter 4.

Mickovski *et al.* (2007) obtained a large database of root pull-out tests. These included: wet (-2.5 kPa) and dry sand; stiff (wood) and more easily deformable (rubber) root analogues, which cover the full range of elastic modulus measured for real plant roots; and buried real roots. Using this database, this Chapter reports on and further analyses; (i) a series of full section-centre uprooting tests, with a view to determine the requirements of calculation and numerical models that are to quantify and predict uprooting behaviour; and (ii) a series of half section-front uprooting tests, with a view to assess their comparability to full section-centre tests and their suitability for an alternative GeoPIV analysis that measures appropriate displacement fields for the application of a calculation model that uses *t-z* methodology.

3.2 Material selection and sample set up

Mikovski *et al.* (2007) provide a detailed description of material selection and sample setup. Soil samples containing roots were prepared in a soil box as shown in Figure 3.2. The soil box was made of aluminium with Perspex viewing panels to its front and back. It had no lid and therefore modelled a free soil surface, as is expected during root pull out. To accommodate the preparation and equilibrium of wet soil samples, the box included a drainage system at its base. This was provided by a geotextile layer above a porous stone drain and a PVC drainpipe (*Mickovski et al., 2007*). A knife edge was placed around the rim of the box in order to minimise any variation in soil density that may be caused by sand particles bouncing off the box edges during sand pluviation (*Mickovski et al., 2007*). This was removed before the pull out tests began.

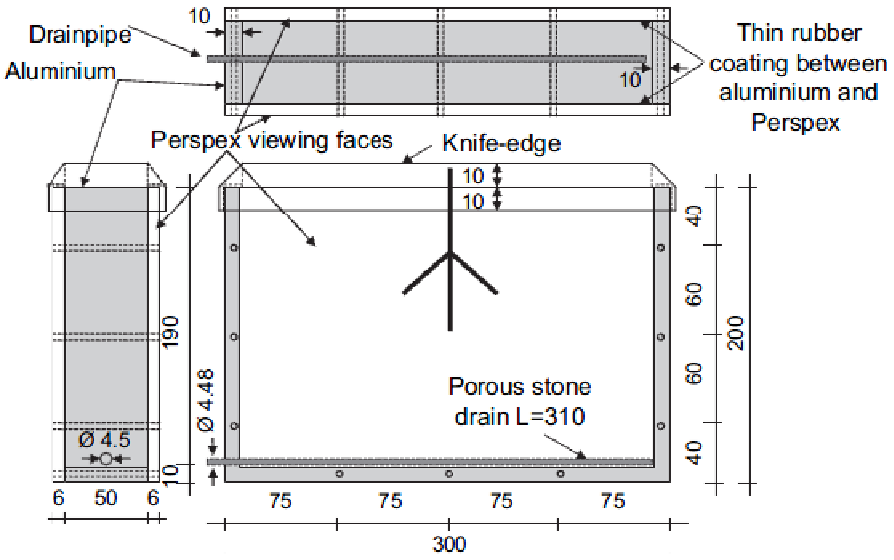

Figure 3.2: Soil box used for pull out tests, Mickovski *et al.* (2007). All dimensions are provided in mm.

3.2.1 Root material properties

Mickovski *et al.* (2007) used root analogues to control the biological variance within and between plant roots. For comparison, they also carried out a small number of tests using excavated segments of three year old Willow roots, grown at the James Hutton Institute, Invergowrie (formerly the Scottish Crop Research Institute). Through controlling the root properties in this manner, they were able to conduct a study that looks into the effect of changing specific material and architectural properties on the ability of a root system to resist pull out (*Mickovski et al., 2007*). In this Thesis, this

control allows a calculation technique that is designed for predicting the response of a pile foundation to loading to be applied to a root system. Pile foundations are considerably larger and stiffer than plant roots, as well as having simpler architecture and more uniform material properties. Through controlling root properties, however, the pile calculation technique can be applied to very small, flexible piles rather than complex biological plant root systems. The suitability of the pile calculation technique for this application can therefore be studied in detail.

To model a wide range of root stiffness's two contrasting materials were selected for the root analogues. Woody, lignified roots were modelled using lengths of 2.3 mm diameter linden wood (sourced from Fricke, Weimar, Germany) and flexible roots were modelled using lengths of 1.6 mm diameter Viton O-ring rubber (sourced from RS components, Corby, UK) (*Mickovski et al., 2007*). These materials were extensively tested by Mickovski *et al.* (2007) and Sonnenberg (2008), and were shown to behave mechanically in a similar way to real woody and non-woody roots. Figure 3.3 compares the Young's modulus of linden and Viton to segments of three year old Willow roots (with various diameters) (Viton: E_{vit} = 29 MPa, Linden: E_{lin} = 1264 MPa, and Willow: $E_{will} = 306.82 \cdot D_{root}^{-1.3248}$ MPa, where D_{root} is the root diameter) (*Mickovski et al., 2010*). As demonstrated, the analogue root materials represent the extreme stiff and extreme flexible Willow root properties.

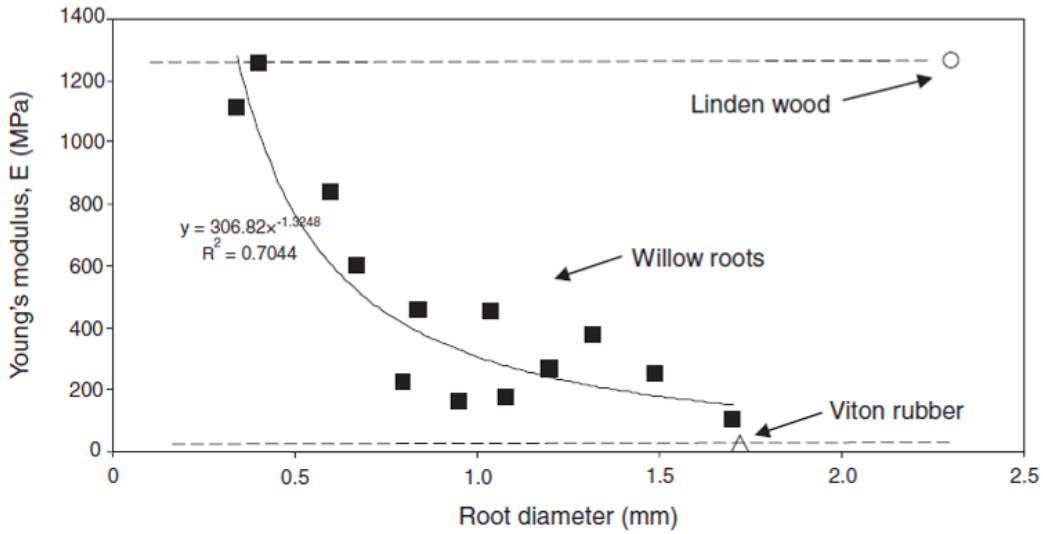

Figure 3.3: Comparison of Young's modulus values for Linden wood, Viton rubber and three month old Willow roots (*Mickovski et al., 2010*)

The Viton data, however, is incomplete. Rubber is a complex non-linear elastic material with a stiffness that varies with strain, but the data provided by Mickovski *et al.* (2007) does not represent the range of strain for which E_{vit} = 29 MPa. In order to understand, and ultimately predict, the

behaviour of rubber root analogues, it is important that the Young's modulus considered corresponds to the range of strain experienced during loading (uprooting in this case). A series of tensile tests were therefore carried out. Tensile tests are commonly used to measure the force required to stretch a specimen by a known amount, and thus calculate the materials stress (σ) - strain (ε) relationship, the slope of which represents Young's modulus. Stress and strain are calculated as follows:

$$\varepsilon = \frac{\Delta L}{L_0} \qquad \text{Eq 3.1}$$

$$\sigma = \frac{F_a}{A_t} \qquad \text{Eq 3.2}$$

Circular cross section $$A_t = \frac{\pi \cdot \left[D_{root} - \varepsilon \cdot \nu \cdot D_{root}\right]^2}{4} \qquad \text{Eq 3.2(a)}$$

Semi-circular cross section $$A_t = \frac{\pi \cdot \left[D_{root} - \varepsilon \cdot \nu \cdot D_{root}\right]^2}{8} \qquad \text{Eq 3.2(b)}$$

Where, at time t; $\boldsymbol{\sigma}$ is axial stress; $\boldsymbol{F_a}$ is the force required to stretch the sample; $\boldsymbol{A_t}$ is the cross sectional area of the sample (accounting for the reduction in area as the root stretches); $\boldsymbol{\varepsilon}$ is the axial strain; $\boldsymbol{\Delta L}$ is the change in length of the sample, and; $\boldsymbol{L_0}$ is the original length of the sample.

An Instron 5966 (Instron, High Wycombe, UK), with a 1 kN load cell, was used to perform the tensile tests on 50mm lengths of Viton, as shown in Figure 3.4. In line with the full section-centre and half section-front tests, both samples with a full cross section and samples with a half cross section were tested (see Section 3.2.2 for details of specimen preparation). Each sample was clamped in place using pneumatic grips, the pressure of which could be increased during testing to eliminate slippage, and the Instron was programmed to move the upper grip at a rate of 2 mm/minute, recording the consequent force and cross-head displacement. Additionally, two white dots, with a spacing of 20mm, were drawn on the surface of each specimen and an infra-red camera was used to trace and record their displacements. This ensured accurate readings of axial strain. Each sample was displaced by a maximum of 50mm (i.e. 100% strain).

Using the force (F_a) and displacement (ΔL) data gathered from the tensile tests, along with Equations 3.1 and 3.2, stress-strain curves for the full and half Viton samples (over a range of Poisson's ratio between 0.48 - 0.499, as per *James and Lord, 1992*) were plotted. These are shown in Figure 3.5. As

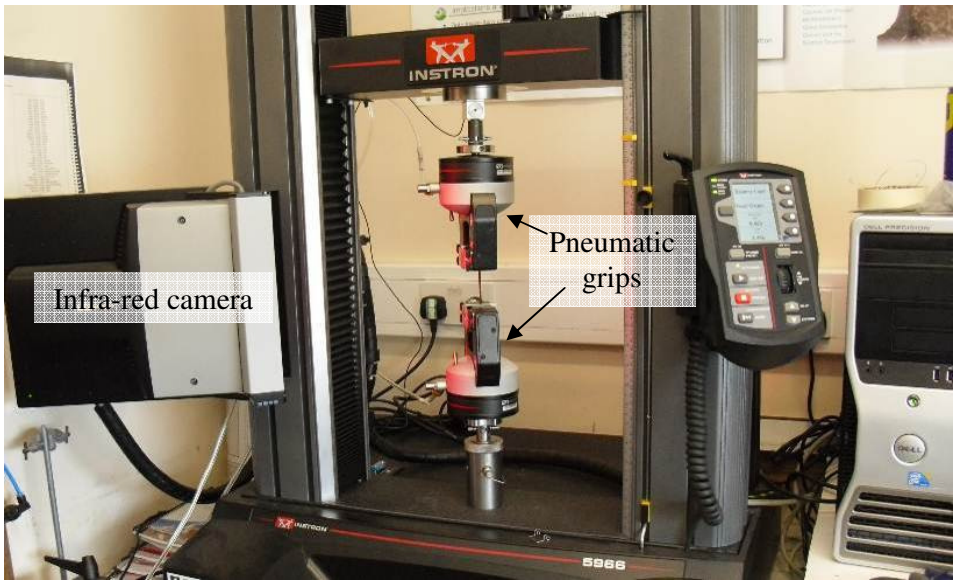

Figure 3.4: Set up used to conduct tensile tests on Viton rubber.

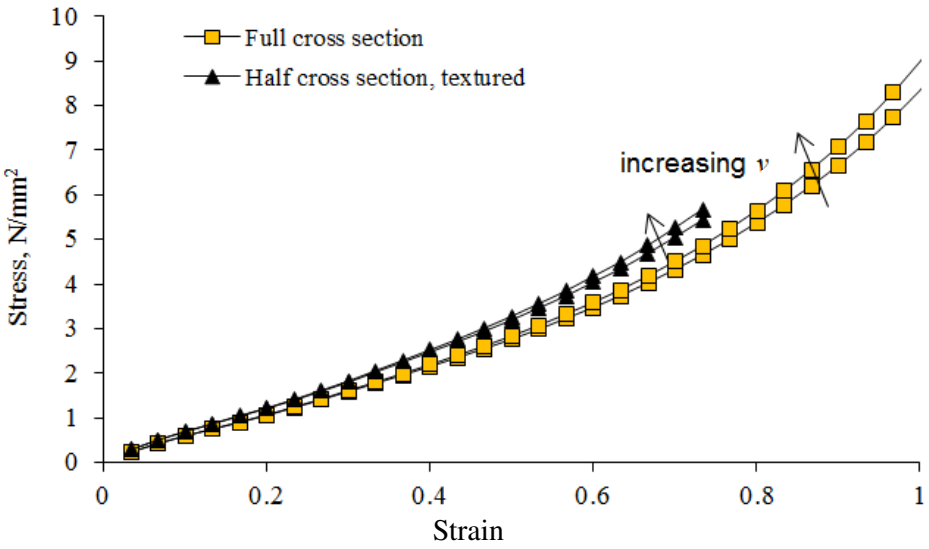

Figure 3.5: Stress-strain relationship for Viton rubber over a range of 0 - 100% strain.

demonstrated, the stress-strain curves are non-linear, confirming the complex behaviour of rubber, and reveal an increase in slope when the half samples are considered. It is likely that this change in material properties between the full and half root analogues is the result of differences in their preparation (in which the half samples are additionally exposed to pre-stressing and painting, see Section 3.2.2). Figure 3.5 also shows that the selection of Poisson's ratio, ν, has little impact on the calculated stress behaviour, particularly at low strains (which are expected during uprooting). The range of Poisson's ratio considered is typical of rubber (*James and Lord, 1992*). Hereon, ν will be

taken as 0.49 (central to the possible range of values for rubber). The Poisson's ratio of Linden wood is reported to be 0.022 (*Kretschmann, 2010*).

Using Equation 3.3 and the stress strain relationships presented in Figure 3.5, the Young's Modulus of Viton rubber was calculated to range between 5 MPa (at low strains: < 40 %) and 10 MPa at 100% strain. This is considerably smaller than the 29 MPa reported by Mickovski *et al.* (2007), indicating that their study considered a significantly higher level of strain (possibly corresponding with the failure of Viton (strain at failure ~290%, *RDS Components product specification*)).

$$E = \frac{\Delta\sigma}{\Delta\varepsilon} \qquad \text{Eq 3.3}$$

Where: $\boldsymbol{E}$ is the Young's modulus; $\boldsymbol{\sigma}$ is stress, and; $\boldsymbol{\varepsilon}$ is the strain.

3.2.2 Root preparation

Mickovski *et al.* (2007) used a variety of root architectures, materials and cross sectional areas in their pull out tests, which created a wide variety of root properties. Figure 3.6 demonstrates the architectural forms considered. These are: individual tap roots, roots with lateral branches located halfway along their anchor length (herringbone) and roots with lateral branches located at their base (dichotomous). The length, L_{root}, and anchor length, L_{anc}, of these systems were 110 mm and 100 mm, respectively. All lateral branches had a length, a, of 30 mm, were angled, α, at 45° to the primary root and were attached to the primary root using cyanoacrylate glue (sourced from RS Components, Corby, UK). The cyanoacrylate glue created rigid joints, which are representative of the bifurcating points in real root systems (*Mickovski et al., 2007*). These simplified architectural forms ensured that the root systems were symmetrical through a vertical plane and therefore allowed axially loaded root behaviour to be observed and measured (*Mickovski et al., 2007*). In the initial development of a calculation model, only the tap root system will be considered, as this architectural form is very similar to pile foundations.

To create the half root analogues, lengths of wood and rubber were halved along their length and coated with fine specks of colour (termed optical texture in this Thesis). Texture was added to the materials because their natural surfaces had no (or poor) variation in colour and shading, an essential quality for successful GeoPIV analysis (see Sections 3.5 and 3.6). It was applied to the flat surface of the root analogues by painting fine dots and lines, using a mixture of ink and paint in a variety of

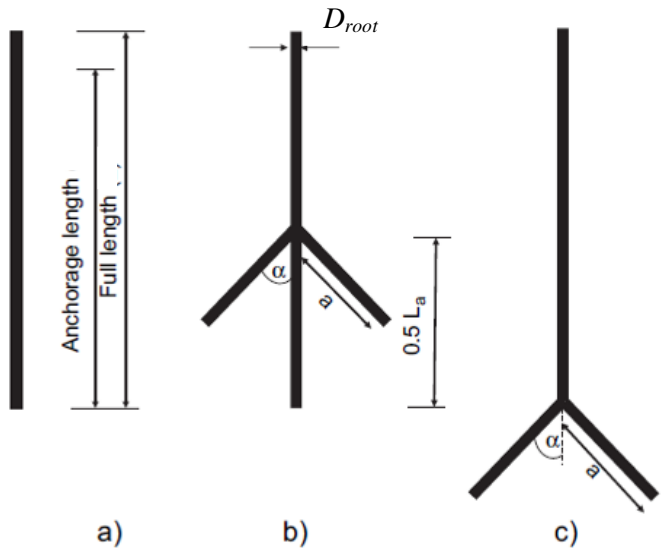

Figure 3.6: Root architecture considered by Mickovski *et al.* (2007). (a) Tap root, (b) Herringbone, (c) Dichotomous. In all cases, L= 110mm, L_a = 100mm, a=30m and α = 45°.

colours. Wood was halved by sanding it on a flat surface that was covered in fine sandpaper, while rubber was halved by clamping it between two blocks of wood and running a craft knife along the join. Channels within the wooden blocks allowed the rubber to be cut close to its centre line. Viton, however, can stretch to 290% before breaking (*RDS Components product specification*), making it difficult to control. Consequently, the half rubber root analogues had slight variation in cross section along their lengths. This could be minimised by cutting the rubber using one quick movement but could not be eliminated.

The half root analogues were positioned in the soil box by applying silicon grease (sourced from RDS components, Corby, UK) to their flat surface and adhering them to the front face of the soil box. This proved to be an efficient means of holding the root analogue in place while soil was prepared behind it. During testing, the silicon grease acted to reduce any friction and helped decrease the ingress of soil particles between the root analogue and Perspex.

The full root analogues were cut to length and suspended in the centre of the soil box by threading them onto a stiff PVC chord (details provided by *Mickovski et al., 2007*). This chord held the root analogues in position during the soil packing process and was cut prior to testing.

To prepare the real roots, segments of three year old willow root were excavated, washed and classified by length and diameter. The segments that best resembled the architecture of the root

analogue systems were positioned in the soil box by suspending them from a stiff PVC chord, as before. The real root segments had full cross sections and an average diameter of 3.5mm (*Mickovski et al., 2007*).

3.2.3 Soil material properties

The soil material selected for the Mickovski *et al.* (2007) root pull out tests was washed, uniformly graded silica sand, sourced from Lower Greensand, Redhill, Surrey (WBB Minerals Ltd.). This material has an average particle size, D_{50}, of 0.12 mm and standard minimum, γ_{min}, and maximum, γ_{max}, density values of 1516 kgm^{-3} and 1716 kgm^{-3}, respectively (*Mickovski et al., 2007*).

3.2.3.1 Soil shear strength

The shear strength of the silica sand was determined through a series of direct shear box tests. A shear box, with a depth of 50 mm and a diameter of 100 mm (as used in the root reinforced shear box tests of Chapter 6), was operated using a standard shear box table (see Figure 3.7). The sand was packed into the shear box to a density of 1692 kg/m^3 (for preparation technique, see Section 3.2.4), providing very dense soil samples with a relative density, I_D, of 0.89. Relative density can be calculated through Equation 3.4 and categorised using Figure 3.8.

$$I_D = \frac{1/\gamma_{min} - 1/\gamma}{1/\gamma_{min} - 1/\gamma_{max}} \qquad \text{Eq 3.4}$$

Where; $\boldsymbol{I_D}$ is the relative density of the soil sample; $\boldsymbol{\gamma_{min}}$ is the minimum density (kgm^{-3}); $\boldsymbol{\gamma_{max}}$ is the maximum density (kgm^{-3}), and; $\boldsymbol{\gamma}$ is the density in question (kgm^{-3}).

After packing the sand into the shear box, loads of 9.8N, 34.1N and 73.6N (providing respective normal stresses of 1.26kPa, 4.35kPa and 9.37kPa) were applied to its surface and the lower shear box was displaced, at a rate of 2mm/minute, to a maximum of 20mm. Note: small normal stresses were considered in order to mimic the soil state that would be present during the uprooting and root reinforced soil shearing tests. In these tests, the soil has a free surface and the root length does not exceed 150 mm. As such, the normal stress at the root tip reaches a maximum of only 2.5 kPa. A load cell and linear variable differential transformer (LVDT) were connected to a computer and, using LabView on a Windows XP platform, were used to record the force and displacement during loading. Additionally, a shear box test with no soil present was conducted. This allowed the friction

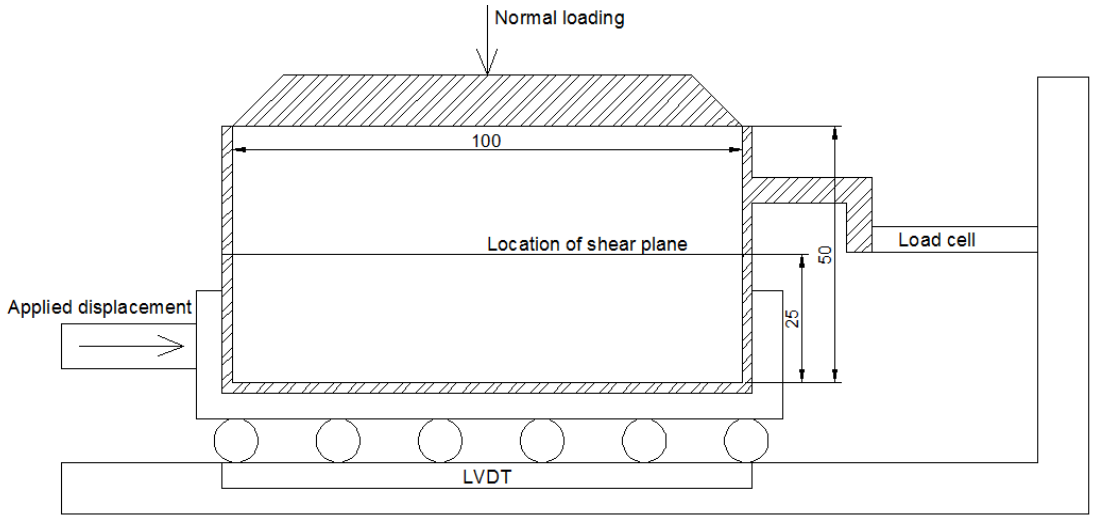

Figure 3.7: Schematic of the shear box apparatus used to conduct the direct shear box tests. Note: measurements are in mm.

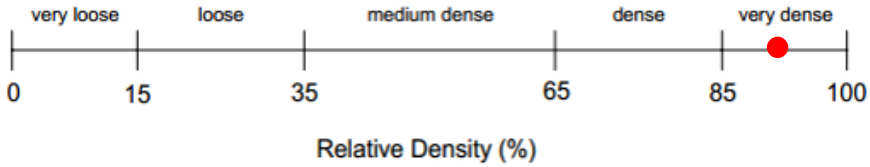

Figure 3.8: Definition of soil density as a function of relative density (*Lambe, 1969*). Highlighted in red is the density of the soil samples used in this study.

between the upper and lower shear boxes to be measured and used to correct the soil shear measurements.

Figure 3.9 presents the shear stress - displacement curves for the silica sand, at different values of normal stress, where shear and normal stress are calculated respectfully through Equations 3.5 and 3.6:

$$\tau_s = \frac{F_R}{A_{FS}} \qquad \text{Eq 3.5}$$

$$\sigma_n' = \frac{P_V}{A_{FS}} \qquad \text{Eq 3.6}$$

Where; $\boldsymbol{\tau_s}$ is the shear stress in the soil (N/mm^2); $\boldsymbol{F_R}$ is the force resisting the lower shear box displacements, as measured by the load cell (N) (Note: F_R is equal to the force resisting the lower shear box less the soil box friction); $\boldsymbol{A_{FS}}$ is the area of the shear plane (mm^2); $\boldsymbol{\sigma_n'}$ is the normal load (N/mm2), and; $\boldsymbol{P_V}$ is the applied vertical load (N).

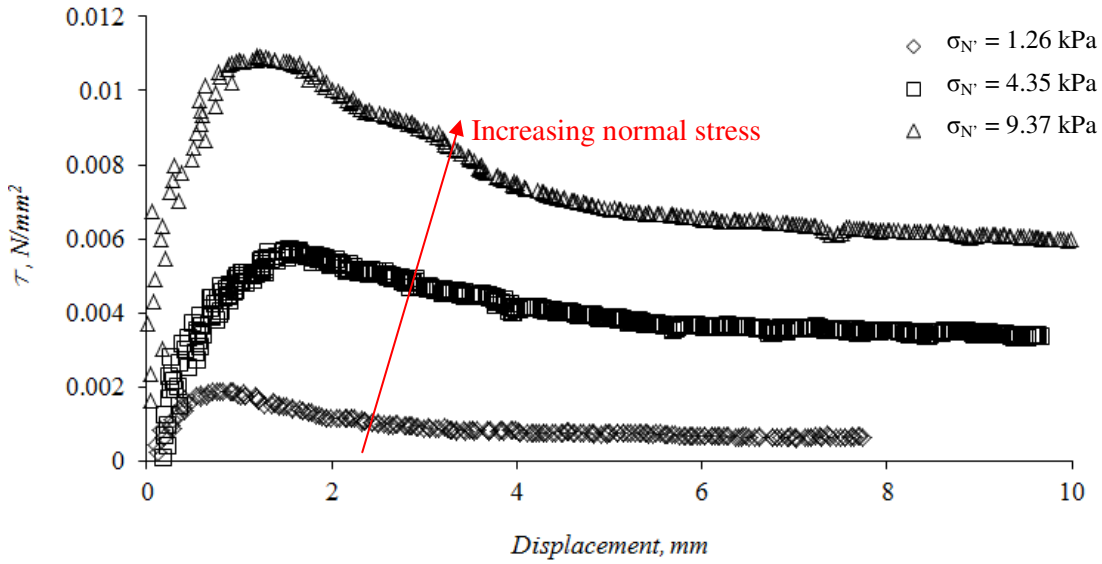

Figure 3.9: Typical shear stress – displacement curves describing the soil shear behaviour under normal stresses of 1.26kPa, 4.35kPa and 9.37kPa.

The area of the shear plane, A_{FS}, considers the area of soil contact between the upper and lower shear boxes. As the lower box is pushed past the upper box, this area reduces (as a function of applied displacement and soil area shape). This study considers two circular soil sections of the same size. A_{FS} is therefore calculated as shown below:

$$A_{FS} = 2 \cdot R^2 \cdot \cos^{-1}\left(\frac{X}{2R}\right) - \frac{1}{2} \cdot X \cdot \sqrt{4 \cdot R^2 - X^2} \qquad \text{Eq 3.7}$$

Where; ***R*** is the radius of the shear box (mm), and; ***X*** is the lateral displacement of the lower shear box (mm).

The curves displayed in Figure 3.9 have peak behaviour. This indicates that the samples of silica sand have a high number of interlocking particles that need to be overcome before the sand can shear in its critical state (*Knappett and Craig, 2012*), thus confirming their calculated density (very dense). Figure 3.10 (a) shows the values of peak and critical shear stress from each shear box test. These values can be used to define the peak and critical angles of friction for the soil, ϕ', through application of the following equation:

$$\phi' = \tan^{-1}\left(\frac{\tau_s}{\sigma_n'}\right) \qquad \text{Eq 3.8}$$

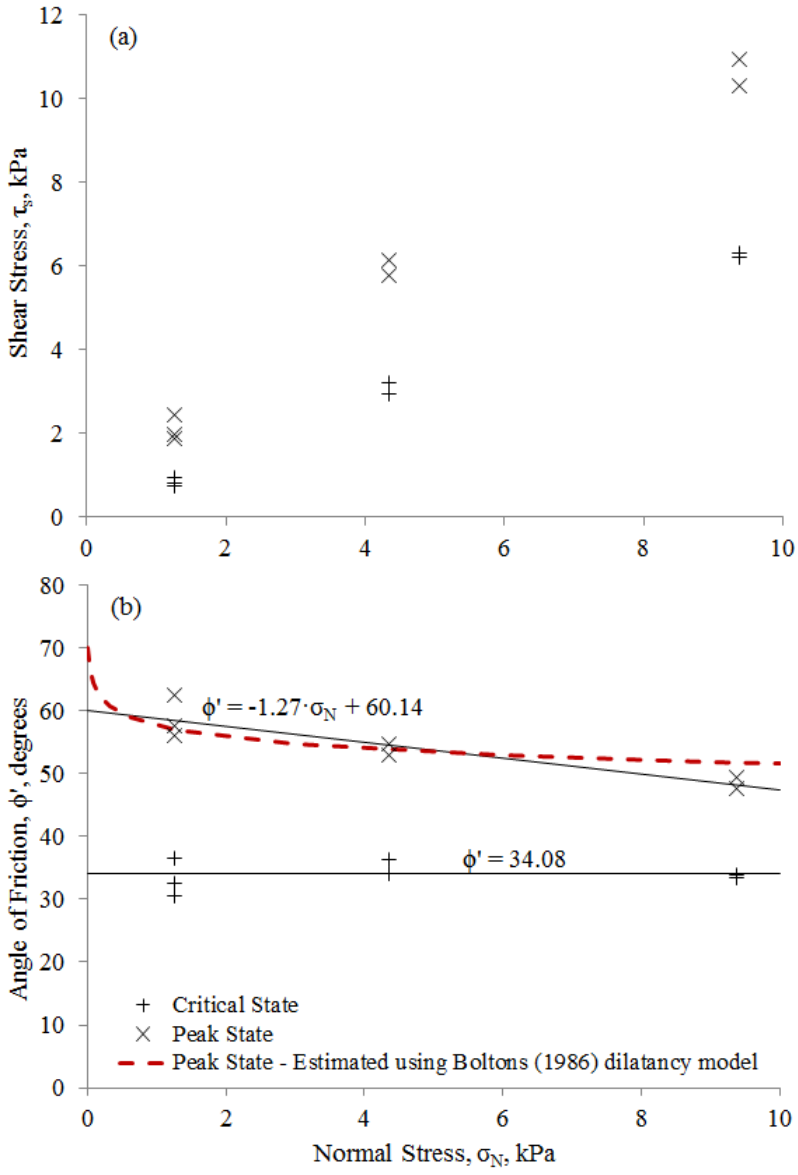

Figure 3.10: Mohr coulomb failure criteria, (a) Normal Stress vs. Shear Stress, (b) Normal Stress vs. Angle of Friction, showing critical and peak state behaviour.

The following shear properties have been defined for the silica sand:

- Peak angle of shear resistance, $\phi_{pk}' = 60.14^{\circ}\text{-}1.27 \cdot \sigma_n'$
- Critical angle of shear resistance, $\phi_{cr}' = 34.08^{\circ}$

Figure 3.10 (b) demonstrates that critical state friction remains constant as normal load is increased, while peak state friction reduces. This indicates that dilation at low effective stress reduces with increasing normal load, which is consistent with past literature (*e.g. Bolton, 1986*). Bolton (1986)

proposed a model to quantify the effects of dilation at low effective stress in terms of an increase in a soils maximum shearing resistance, as shown below;

$$\phi_{pk}' - \phi_{cr}' = A_1 \cdot I_R \qquad \text{Eq 3.9}$$

$$I_R = I_D \cdot (10 - \ln(p_o')) - 1 \qquad \text{Eq 3.9 (b)}$$

Where; ϕ_{pk}' is the peak angle of shearing resistance (˚); ϕ_{cr}' is the critical angle of shearing resistance (˚); A_1 is a dimensionless factor to account for stress type, 3 for tri-axial stress and 5 for plane stress; I_R is the relative dilatancy index; I_D is the relative density of the soil, and; p_o' is the overburden pressure in the soil at a known depth, x (kN/m^2).

As demonstrated, this model utilises the relative density of a soil sample and the overburden pressure at a depth of x in order to establish a dilatancy index and, thus, the expected change in the shearing resistance, $\phi_{pk}' - \phi_{cr}'$, of the soil. With an I_D value of 0.89 and an assumed A_1 value of 3, Figure 3.10 (b) shows the estimated soil strength, as a function of normal load (overburden pressure), for the silica sand used in this project. In this Figure, the significance of a low overburden pressure to the shear strength of this particular soil is evident. In particular, between the soil surface and a depth of 0.1m, the silica sand has a friction angle, ϕ', ranging between 70.0˚ at the soil surface and 54.7˚ at the root tip. This is akin to the range of ϕ_{pk}' values measured through shear box testing (60.1˚- 57.0°).

3.2.4 Soil preparation

Mickovski *et al.* (2007) placed silica sand into the soil box by way of pluviation. This technique provides a consistent density of sand both throughout the soil box and between each experiment, ensuring repeatability. Both wet and air dry samples were prepared, with preparation of the dry samples ending after pluviation. For preparation of wet samples, pluviation was followed by connecting the PVC drainage pipe (see Figure 3.2) to a water supply and raising the water level to the top of the soil sample over a 20 minute period, ensuring entrapped air could escape (*Mickovski et al., 2007*). Once saturated, the PVC drainage pipe was placed in a water reservoir, which was lowered to 450 mm below the top surface of the sand. The sample was then left to drain over a 24 hour period, during which a plastic bag was placed over the sample to prevent evaporation (*Mickovski et al., 2007*). The pore water pressure at the base of the box was -2.5 kPa during testing (*Mickovski et al., 2007*).

The following equipment was required for pluviation: a hopper (open topped rectangular vessel that tapers towards an open slit at its base), a pulley system, a measuring device, runners and a knife edge. This equipment was set up as depicted in Figure 3.11. A scale with 10 mm intervals was marked on

the side of the box, along with a corresponding scale marked on the pulley rope. The hopper was then raised to a height of approximately 360 mm above the base of the box, filled with sand and set to oscillate. The runners prevented the hopper from swinging out of plane. As the sand poured into the box, its surface rose and as it reached the marks on the scale, the height of the hopper was increased accordingly (using the scale on the rope). This allowed the hopper to maintain an approximately constant height above the rising sand surface and thus ensured a consistent density throughout the soil sample. Oscillation was maintained by nudging the hopper gently by hand. The outer surface of the Perspex viewing panel was protected against abrasion (caused by the sand particles) by coating it in a layer of thin plastic. This was carefully removed after pluviation.

As suggested in Figure 3.11, the rotation of the hopper about a point results in an arched (rather than flat) sand surface. This could be improved by a system that moves horizontally from side to side. Nevertheless, using the simpler technique with a swinging hopper generated samples with an average bulk density of 1698 ± 1 kgm^{-3} (*Mickovski et al., 2007*). This small margin of error demonstrates the repeatability of this technique and suggests that a more accurate technique is not required.

Figure 3.11: Experimental set up used for sand pluviation

3.3 Experimental set up

An Instron S5536 mechanical testing frame (Instron, High Wycombe, UK), with a 5N load cell, was used to perform the uprooting tests (*Mickovski et al., 2007*). The prepared soil boxes were placed on the Instron platform and the protruding roots were clamped to the load cell using a screw-clamp grip. The Instron was then programmed to move the clamp vertically at a rate of either 1mm/minute or 5mm/minute and to continually record the force and cross head displacement. Displacement measurements were accurate to 1µm, while force measurements were accurate to 0.2mN (*Mickovksi et al., 2007*). Care was taken to ensure minimal soil and root disturbance during the clamping process.

A Nikon D100 camera was used to take digital images of the cross section-front uprooting tests at 10 second intervals (allowing 0.167 mm or 0.833 mm of root displacement between each image, for displacement rates of 1mm/min and 5mm/min, respectively). The camera was equipped with a 60mm macro lens and produced images with a resolution of 1500 x 1000 pixels (*Mickovski et al., 2007*). With advances in and wider availability of high quality digital cameras, more recent cross section-front experiments, such as the shear box tests carried out by Loades *et al.* (2009), advantage from significantly improved image quality (resolution of 4288 x 2848 pixels). Care was taken to ensure that the lens sat parallel to the Perspex viewing panel, to minimise image distortion, and that the lens was focussed. To ensure a constant camera position during testing, the camera was placed on a tripod and was controlled remotely using a PC. A light was positioned at a 45° angle to the Perspex surface to improve image quality. Figure 3.12 shows the experimental set up for the cross section-front modelling technique.

Table 3.1 outlines the system properties that were considered for the Mickovski *et al.* (2007) uprooting test series. A full set of data (i.e. pull out force and cross head displacement data and, where appropriate, digital images) has been provided for each test group, unless otherwise stated. The labelling system presented in this table will be used to describe each test group hereon.

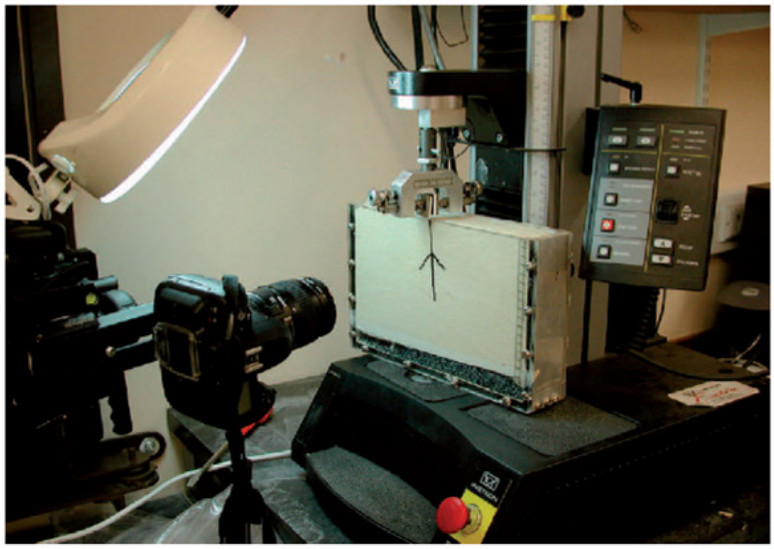

Figure 3.12: Overview of experimental set up used for cross section tests (*Mickovski et al., 2007*).

Table 3.1: Overview of the soil–root combinations considered in the Mickovski *et al.* (2007) uprooting test series.

		Dry soil (d)			Wet soil (w)		
		Tap (T)	Herringbone (H)	Dichotomous (D)	Tap (T)	Herringbone (H)	Dichotomous (D)
Viton (V)	Full section-centre (f)	TVdf†	HVdf†	DVdf†	TVwf*	HVwf*	DVwf*
	Half section-front (h)	TVdh†	HVdh†	DVdh†	TVwh*	HVwh*	DVwh*
Linden (L)	Full section-centre (f)	TLdf*	HLdf*	DLdf*	TLwf*	HLwf*	DLwf*
	Half section-front (h)	TLdh*	HLdh*	DLdh*	TLwh*	HLwh*	DLwh*
Willow (W)	Full section-centre (f)	TWdf*	HWdf*	DWdf*	-	-	-
	Half section-front (h)	-	-	-	-	-	-

Key: * pull out rate = 1 mm/minute; † pull out rate = 5 mm/minute; Text shaded in grey indicates the tests for which the force-displacement data was not available.

3.4 Output

The output of the uprooting tests, described in Table 3.1, was studied with a view to develop calculation and numerical models that predict uprooting. For a full discussion, see Mickovski *et al.* (2007; 2010). A summary of the existing global pull out force-displacement curves will first be given, followed by a discussion of the new analysis conducted on this data.

3.4.1 Full section-centre root pull out tests

Typical pull out force – uprooting displacement curves, one from each of the full section-centre uprooting test groups, are presented in Figures 3.13 (a) to (e). As demonstrated, there is a strong similarity between the uprooting data collected from real (woody) willow roots in dry sand (Figure 3.13 (e)) and wooden analogue roots in dry sand (Figure 3.13 (b)). This indicates that the analogue roots are successfully modelling the behaviour of real roots during pull out. Some differences, however, do exist. For example, the force required to uproot a willow tap root is approximately three times the force required to uproot a linden tap root. This increased force is likely to be the result of a combination of factors, including: the organic form of a real root (i.e. varying profile, tortuosity, root hairs), which increases soil deformation and interface strength during uprooting; and the slightly larger diameter of the willow root samples, which increases the area of contact between the root and soil (*Mickovski et al., 2010*). The impact of these factors, however, is shown to reduce when the root architecture is complicated (see Figures 3.13 (b) and (e)), resulting in much stronger comparability between the real and analogue dichotomous and herringbone roots (*Mickovski et al., 2007*). This demonstrates that complexity in root profile influences soil root interaction. It should be possible to account for this in any calculation and numerical models developed.

Regardless of soil type or root material, Figure 3.13 shows that adding lateral branches to a root system results in an increase in the force (and vertical displacement) required to dislodge it from its surrounding soil. From this, it can be assumed that lateral branches increase the deformation of the soil during uprooting (*Mickovski et al., 2007*). Building on this, Figure 3.13 also suggests that soil deformation is increased by; (i) locating lateral branches near the base of a primary root (i.e. dichotomous architecture) and (ii) increasing root stiffness; and is made more difficult (indicated by an increase in uprooting force and a change in the force - displacement relationship) by enhancing the shear properties of the soil (in this case, provided through the addition of moisture). Such behaviour is consistent with the findings of Stokes *et al.* (1996) and indicates that root architecture, root material properties and soil properties are all important factors in determining uprooting behaviour. It is important, therefore, that these variables can be easily specified in predictive calculation and numerical models (which will be developed in Chapter 4). Understanding the behaviour of geometrically simple root systems, however, is the first step in addressing this complex challenge.

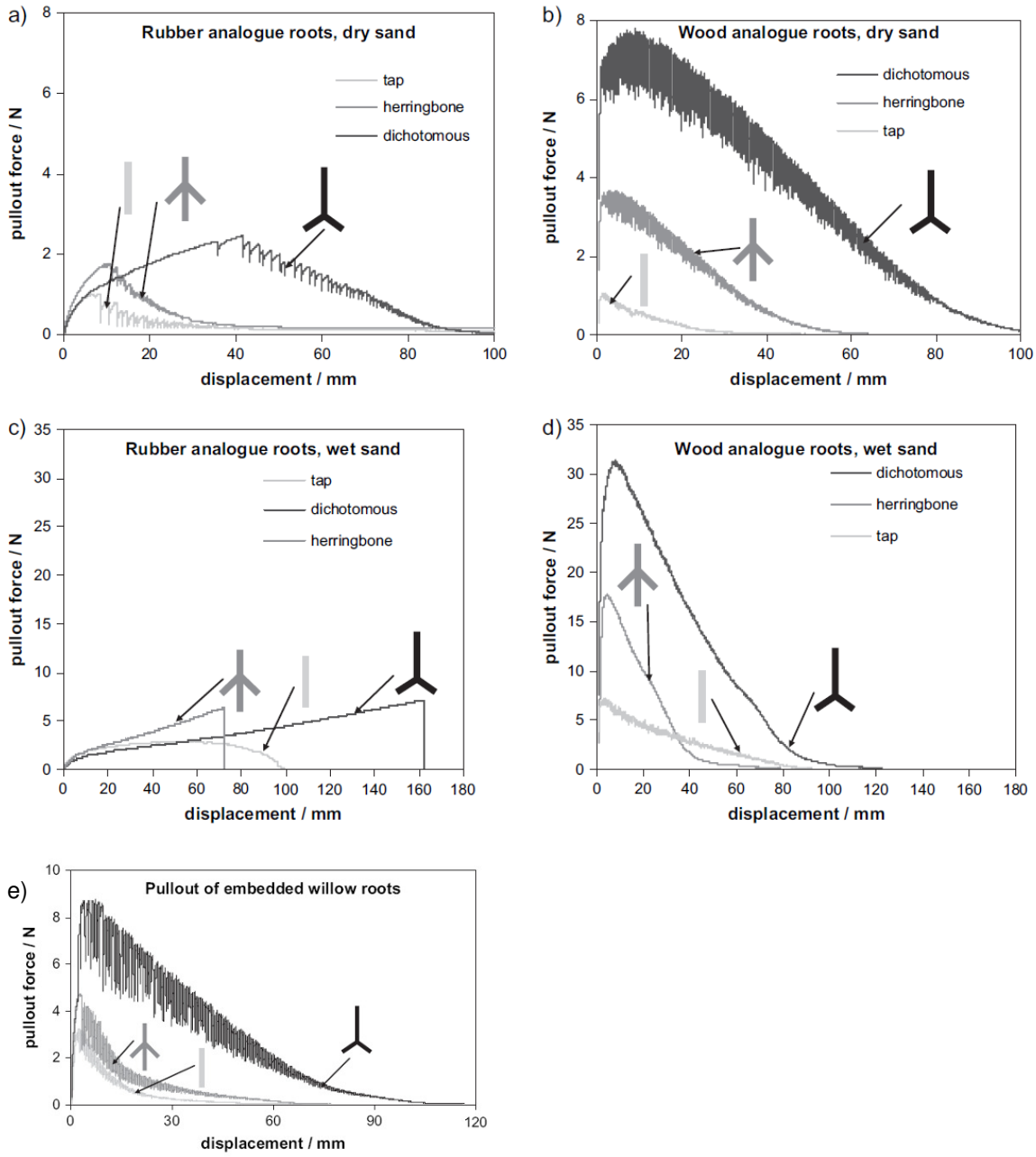

Figure 3.13: Pull out force – displacement curves from full section-centre uprooting tests: (a) Viton root analogues in dry sand, (b) Linden root analogues in dry sand, (c) Viton root analogues in wet sand, (d) Linden root analogues in wet sand, and (e) Willow root segments in dry sand (*Mickovski et al., 2007*).

In dry sand (Figures 3.13 (a), (b) and (e)), the pull out force - displacement curves show a high degree of post peak oscillation, the frequency of which is at its highest when considering wooden roots (Figures 3.13 (b) and (e)). It is likely that this behaviour is driven by the small root diameter to average soil particle size ratios (D_{root}/D_{50}), which are 13.3 and 19.1 for the respective rubber and

wooden root analogues. In scaled pile tests, the D_{pile}/D_{50} ratio is typically kept above 80 (or 100 if being conservative), a value that is generally agreed to be the minimum required to sufficiently mitigate grain size effects (*Garnier, 2002; Fioravante, 2002*) (where D_{pile} is the pile diameter). This is significantly higher than the D_{root}/D_{50} values reported for the uprooting tests. A small ratio makes individual soil particles significant players during loading and, given that a degree of particles will move to obstruct the root as the soil mass deforms, could explain the oscillations. Unlike wood, rubber is flexible and can absorb these obstructions, which could result in a lower oscillation frequency. Oscillations are negligible when considering wet soil (Figures 3.13 (c) and (d)). Adding moisture to the soil, however, reduces the likelihood of free particles and introduces a lubricant, which could significantly reduce the impact of the grains. The intricacies of this behaviour will not be replicated in an uprooting simulation that is based on *t-z* methodology (see Chapter 4), as this modelling approach assumes the soil to act as a continuum.

Root breakage is apparent in Figure 3.13 (c), characterised by a sudden drop in pull out force. This is a common failure mechanism of real roots during uprooting and it is therefore important that is can be incorporated into predictive calculation and numerical models, such as those developed in Chapter 4.

In conclusion, controlled changes in root architecture, root material properties and soil properties provide distinct changes in the pull out force – applied displacement behaviour of the sample. These changes were consistent amongst repeat tests, indicating that the material and architectural changes under investigation provide measurable changes in uprooting behaviour and, ultimately, that uprooting behaviour is repeatable.

3.4.2 Cross section-front root pull out tests

3.4.2.1 Pull out force-displacement curves

Figures 3.14 (a) and (b) display typical pull out force - displacement curves for the half rubber root analogues being pulled from dry and wet sand, respectively. Ideally, each of these curves should have an identical shape to, and half the magnitude of, its corresponding full section-centre pull out force - displacement curve. This would confirm the same mechanical soil root interaction and equivalence between the half and whole soil root systems. Similar data for the half wooden root analogues was not available. In its absence, it has been assumed that any differences between the half

section-front and full section-centre tests when using rubber root analogues is consistent with the differences experienced when using wooden root analogues.

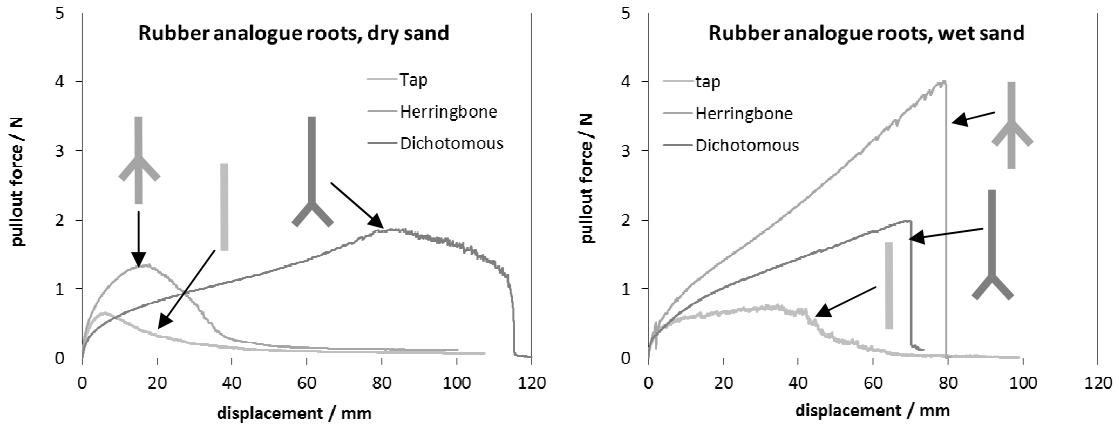

Figure 3.14: Pull out force - displacement curves from cross section-front uprooting tests (a) Viton root analogues in dry sand, and (b) Viton root analogues in wet sand. Images created using Mickovski *et al.* (2007; 2010) data.

The half section pull out force - displacement curves, displayed in Figures 3.14 (a) and (b), are very similar in shape to their corresponding full root curves, displayed in Figures 3.13 (a) and (c). The lack of significant post peak oscillations when uprooting a half rubber root analogue from dry sand (Figure 3.14 (a)), however, indicates that the intricacy of soil root interaction varies slightly between the two testing techniques. It is likely that this results from the addition of: (i) the Perspex surface, which introduces a boundary at the cross section of the soil root system; and (ii) the silicon grease, which introduces cohesion to the soil that immediately surrounds the root (at the interface between the root, the soil and the Perspex) and to the soil that fills the cavity left behind as the root displaces. The overall soil root interaction, however, is very comparable.

In dry sand, the respective forces required to uproot the half tap, herringbone and dichotomous root analogues are approximately 60%, 80% and 85% of the forces required to uproot equivalent full root analogues. In wet sand, this is reduced to 40%, 55% and 55%, respectively. The inconsistency of these values to the desired 50% may result from the limitations of the cross section-front testing technique. Rather than a plane through a full system, as assumed, the cross section-front tests consider half a system bound by a Perspex surface. When compared to the full section-centre tests, this alters: (i) the soil packing around the root, due to edge effects; (ii) the stress distribution across the roots profile, due to the change from a uniform (circular) to a non-uniform (semi-circular) shape;

and (iii) the friction acting at the plane, which is only present in the half section-front testing. Additionally, the preparation of the half root analogues may be influencing these results, through introducing: non-uniformity in the roots profile, material pre-stressing and additional surface texture (see Section 3.2.2). Friction between the root and Perspex, when considering rubber root analogues in dry sand, is suggested by the consistently high relative pull-out forces of the half root analogues (>50% of the full root analogue pull-out forces), which increase with the addition of lateral branches (or increase in root-Perspex contact area). Friction, however, is not suggested between the root and Perspex when considering roots in wet sand, as the relative pull-out force sits around or below 50% for all tests. In this case, the more subtle factors, mentioned above, are likely to be driving any difference between the expected and measured root pull-out forces. The mitigation of friction, in this case, is likely to be caused by the lubricating effect of water.

Overall, it is evident that the cross section-front testing technique is a fair representation of a plane passing through the centre of a full section-centre test. Some limitations in experimental design, however, create slight disparity between the desired and obtained results. With current advances in the optical imagery of roots in transparent soil (e.g. *Downie et al., 2012*), however, it may soon be possible to replace the cross section-front testing technique with a full section-centre test that uses transparent soil. This method would eliminate the limitations of the cross section-front tests, whilst providing clear images of roots, with full cross sections, during pull out.

3.4.2.2 Digital image data set

The *t-z* calculation model, which will later be employed to calculate soil root interaction, uses the distribution of vertical movement along the length of a pile (or root, in this case) during tensile (or compressive) loading to back calculate the distribution of vertical shearing force acting at the soil-pile interface (i.e. to calculate soil-pile interaction). Using GeoPIV analysis (see Section 3.5) and the digital images taken during the cross section-front uprooting tests, the distribution of vertical movement along the length of each root analogue can be measured during loading. The precision of these measurements is crucial to the success of the back calculation technique and it is therefore important that the root analogues are clearly optically textured and visible throughout each image series. The requirements of the GeoPIV analysis carried out by Mickovski *et al.* (2007), which mapped soil body deformation during loading, differs from the requirements of this project. For their purpose, and therefore in the execution of the root pull out tests, root visibility was not a key concern.

A selection of images taken during the cross section-front uprooting tests is displayed in Table 3.2. As demonstrated, the rubber root analogues (test references: TVdh, HVdh, DVdh and TVwh) contrast significantly against the silica sand, have good optical texture, and are clearly visible throughout testing, with minimal disturbance from stray sand particles becoming dislodged between the root analogue and Perspex surfaces. The wooden root analogues (test references: TLdh, HLdh, DLdh and TLwh), on the other hand, are not clearly visible throughout testing. Sand particles between the root and Perspex are present at the start of each test and increase in volume during loading (particularly when lateral branches are included in the root model). Furthermore, the wood does not contrast clearly against the silica sand and has poorly detailed optical texture. Root visibility is, however, improved when moisture is introduced to the soil. This is likely to be the result of increased soil friction and, therefore, fewer stray sand particles.

Table 3.2: Images of the soil root system taken during uprooting, courtesy of S.B. Mickovski, James Hutton Institute, Invergowrie.

Test reference:	Image taken at the beginning of the uprooting test.	Image taken towards the middle of the uprooting test.	Image taken towards the end of the uprooting test.
TVdh			
TLdh	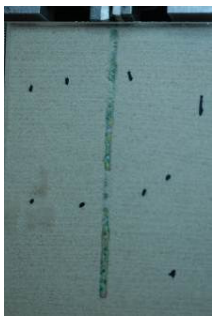	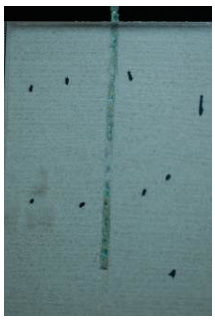	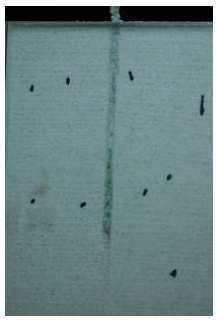

Test reference:	Image taken at the beginning of the uprooting test.	Image taken towards the middle of the uprooting test.	Image taken towards the end of the uprooting test.
HVdh	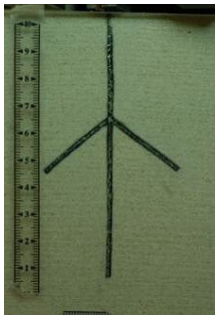		
HLdh	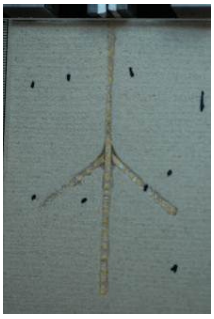	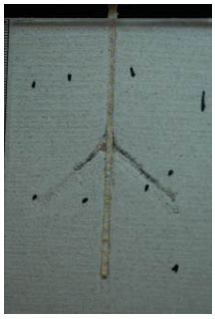	
DVdh	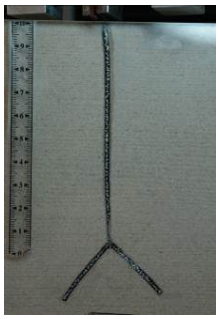	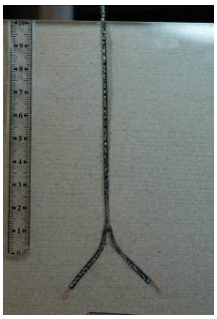	
DLdh	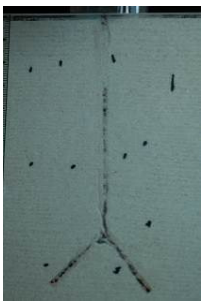	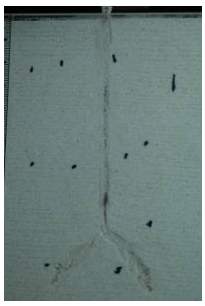	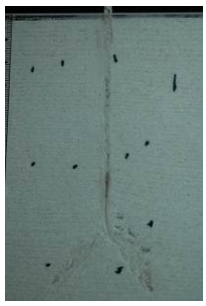

Test reference:	Image taken at the beginning of the uprooting test.	Image taken towards the middle of the uprooting test.	Image taken towards the end of the uprooting test.
TVwh			
DLwh			

From observation, the onset of stray sand particles is likely to be the result of experimental set up. Although care was taken to minimise any disturbance to the soil root system while the root head was being clamped to the Instron's mechanical grip (*Mickovski et al., 2007*), disturbance is evident in the initial images within each test series. The initial images of the stiffer wooden roots suggest (through sand obstructing root visibility along its entire length) that disturbance at the root head has translated to the root tip, creating a space between the root and Perspex. The initial images of flexible rubber roots, on the other hand, suggest (through sand blocking root visibility towards the root head only) that disturbance at the root head has translated very little.

As a result of poor root visibility, the image sets for branched wooden roots (HLdh, DLdh, HLwh and DLwh) were not considered for GeoPIV analysis.

3.5 GeoPIV Image Analysis

Particle image velocimetry (PIV) is an image analysis tool, coded in and run by MatLab, that measures the displacement fields along a plane within a deforming zone of material. It operates by evaluating the variation in spatial brightness (i.e. optical texture) through a series of digital images that capture the deformation process. PIV was originally created for applications in fluid mechanics

but has since been developed, by White *et al.* (2003), to evaluate geotechnical processes. The geotechnical version of the program is named GeoPIV.

Figure 3.15 outlines the GeoPIV method for establishing movement between images. On the first image in a series, the user defines areas of texture (known as test patches) that they wish the program to trace. Test patches are sized and located using one of a range of specially designed MatLab files, such as *mousemeshrandom* and *mousemeshrectangle*. These files vary depending on patch requirements. For example, mousemeshrandom allows the user to define the specific location of each test patch within the initial image (useful for seeding patches along an object or failure within a soil mass), while mousemeshrectangle allows the user to define a spacing between patches, which the file will locate within a user defined area on the initial image (useful for seeding patches evenly over a large area). Having established a suitable series of test patches, the user can define suitable search patches, where each search patch defines an area in the following image that will house the displaced test patch (see Figure 3.15). Search patches are defined by indicating the maximum displacement of each test patch (between two consecutive images) within the GeoPIV input file. With test and search patches defined, GeoPIV compares the variation in optical texture between each test patch and its corresponding search patch, noting the degree of match for all possible locations of the test patch within the search patch (*White and Take, 2002*). The position of the peak degree of match indicates the final test patch location (*White and Take, 2002*). For full details of the GeoPIV analysis process, see White and Take (*2002*) and White *et al.* (*2003*).

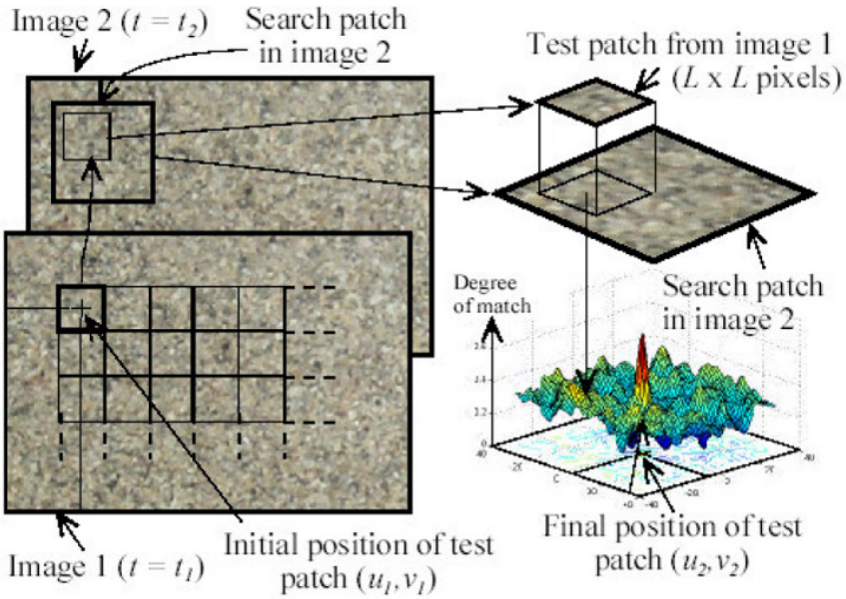

Figure 3.15: Process followed to run a geoPIV analysis (*White and Take, 2002*)

3.5.1 Converting image space to object space

GeoPIV calculates displacement fields in image space only (i.e. the output is measured in pixels on the image (*White and Take, 2002*)). It is necessary, therefore, to convert the output into object space (i.e. in millimetres or metres on the object). This can be achieved by either: assuming a constant image scale, and multiplying the output accordingly, or using a photogrammetry technique. The latter will provide more accurate results, but involves a more complex process (*Take and White, 2002; White et al., 2003*). A comprehensive overview of the photogrammetry technique is provided by White *et al.* (2003).

In this Thesis, a constant image scale (*CIS*) was assumed. In each of the cross section-front pull out tests, a ruler with 1mm spacing was placed on the Perspex surface. One digital image from each test could therefore be selected and the average distance between the 1mm markers, $x_{0.001}$, measured in pixels. This allowed a *CIS* value for each test to be realised, through the following equation:

$$CIS\,(metres) = \frac{0.001}{x_{0.001}\,(pixels)} \qquad \text{Eq 3.10}$$

Where: ***CIS*** is the constant image scale, and; $\boldsymbol{x_{0.001}}$ is the number of pixels measured along a 1 mm stretch of image

3.5.2 Sensitivity of GeoPIV analysis to experimental factors and data input

The displacement fields provided by a GeoPIV analysis are not necessarily exact measurements of particle movements. They are, instead, the most probable measurements, given the information provided. The precision of an analysis can therefore be improved through improving the quality of the input information, which can be categorised into two key areas: (1) the input required to run a GeoPIV analysis (i.e. patch properties), and (2) the quality of the digital images.

The location and size of the test and search patches have a direct influence on the ability of GeoPIV to accurately select the peak degree of match. White and Take (2002) report, from their work in developing the approach, that patch size is the most significant factor in determining the success of a GeoPIV analysis, with patch content bearing a lesser influence. In particular, they found that increasing patch size improves the accuracy of an analysis, although they also note that this reduces the precision of the measurement points and so advise that a balance must be drawn. To find an optimum patch size and location, a trial and error approach can be adopted, as follows:

1. Locate and size a series of test and search patches that are appropriate for assessing the geotechnical process in question.

2. Once an analysis has run, study the output. If there are unusually displaced patches, clearly varying from neighbouring patch displacements (termed wild patches), consult White and Take (2002). They present a comprehensive troubleshooting guide that outlines the causes of such errors and the steps that can be taken to overcome them. In most cases, the errors can be resolved through altering the location and/or size of the test and search patches. If, however, it transpires that the cause of error is insufficient optical texture (caused by poor image quality and/or uniform regions of an image), too much movement between images or scratches on the Perspex surface, then the experiment itself will have to be improved and repeated.

3. These steps can be repeated until an analysis with as few as possible wild patches is achieved.

Camera positioning and image resolution also require careful planning. It is important that the camera lens sits parallel to the Perspex surface and that the camera is in focus and sits in a constant position during image capture. Any changes in the relative placement between the camera and the experiment will create displacements between the images that are not related to the geotechnical process. This will spoil the displacement fields that are measured by GeoPIV. It is therefore advised that the camera is placed on a stand, set on a timer and controlled remotely. This will not only reduce the likelihood of camera movement but will also ensure even time intervals between images. Increasing image quality and resolution will also improve the results of a GeoPIV analysis as an increase in the number of pixels means that a greater number of test patches or a greater test patch size can be used to measure the displacement of an area. Finally, it is important to ensure that the geotechnical process to be measured is clearly visible throughout all of the images. GeoPIV can be used to analyse a process in a single plane only and, therefore, if the elements to be measured move away from this plane then they can no longer be traced. This will result in wild or stuck patches.

3.6 GeoPIV analysis of cross section-front uprooting tests

GeoPIV analysis was applied to the digital images, which depict cross section-front uprooting tests, to measure root movement during pull out. Ideally, each analysis would encompass the entirety of a test, from its start to the point at which the root is completely removed from its surrounding soil. The practicalities of this, however, make it difficult. In particular, as a section of root is removed from its

surrounding soil, it is also removed from the digital images (see Table 3.2). This means that, during a GeoPIV analysis, the test patches associated with the removed section of root 'stick', which leads to nonsensical output. To overcome this, and to ensure useful output, root displacement was measured from the start of each test to the minimum applied displacement required to bring about the residual pull out force (see Figure 3.13). In each analysis, therefore, the root analogues were seeded with test patches from their tips to a distance below the soil surface, where the distance corresponded to the section of root that would be removed from the soil (and thus digital images) during GeoPIV analysis.

In this project, the freely available version of GeoPIV, named GeoPIV8, was used. It was run using MatLab R2007a on a Windows XP platform.

3.6.1 Establishing input parameters

3.6.1.1 Conversion Factor

The digital images were converted from image to object space as described in section 3.5.1. A scale rule, however, was not provided in a number of the image sets, making them unsuitable for analysis. Test groups that remained suitable were: All Viton root analogues in dry sand (TVdh, HVdh, DVdh), Viton tap root analogues in wet sand (TVwh), and Linden tap root analogues in dry sand (TLdh).

3.6.1.2 Number of images

Equation 3.10 combines pull out rate (R_{po}), image capture interval (t_{ic}) and applied displacement (AD) to estimate a suitable minimum number of images to use in a GeoPIV analysis.

$$NI = \frac{AD}{\left(\frac{R_{po}}{60}\right) \cdot t_{ic}} \qquad \text{Eq 3.11}$$

Where; NI is the number of images required; AD is the desired applied displacement (measured in mm); R_{po} is the pull out rate (measured in mm/minute) and t_{ic} is the image capture time interval (measured in seconds).

In each uprooting test, the image capture interval was 10 seconds and the pull out rate was either 1mm/minute or 5mm/minute (see Table 3.1). Suitable values of applied displacement were related to the onset of residual pull out force and could be measured from Figure 3.13. Applied displacement

was taken as: 20 mm for test group TLdh; 30 mm for test groups HVdh, TVdh and TVwh; and 60 mm for test group DVdh. The minimum number of images to include in each GeoPIV analyses was therefore calculated to be: *NI* = 120 for test group TLdh, *NI* = 36 for test groups HVdh and TVdh, *NI* = 180 for test group TVwh and *NI* = 60 for test group DVdh.

3.6.1.3 Patch properties

A parametric study, using an image set from test group TVdh (Viton tap root in dry sand), was carried out to determine the effect of test patch size, search patch size and test patch spacing to the output of a GeoPIV analysis. This allowed a suitable range of patch sizes and patch spacing to be realised.

On the first image in the set, mousemeshrandom was employed to seed the root analogue with a series of 20 x 20 pixel test patches, spaced at approximately 120 pixels centre to centre (c.t.c). Care was taken to ensure that the patches: (i) sat along the axis of the root analogue, and (ii) covered areas of root analogue only. A search patch size of 30 x 30 pixels was also specified. Changing one parameter at a time, a series of GeoPIV analyses were run. Figure 3.16 presents the output in terms of a series of plots that show the vertical movement along the length of the root analogue after 10 mm of applied displacement.

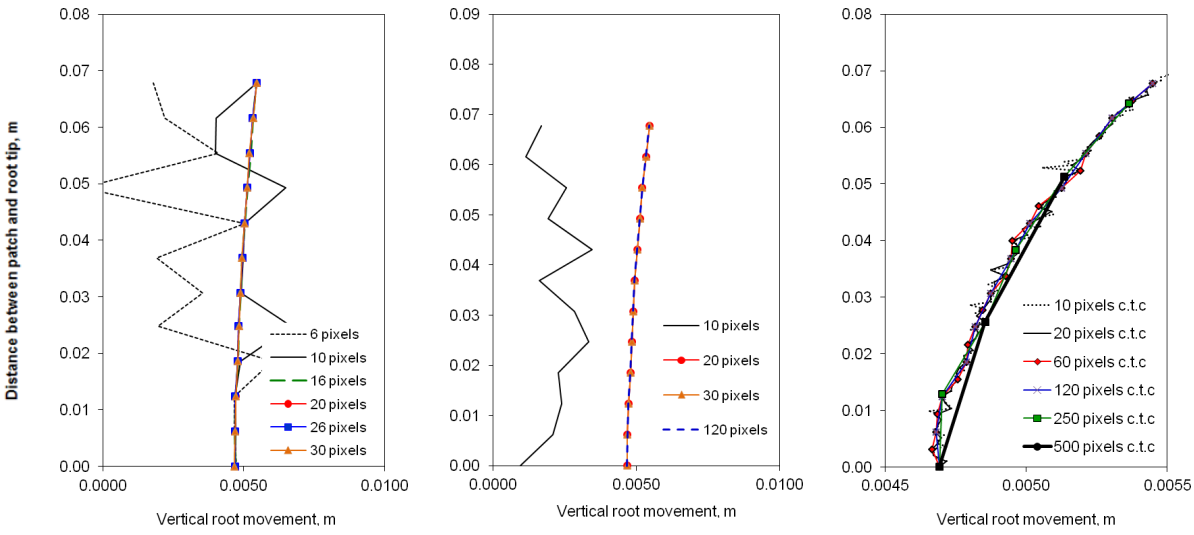

3.16: Plots show the vertical root movement along the length of a root, following 10mm of applied displacement (test TVdh). (a) effect of test patch size, (b) effect of search patch size, and (c) effect of patch spacing.

Figure 3.16 (a) demonstrates the impact of test patch size on the vertical root displacement measurements that are generated by GeoPIV analyses. Analyses that considered test patches equal to or greater than 16 x 16 pixels generated alike curves, which show a progressively increasing vertical root displacement towards the root top (indicating stretching, as expected). Analyses that considered smaller test patches, however, generated very different curves, which show erratic vertical displacements along the roots length. This indicates wild patches, caused by insufficient optical texture. Due to the requirement to keep test patches within the boundary of the root, patches larger than 30 x 30 pixels could not be used. Any problems that may be associated with using test patches that are too large were therefore not an issue in this project.

Search patch size is also a significant factor in GeoPIV analyses. If, for example, a test patch moves by 20 pixels between two images, but a search patch of only 10 pixels has been specified, then it is not possible for GeoPIV to trace the movement of the test patch. Instead, GeoPIV assumes a peak degree of match within the 10 pixel search zone, which results in wild vectors. In Figure 3.16 (b), which shows the impact of search patch size on vertical displacement measurements, this is represented by an unpredictable curve with a stunted overall vertical displacement (when a search patch of 10 pixels is considered). Figure 3.16 (b) also shows that, provided the search patch is large enough to encompass the displacement of the test patch, there is no benefit in increasing search patch size. Moreover, increasing the search patch increases the time taken to run the analysis.

Figure 3.16 (c) shows the effect of test patch spacing on the vertical root displacement measured by GeoPIV. As demonstrated, an increase in patch spacing goes hand in hand with a decrease in data points, which eventually leads to a crude representation of root movement. Increasing data points, however, increases both the time taken to seed the patches and the time taken to run the analysis. A compromise must therefore be made between analysis efficiency and required data output. During the parametric study, emphasis was placed on patch spacing rather than patch content (i.e. optical texture within the patch). This resulted in a small number of wild vectors. In future analyses, emphasis will be placed on patch content and, therefore, sections of root with insufficient texture will not be seeded. Patch spacing would then be more approximate.

Finally, Figure 3.16 shows that the maximum distance selected between the root tip and a test patch is 70mm. This is because, through the number of images used in this analysis (see Section 3.6.1.2), the top 30mm of the root is removed from the soil (and images) and can therefore not be traced.

Having analysed the impact of test patch size, search patch size and test patch spacing, the following criteria were used for GeoPIV input parameters:

(i) Test patch size must fall within the following range: 16 pixels to width of root.
(ii) Search patch size must fall between 30 and 40 pixels.
(iii) Test patch spacing must be approximately 100 pixels c.t.c and patches must be placed on areas of high optical texture.

3.6.2 Results and discussion

Figure 3.17 displays plots showing the distribution of vertical displacement along the length of the rubber root analogues after 10mm of applied displacement. Overall, these plots show uniform curves, indicating that the GeoPIV analyses were successful. A minority of the curves (particularly those in Figure 3.17 (b)), however, are irregular (indicating wild patches). This follows the careful design of the input files (see Section 3.6.1) and generally coincides with a larger number of images being considered in the analyses (see Section 3.6.1.2). It is therefore suggested that either (i) the images were not of a high enough quality or (ii) there were too many images, which can increase the risk of accumulative errors due to the numerical integration of displacement increments. Nevertheless, the general shape and displacement of these curves appears to be appropriate.

Figure 3.17 (a) shows that, after 10 mm of applied vertical displacement, rubber tap root analogues being pulled from dry sand displace along their entire length, but more so at their top (near the soil surface) than at their tip. This indicates that the root analogues are stretching. A range of tip displacements, between 4.2mm and 7.5mm, is observed between repeat tests. Increased stretching (i.e. reduced tip displacements), as opposed to pull out, indicates stronger soil root bonds and, therefore, better anchorage. This is confirmed by Figures 3.17 (c) and (d), which show significantly smaller root tip displacements (less than 1mm) when lateral branches (or anchors) are introduced to the root system. The slight inconsistency between the repeat uprooting tests is likely to result from sample preparation (i.e. no two tests will have an identical soil density or root profile, see Section 3.2).

The curves in Figure 3.17 (b), which represent rubber tap root analogues being pulled from wet sand (-2.5 MPa), are very similar to those in Figure 3.17 (a). The displacement of the root tips, however, is generally smaller (ranging between 3.8 mm and 5.8 mm). This finding is consistent with the traditional pull out force-displacement curves (see Figure 3.13), which suggest that roots being pulled

from wet sand maintain a strong soil root bond even after very large applied displacements, while roots being pulled from dry sand lose strength in the soil root bond after the peak pull out force has been reached.

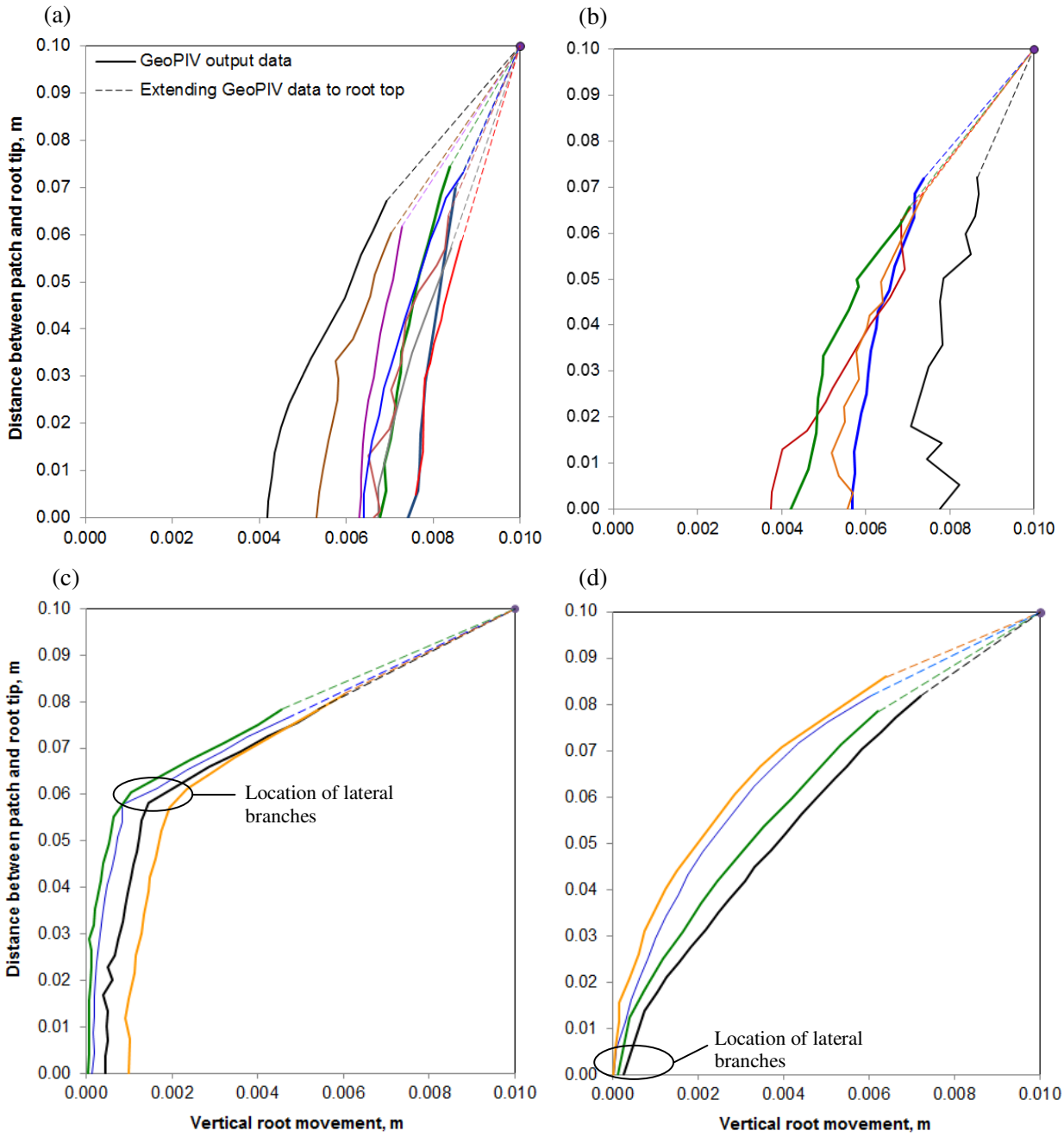

Figure 3.17: Vertical root movement along the length of a viton rubber root analogue after an applied dispalcement of 10mm (at the root head). Each curve in each plot represents the GeoPIV analysis of a repeat uprooting test. (a) Tap root being pulled from dry sand, (b) Tap root being pulled from wet sand, (c) Herringbone root being pulled from dry sand, and (d) Dichotomous root being pulled from dry sand.

In Figures 3.17 (c) and (d), which represent branched rubber root analogues in dry sand (after 10mm of applied vertical displacement), the anchoring effect of root branches is demonstrated. In particular, there is very little root displacement at (or below) the branch location, but increased displacement above. When considering herringbone architecture (Figure 3.17 (c)), this indicates that the section of root below the branch location contributes very little to the uprooting resistance of the system. As a result, dichotomous architecture provides greater resistance to uprooting (see Figure 3.13). This finding is confirmed in literature (*e.g. Stokes et al., 1996*). Increasing the strain in the root analogues (through increased stretching), and increasing the soil root bond through the addition of moisture, can result in system failure through root breakage rather than failure of the soil root bond (see Figure 3.13).

Figure 3.18 shows the apparent distribution of vertical displacement along the length of a wooden root analogue being uprooted from dry sand after 2mm of applied displacement. As demonstrated, only one image series was suitable for a GeoPIV analysis and the results were less than satisfactory. Observation of the digital images, see Table 3.2, showed sand sitting between the root and the Perspex and this interfered with the success of the GeoPIV analysis. The irregular form of the curve suggests wild vectors and the distribution of vertical displacement suggests that they significantly impact the displacement measurements. In particular, the curve proposes that the root displaces more

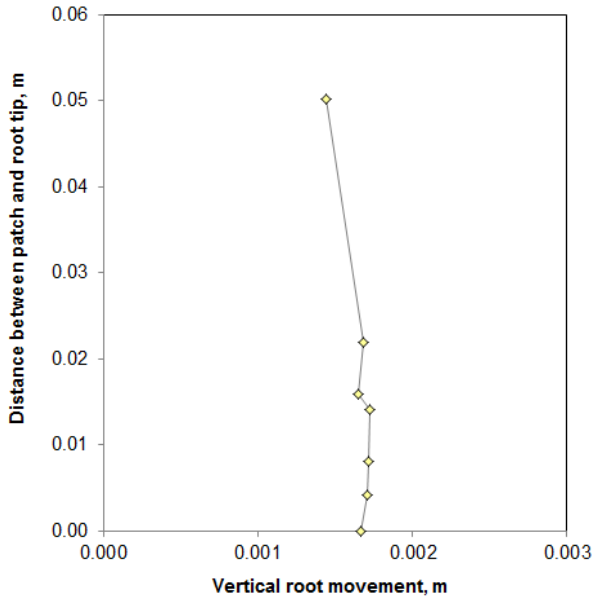

Figure 3.18: Plot shows the vertical root movement along a roots length after an applied dispalcement of 2 mm (at the root head). The root is made of Linden wood and was pulled from dry sand.

at its tip that it does at its top, where the loading is applied. Moreover, the general root displacement does not tend towards the applied displacement of 2mm. As such, the output is unusable. It is thought that using a soil material with a smaller particle size (such as silica flour) may improve these tests, but it would present difficulties in sample preparation by pluviation.

In conclusion, the GeoPIV analysis that was used to measure the distribution of vertical root displacement ranged from very successful to very poor, depending on root material. Unfortunately, the problems associated with setting up the wooden root systems made them unsuitable for analysis. The analysis of rubber root analogues, on the other hand, was extremely successful and will be used in the development of the calculation and numerical models. Data for rubber roots are extremely valuable as previous PIV analysis and numerical modelling has been abundant for relatively rigid, steel soil nails, and steel and concrete piles, but minimal for materials with low stiffness like some plant roots. There is a variation in behaviour within each test group, which is most prevalent when considering rubber tap roots in either wet or dry sand. Even when using controlled tests, therefore, natural variation of properties is apparent. This supports the decision to use simplified root and soil properties in the development of a calculation model as a less controlled test (i.e. using real roots) would ultimately result in even more variance.

3.7 Chapter summary

Mickovski *et al.* (*2007; 2010*) conducted a series of uprooting tests, which looked into the influence of root material properties, root architecture and soil properties on uprooting behaviour. Each uprooting test was performed using both traditional and cross sectional modelling techniques (see Figure 3.1), the latter of which allowed the root to be observed during uprooting. Having studied the consequent output database, the subtleties of uprooting behaviour have been observed and an accurate technique for measuring root displacement during loading has been confirmed. Furthermore, the requirements of developing calculation and numerical models that are to quantify soil root interaction and predict uprooting behaviour, respectively, have been realised.

Despite the considerable test controls that were put in place during the experiments (i.e. using analogue roots with known, homogenous material properties and simplified, axially symmetrical architecture and using silica sand), a relatively large variance in output between repeat tests was noted. This was a reminder of the complex interaction that occurs between the root and its surrounding soil during uprooting, the intricacies of which are difficult to predict. Some simple

changes to system features, however, uncovered key relationships between uprooting behaviour and: (i) Root architecture / branching pattern, (ii) Root material properties / stiffness, and (iii) Soil material properties / shear strength and moisture content.

In particular, it was observed that the anchorage capacity of a root is improved by including lateral branches, locating lateral branches towards the root tip, increasing root stiffness and increasing the soils shear strength. The variance between tests comprising different system properties was much larger than that observed between repeat tests. Moreover, the general shape of the pull out force-displacement curves within each repeat test group was consistent. This highlights that the system features studied have a significant and measurable impact on uprooting behaviour, which is ideal for the development of calculation and numerical models. In a bid to ensure that these models are computationally efficient, the intricate details of soil root interaction that created variance between repeat tests, will be assumed negligible. The calculation and numerical models will therefore focus on the system features that have a significant impact on soil root behaviour.

The movement of the rubber root analogues during uprooting was successfully measured by applying GeoPIV analysis to the digital image series that were taken during the cross sectional pull out tests. The images in these series were sharp, displaying well-defined and sufficiently textured roots. This allowed GeoPIV to accurately follow patches of texture through each image series. Root visibility in the images taken during the uprooting of the wooden root analogues, however, was poor. This impaired the success of the GeoPIV analysis and, as a result, the measurements were inaccurate and unusable. Attempts by the author to rectify this were ineffective.

The cross sectional modelling technique was shown to be a successful method for modelling a plane within a traditional test. Indeed, the shape of each cross sectional pull out force-displacement curve was very similar to its equivalent traditional curve, indicating comparable soil root interaction. The force required to uproot the half root analogues from dry sand, however, was higher than that expected if the half roots are to truly represent the full roots. This is likely to be the result of friction between the root and Perspex and has implications when using the measurements obtained from the GeoPIV analysis of cross sectional tests for the development of a calculation model that is to represent traditional tests. Root-Perspex friction will therefore have to be analysed.

Chapter 4 Developing a tool to predict uprooting

4.1 Introduction

Plant roots have complex system morphology and heterogeneous material properties (see Section 2.2). This complicates their response to pull out loading and has inhibited the development of an accurate and reliable predictive tool (*Mickovski et al., 2007*). As such, existing tools are either: (i) good at approximating uprooting behaviour, but are time consuming, difficult to use and inappropriate for large scale modelling (e.g. Dupuy *et al.*, 2007), or (ii) efficient, but poor at approximating uprooting (e.g. Ennos, 1993).

A problem akin to predicting uprooting, and more familiar to the engineer, is that of predicting the effects of axial loading on pile foundations (see Section 2.3.2). Pile foundations are primarily designed to work in compression (to carry dead load through unstable layers of soil), but also need to resist the pull out forces that occur when wind, waves or slope failure inflict lateral or moment loading. To estimate pile soil interaction and, therefore, the amount of settlement or pull out that will occur, the well-known *t-z* calculation model (introduced in Section 2.3.2) can be applied. Balancing efficiency with detail, this technique can provide accurate predictions that are well trusted in the field of geotechnical engineering.

The simple geometry of the tap root analogues considered in Chapter 3 provides a bridge between root and pile architecture. In particular, their material uniformity and circular cross sections allow them to be considered as very small, flexible piles. It was hypothesised, therefore, that through combining *t-z* theory with finite element modelling an ideal predictive tool could be developed.

4.1.1 Method

Following *t-z* theory, a Finite Element Model (FEM) that considers the soil root system as a beam-column (root) supported by a series of discrete axial springs (soil) was developed and used to predict the laboratory uprooting tests in Chapter 3. In this model, the beam-column is defined by the physical properties of the root, while the stiffness of each spring is defined by the local amount of shear transfer at the root soil interface during uprooting.

In the case of piles, there are a number of existing design codes that can be used to estimate the stiffness of a *t-z* spring, based on the physical properties of both the soil and the inclusion (e.g. API

RP 2A-WSD, 2000; and Eurocode 7, 1997). Alternatively, spring stiffness can be calculated empirically (see Section 2.3.2). In this study, empirical *t-z* springs were realised by applying beam-on-elastic foundation theory to the root displacement data generated during uprooting (using GeoPIV analysis and the cross section-front testing technique (see Chapter 3)). Due to the difficulties encountered when measuring the displacement of stiff wooden root analogues during testing, however, they could not be considered for empirical *t-z* calculations. Laboratory tests were used to quantify the physical properties of the root and soil.

This chapter reports on the development and validation of the proposed predictive tool and on the process required to establish root, soil and interaction properties. The suitability of existing pile design techniques for estimating the interaction between soil and small flexible inclusions is therefore determined.

4.2 FE analysis system selection and design of numerical model

FE analysis is a process of computational modelling and is widely used in the fields of engineering design and analysis, including the bioengineering of soils with vegetation. It allows the simulation of complex situations that could not be carried out by hand and, therefore, lends itself to the study of soil root interaction. There are a number of FEA software packages available, of which Abaqus/CAE (Complete Abaqus Environment) 6.8-3 was selected for this study. This program is used extensively in research and design as it has a simple, user friendly interface, which provides ease of model development. Moreover, there is general agreement that Abaqus can deliver accurate results for non-linear problems.

Figure 4.1 displays the FEM that was designed to predict uprooting in this study. As demonstrated, it comprises a series of element-spring sets, which combine to form a vertical (cylindrical) beam-column that is axially supported by non-linear springs. Each spring connects the mid-point of an element to a fixed point that sits axially below, ensuring that the soil not adjacent to the root (which should be unaffected by the uprooting process) does not move during loading. The ability of the beam-column (root) to resist an applied axial displacement is therefore dependent on its own physical properties and on the stiffness of the springs, which model the soil root interaction. The parameters required to model the beam and springs are highlighted in Figure 4.1.

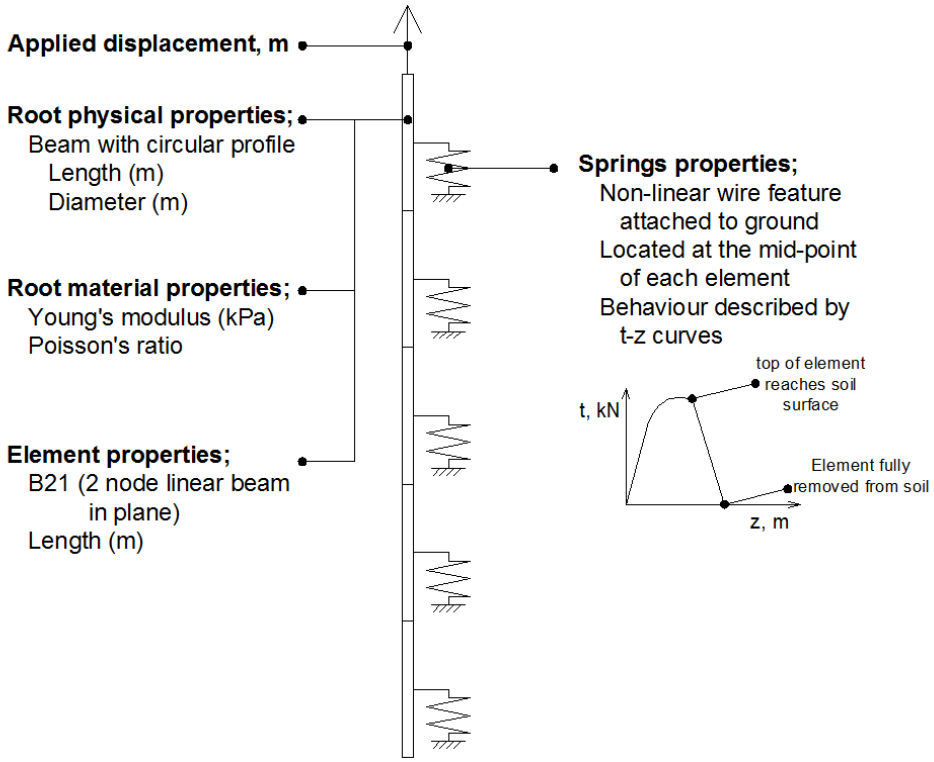

Figure 4.1: Scope of proposed finite element model, using Abaqus CAE.

The proposed FEM is simple yet still encompasses a comprehensive range of soil and root properties. It can be easily adjusted to represent soil root systems that are more complex than the uniform tap root-sand systems that are considered in this Thesis. In particular, each element-spring set models the average axial properties of a horizontal slice within the soil root system. These slices are considered independently of adjacent slices, allowing root material properties, root diameter and soil properties to vary if necessary between element-spring sets (*Knappett and Craig, 2012*). The proposed numerical model, therefore, largely satisfies the modelling requirements set out in Chapter 3. In particular;

- A complex non-linear root profile, with varying stiffness and/or diameter, can be modelled through specifying different properties for each element.
- A complex soil system, with layers of different material properties, can be modelled through specifying different properties for each spring.
- Root branching can be accounted for by including inclined beams with axial springs along their lengths.

- Root breakage, rather than uprooting, will be modelled if a tensile strength is specified for the root.

This modelling technique does, however, have limitations. It ignores shear transfer between different layers of soil and provides a uniaxial simplification of soil root interaction, ignoring any radial or three dimensional components. In addition, it assumes that each soil layer acts as a continuum, while the laboratory uprooting tests in Chapter 3 indicate that individual soil particles may be playing a significant role in uprooting behaviour. This modelling technique, however, works extremely well for predicting pile soil behaviour under axial loading and it was therefore anticipated that, despite these limitations, the same may be true of soil root behaviour, if appropriate *t-z* curves can be found for this application.

4.3 Defining the root

The proposed numerical model defines the beam-column (root) using the following properties: diameter (D_{root}), length (L_{root}), Poisson's ratio (v), and Young's modulus (E_{root}). For the Viton rubber and Linden wood root analogues, these properties are defined in Chapter 3 (Section 3.2.1). The strength properties of the materials were not measured as the tap root analogues were not shown to break during the uprooting tests.

4.4 Defining t-z springs

The stiffness of a *t-z* spring is defined by the relationship between the local relative axial movement of the inclusion with respect to the soil (z) and the local vertical shear force between the inclusion and the soil (t), where local is defined by the spring location and element length. In this study, the FEM comprises 5 equal elements, of length 0.02 m, with a spring located at the midpoint of each, as shown in Figure 4.1. Using this element-spring system, this Section reports the development of suitable theoretical and empirical *t-z* spring sets.

4.4.1 Design code

American Petroleum Institute (API) standards (*API RP 2A-WSD, 2000*) are used globally within the oil and gas industry for the design and maintenance of off-shore infrastructure. Section 6.7 of these codes, entitled *Soil reaction for axially-loaded pile*s, sets out a procedure for estimating the behaviour of *t-z* springs, while Sections 6.4 and 6.5, entitled *Pile capacity for axial bearing loads* and *Pile*

capacity for axial pull out loads, respectively, set out the required background calculations. This code of practise is easy to use but fails to accurately define axail pile capacity. It was therefore used in this study, in partnership with more common approaches, to estimate soil root behaviour based on routinely measured soil parameters in geotechnical engineering. It should be noted, however, that API RP 2A-WSD (2000) considers drained soil behaviour only (i.e. soil with no stress induced pore pressure). It is therefore not suitable for estimating *t-z* springs to describe root analogues uprooting from damp sand.

The *t-z* relationships proposed by API RP 2A-WSD (2000), to quantify the interaction between piles and either sand (cohesionless soil) or clay (cohesive soil), are shown as curves in Figure 4.2. In these curves, the interface shear force, *t*, is represented as a proportion of the maximum interface shear force, t_{max}. As demonstrated, piles interacting with cohesionless soil are assumed to form a *t-z* relationship that is linear until t_{max} is reached. After this point, any further pile displacement has no impact on the interface shear force, which continues indefinitely at a value of t_{max}. A pile interacting

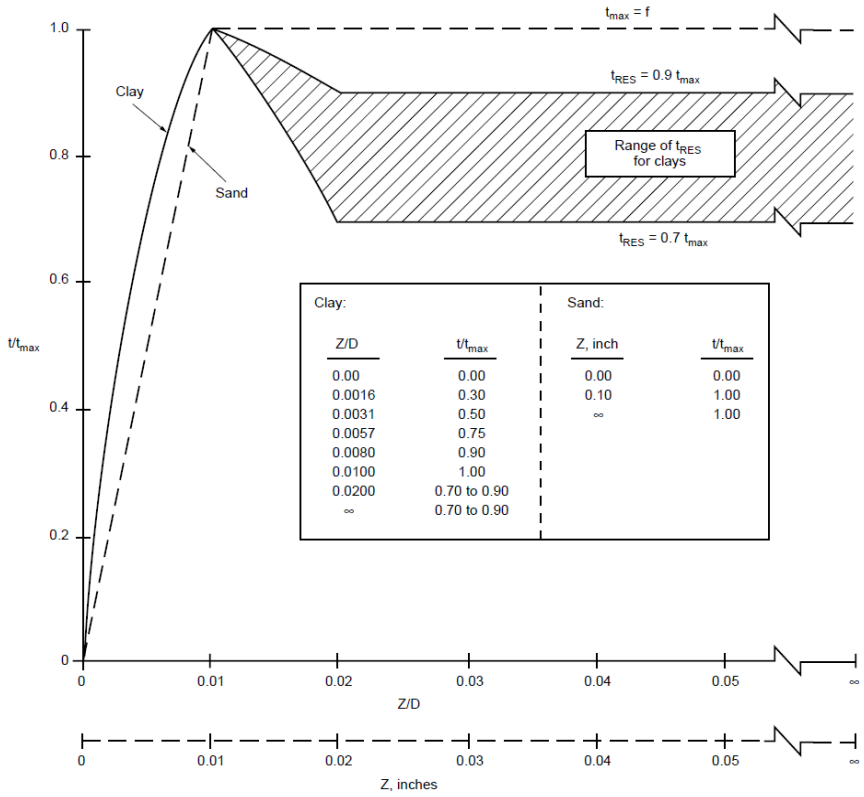

Figure 4.2: typical t/t_{max}-*z* curves for sand and clays, according to API codes (*API RP 2A-WSD, 2000*).

with a cohesive soil, on the other hand, is assumed to form a more complex *t-z* relationship. In particular, Figure 4.2 shows that t/t_{max} increases non-linearly with increasing pile displacement until t is equal to t_{max}. Past this point, strain softening is assumed until t reaches a value in the range of 0.7 to $0.9t_{max}$. From this point, the pile continues to displace with no change in interface shear force, as in a cohesionless soil.

The value of t_{max}, which is used to scale the recommended *t-z* relationships, is defined in API RP 2A-WSD (2000) as a function of the skin friction acting at the pile interface (f). Skin friction can be estimated in cohesive (Equation 4.1) and cohesionless (Equation 4.2) soils through the following equations (*API RP 2A-WSD, 2000*);

$$f = \alpha_1 \cdot c_u \qquad \text{Eq 4.1}$$

$$f = K \cdot p_o' \cdot \tan\delta \qquad \text{Eq 4.2}$$

Where; $\boldsymbol{f}$ is the interface friction between the soil and pile (kPa); $\boldsymbol{\alpha_1}$ is a dimensionless factor; $\boldsymbol{c_u}$ is the undrained shear strength of soil (kPa); $\boldsymbol{K}$ is the coefficient of lateral earth pressure; $\boldsymbol{p_o'}$ is the effective overburden pressure (kPa), and; $\boldsymbol{\delta}$ is the angle of friction between the pile and soil (˚).

With a focus on cohesionless soil (like the silica sand used in this project), the parameters in Equation 4.2 can be defined using a general approach, as follows:

p_o' is defined through considering the unit weight of the soil, the unit weight of the pore water (if any) and the depth at the point in question, as shown below;

$$p_o' = (\gamma_s \cdot h_s) - (\gamma_w \cdot h_w) \qquad \text{Eq 4.2 (a)}$$

Where; $\boldsymbol{p_o'}$ is the effective overburden pressure (kPa), $\boldsymbol{\gamma_s}$ is the unit weight of the soil (kNm^{-3}), $\boldsymbol{\gamma_w}$ is the unit weight of water (kNm^{-3}), $\boldsymbol{h_s}$ is the height of soil above the point in question (m), and; $\boldsymbol{h_w}$ is the height of water above the point in question (m).

With no test data generated in this study to establish the interface friction angle between the silica sand and Viton rubber or Linden wood, the following interface friction angles were considered (based on published data):

Sand/Timber (*e.g. Tomlinson and Woodward, 2007*) $\delta = 0.8\phi'$ *to* $0.9\phi'$ Eq 4.2 (b)

Sand/Rubber (*Newson et al., 2003*) $\delta = 26.5°$ Eq 4.2 (c)

Very little to no change is expected in the shape of the Linden wood or Viton rubber tap root analogues as they are uprooted from the silica sand. As such, dilation is not expected to control the interface friction angle. The branched Viton rubber root analogues that are considered in Chapter 3 (but not used in this Chapter to develop a predictive tool), however, stretch significantly during uprooting. This allows significant volume change at the soil-root interface. In this case, it may be that ϕ_{pk}' governs interface friction, rather than ϕ_{cr}'. This would require investigation when developing the uprooting model to consider branched roots. To describe the Sand-Linden wood interface friction, angles of δ = 27.2° to 30.6° (critical state, ϕ_{cr}' =34°) were considered. To describe the Sand-Viton rubber interface friction, an angle of δ = 26.5° was considered (Note that the sand used by Newson *et al.* (2003) to determine the Sand-Rubber interface friction has very similar properties to the sand used in this Thesis).

The earth pressure coefficient for helical anchor piles being pulled from sand was defined by Meyerhof and Adams (1968) and Mitsch and Clemance (1985) as a function of soil density and the ratio of depth to diameter, as shown in Figure 4.3 (a). Using the more recent Mitsch and Clemance (1985) relationship, and a critical soil friction angle of 34° (see Section 3.2.3.1), a lateral stress coefficient of K = 1.1 can be considered. At peak state, however, the angle of friction (59.9°) exceeds the range considered by Mistch and Clemence (1985). Jeffrey *et al.* (2015) consider a large ratio of depth to diameter (suitable for the analogue roots considered in this Thesis, which have length to depth ratios of 62.5 (Viton rubber) and 43.5 (Linden wood)) and extrapolate the relationship proposed by Mitsch and Clemence (1985) as a function of the soils peak friction angle, as shown in Figure 4.3 (b). Using this extrapolation, a peak K value of 10.8 can be considered (when ϕ_{pk}' = 59.9). Jeffrey *et al.* (2015), however, also found that the pile installation technique has a significant influence on K. In particular, when a pile is wished in place (WIP, such as the roots considered in this Thesis), the K value is significantly reduced. For model piles wished in place and subjected to a compressive force, they found a linear relationship of $K = 0.0467 \cdot \phi_{pk}' - 1.101$ (see Figure 4.3 (b)). This would suggest a much smaller K value of 1.7, when ϕ_{pk}' = 59.9°. Using Equation 4.2, the maximum pull out measurements shown in Figure 3.13, and the assumed maximum δ values for Linden and Viton, values of K were estimated to range between 2.4 (Linden) and 2.8 (Viton) (Note that the discrepency between the K values for Linden and Viton is thought to result from the uncertainty in the δ values, this could be eliminated by conducting friction tests). The wished in place data provided by Jeffrey *et al.* (2015), therefore, provides a better match to the expected behaviour of the root analogues. As the

data provided in Figure 4.3 (a) has been well researched, a conservative K value of 1.7, when ϕ_{pk}' = 59.9°, will be considered hereon.

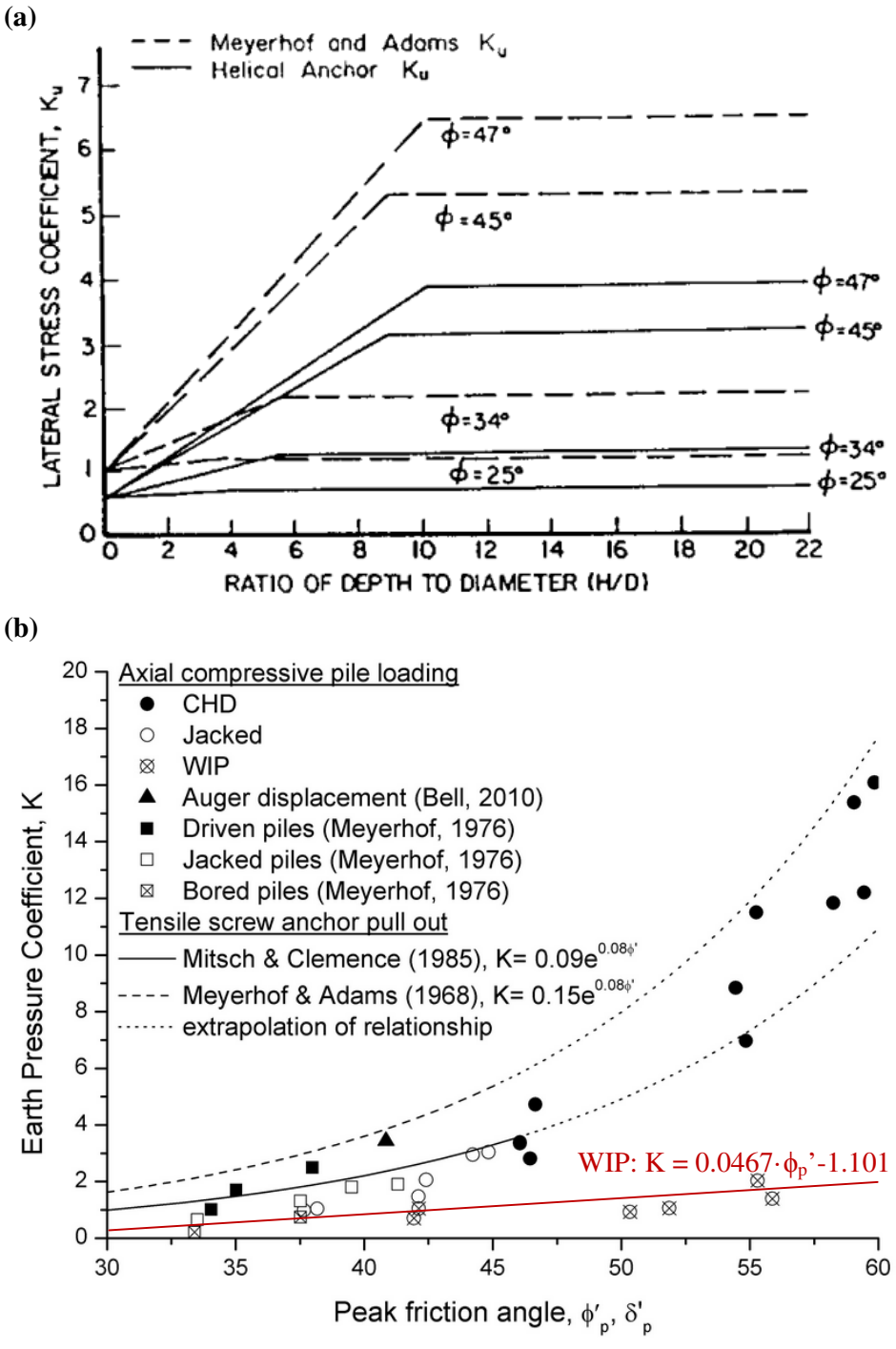

Figure 4.3: (a) Lateral stress values recommended for helical anchor piles in uplift (*Mitsch and Clemance, 1985*). (b) Earth pressure coefficient as a function of peak angle of friction (*Jeffrey et al., 2015*).

From Equation 4.2, it is apparent that the magnitude of skin friction is depth dependant. This is also true, therefore, of the magnitude of interface shear force. Interface shear force, however, is also dependant on the beam and element properties. This is highlighted in Equation 4.3, which transforms the value of *f* from a pressure acting across the surface of an element to a force acting at the spring location through multiplying it by the surface area of the element;

$$t_{\max} = f \cdot \pi \cdot D_{root} \cdot L_E \qquad \text{Eq 4.3}$$

Where; $\boldsymbol{t_{max}}$ is the maximum interface shear force; $\boldsymbol{f}$ is the interface friction between the soil and pile (kPa), see Equations 4.1 and 4.2; $\boldsymbol{D_{root}}$ is the diameter of the pile or root (m), and; $\boldsymbol{L_E}$ is the length of the element.

4.4.2 Empirically (rubber tap roots only)

The beam-on-elastic foundation theory states that, when subjected to tensile axial loading, a beam sitting in an elastic foundation (i.e. soil) will experience a resisting force that is proportional to both its displacement and its stiffness, as shown in Equation 4.4 (*Knappett and Craig, 2012*).

$$RF = (\varepsilon \cdot E) \cdot A_t \qquad \text{Eq 4.4}$$

$$\varepsilon = \frac{dz}{dx}, \text{ or} \qquad \text{Eq 4.4 (a)}$$

$$\varepsilon = \frac{\Delta L}{L_e} \qquad \text{Eq 4.4 (b)}$$

Where; $\boldsymbol{RF}$ is the reaction force in the beam (kN); $\boldsymbol{\varepsilon}$ is the strain in the beam; $\boldsymbol{E}$ is the beam's Young's modulus (kPa); the product $\boldsymbol{\varepsilon \cdot E}$ is the stress within the beam (kPa); $\boldsymbol{A_t}$ is the beam's cross sectional area (m^2); $\boldsymbol{z}$ is the vertical displacement of the beam (m), and; $\boldsymbol{x}$ is the location on the beam (m).

Assuming that the rubber root analogues can be modelled as very flexible beam-columns, their reaction to uprooting can also be measured in this way. Note: As per Figure 3.5, the stiffness of the rubber at low strains, such as those present in the root analogues during uprooting, is taken as linear.

Having established a means of quantifying the distribution of internal force within a root during uprooting, the distribution of axial interface shear force (between the root and soil) can be calculated. Figure 4.3 demonstrates the forces acting on each element within a soil root system during loading. As shown, the top of each element is subjected to an uprooting force (F_j) and the base to a resisting

force (F_{j+1}), which is equal to zero at the very bottom of the root (in the absence of suction). An additional resisting force is provided, along the length of each element, by the interaction between the root and the root-adjacent soil (t_i). By equilibrium, the force measured at the top of each element, F_j, must be equal to the sum of the resisting forces, as shown in Equation 4.5;

$$F_j = t_i + F_{j+1} \qquad \text{Eq 4.5}$$

Where, in element $\boldsymbol{i}$; $\boldsymbol{t_i}$ is the interface shear force acting along the element (kN); $\boldsymbol{F_j}$ is the force acting at the top of the element, and $\boldsymbol{F_{j+1}}$ is the force acting at the bottom of the element (note: F_{j+1}=0 at the root tip).

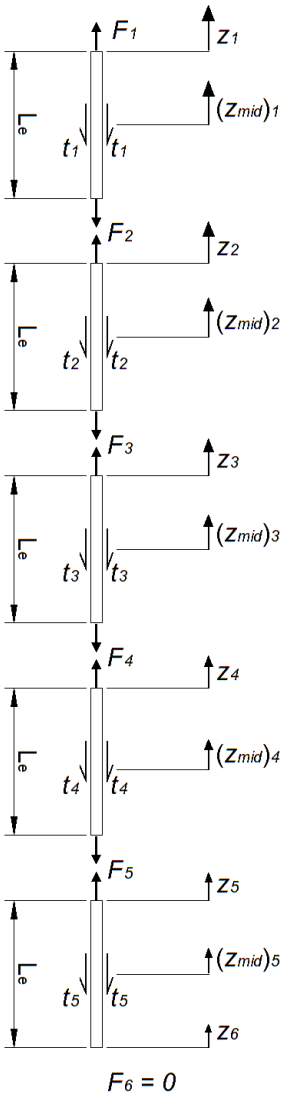

Figure 4.3: Forces acting on each element within the soil root system during uprooting, where $\boldsymbol{F}$ is the root internal forces, $\boldsymbol{z}$ is the depth from the soil surface, $\boldsymbol{t}$ is the interface shear force, $\boldsymbol{L_e}$ is the element length.

This equation can be rearranged to find t_i, as shown below;

$$t_i = F_j - F_{j+1} \qquad \text{Eq 4.5 (a)}$$

Using Equations 4.4 and 4.5 (a), therefore, the distribution of axial interface shear force, t, along the length of a root can be established at any time interval during pull out, if the force distribution can be determined using Equation 4.4. As such, if the axial stiffness of a root is known and a series of x-z curves are established at known intervals throughout an uprooting test; a series of x-t curves over time can be calculated, where x represents the location on the root, z represents the vertical displacement at point x and t describes the axial shear force at point x. Through combining and rearranging these x-z and x-t curves at each time interval, the t-z relationship at various points along the roots length, x, can be established. This process is demonstrated in Figure 4.4 and was used in this project to quantify soil root interaction during uprooting (by using the strain distribution in the root, which was determined from the GeoPIV analysis measurements for the half-root pull out tests (Chapter 3)).

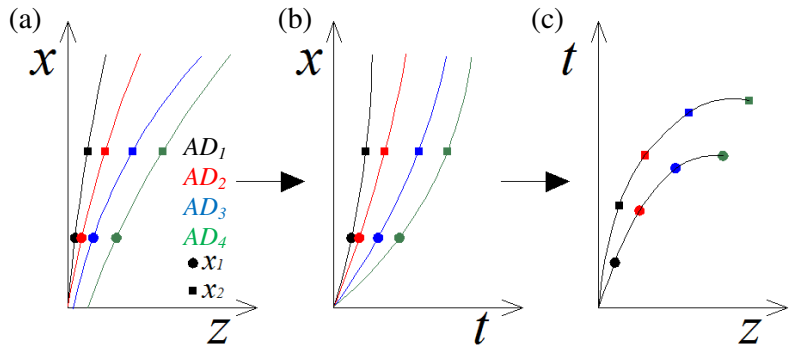

Figure 4.4: Calculating t-z curves using the relationship between applied displacement AD, location on root x, vertical root movement z and vertical shear force t. (a) x-z relatioinship is measured during testing, (b) Equation 4.3 is employed to estimate x-t relationship, (c) Data from (a) and (b) are rearranged to establish t-z curves at various points, x, along the root length.

4.4.2.1 Application of first principles to laboratory uprooting tests

The x-z relationships for the half Viton tap root analogues being pulled from wet and dry sand were measured at various values of applied displacement using GeoPIV analysis and cross section-front uprooting tests (see Chapter 3). Best fit polynomial equations were applied to these data and used directly to calculate suitable t-z curves for the half root analogues during loading (as described in Figure 4.4). In addition, they were used to estimate suitable t-z curves for the full root analogues during loading.

For simplicity, it was assumed that the distribution of vertical root movement is consistent between the cross section-front and full section-centre tests and that the consequent soil root interaction is comparable. Figure 4.5 depicts this assumed behaviour, suggesting that the soil root interaction during cross section-front testing should be exactly half of that present during full section-centre testing. Under these assumptions, the distribution of axial resisting force, F, along a full root analogue, F, can be calculated to be twice the distribution of F along a half root analogue, F_{half} (see Equation 4.6). The suitability of these assumptions was confirmed in Section 3.4.2. It was noted, however, that in half section-front tests, friction was present along the cross section of the root (where the half root analogue meets with the boundary edge of the test sample, see Figure 4.5) and that this may be playing a significant role during the cross section-front testing in dry sand. It was also noted that the value of Young's modulus is inconsistent between half and full root analogues (Section 3.2.1). In order to account for these anomalies, Equation 4.6 was modified, allowing the distribution of axial force along a full root analogue to be accurately estimated using the x-z relationships generated from half root analogues, as shown below;

$$F = 2 \cdot \left[E_{root} \cdot A_{root} \cdot \frac{dz}{dx} \right] \qquad \text{Eq4.6}$$

$$F_{full} = E_{r,half} \cdot A_{r,full} \cdot \frac{dz}{dx} - 2 \cdot \tau_{pers} \qquad \text{Eq 4.6(a)}$$

Where; $\boldsymbol{F_{full}}$ is the axial resisting force within a full root; $\boldsymbol{E_{r,half}}$ and $\boldsymbol{E_{root}}$ are the Young's modulus of a half and full root, respectively; $\boldsymbol{A_{r,half}}$ and $\boldsymbol{A_{root}}$ are the areas of a half and full root, respectively, and; $\boldsymbol{\tau_{pers}}$ is the friction at the root-Perspex interface.

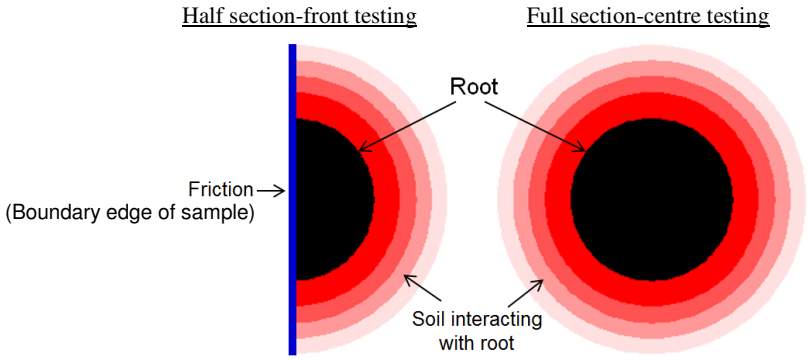

Figure 4.5: Plan view of assumed distribution of soil root interaction during full and cross sectional modelling.

4.4.2.1.1 Fitting polynomial equations to x-z data

A polynomial equation in the following form was chosen to represent the measured *x*-*z* data;

$$z = a_1 + c_1 \cdot x^2 + d_1 \cdot x^3 + e_1 \cdot x^4 \qquad \text{Eq 4.7}$$

Where; a_1, c_1, d_1 and e_1 are constants that need to be defined; z is the axial root movement (m); and; x is the location on the root (m).

The exclusion of the x^1 term was chosen to engineer a value of $\varepsilon = 0$, and therefore $F=0$, at the root tip (see Figure 4.4), where the root tip sits at the origin of Equation 4.7 (i.e. the location at which $x = 0$). If present, an x^1 term would differentiate to leave a constant, b_1, in the derivative equation and thus $F \neq 0$ when $x = 0$. Figure 4.6 compares the fit of 2, 3 and 4 degree polynomial equations to three unique sets of measured *x*-*z* data, using the Microsoft Excel best fit function. As demonstrated, the four degree polynomial provides the superior best fit curve for all data sets.

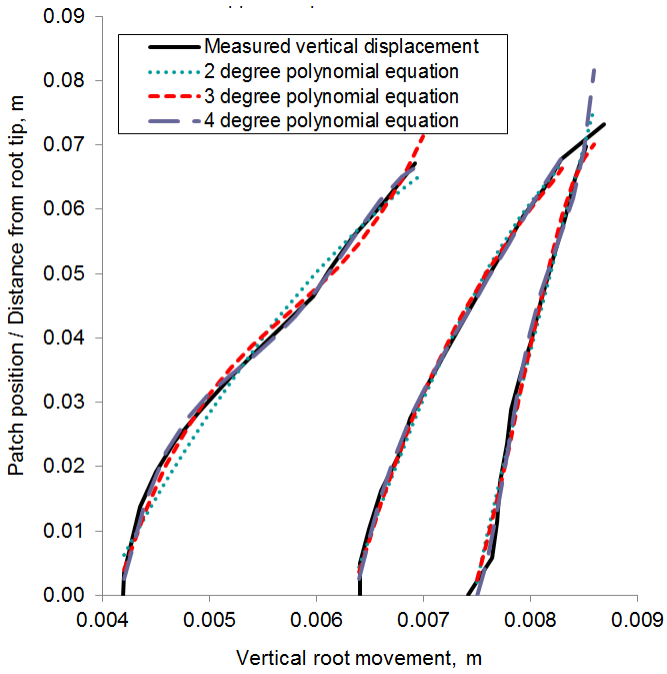

Figure 4.6: Comparison of 2, 3 and 4 degree polynomials for representing three *x*-*z* curves (from three repeat tests) of half Viton tap root analogues being uprooted from dry sand after 10 mm of applied displacement.

The constants a_1, c_1, d_1 and e_1 in Equation 4.7 define the ability of the polynomial to fit each set of *x*-*z* data. A number of methods exist for calculating these values of which this study uses Gaussian elimination with back substitution. This method is accurate and efficient, even with large data sets,

and is therefore ideal for calculating equation constants. A brief overview of the process of this calculation method follows;

Stage 1: For every data point (x_n, z_n) within a measured *x-z* data set Equation 4.7 can be employed. This generates a series of equations that share the same constants (a_1, c_1, d_1 and e_1), see below;

$$\begin{aligned} a_1 + c_1 \cdot x_1^{\,2} + d_1 \cdot x_1^{\,3} + e_1 \cdot x_1^{\,4} &= z_1 \\ a_1 + c_1 \cdot x_2^{\,2} + d_1 \cdot x_2^{\,3} + e_1 \cdot x_2^{\,4} &= z_2 \\ a_1 + c_1 \cdot x_3^{\,2} + d_1 \cdot x_3^{\,3} + e_1 \cdot x_3^{\,4} &= z_3 \\ \Downarrow \qquad\quad \Downarrow \qquad\quad \Downarrow & \\ a_1 + c_1 \cdot x_n^{\,2} + d_1 \cdot x_n^{\,3} + e_1 \cdot x_n^{\,4} &= z_n \end{aligned} \qquad \text{Eq 4.8}$$

Stage 2: The unknown terms, a_1, c_1, d_1 and e_1, can be isolated by considering the equations in matrix form, as shown below;

$$\begin{bmatrix} 1 & x_1^{\,2} & x_1^{\,3} & x_1^{\,4} \\ 1 & x_2^{\,2} & x_2^{\,3} & x_2^{\,4} \\ 1 & x_3^{\,2} & x_3^{\,3} & x_3^{\,4} \\ \vdots & \vdots & \vdots & \vdots \\ 1 & x_n^{\,2} & x_n^{\,3} & x_n^{\,4} \end{bmatrix} \cdot \begin{bmatrix} a_1 \\ c_1 \\ d_1 \\ e_1 \end{bmatrix} = \begin{bmatrix} z_1 \\ z_2 \\ z_3 \\ \vdots \\ z_n \end{bmatrix} \qquad \text{Eq 4.8 (a)}$$

Stage 3: Elementary row operations (i.e. swapping two rows or columns; adding a multiple of a row or column to another; or multiplying any row or column by a non zero integer) can be carried out until the matrix of *x* values has been reduced to an *upper triangle* matrix, as shown in Equation 4.9. This process is known as Gaussian elimination.

$$\begin{bmatrix} 1' & x_1^{\,2'} & x_1^{\,3'} & x_1^{\,4'} \\ 0 & x_2^{\,2'} & x_2^{\,3'} & x_2^{\,4'} \\ 0 & 0 & x_3^{\,3'} & x_3^{\,4'} \\ 0 & 0 & 0 & x_4^{\,4'} \end{bmatrix} \cdot \begin{bmatrix} a_1 \\ c_1 \\ d_1 \\ e_1 \end{bmatrix} = \begin{bmatrix} z_1' \\ z_2' \\ z_3' \\ z_4' \end{bmatrix} \qquad \text{Eq 4.9}$$

Where; **'** denotes terms that have undergone elementary row operations and may therefore not be equal to their original value (i.e. $1' \neq 1$)

Stage 4: Equation 4.9 is equivalent to Equation 4.8 (a) but has been simplified such that it can be immediately solved to find e_1, as shown below;

$$e_1 \cdot x_4{}^{4\prime} = z_4{}' \quad \Rightarrow \quad e_1 = \frac{z_4{}'}{x_4{}^{4\prime}} \qquad \text{Eq 4.10}$$

Back substitution allows the values of constants *d, c* and *a* to be found, see below;

$$d_1 \cdot x_3{}^{3\prime} + e_1 \cdot x_3{}^{4\prime} = z_3{}' \quad \Rightarrow \quad d_1 = \frac{z_3{}' - e_1 \cdot x_3{}^{4\prime}}{x_3{}^{3\prime}} \qquad \text{Eq 4.11}$$

$$c_1 \cdot x_2{}^{2\prime} + d_1 \cdot x_2{}^{3\prime} + e \cdot x_2{}^{4\prime} = z_2{}' \quad \Rightarrow \quad c_1 = \frac{z_2{}' - \left(e_1 \cdot x_2{}^{4\prime} + d_1 \cdot x_2{}^{3\prime}\right)}{x_2{}^{2\prime}} \qquad \text{Eq 4.12}$$

$$a_1 \cdot 1' + c_1 \cdot x_1{}^{2\prime} + d_1 \cdot x_1{}^{3\prime} + e_1 \cdot x_1{}^{4\prime} = z_1{}' \quad \Rightarrow \quad a_1 = \frac{z_1{}' - \left(e_1 \cdot x_1{}^{4\prime} + d_1 \cdot x_1{}^{3\prime} + c_1 \cdot x_1{}^{2\prime}\right)}{1'} \qquad \text{Eq 4.13}$$

Figure 4.7 compares measured and predicted (best fit) *x-z* data, at various intervals of applied displacement, throughout an uprooting test (using a Viton tap root analogue being pulled from dry sand as an example). As demonstrated, the proposed curve fitting model is very successful. It is limited, however, to modelling the length of root that was measured during GeoPIV analysis (i.e.it cannot necessarily be accurately extrapolated to estimate the *x-z* relationship over the length of root that has not been measured by GeoPIV analysis). It is important, therefore, that the GeoPIV analysis covers as much of the root as possible.

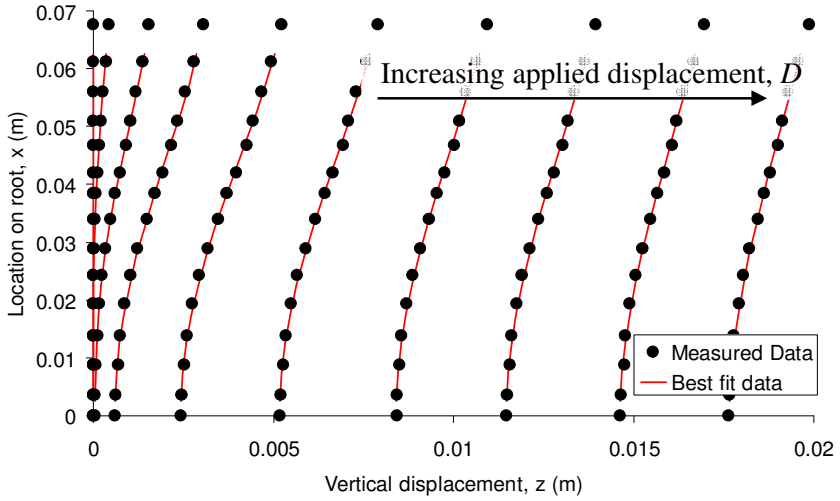

Figure 4.7: Using equation $z = a_1 + c_1 \cdot x^2 + d_1 \cdot x^3 + e_1 \cdot x^4$ to represent measured *x-z* data.

4.4.2.1.2 Calculating Viton-Perspex friction

Viton-Perspex friction, which was present in the cross-section front tests (see Section 3.4.2), was measured in the laboratory by sliding 100mm lengths of halved, optically textured Viton over a

greased Perspex surface (as shown in Figure 4.8) and recording the force required to do so. The Viton was displaced at a rate of 5mm/minute using an Instron 5966, with a 5N load cell. The consequent force-displacement curves are shown in Figure 4.9 (a). These show a general trend of reducing force with increasing displacement but are somewhat unpredictable. In particular, there is a large range in shape and magnitude. Nevertheless, friction appears significant, ranging between 0.03N and 0.08N at the start of testing, and 0N and 0.02N at the end. This corresponds to approximately 0 - 13% of the total force required to uproot a half tap root from dry sand, which confirms the role of friction in the cross sectional uprooting tests.

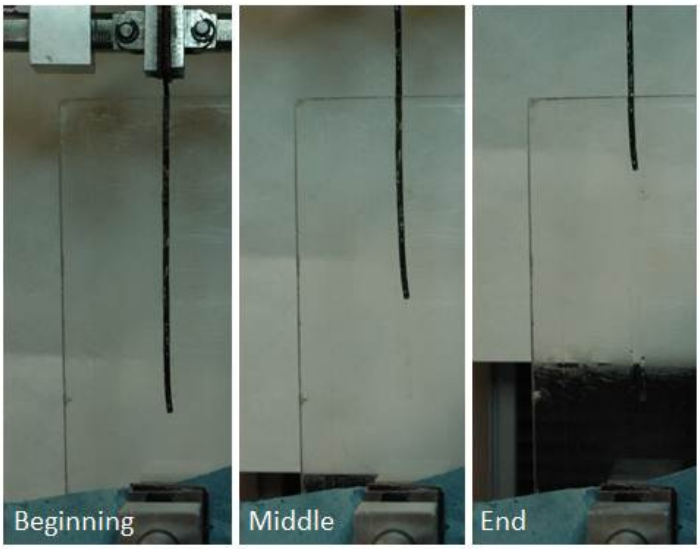

Figure 4.8: Test set up used to measure Viton-Perspex friction (images courtesy of S. B. Mickovski).

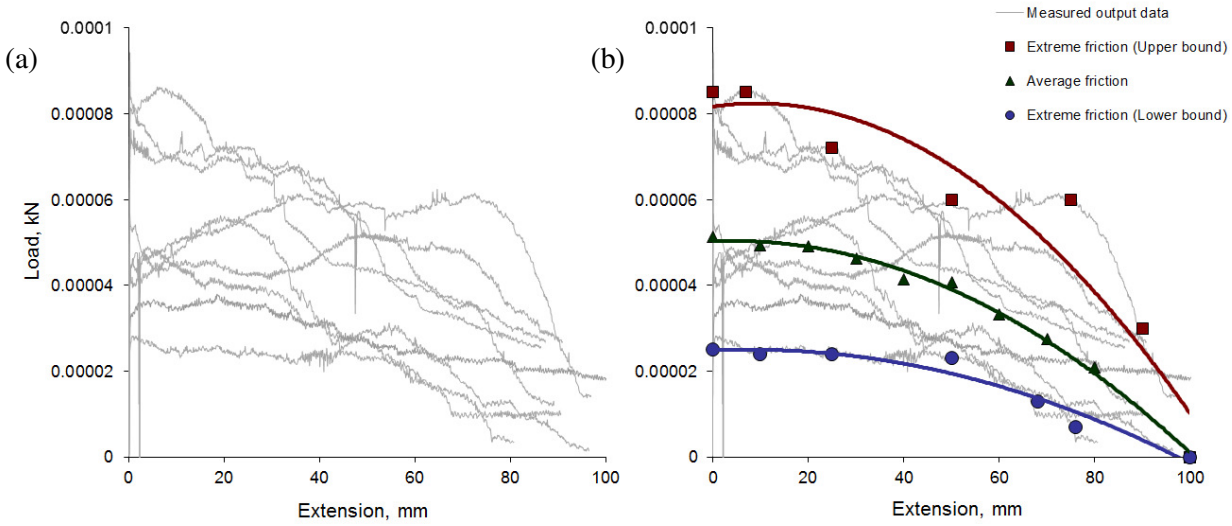

Figure 4.9: (a) Force-displacement data gather from pulling 100mm lengths of Viton O-ring rubber over a Perspex surface, (b) Average, upper and lower bound friction models.

In order to develop a friction model that can be used in *t-z* calculations (i.e. in Equation 4.7 (a)), the average frictional force was measured at intervals of 10mm of applied displacement and a two degree polynomial curve was fitted to the consequent data (using the Microsoft Excel trend-line function, see Figure 4.9 (b)). Using the same form of polynomial equation, best fit curves were also fitted to the extreme data sets and used to provide upper and lower bound friction models. These curves are shown below;

Average friction model $\tau_{pers\text{-}av} = -5.37x10^{-9}AD^2 + 4.45x10^{-8}AD + 5.03x10^{-5}$ Eq 4.14 (a)

Upper bound friction model $\tau_{pers\text{-}u} = -8.78x10^{-9}AD^2 + 1.62x10^{-7}AD + 8.17x10^{-5}$ Eq 4.14 (b)

Lower bound friction model $\tau_{pers\text{-}l} = -3.11x10^{-9}AD^2 + 4.83x10^{-8}AD + 2.48x10^{-5}$ Eq 4.14 (c)

Where; $\boldsymbol{\tau_{pers\text{-}av}}$, $\boldsymbol{\tau_{pers\text{-}u}}$, $\boldsymbol{\tau_{pers\text{-}l}}$, are the average, upper and lower bound friction models (kN), and; ***AD*** is the applied displacement at the root top (mm).

Through combining these friction models with the average uprooting force-displacement data that was measured experimentally during cross section-front uprooting tests (in dry sand), as shown in Equation 4.15, the suitability of the friction models was assessed. If successful, the *F* data generated from Equation 4.15 should match the average uprooting force-displacement data measured during the full section-centre uprooting tests (again, in dry sand).

$$F = 2\cdot(F_{half} - \tau_{pers}) \quad \text{Eq 4.15}$$

Where; At an applied displacement, ***AD***; ***F*** is the force required to uproot a full root; $\boldsymbol{F_{half}}$ is the force required to uproot a half root, and; $\boldsymbol{\tau_{pers}}$ is the Viton-Perspex friction.

Figure 4.10 presents the consequent uprooting force-displacement curves. As anticipated, the predicted *F* curve exceeds the measured data when the effects of friction are excluded (i.e. when $F = 2\cdot F_{half}$). Using the upper bound friction model provides a good estimate of force over the early range of applied displacement, but underestimates *F* in the later stages of uprooting, indicating an over estimation of friction. Conversly, when using the lower bound friction model the calculated values of *F* are too high, indicating that the predicted friction is too low. The average friction model, on the other hand, provides a successful overall fit to the measured data. This model will therefore be used to estimate the friction present during the cross section-front uprooting tests in dry sand.

Uprooting from wet sand is more complex. In the cross section-front tests, the presence of moisture within the system encourages a loss of uprooting resistance after approximately 20-30mm of applied

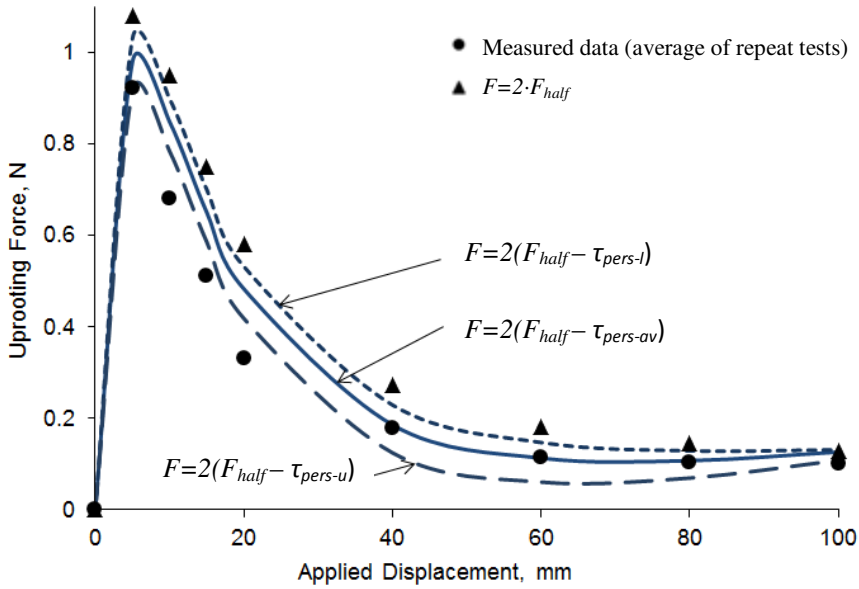

Figure 4.10: Comparison of measured pullout force-displacement curve and calculated pullout force-displacement curve for a traditional uprooting test in dry sand.

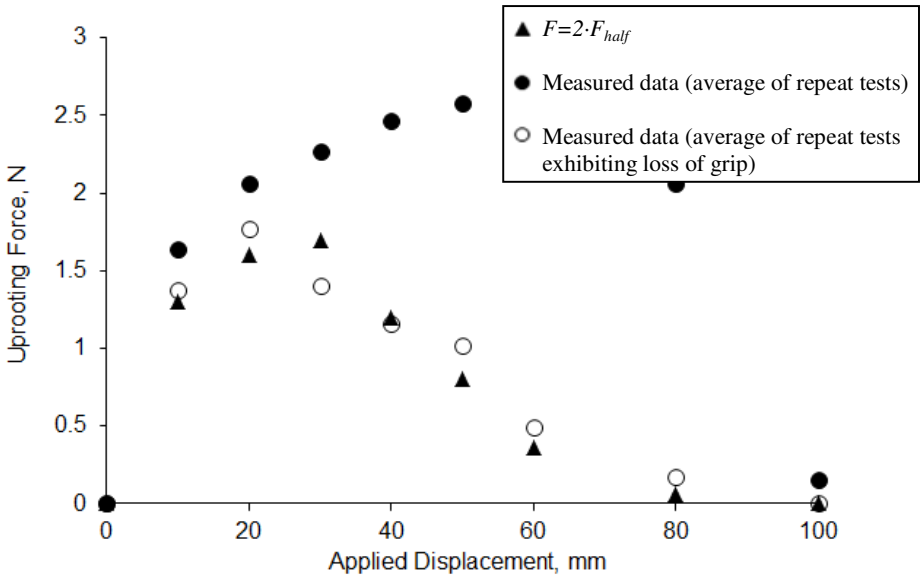

Figure 4.11: Comparison of measured pullout force-displacement curve and calculated pullout force-displacement curve for a traditional uprooting test in wet sand.

displacement. This behaviour, however, does not generally occur during the corresponding full section-centre tests. As a result, the force-displacement data measured during the full section-centre and cross section-front tests are not wholly comparable. This is shown in Figure 4.11. A small number of the full section-centre uprooting tests, however, did exhibit a loss of uprooting resistance.

The average of these data is very comparable to the estimated F curve when calculated without the use of a friction model (i.e. when $F = 2 \cdot F_{half}$). A friction model will, therefore, not be included in the development of t-z curves for uprooting from wet sand.

4.4.2.1.3 Improving calculation efficiency

To improve the efficiency of calculating t-z springs using the cross section-front test data, a MatLab .m file was created. This file scripts the calculation process outlined in section 4.4.2 and requires input in the form of: (i) GeoPIV analysis output files (i.e. x-z data, see Chapter 3), (ii) a conversion factor (to convert GeoPIV output from pixels to metres), (iii) basic root and soil properties, and (iv) the desired spring spacing. This file is named TZCurve and its script is presented in Appendix A.

Figure 4.12 outlines the process required to complete a t-z calculation using TZCurve (assuming that the GeoPIV analysis has already taken place). As demonstrated, the first step involves entering the necessary input information into section 1 of the code. The second, and final, step involves entering the text 'TZCurve' into the MatLab command line and selecting the 'GeoPIV_launcher' file from the consequent pop up window (this file will search for the GeoPIV analysis output files, and will be created during the GeoPIV analysis). Within approximately 5 seconds of completing these steps, TZCurve runs through the calculation procedure and returns plots of the x-z, x-t and t-z relationships. It also prints the t-z data, which can be input directly into Abaqus/CAE to determine spring properties. The following files are required to run TZCurve: consolidate8.m, GeoPIV_launcher.txt and all GeoPIV output files.

MatLab was considered an ideal tool for carrying out these calculations as; (i) it is the platform on which GeoPIV runs and, therefore, the GeoPIV analysis output files can be used directly. (This reduces data handling, which both increases efficiency and reduces the risk of possible errors.) (ii) It is designed to handle large data sets and perform complex mathematical operations.

```
SECTION 1
INPUT INFORMATION

   Root properties;
   diameter=0.0016;    %Diameter of the root; UM
   PoiRat=0.4895; %Poissons ratio of root; no u
   Erhalf=5652; %Youngs modulus of a half root,
   Erfull=5001; %Youngs modulus of a half root,

   Soil properties;
   Soil=0; %(0=dry soil; 1=wet soil)

   Data Conversion;
   FACTOR=5.227E-05;   %(1 pixel =[x]FACTOR mm)

   Spring Properties
   SpringSpacing=0.02 %metres

SECTION 2
```

Stage 1: Open TZCurve.m, enter input information and save.

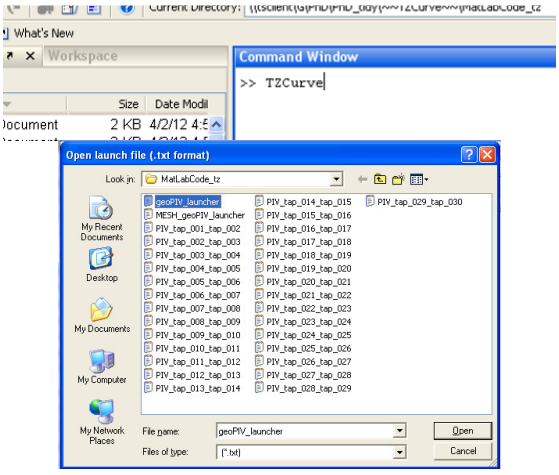

Stage 2: Type 'TZCurve' into MatLab command line. Select GeoPIV_launcher from pop-up window.

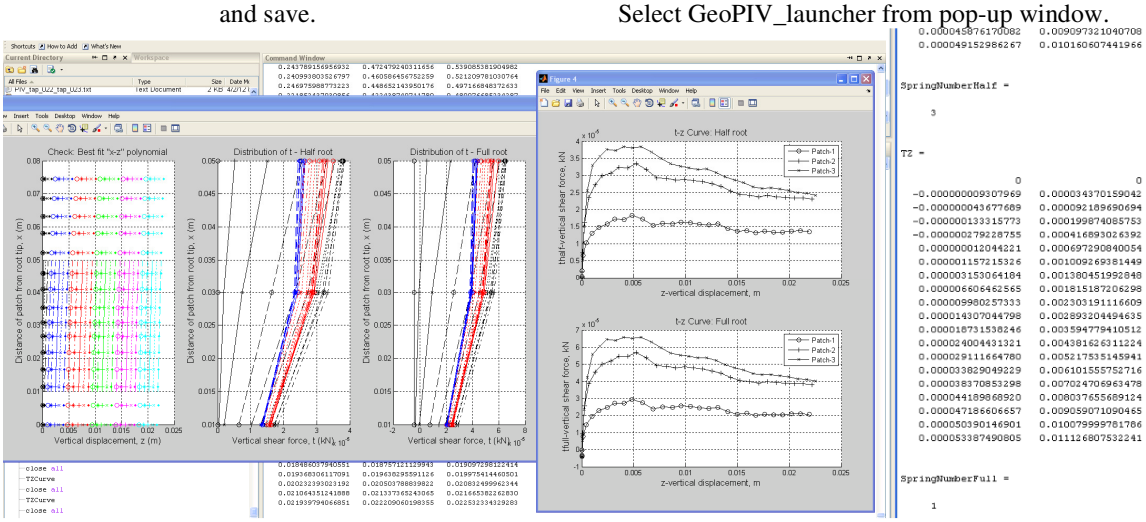

Stage 3: TZCurve produces *t-z* spring data and plots *x-z*, x-*t* curves and *t-z* curves.

Figure 4.12: Procedure required to run the TZCurve.m file.

4.4.3 *t-z* curves

4.4.3.1 Root analogues in dry sand

Figure 4.13 presents t/t_{max}–z curves for both rubber and wooden root analogues being uprooted from dry silica sand. These curves were calculated both theoretically (rubber and wooden roots) and empirically (rubber roots only) at depths of 0.03m, 0.05m, 0.07m and 0.09m from the soil surface. As demonstrated, the API standard curves do not change with changing root material properties or depth from the soil surface. This is in contrast to the empirically derived curves, suggesting that these features may be important when defining soil root interaction but not when defining soil pile interaction. The empirical curves show an initial non-linear increase in shear transition with applied

displacement as well as post-peak strain-softening behaviour, both of which are not present in the API standard curves. Additionally, the empirically derived curves indicate slightly different t/t_{max}-z relationships at different depths.

The empirical curves in Figure 4.13 indicate that the soil surrounding rubber root analogues softens during uprooting. This is akin to the behaviour of cohesive soils when interacting with pile foundations, as shown in the API standard curve for cohesive soil in Figure 4.2. Rather than exhibiting the same deformation behaviour as a cohesive soil, however, it is likely that the strain-softening of this very densely packed silica sand is the result of a change in state, from peak to critical, during uprooting. It could also be the result of the Viton rubber stretching in length, and so reducing in cross section, during uprooting. This will allow the sand to expand around the root, reducing its density and therefore reducing its peak state behaviour.

The empirical t-z curves in Figure 4.13 show that the applied displacement required to attain peak shear force (t_{max}) varies between 1mm and 4.5mm. The API standard curves estimate peak behaviour at 2.5mm. This value sits comfortably within the empirically derived range. The API standard curves, however, propose that a constant value of applied displacement is required to attain peak shear at different depths, while the empirical curves suggest a slower mobilisation of peak shear force at the top and tip of the root.

The API standard curves presented in Figure 4.13 were developed for predicting the cohesion-less soil-pile interaction that occurs in offshore foundations. The typical structural materials that form these foundations, namely concrete and/or steel, have a stiffness in the range of 25,000 MPa to 250,000 MPa. This is significantly larger than the range of stiffness offered by plant roots, as shown in Figure 4.14. Moreover, this is significantly stiffer than soil. A very dense sand sample, such as that used in the uprooting tests, has a Young's modulus that is typically in the range of 50-80MPa (*Bowls, 1996*). This is considerably less stiff than the stiffness of an offshore pile foundation (< 0.3%) and of the wooden root analogues used in this study (< 0.8%). It is, however, approximately 10 times larger than the Young's modulus of Viton rubber (or flexible plant roots). Moreover, the rubber and wood materials used in the uprooting experiments are much smoother than conventional pile foundations. This change in dynamics between the assumed soil inclusion characteristics and those that are present in the rubber root analogue soil system is likely to contribute to the discrepancy between the API standard and empirically derived curves, along with the difference in scale between root and pile systems.

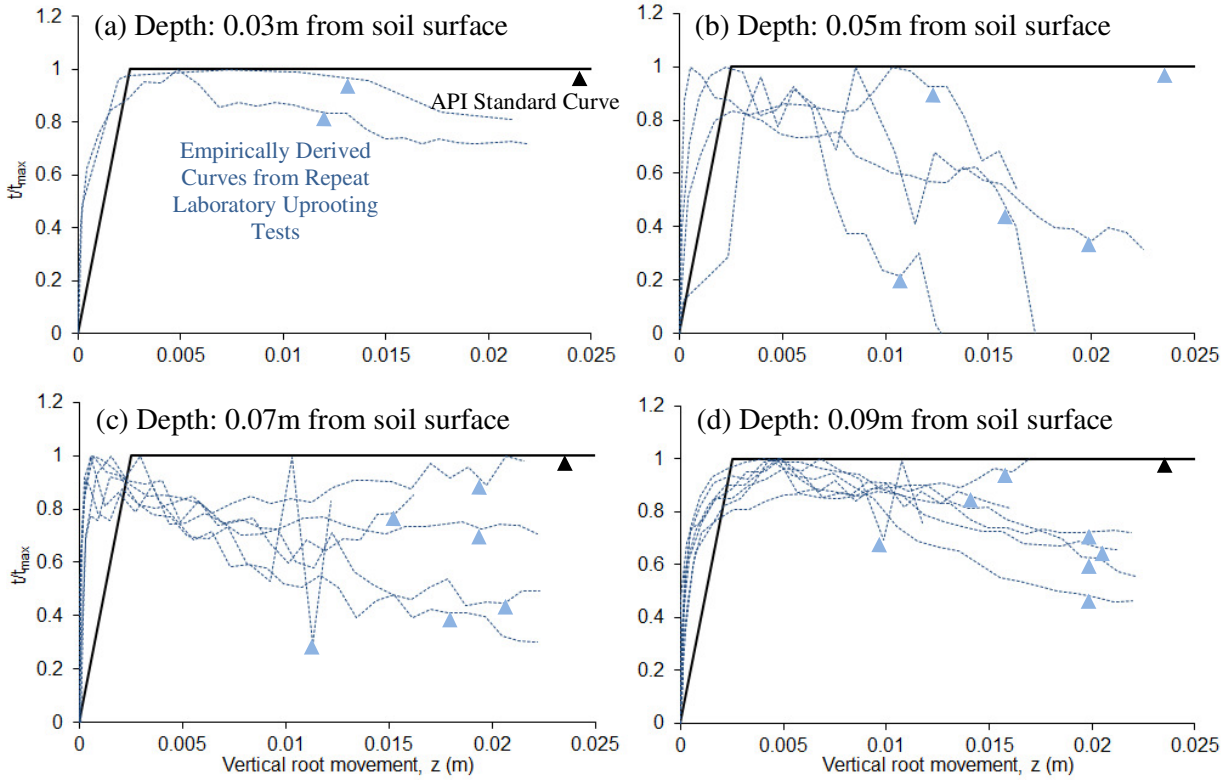

Figure 4.13 Comparison of theoretical (API Standard) and empirical (TZCurve Code) t/t_{max}-z curves at depths of (a) 0.03m, (b) 0.05m, (c) 0.07m and (d) 0.09m from the soil surface. Each dotted empirical curve represents a t/t_{max}-z curve calculated from a repeat laboratory uprooting test.

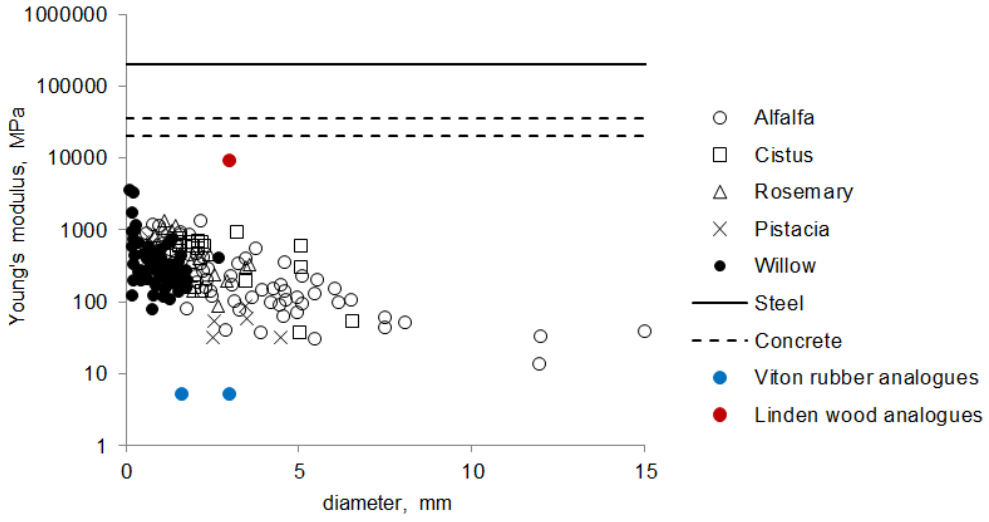

Figure 4.14: Comparison of root and pile foundation material properties (real root data taken from Operstein and Frydman, 2000)

Figure 4.15 shows a standardised version of the empirically derived t/t_{max}-z curves, where the t/t_{max}-z relationship during the later stage of pull out has been estimated (Note: the later stages of pull out

could not be calculated using TZCurve.m as a result of GeoPIV modelling restraints, see Chapter 3). The curves were standardised to the two trending t/t_{max}-z relationships shown in Figure 4.13. Curve A represents a gradual mobilisation and reduction of shear force (averaged using the data in Figures 4.13 (a) and (d)), while curve B represents fast peak behaviour (averaged using the data in Figures 4.13 (b) and (c)). The later stages of pull out were estimated both without (Figure 4.15 (a)) and with (Figure 4.15 (b)) a loss of interaction between the root and the soil. This allowed the curves to encompass the range of possible uprooting behaviours. To model continued interaction, the final measurement of t/t_{max} was continued indefinitely (or until the element was entirely removed from the soil). Loss of interaction, on the other hand, was estimated by taking the final gradient of the measured t/t_{max}-z curve and continuing this slope until t/t_{max} was equal to zero. As shown in Figure 4.15 (b), these curves predict a total loss of interaction between the root and soil at approximately 0.045 or 0.055m of vertical root displacement, for curves B and A respectively.

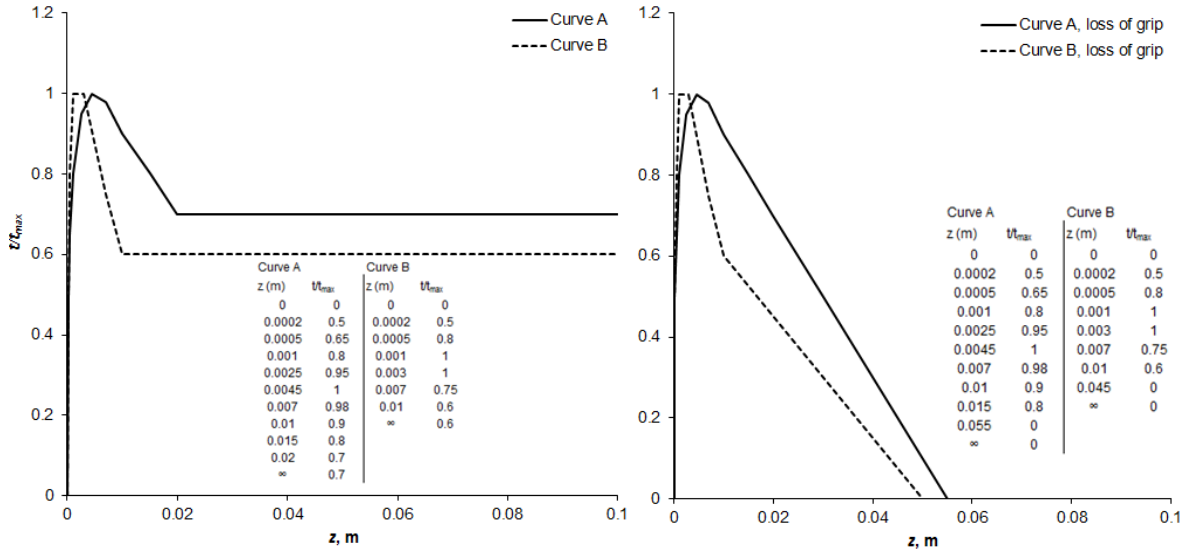

Curve A		Curve B	
z (m)	t/tmax	z (m)	t/tmax
0	0	0	0
0.0002	0.5	0.0002	0.5
0.0005	0.65	0.0005	0.8
0.001	0.8	0.001	1
0.0025	0.95	0.003	1
0.0045	1	0.007	0.75
0.007	0.98	0.01	0.6
0.01	0.9	∞	0.6
0.015	0.8		
0.02	0.7		
∞	0.7		

Curve A		Curve B	
z (m)	t/tmax	z (m)	t/tmax
0	0	0	0
0.0002	0.5	0.0002	0.5
0.0005	0.65	0.0005	0.8
0.001	0.8	0.001	1
0.0025	0.95	0.003	1
0.0045	1	0.007	0.75
0.007	0.98	0.01	0.6
0.01	0.9	0.045	0
0.015	0.8	∞	0
0.055	0		
∞	0		

Figure 4.15: Standardised empirical t/t_{max}-z behaviour describing the interaction between silica sand and rubber root analogues. (a) continued interaction. (b) loss of interaction.

Figure 4.16 shows the estimated distribution of t_{max} along the length of the wooden and rubber root analogues, again calculated both empirically and using API codes. As demonstrated, the API standard distribution indicates that t_{max} increases with both increasing depth from the soil surface and increasing root diameter. The empirical data, however, shows a different relationship, with t_{max} reducing with depth at a rate of;

$$t_{\max} = -4x + 1.8 \quad (\times 10^{-4}) \qquad \text{Eq 4.16}$$

Where; t_{max} is the maximum shear transfer (kN), and; x is depth (measured from the soil surface) (m).

This inconsistency between distributions is thought to be driven by soil dilation at low effective stress. In particular, the large depth of an offshore pile foundation (in excess of 3m) ensures that the majority of its length interacts with soil at a large effective stress. As this governs the overall behaviour of the soil pile system, the low effective stresses towards the top of the pile are generally considered negligible and their effects are therefore not included in API design codes. The shallow 0.1m depth of the soil root system considered in this Thesis, however, results in the entire system being subjected to low effective stresses and, therefore, high dilatancy.

The effect of changing the interface friction angle (δ) for wood, as per Equation 4.2 (b), doesn't have a significant impact on the output of the calculation, though a higher interface friction angle does result in an increased t_{max} distribution. The upper bound friction angle for wood will be used hereon (i.e. $\delta=0.9\phi_{cr}$' for sand-wood).

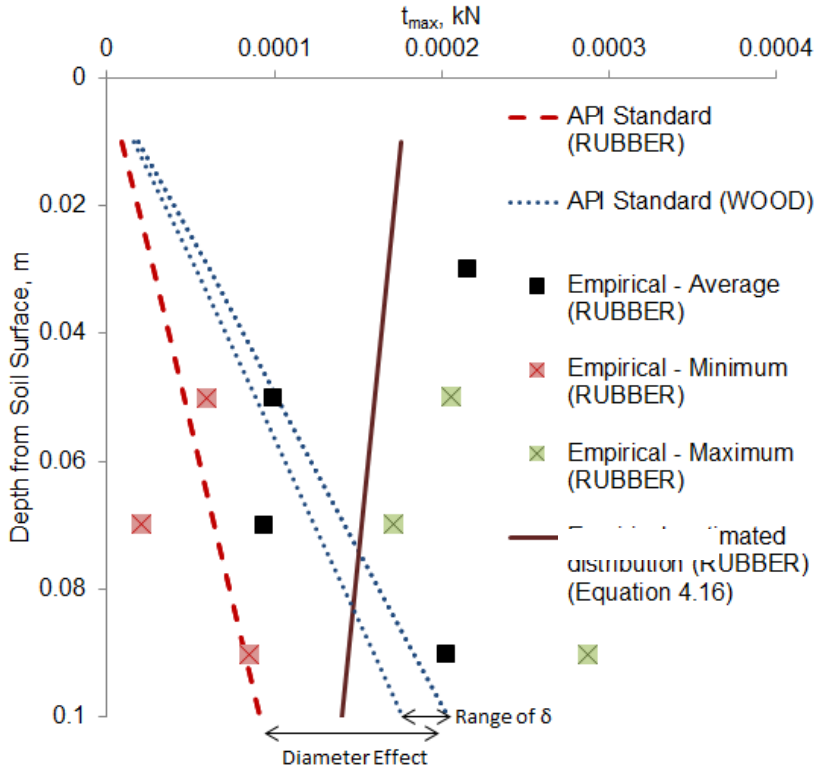

Figure 4.16: Estimated distribution of maximum shear transition, t_{max}, with depth according to API Codes and 'first principles'.

Using the peak soil shear strength, to account for dilatancy, the API standard distributions of t_{max} along root lengths were re-assessed, as shown in Figure 4.18. As demonstrated, the estimated effects of dilatancy at low effective stresses have a significant impact on the distribution of t_{max} along the roots length. Under the modelling framework provided by the API codes, however, an increase in t_{max} with depth is still predicted, and thus these revised curves still contradict the relationship estimated empirically.

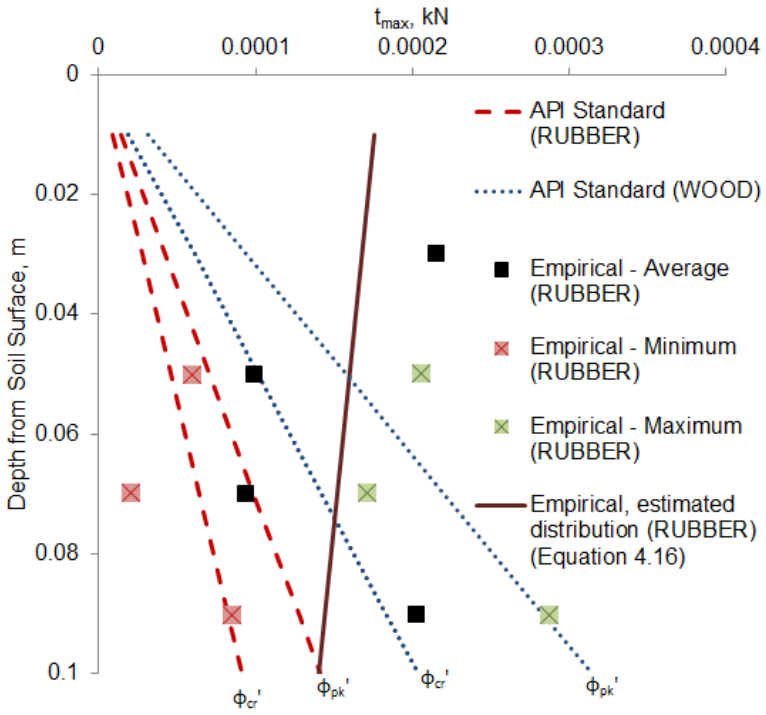

Figure 4.18: Effect of soil dilatancy on 'API standard' t_{max} distribution.

4.4.3.2 Root analogues in damp sand

Figure 4.19 shows the empirically derived $t/t_{0.005m}$-z behaviour of the rubber root analogues interacting with damp sand, where $t_{0.005m}$ is the value of t after 0.005m of applied displacement. Unlike the empirically derived t -z curves for rubber roots in dry sand, these curves do not generally display peak behaviour and were therefore normalised using the value of t at 0.005m. This value was chosen to correspond with the displacement required to generate t_{max} in the dry uprooting tests. As demonstrated, these curves are much more variable than those shown in Figure 4.13 (i.e. empirically derived t/t_{max}-z curves for rubber root analogues in dry sand) and therefore provide a much less obvious relationship between interface shear force, vertical root displacement and depth from the soil surface.

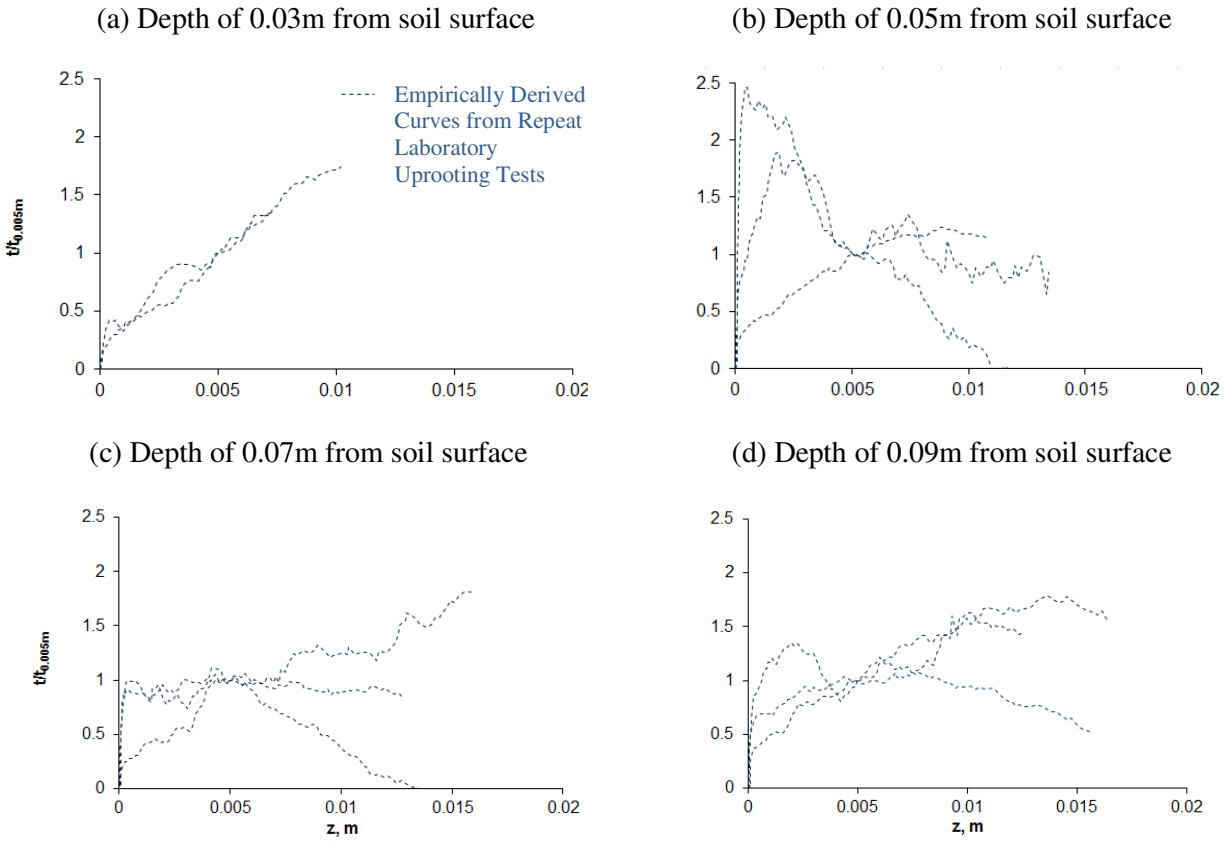

Figure 4.19: Empirically derived $t/t_{0.005m}$-z curves for rubber roots sitting in damp sand at depths of (a) 0.03m, (b) 0.05m, (c) 0.07m and (d) 0.09m from the soil surface. Each dotted empirical curve represents the $t/t_{0.005m}$-z calculated for a repeat laboratory uprooting test.

There is a strong similarity between Figures 4.19 (a) and 4.19 (d), which both show a general trend towards increasing $t/t_{0.005m}$ with increasing displacement at a very similar rate. The curves shown in Figures 4.19 (b) and 4.19 (c) are much more variable and, in some cases, show peak behaviour followed by a rapid decrease in $t/t_{0.005m}$ until zero is reached. As with the t/t_{max}-z curves that describe roots uprooting from dry sand, the curves located towards the centre of the root show a faster initial mobilisation of shear transfer than those sitting towards the top and tip of the root. Additionally, the later contribution of these curves to the total interface shear force is much less than that offered by the curves in Figures 4.19 (a) and (d).

Using the trending behaviour of these curves, standardised $t/t_{0.005m}$-z relationships were created. These are displayed in Figure 4.20. As with the standardised t/t_{max}-z curves in Figure 4.15, the later stages of pull out were estimated assuming both continued and loss of interaction. Curve C models a slow mobilisation of interface shear force, while curve D models fast mobilisation. Curve D with loss of

interaction indicates no soil root interaction after 30mm of applied displacement. Given the measured uprooting force displacement curves in Figure 3.13, it is assumed that this underestimates the later stages of soil root interaction.

Figure 4.21 and Equation 4.17 show the estimated relationship between $t_{0.005m}$ and depth;

$$t_{0.005m} = -3.17x + 0.42 \quad (\times 10^{-3}) \qquad \text{Eq 4.17}$$

Where; $\boldsymbol{t_{0.005m}}$ is the shear force after 0.005m of vertical root movement (kN), and; $\boldsymbol{x}$ is depth (measured from the soil surface) (m).

As demonstrated, there is a clear trend of decreasing $t_{0.005m}$ with increasing depth from the soil surface. This is akin to the t_{max}-x relationship that was calculated for rubber roots in dry sand (see Figure 4.18). In damp sand, however, the t-x curve has a much shallower gradient and therefore estimates higher values of t towards the root top. Moreover, the standardised $t/t_{0.005m}$-z curves with continued interaction predict that after 100mm of applied vertical movement, the value of t is up to 7 times larger than is was at 0.005m of applied displacement ($t_{0.005m}$). This suggests that the rubber root analogues in damp sand have a greater resistance to uprooting than those in dry sand and, therefore, that the proposed calculation technique can suitably differentiate between different soil root systems.

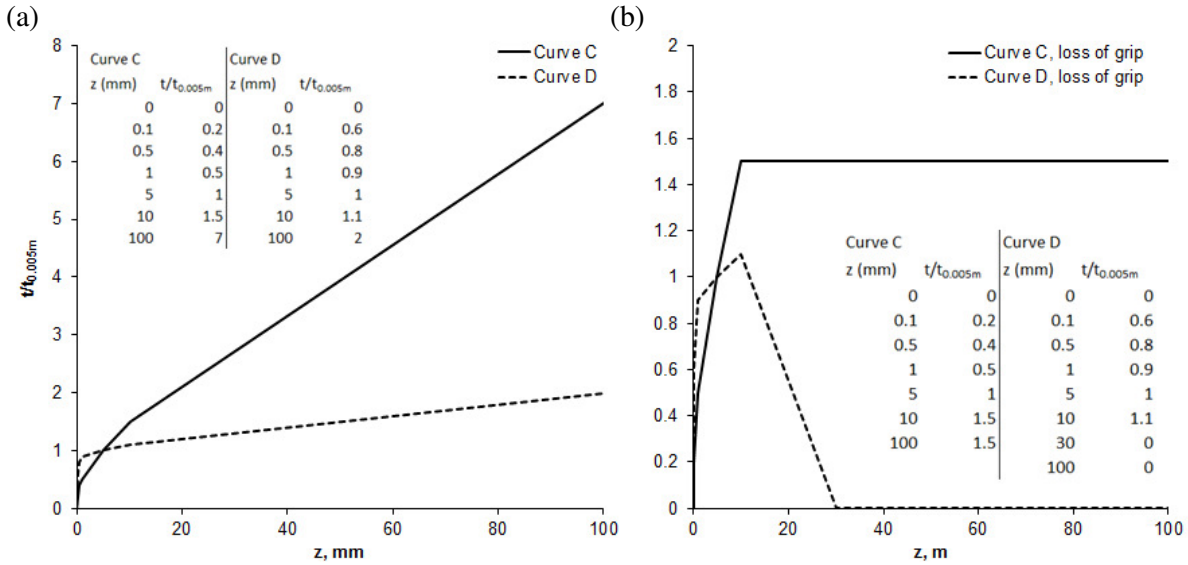

Figure 4.20: Standardised $t/t_{0.005m}$-z curves, accounting for (a) continued interaction and (b) loss of interaction.

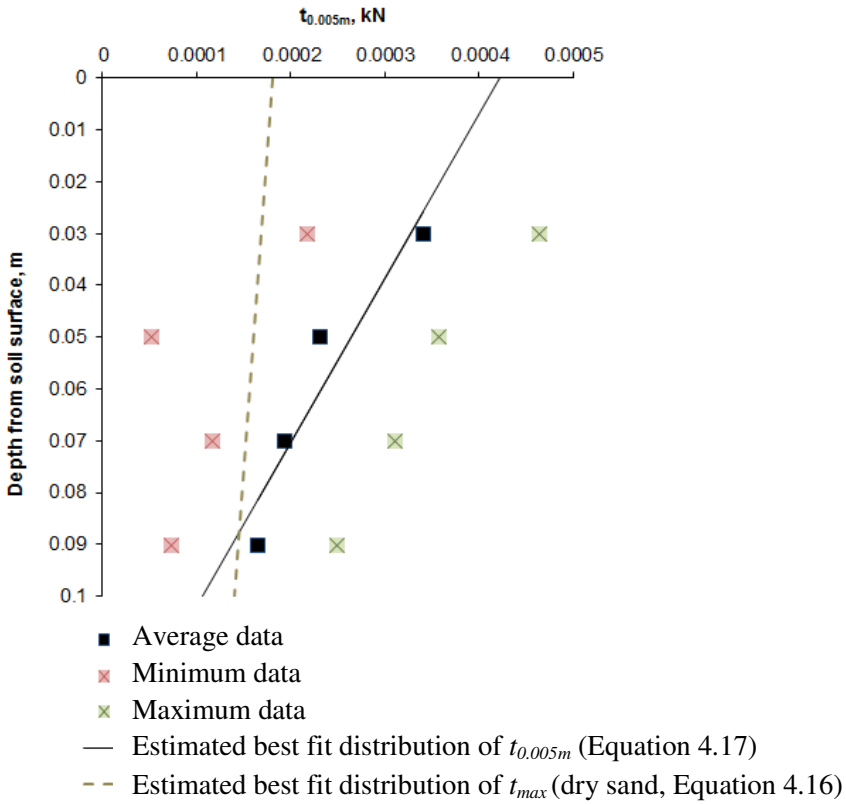

Figure 4.21: Empirically derived distribution of $t_{0.005m}$ with depth from soil surface.

4.4.3.3 *t-z* spring sets for input into Abaqus/CAE

The *t-z* spring sets that were incorporated in the Abaqus/CAE uprooting model are presented in Figures 4.22 through to 4.25. As demonstrated, each spring accounts for the removal of its corresponding element from the soil mass. This is because as an element begins to displace from the soil, its contribution to the interface shear force, *t*, gradually reduces towards zero (at which point the element is no loger submerged within, and thus no longer interacts with, the soil). This process is illustrated in Figure 4.26. For simplicity, it was assumed that the reduction of *t* as the root displaces from the soil is linear, as follows;

For: $x_{elem\ top} \leq z \leq x_{elem\ base}$

$$t = t_{z,top} \cdot \left(\frac{L_{e,sub}}{L_e} \right) \qquad \text{Eq 4.18}$$

Where; $\boldsymbol{x_{elem\ top}}$ is the location of the top of the element (m); $\boldsymbol{x_{elem\ base}}$ is the location at the base of the element (m); $\boldsymbol{t}$ is the shear transfer (kN); $\boldsymbol{t_{z,top}}$ is the value of t at z = location of element top (kN); $\boldsymbol{L_{e,sub}}$ is the length of element still submerged in the soil (m), and; $\boldsymbol{L_e}$ is the total element length (m).

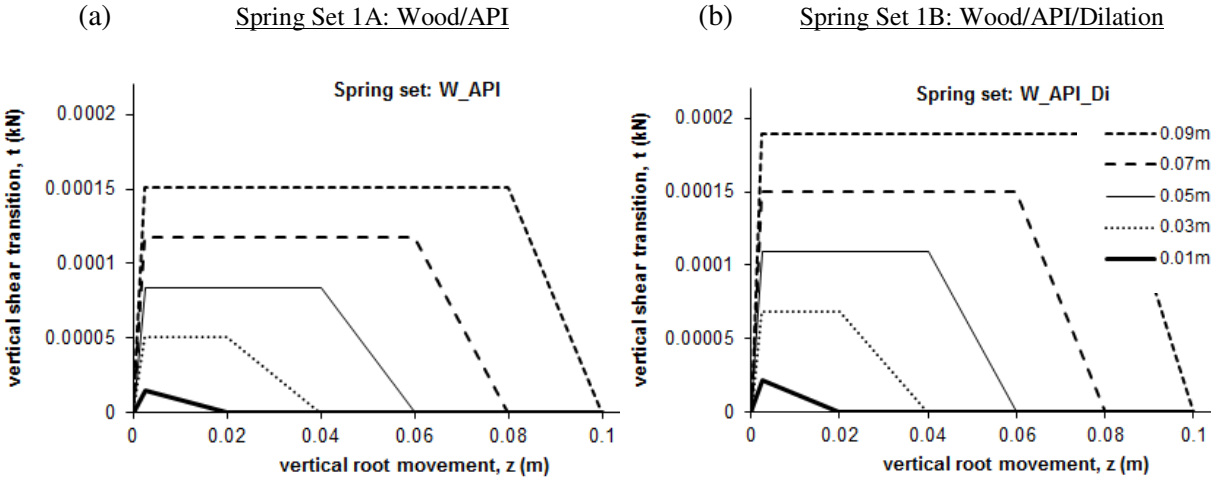

Figure 4.22: Spring sets used to represent ***wooden root analogues*** being uprooted from ***dry silica sand***, calculated using ***API Standards***. (a) No dilation ($\phi'=\phi_{cr}'$), (b) Accounting for the effects of dilation ($\phi'=\phi_{pk}'$)

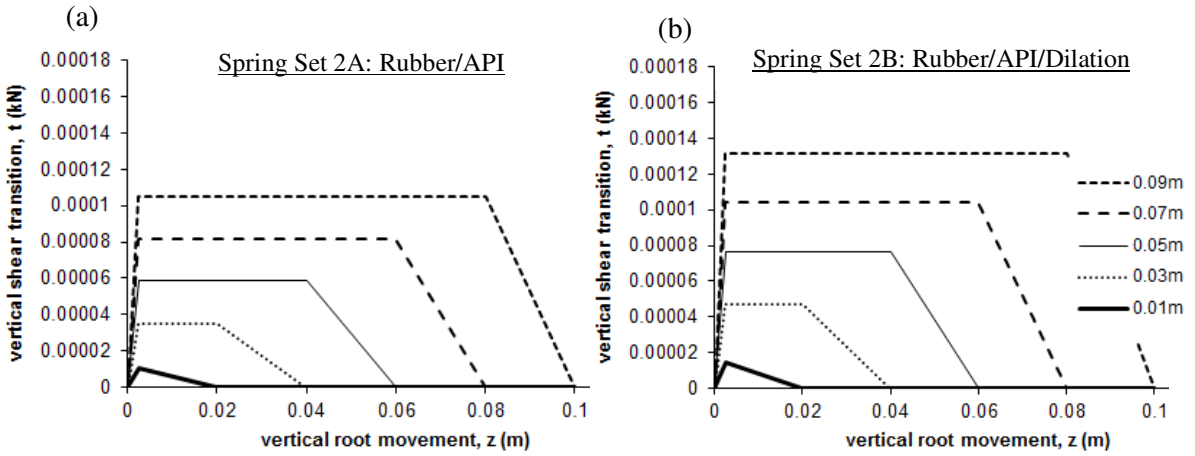

Figure 4.23: Spring sets used to represent ***rubber root analogues*** being pulled from ***dry silica sand***, calculated using ***API Standards***. (a) No dilation ($\phi'=\phi_{cr}'$), (b) accounting for the effects of dilation ($\phi'=\phi_{pk}'$).

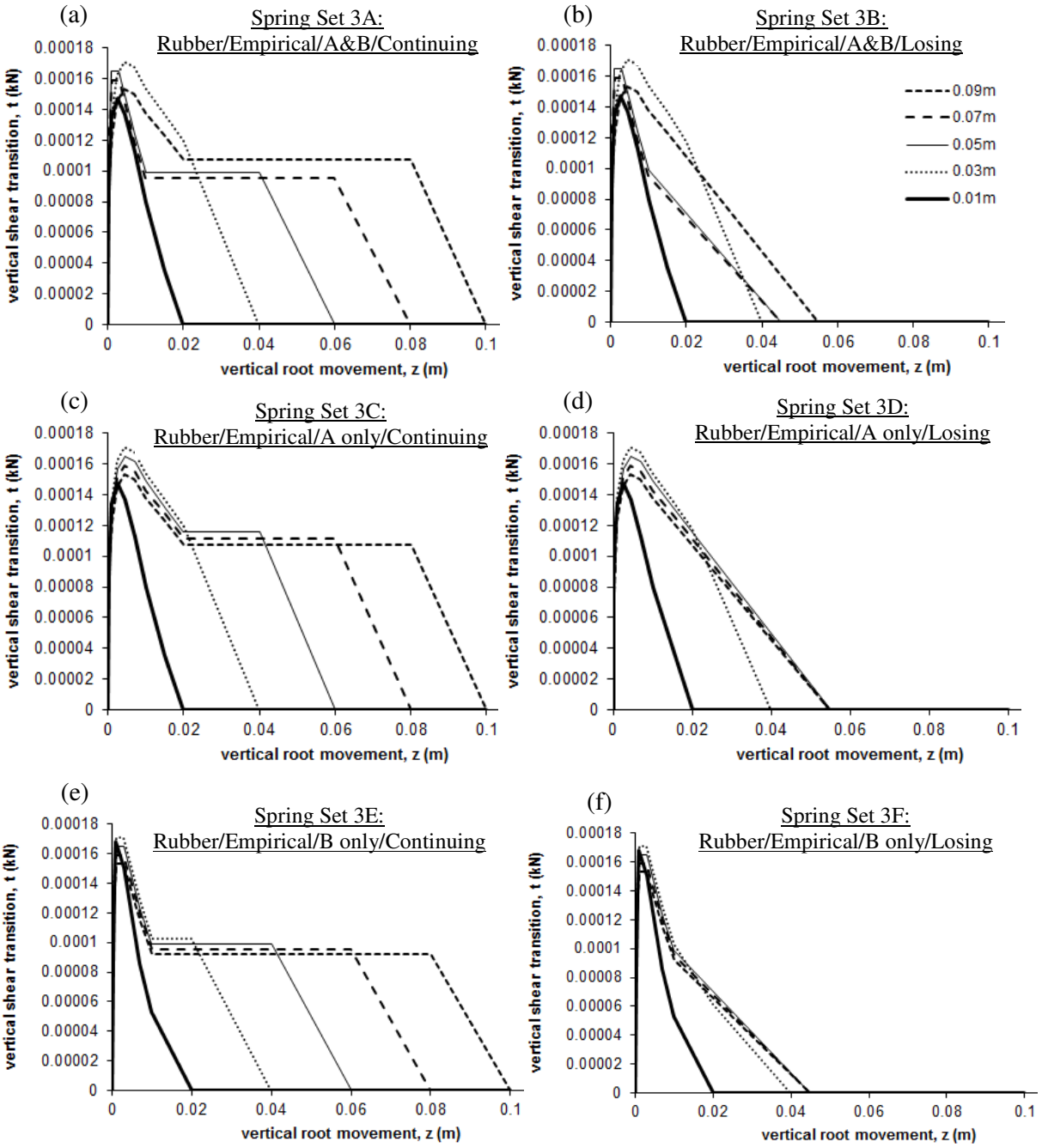

Figure 4.24: Spring sets used to represent ***rubber root analogues*** being uprooted from ***dry silica sand***, calculated ***empirically***. (a) Spring set considers Curve A with continued interaction at the root top and tip (0.09m and 0.01m) and Curve B with continued interaction at the remaining locations. (b) As spring set 3A, but considering Curves A and B with loss of interaction. (c) Spring set considers Curve A, with continued interaction, at all depth locations. (d) As spring set 3C, but considering Curve A with loss of interaction. (e) Spring set considers Curve B, with continued interaction, at all depth locations. (f) As spring set 3E, but considering Curve B with loss of interaction.

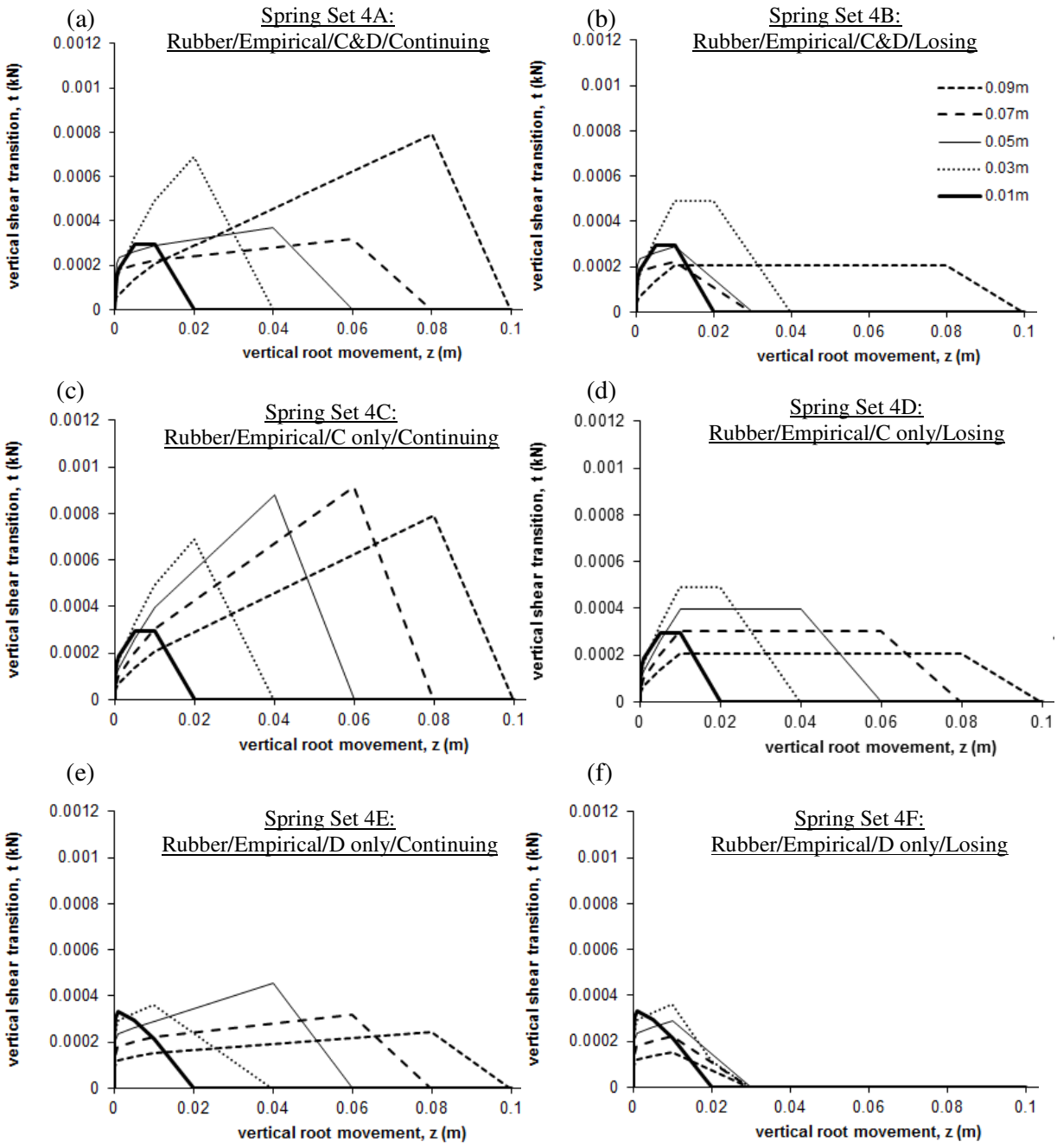

Figure 4.25: Spring sets used to represent ***rubber root analogues*** being uprooted from ***damp silica sand***, calculated ***empirically***. (a) Spring set considers Curve C with continued interaction at the root top and tip (0.09m and 0.01m) and Curve D with continued interaction at the remaining locations. (b) As spring set 4A, but considering Curves C and D with loss of interaction. (c) Spring set considers Curve C, with continued interaction, at all depth locations. (d) As spring set 4C, but considering Curve C with loss of interaction. (e) Spring set considers Curve D, with continued interaction, at all depth locations. (f) As spring set 4E, but considering Curve D with loss of interaction.

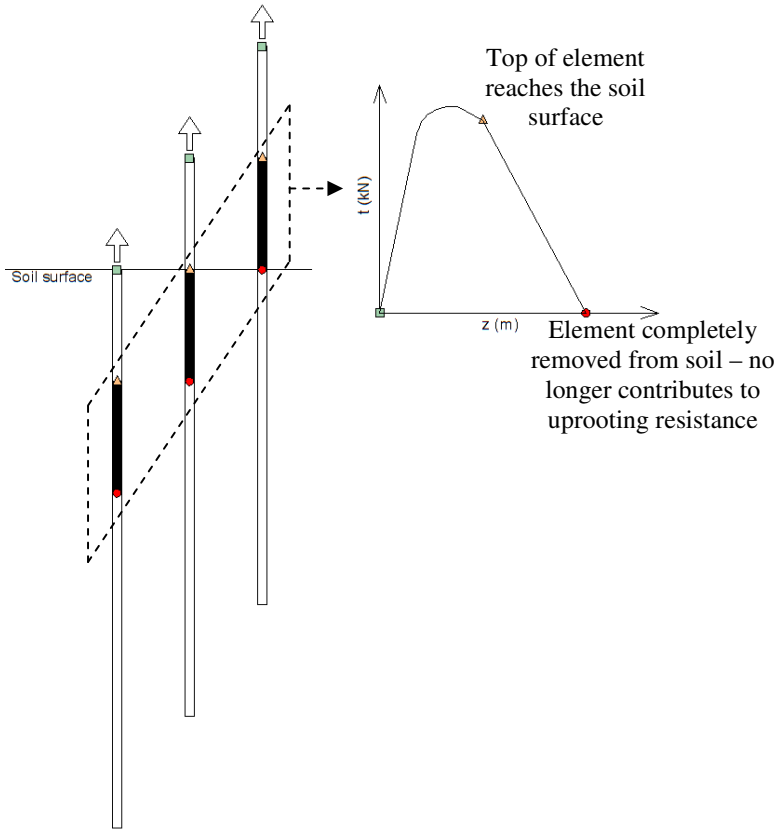

Figure 4.26: Accounting for the removal of elements from the soil mass within the *t-z* curves.

Figures 4.22 and 4.23 show the proposed *t-z* spring sets for wooden and rubber root analogues in dry sand, as calculated using API standards, while Figures 4.24 and 4.25 show the empirically derived *t-z* spring sets for rubber root analogues being uprooted from dry and wet sand. The empirical calculation technique suggested a *t-z* relationship at the top and tip of the root that differed from that at its centre. This was accounted for in the spring sets by combining the standardised curves A and B (Figure 4.24 (a) and (b)), and C and D (Figure 4.25 (a) and (b)) to model roots in dry and wet sand. These curves, however, were also considered independently in order to assess the suitability of different shaped curves for modelling soil root interaction.

4.5 Numerical modelling of a root subjected to pull out

Abaqus/CAE has a user friendly interface that is divided into eight construction modules, named; part, property, assembly, step, interaction, load, mesh and job. Each module carries the tools required for a specific construction phase. They are ordered in a logical sequence, which should be followed to minimise the risk of overlooking aspects of the finite element model. Abaqus/CAE does not have a

built in system of units and, as such, demands that the user provides consistent input data during model construction. For the uprooting models considered in this Thesis, the following units were chosen:

- Length = m
- Force = kN

Figure 4.28 shows the uprooting model (described in Figure 4.1) within the Abaqus/CAE interface, highlighting the key construction features. As demonstrated, the root was created in the *part* module using a 2D, deformable wire feature that was partitioned along its length in order to create a node at each spring location. Its properties were then defined in the *property* module, using root material and

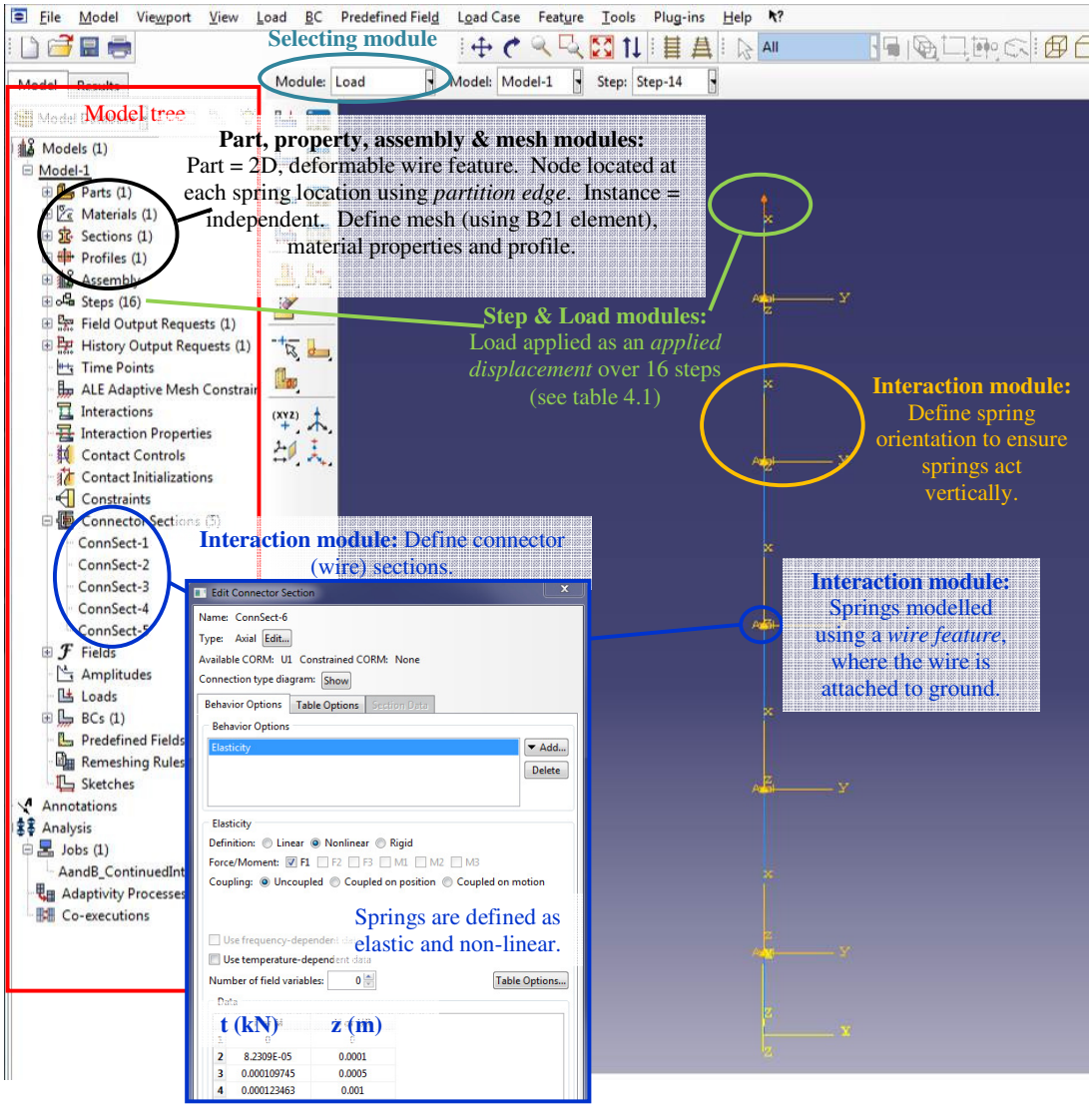

Figure 4.27: Overview of Abaqus/CAE input for modelling an analogue tap root in sand.

profile properties. Having created this feature, the *assembly* and *mesh* modules were used to transfer the root to the model assembly as an *independent instance* and to create a mesh, using B21 elements. These are 2 node linear beam elements, which are able to tolerate axial, bending and torsional deformation.

The *t-z* springs were constructed in the *interaction* module and were modelled using *wire features* that were connected between the ground at the root nodes. They were defined as axial connections with elastic, non-linear behaviour (which was described by the *t-z* spring data) and were assigned a localised orientation in order to ensure that they acted in the vertical direction. The spring properties could be easily edited in the *edit connector section* dialogue box (shown in Figure 4.28), which allowed for a quick parametric study.

In the *step* and *load* modules, 16 analysis steps were created. A *displacement* boundary condition was then applied to the root top, simulating the effects of an uprooting force. It was set to displace from zero to 90mm over the 16 steps, as shown in Table 4.1. In line with the laboratory uprooting tests, which showed peak pull out behaviour to occur within 10mm of applied displacement, closely-spaced displacement increments were chosen in the early analysis steps. The ability of the numerical model to capture this measured behaviour could therefore be studied.

Table 4.1: Loading steps considered in Abaqus/CAE uprooting model

Step	1	2	3	4	5	6	7	8	9	10	11	12	13	14	15	16
Applied displacement, mm	0	0.1	0.5	1	2	3	4	5	6	8	10	15	20	40	65	90

4.5.1 Initial results and discussion

Using the numerical model outlined in Figure 4.27, the root properties described in Section 3.2 and the *t-z* spring sets shown in Figures 4.22 to 4.25, a series of numerical models were established and analysed. Their outputs are presented in Figures 4.28 and 4.29, which respectively consider API Standard and Empirical *t-z* curves. Figure 4.29 confirms the suitability of the *t-z* modelling technique for this application.

Figure 4.28 indicates that the API Standard *t-z* springs provide a poor representation of soil root interaction. In particular, their use in numerical simulations result in an underestimation of peak pull

out force and an overestimation of the force during later pull out. To its merit, however, it successfully estimates the vertical displacement required to achieve the peak pull out force. In Figures 4.16 and 4.18, it was shown that the API Standard distribution of t_{max}-x underestimates shear force towards the root top (when compared to a corresponding empirical distribution). This is likely to be the cause of the underestimated peak pull out forces shown in Figure 4.28. The overestimation of pull out force in the later stages of uprooting, on the other hand, can be explained through the exclusion of strain softening in the API Standard curves (See Figure 4.14). The API springs, shown in Figures 4.22 and 4.23, predict a loss of interaction between the sand and inclusion as a result of elements removing from the soil only. This is not consistent with the laboratory test output, which shows a significant loss of friction between a root and dry soil after the peak pull out force has been

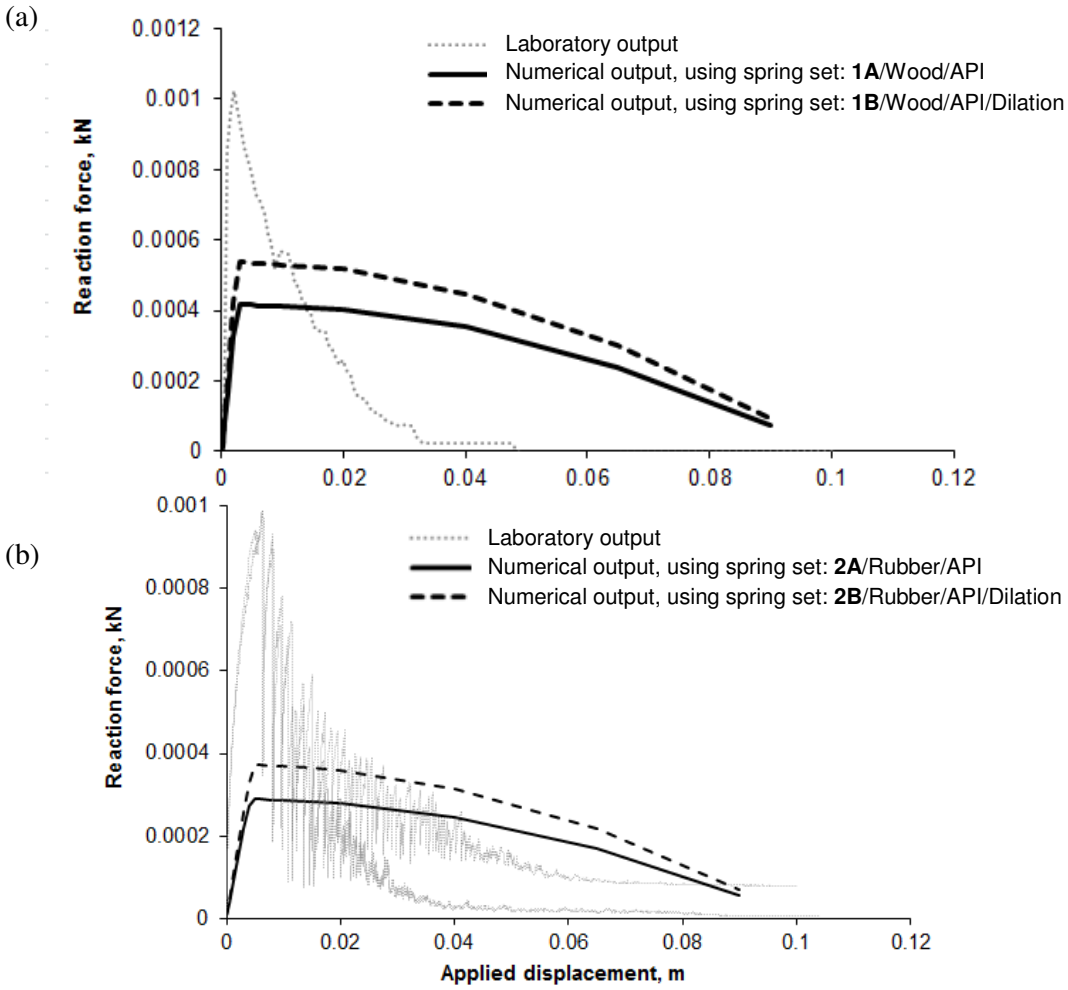

Figure 4.28: Comparison of numerical modelling output and laboratory testing output for (a) wooden roots being uprooted from dry sand, and (b) rubber roots being uprooted from dry sand. t-z springs calculated using API codes with and without accounting for the effects of dilation.

reached (see Figure 4.2). Whilst continued friction is expected with increasing displacement for piles under axial loading (*Khare and Gahndi, 2007*), it is clearly not a suitable assumption for modelling root pull out. Furthermore, the inclusion of dilation in the API spring definition does not significantly improve the numerical modelling. It favourably increases the peak uprooting force but worsens the accuracy of the later stages of pull out.

The empirical spring sets developed for rubber roots in dry sand (Figure 4.24) incorporate both peak behaviour and the removal of the root from the soil. As a result, numerical simulations that use these springs predict a force-displacement behaviour that is very similar to the laboratory measurements,

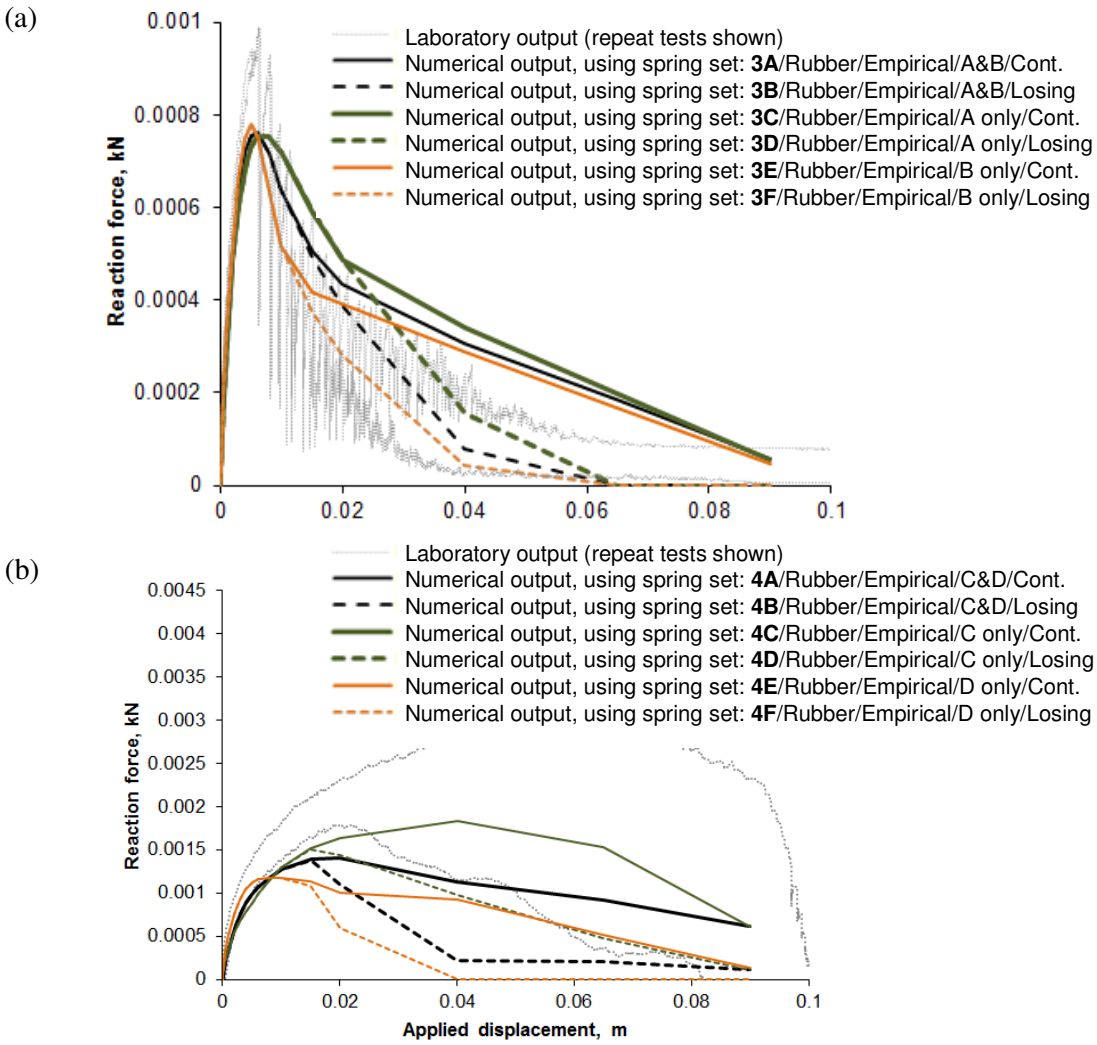

Figure 4.29: Comparison of numerical modelling output and laboratory testing output for (a) rubber roots being uprooted from dry sand, and (b) rubber roots being uprooted from wet sand. *t-z* springs calculated empirically.

particularly when springs with a post-peak loss of interaction are employed (Figure 4.29(a)). The assumption of a post-peak continuation of interaction, however, is shown to be unsuitable, as it overestimates the later stages of pull out. Figure 4.29 (a) also shows that the predicted value of peak uprooting force underestimates laboratory measurements by around 20%. While this is a large improvement on the output of the numerical simulations that utilise the API defined springs, it signifies that there is room for improvement in the calculation technique. The most successful simulations used spring set: 3F/Rubber/Empirical/B only/Losing.

The numerical modelling of rubber roots being uprooted from damp sand, using the empirical spring sets shown in Figure 4.25, were expected to simulate the full section-centre laboratory tests that experienced a loss of interaction only (due to the discrepancy between the full section-centre and cross section-front testing techniques). Use of spring set 4D (Rubber/Empirical/Conly/Losing) provides a very good estimation of the laboratory test data but, again, underestimates the peak pull out force by around 20%. Use of the remaining spring sets (except set 4C (Rubber/Empirical/Conly/Cont.)), however, significantly underestimates the laboratory uprooting behaviour. These curves were therefore deemed unsuitable for modelling damp soil-rubber root interaction. Interestingly, incorporating spring set 4C (Rubber/Empirical/Conly/Cont.) into a numerical simulation provides a force-displacement curve that closely shadows the measured force-displacement curves within traditional uprooting tests that did not experience a loss of interaction. The scale of the predicted curve, however, underestimates the required uprooting force by around 45%. Nonetheless, this output provides an indication of the form of *t-z* curve that is required to model interaction in damp soil.

The numerical simulations that use empirical spring sets have shown that the *t-z* technique can capture most of the essential soil root interaction behaviour, and can therefore predict root pull-out behaviour over a large displacement range, provided that accurate *t*-z relationships can be found. API codes propose standardised *t-z* relationships for the design of pile foundations, which can be easily and quickly adapted for the soil-pile system in question, using only routinely measured soil properties. These curves, however, do not transfer to the study of soil root interaction. Using a simplification technique that is similar to that used in the API codes, however, the empirical *t-z* curves were standardised, as shown in Table 4.2. Curves B (with loss of interaction only) and C (see Figures 4.15 and 4.20) were selected to represent rubber root analogues being pulled from dry and wet sand, respectively. The magnitude of these curves can be realised empirically through

application of Equations 4.16 (Curve B) and 4.17 (Curve C). It is also possible to theoretically scale these curves using the Ennos (1993) uprooting model (see Section 2.2.3). A theoretical, rather than empirical, scalar is beneficial as it allows the model to be applied universally to different soil root systems. It is likely, however, that the *t-z* curves proposed in Table 4.2 are limited to modelling the uprooting of flexible roots. It would be beneficial, therefore, to develop equivalent standardised *t-z* curves for stiff roots.

Table 4.2: Standardised *t-z* curves for use in numerical modelling

Curve B (Dry sand) Loss of interaction		Curve C (wet sand) Loss of interaction		Curve C (wet sand) Continued interaction	
z (mm)	t/t_{max} (kN)	z (mm)	t/t_{max} (kN)	z (mm)	t/t_{max} (kN)
0.0	0.00	0.0	0.00	0.0	0.00
0.2	0.50	0.1	0.20	0.1	0.20
0.5	0.80	0.5	0.40	0.5	0.40
1.0	1.00	1.0	0.50	1.0	0.50
3.0	1.00	5.0	1.00	5.0	1.00
7.0	0.75	10.0	1.50	10.0	1.50
10.0	0.60	∞	1.50	100.0	7.00
45.0	0.00				
∞	0.00				

Ennos (1993) suggests a simplistic model, shown in Equation 2.4, that employs the roots surface area and the soils shear strength to quickly estimate values of the peak and critical state pull-out forces (see Section 2.2.3). The simplicity of this method is thought to be valid for the experiments considered in this project (where the roots sit vertically in the soil, as assumed by Ennos (1993)). It should be noted, however, that the model does not include a parameter to account for the effect of orientation on a roots resistance to pull out and therefore has limited applicability. Figure 4.30 compares the output of this model to those of the numerical simulations and laboratory tests (all considering uprooting from dry silica sand).

$$F_{pk} = A_{RS} \cdot \tau_{pk} \qquad \text{Eq 4.19 (a)}$$

$$\tau_{pk} = \sigma_v' \cdot \tan \phi_{pk}' \qquad \text{Eq 4.19 (b)}$$

$$\phi_{pk}' = 59.9° \quad (measured\ from\ shear\ box\ test) \qquad \text{Eq 4.19 (c)}$$

Where; $\boldsymbol{F_{pk}}$ is the peak pull out force (kN); $\boldsymbol{A_{RS}}$ is the surface area of the root (m^2); $\boldsymbol{\tau_{pk}}$ is the peak shear strength of the soil (kN/m^2); $\boldsymbol{\sigma_v'}$ is the vertical stress, which is equal to $\boldsymbol{p_o'}$ in this study as no loads were added to the soil surface (kN/m^2), and; $\boldsymbol{\phi_{pk}'}$ is the peak state angle of friction (°)

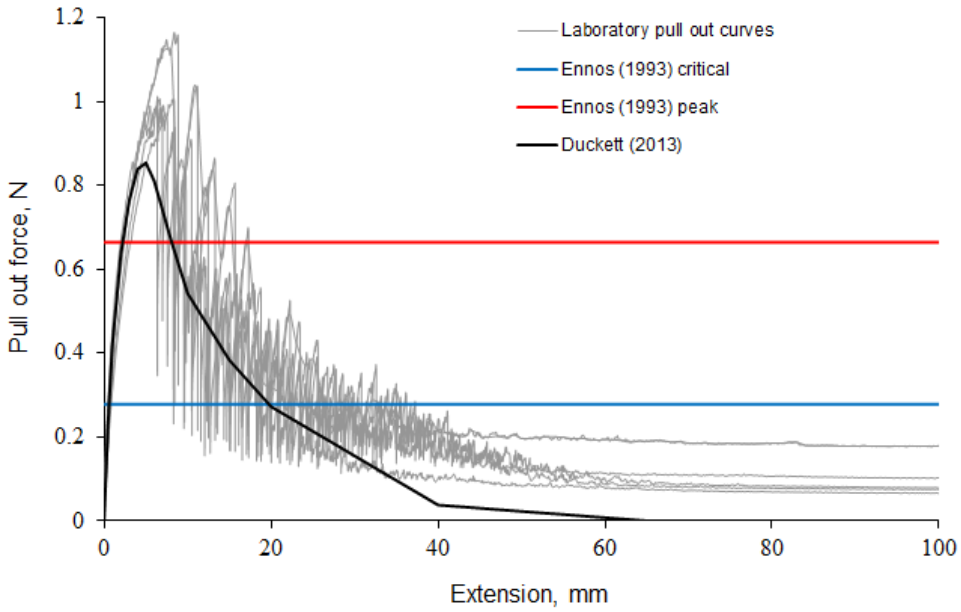

Figure 4.30: Comparison of proposed calculation model (Duckett, 2013) to existing model proposed by Ennos (1993). Output shows uprooting of rubber tap root analogue from dry silica sand.

The Ennos (1993) model is extremely easy to use, but provides a very rough estimate of the peak and critical state uprooting forces. As demonstrated in Figure 4.30, it underestimates the peak force (required to initiate root pull out) and overestimates the residual force (required to continue root pullout).

Considering the *t-z* model in Figure 4.1 and the Ennos (1993) uprooting model, the value of peak uprooting force (F_{pk}) was calculated at each spring depth (A_{RS} was taken as the element area). These F_{pk} values were then used to scale Curve B (Table 4.2) at the required depths, through simple multiplication. The consequent, theoretically scaled, *t-z* springs are shown in Figure 4.31 along with the empirically scaled springs. As demonstrated, these two spring sets differ in magnitude. Moreover, the peak shear force is anticipated to increase with depth in the theoretical model (as with API codes), and decrease with depth in the empirical model. Using these spring sets, a numerical simulation was completed, with the results shown in Figure 4.32. As anticipated, use of the Ennos (1993) uprooting model to scale the standardised *t-z* springs results in a less accurate output than that achieved when using the empirically derived scaling model. Unlike API design codes, therefore, which propose two *t-z* relationships that differentiate between soil type only (see Figure 4.2), a codified procedure designed to model soil root interaction will require a larger range of parameters in order to account for the increased complexity of both the material properties of the inclusion and the soil behaviour at low effective stresses.

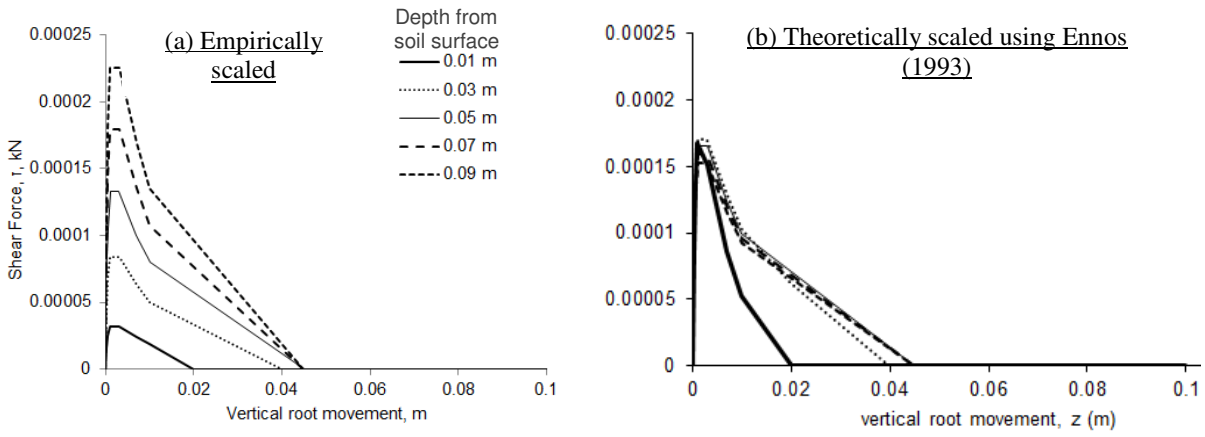

Figure 4.31: Comparison of (a) theoretically scaled (using Ennos (1993) and considering dilation) and (b) empirically scaled (using laboratory tests) *t-z* curves (using Curve B)

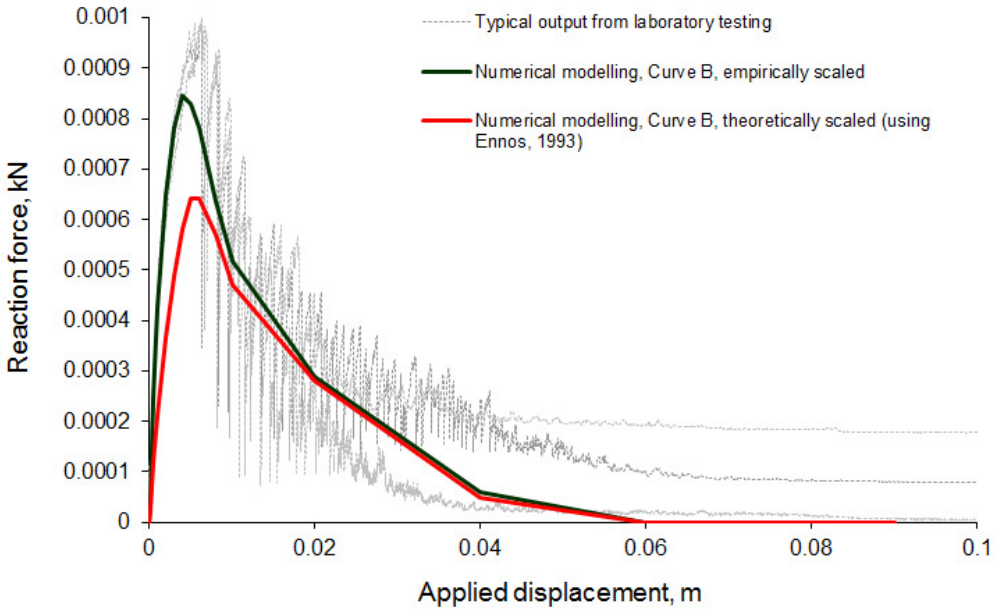

Figure 4.32: Comparison of numerical models that use theoretically scaled *t-z* springs (using Ennos, 1993) and empirically scaled *t-z* springs (using laboratory tests).

Figure 4.33 shows the development of axial strain within the root, as predicted by the numerical simulations that employed spring sets (a) 3F (Rubber/Empirical/Bonly/Losing) and (b) 4D (Rubber/Empirical/Conly/Losing). As with the development of strain measured from laboratory testing (see Chapter 3), this figure shows that (i) the maximum volume of strain coincides with the maximum volume of root pull out force, (ii) the root stretches progressively from its top to its tip,

with strain taking longer to mobilise in the deeper elements and reaching a maximum volume of strain at the root top, and (iii) roots being pulled from damp soil stretch more than roots being pulled from dry soil. Furthermore, the predicted maximum volumes of strain, for rubber roots in dry and wet sand, are approximately the same as those measured using the laboratory test data.

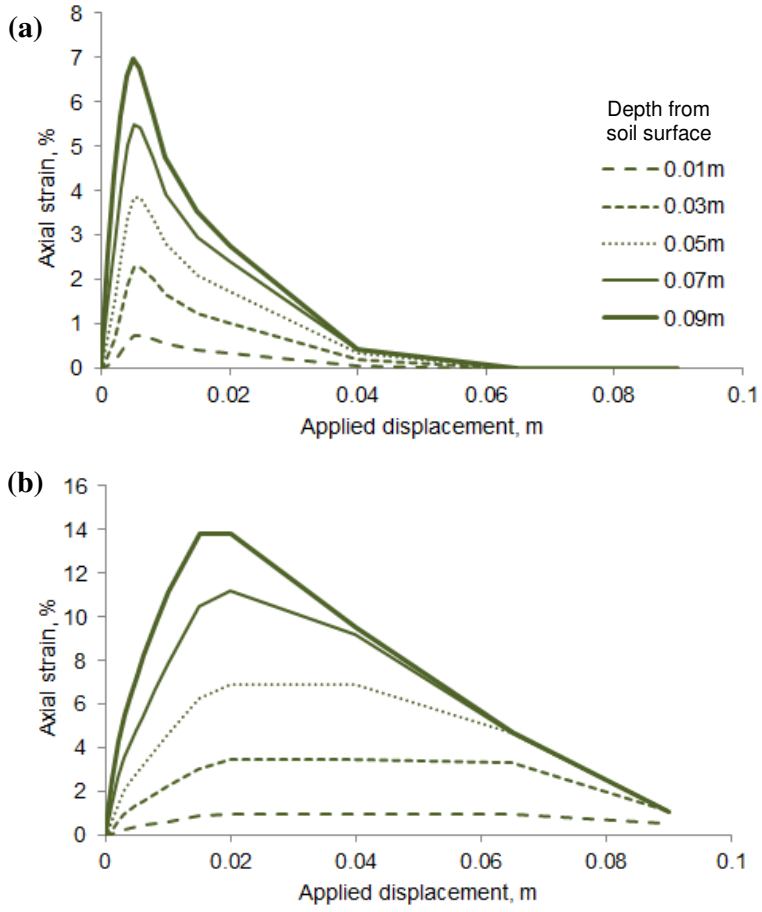

Figure 4.33: Numerical modelling of the development in strain in each element within a rubber root being uprooted from (a) dry soil and (b) wet soil.

4.5.2 Sensitivity of modelling to changes in parameters

Having established the success of this modelling technique for predicting the laboratory uprooting tests, its sensitivity to system changes was analysed. This was carried out using spring sets 3F (Rubber/Empirical/Bonly/Losing), 4C (Rubber/Empirical/Conly/Cont.) and 4D (Rubber/Empirical/Conly/Losing), and looked at the impact of; t_{max} distribution, number of springs, root material properties and increments of applied displacement on the modelling output.

4.5.2.1 Distribution of t_{max} with depth

Estimated distributions with depth of t_{max} (dry sand) and $t_{0.005m}$ (wet sand) are shown in Figure 4.21 and are a linear best fit to the empirically derived data points. These straight line distributions suggest that the interface shear force (between the rubber root analogues and silica sand) will become zero at depths of 0.45m (dry sand) and 0.13m (wet sand). In reality, it is very unlikely that this would be the case. It is anticipated, therefore, that along the length of longer roots, a minimum value of t_{max} or $t_{0.005m}$ will be reached, following which the effects of dilatancy at low effective stress will reduce and t will begin to increase with increasing depth (as predicted by API standard calculations). Furthermore, it is possible that the values of t_{max} in dry sand, as calculated using TZCurve (Figure 4.16), are verifying this assumption through indicating a non-linear distribution with a minimum value of t_{max} at a depth of approximately 0.06m. The calculated distribution of $t_{0.005m}$ in damp sand shows only a reduction in t with depth, but it is possible that this reduction is non-linear and leads to a minimum value of $t_{0.005m}$ beyond the root tip.

Figure 4.34 shows alternative best-fit t_{max}-x and $t_{0.005m}$–x distributions, which are non-linear. As demonstrated, they provide a neater fit to the calculated t_{max}-x and $t_{0.005m}$-x data than the previously assumed linear distributions. As such, they predict both a higher interface shear force towards the soil surface and a reduced interface shear force towards the middle of the root. Furthermore, the non-linear t_{max}-x distribution in dry sand (Figure 4.34 (a)) shows minimum behaviour at a depth of 0.064m, which is the approximate point at which it intersects with the distribution suggested by API codes (when dilation is considered). The rate of increase in t_{max} with depth, however, is much larger than that suggested by API codes. Nevertheless, the API distribution fits neatly into the range of data calculated by TZCurve and it is therefore possible that on longer roots this data will tend towards and eventually match the estimated API distribution.

Figure 4.35 shows the impact of using the non-linear t_{max}-x and $t_{0.005m}$-x distributions to the output of the numerical modelling. In dry sand, the increase in interface shear force towards the root top, as estimated by the non-linear curves, results in an increase in the initial force required to uproot the root and, therefore, an improvement in the numerical modelling. Indeed, the predicted maximum uprooting force now sits at around 85% of the measured maximum uprooting force. In wet sand, the change in distribution between the linear and non-linear $t_{0.005m}$-x curves is much less significant, but does hold a slightly beneficial impact towards the later stages of pull-out.

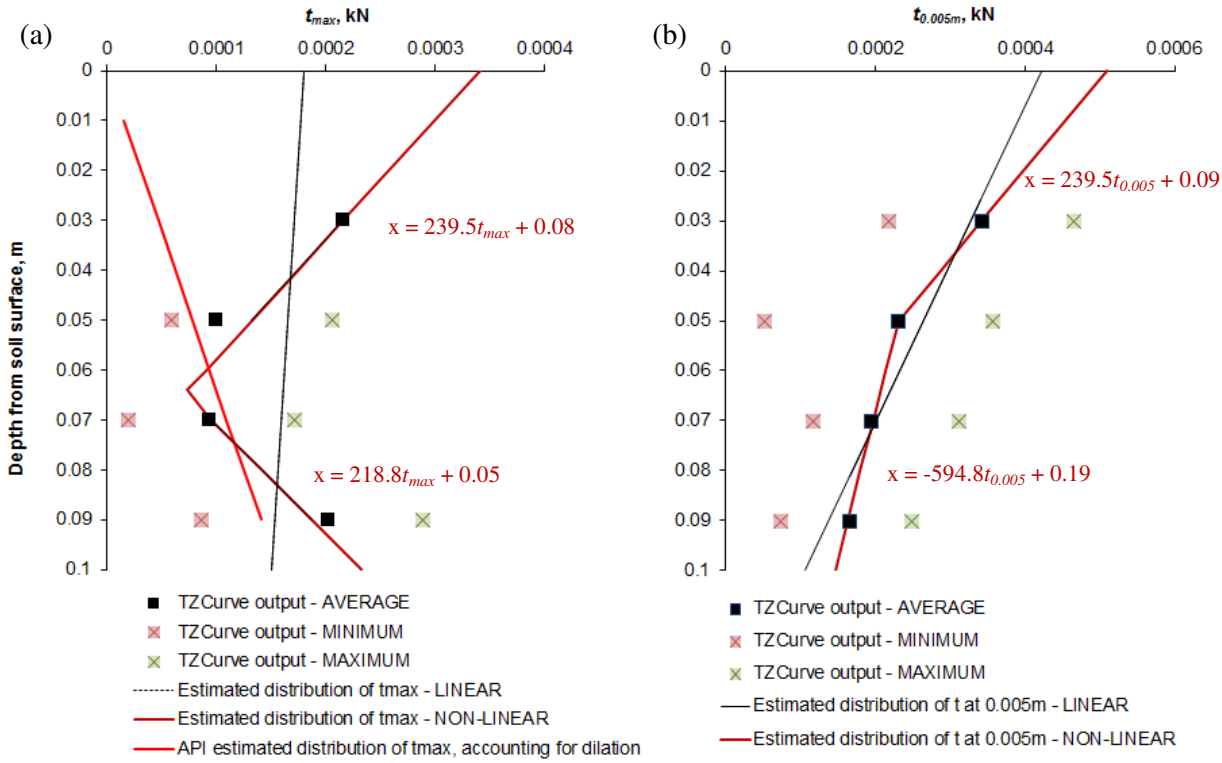

Figure 4.34: Estimated non-linear distributions of (a) t_{max} and (b) $t_{0.005m}$, for rubber root analogues in dry and damp sand, respectively.

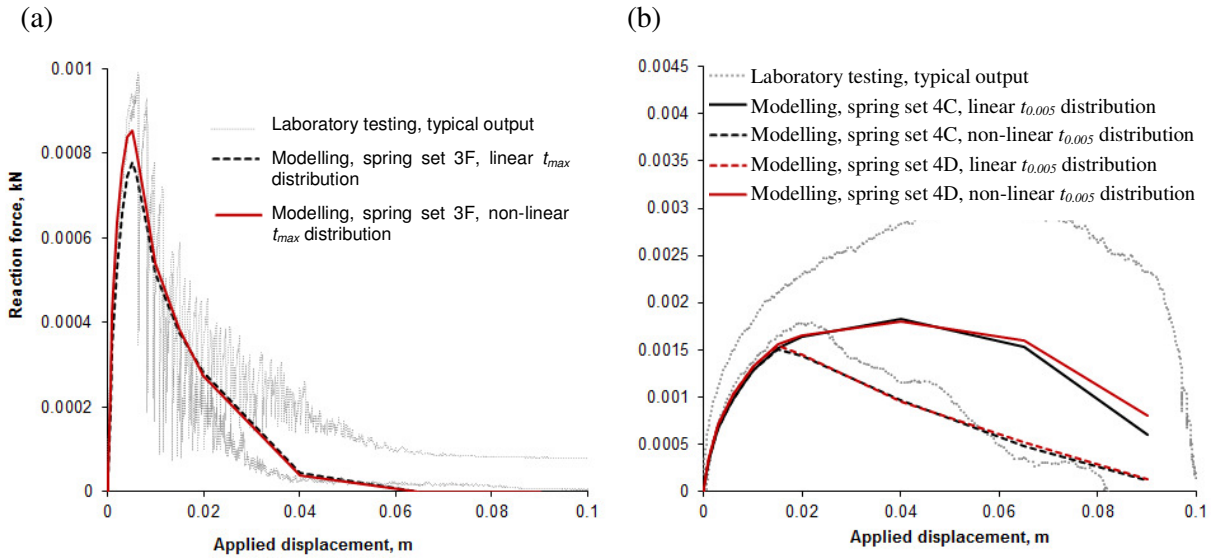

Figure 4.35: Predicted pull-out force displacement data as predicted using linear and non-linear distributions of (a) t_{max} and (b) $t_{0.005m}$, for roots in dry and wet soil, respectively.

.

The assumed distribution of t_{max} or $t_{0.005m}$ is therefore important in defining the numerical model. The initial over-simplification of these distributions resulted in a reduction in the predicted force required to uproot a rubber root from dry sand. While the improved, and more complex, t_{max}-x and $t_{0.005m}$-x distributions improve this data, however, the force-displacement curves still slightly underestimate uprooting behaviour.

4.5.2.2 Number of springs

Increasing the number of springs, or soil root slices, within the proposed calculation model should improve its accuracy. Each spring models the average soil root interaction that acts over a length of root and, as this length reduces, the approximation becomes increasingly accurate. Using the non-linear distributions of t_{max} and $t_{0.005m}$ with depth, Figure 4.36 shows the effect of doubling (10 springs) and quadrupling (20 springs) the number of element-spring sets within the model to the assumed approximation of soil root interaction acting along the length of the root. As demonstrated, the use of 5 springs provides a crude estimate of the t_{max} and $t_{0.005m}$ distributions with depth and this is improved by increasing number of springs. Additionally, this figure shows that the magnitude of the t_{max} and $t_{0.005m}$ distributions reduce as the number of springs is increased. This is because the scale of these

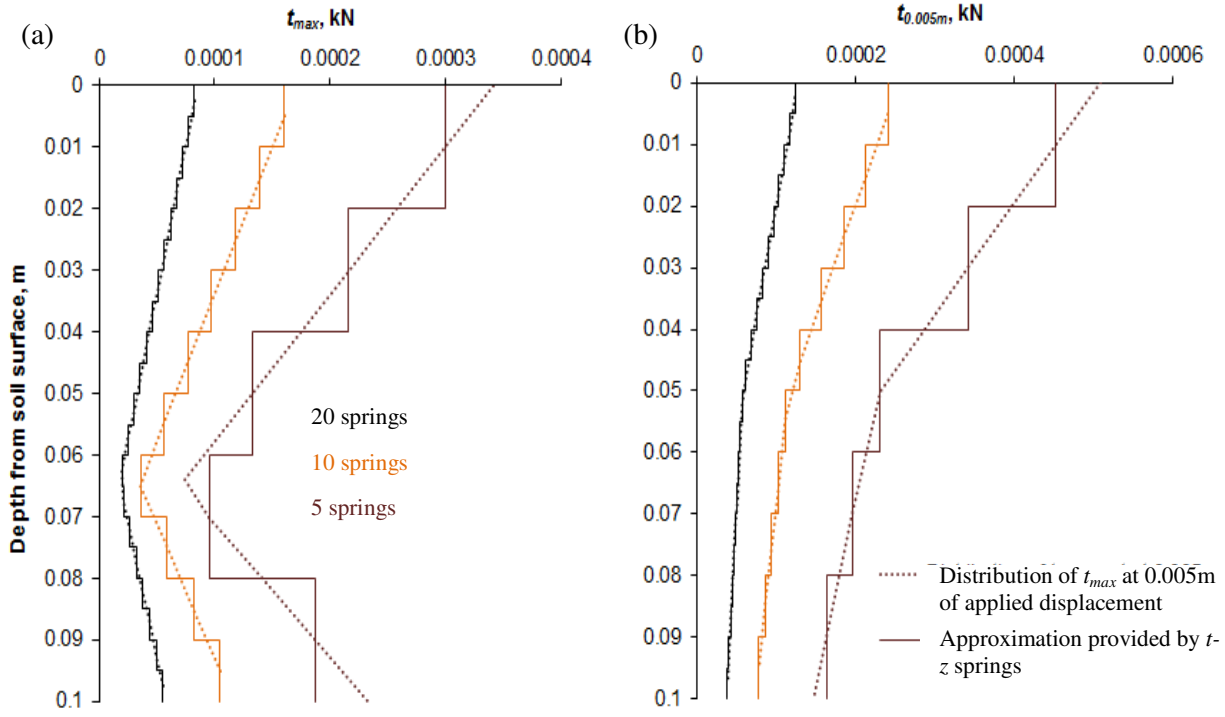

Figure 4.36: Approximation of (a) t_{max} and (b) $t_{0.005m}$ as a function of the number of element-spring sets used in the modelling technique.

distributions is a function of element length such that, regardless of the number of springs, the sum of their forces will be identical, as expected.

Figure 4.37 shows the variation in force-displacement behaviour, as predicted by the numerical models, as the number of springs is increased from 5 to 20. As demonstrated, it has little impact. The selected number of element-spring sets is therefore somewhat immeterial in the development of a numerical model. It should be noted, however, that increasing the complexity of the soil root system (for example, considering a root with a varying cross section) may result in a more dramatic relationship between the number of springs and the output provided by the numerical modelling technique.

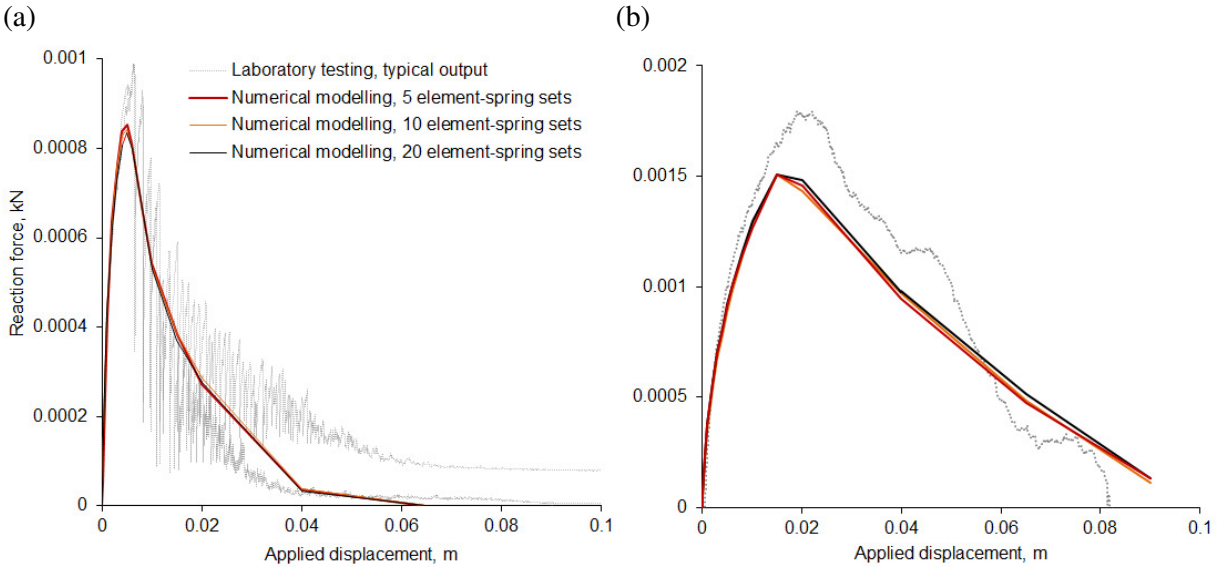

Figure 4.37: Comparison of force displacement curves when using 5, 10 and 20 element spring sets for rubber roots being uprooted from (a) dry sand and (b) damp sand.

4.5.2.3 Root properties

Recognising that the material properties of roots may be more difficult to accurately define than those of analogue materials, Figures 4.38 and 4.39 show the effect of changing Poisson's ratio and Young's modulus to the predicted force-displacement data that is obtained from numerical simulations, using spring set 3F (Rubber/Empirical/Bonly/Losing).

In Figure 4.38, it is demonstrated that both reducing and increasing Poisson's ratio from the actual value of 0.490 does not result in a significant change to the predicted force-displacement relationship, though it does marginally alter the peak pull-out force via an apparent linear relationship (see Figure

4.38 (b)). In particular, a significant 17% reduction in Poisson's ratio (from 0.480 to 0.400) results in a minimal 0.51% increase in uprooting force. This suggests that an incorrect specification of Poisson's ratio will not greatly hinder the output of a numerical analysis. The estimation of $v = 0.490$ is therefore suitable for modelling Viton rubber.

The value of Young's modulus, however, appears more significant. Figure 4.40 shows that small changes in Young's modulus can have a large impact on the magnitude of the predicted force-

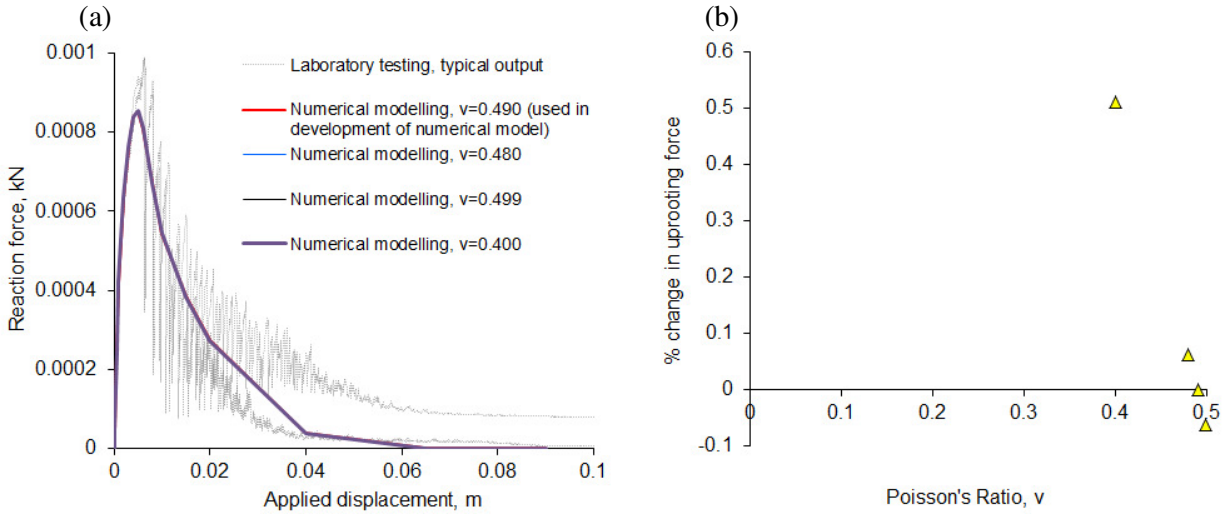

Figure 4.38: Effect of altering Poisons ratio to (a) the force-displacement data, and (b) the estimated peak pull out force (measured in % change from $v = 0.49$)

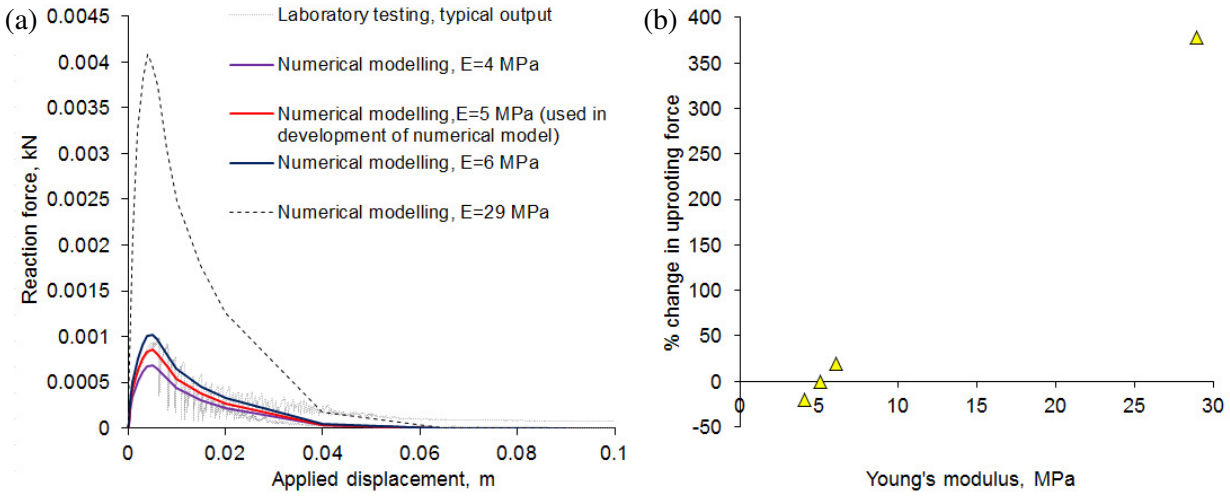

Figure 4.39: Effect of altering Young's modulus to (a) the force-displacement data and (b) the estimated peak pull out force (measured in % change from E = 5 MPa).

displacement curves, with the maximum uprooting force increasing significantly with an increasing value of Young's modulus. It should be noted, however, that failure is not incorporated into the current numerical model. In reality, it may be that increasing the material stiffness pushes the root to, or towards, failure. The increase in uprooting force with increasing Young's modulus is particularly poignant when modelling complex non-linear elastic materials, such as rubber or plant roots. Specifying a Young's modulus of 29MPa, as reported by Mickovski *et al.* (2007; 2010) to describe Viton at high strains, resulted in a 379% increase in the estimated force required to uproot the root analogue. This is a large overestimation of the resisting capacity of the soil root system. Given the complex material properties of plant roots and the reliance of the modelling technique on an appropriate value of Young's modulus, it may be necessary to consider the material properties of the root as a function of strain.

The definition of the root properties is therefore an important aspect of the proposed calculation model.

4.5.2.4 Increments of applied displacement

The increments of applied displacement that are specified in the Abaqus/CAE loading steps define the points during an uprooting simulation at which the spring and root properties are calculated. During the numerical modelling in this chapter, the majority of these increments were concentrated between 0 and 0.01m of applied displacement. This was chosen in order to provide an increase in data surrounding the peak pull out behaviour. Figure 4.40 shows that an arbitrary uniform distribution of applied displacement, which does not take account of the peak uprooting behaviour, can result in an incomplete data set, which could appear to be an incorrect data set. This model considered increments of 0.01m and the output, therefore, excludes the peak pull out behaviour. Maintaining an arbitrary uniform distribution of applied displacement, but increasing the number of loading steps and reducing the displacement intervals will improve the modelling but will increase the preparation and analyses time. It is important when setting up a numerical model to carefully plan the input parameters.

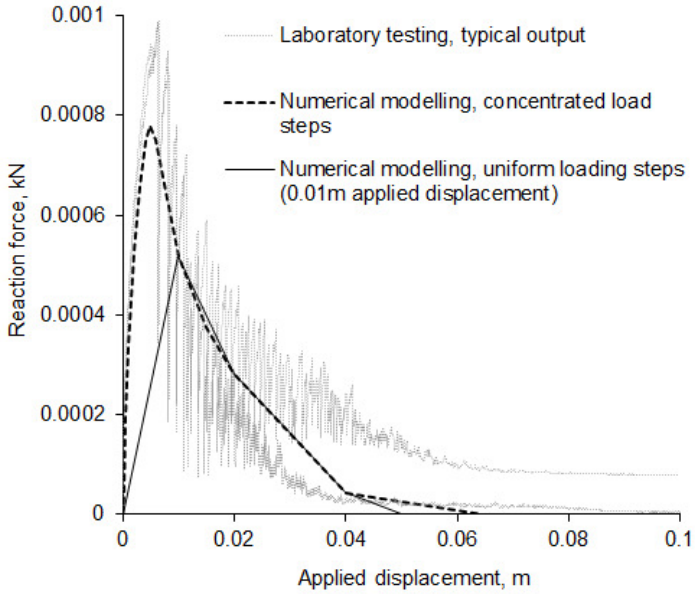

Figure 4.40: Effect of altering the specified loading steps in Abaqus/CAE.

4.5.3 Summary

In this Chapter, a calculation model linking root displacement to the applied force during uprooting was proposed and used to predict the reaction of a root to pull-out. Uprooting tests on analogue roots sitting in sand, in combination with particle image velocimetry, allowed the displacement of the root during uprooting to be measured. These displacements (z) were then linked to the consequent interface shear force (t) acting along the length of the root through application of the t-z calculation model, commonly used for pile design in geotechnical engineering. In this model, the root is represented as a beam and the soil as a series of non-linear springs acting along the beams length. The stiffness of each spring is characterised by a t-z curve. For comparison, t-z curves were also estimated using API pile design codes. Using Abaqus/CAE and t-z modelling, a finite element model of a simplified soil root system was devised and used to simulate a further series of uprooting tests. This modelling technique was shown to successfully translate from pile design applications to the study of soil root interaction, provided that the t-z behaviour can be accurately characterised.

Definition of the t-z springs was found to significantly impact the success of the numerical modelling, with small changes in spring properties resulting in large changes in the predicted force-displacement behaviour. Moreover, the springs proposed by API standards were found to be unsuitable for applications at low stress levels with flexible inclusions. Using first principles, suitable curves for modelling the uprooting of rubber root analogues from dry and wet sand were realised, and are

presented in Table 4.2. These require only the maximum shear resistance force (t_{max}) on the element to be calculated.

The Abaqus/CAE numerical model was found to be relatively insensitive to the number of element-spring sets selected, but poor or incorrect definition of the material properties and/or loading steps significantly impaired its success. The reliance of the model on root material properties is significant for modelling plant roots, which have complex non-linear behaviour. The results of this study suggest that future research effort should focus on characterising t_{max} as a function of the confining stress and developing simplified models for its prediction.

Chapter 5 Shear box tests on soil permeated with model plant roots

5.1 Introduction

In situ and laboratory shear tests on soil permeated with plant roots are widely used in soil bioengineering. They quantify the mechanical contribution of a root system to a soil's shear resistance and assess the stress deformation behaviour within the soil root matrix (*e.g. Abe and Ziemer, 1991; Wu and Watson, 1998; Operstein and Frydman, 2000; Fan and Chen, 2010*). In the laboratory, these experiments typically involve placing a root reinforced soil sample in a shear box, applying a vertical load to its surface and recording the force required to displace either it's upper or lower half horizontally in direct shear. Through repeating this test three, or more, times under different vertical loads, it is possible to calculate the relationship between the shear and confining stresses and thus to employ the Mohr-Coulomb failure criterion to estimate the angle of friction, ϕ', and apparent cohesion, c', of the sample. Through comparing these values to those obtained from testing fallow samples, the contribution of a root system to the properties of a soil can be estimated. This is known as the $\Delta c'$ approach and is widely adopted in practice (*e.g. Schmidt et al., 2001; Chok et al., 2004; Der-Guey et al., 2011*). A handful of studies, however, suggest that when considering granular soils under drained conditions, the increase in soil capacity would be better represented as an increase in ϕ', due to additional dilation, i.e. $\Delta\phi'$ (*e.g. Graf et al., 2009; Diambra et al., 2010*). This would suggest that the root contribution is dependent on the confining stress in the soil rather than stress independent ($\Delta c'$). The force-displacement curves generated for fallow and reinforced samples can be plotted and used to provide visualisation of any changes in shearing behaviour.

As with uprooting tests, the behaviour of a root soil system during shear loading can be assessed once testing has been completed, through excavating and examining the roots. This, however, does not provide an accurate account of soil root interaction, as it does not show how the root and soil deforms during loading. In this study, therefore, a series of cross section-front shear box tests (which provide a window into the soil root system during loading) were performed and used, in conjunction with GeoPIV analysis, to measure and analyse the deformation behaviour (i.e. failure mechanism) of various soil root systems during loading. Following the success of the *t-z* predictive tool that was developed to measure uprooting in Chapter 4, it was assumed that the *p-y* calculation model (introduced in Section 2.3.2) may be suitable for representing this behaviour. Alongside these cross

section-front tests, a series of full section-centre shear box tests were carried out in order to assess the $\Delta c'$ and $\Delta \phi'$ approaches.

This chapter reports a series of shear box experiments that were carried out in both full section-centre and cross section-front form. Full section-centre tests were used to explore the effects of changing root material properties, root area ratio and root length to the shearing behaviour of a root permeated soil sample, while cross section-front tests were used to (i) examine root and soil movement during shearing and (ii) determine the suitability of the cross section-front output for use in a *p-y* calculation model.

5.2 Material selection and sample set up

For comparability, the shear box experiments were designed in line with the Mickovski *et al.* (2007; 2010) uprooting tests (see Chapter 3). As such, the soil root systems were composed of either full or half tap root analogues within silica sand. Unlike the uprooting tests, however, there was a disparity between the full section-centre and cross section-front apparatus, as evidenced in Figures 5.1 and 5.2. This was done in order to focus each test series around its key purpose, which was providing visualisation of the root soil system and providing accurate force-displacement data, for the cross section-front and full section-centre modelling, respectively.

The cross section shear box, shown in Figure 5.1, was designed around the uprooting soil box, which provided an excellent window into the soil root system during loading. It was composed of aluminium walls, with Perspex viewing panels to the front and back. The lower box had dimensions of 300 x 160 x 50 mm, while the upper box has dimensions of 180 x 50 x 50 mm. This provided a shear plane at a depth of 50mm and allowed a maximum lateral displacement of 110mm (past which, sand would empty from the upper box). Loading was applied to the upper box.

A standard shear box, with a diameter of 100mm and a depth of 50mm, was selected for the full section-centre testing and was used in conjunction with a standard shear box table (Wykeham Farrance Engineering Ltd, UK). This apparatus provided a large shearing area, which allowed a variety of root distributions to be incorporated into the soil samples. Its depth, however, significantly restricted the maximum root length. Extensions were therefore added to increase its depth to 150mm (see Figure 5.2), with the shear plane located at a 50mm depth (in order to correspond to the cross section-front apparatus). As shown in Figure 5.2, the ledge of the shear box allowed a maximum

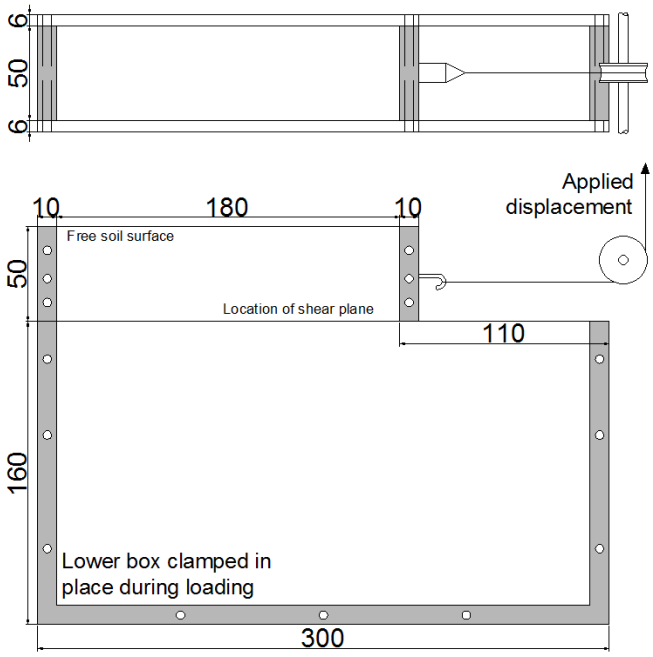

Figure 5.1: Experimental set up used for cross sectional shear box tests (dimensions in mm).

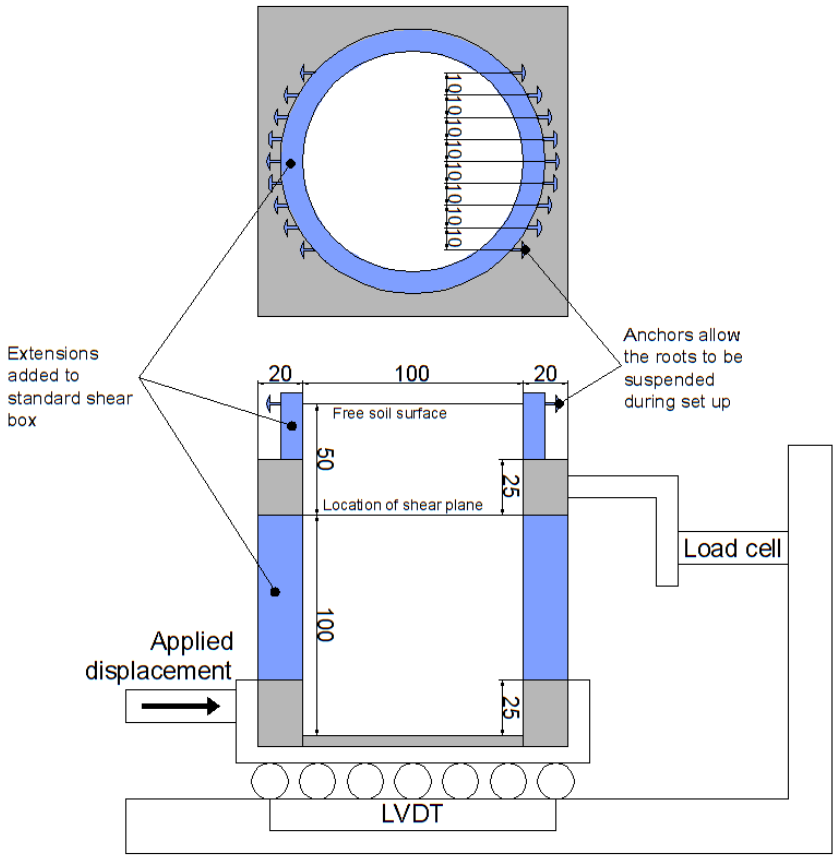

Figure 5.2: Experimental set up used for traditional shear box tests (dimensions in mm).

lateral displacement of 20mm, which was applied to the lower box. Anchors were provided around the rim of the upper box to locate the root analogues during sample set up (this is explained in Figure 5.6).

To accommodate sample preparation, using each apparatus, the upper and lower shear boxes were clamped together and adhesive tape was applied around the shear plane prior to sample pluviation. This minimised: (i) sample disruption and (ii) the number of sand particles becoming trapped between the upper and lower shear boxes. The clamps and adhesive tape were removed prior to testing. Additionally, friction between the upper and lower boxes was reduced by applying silicon grease (sourced from RS Components, Corby, UK) to the split in the box. No drainage was required in the boxes, as only dry samples were tested. All experiments considered a free soil surface, with no normal load.

5.2.1 Root material properties

The materials selected for the root analogues were similar to those outlined in Chapter 3. In particular, Viton O-ring rubber (sourced from RS components, Corby, UK) was employed to model flexible roots, while wood was employed to model stiff roots. In the shear box tests, however, the chosen wood was Beech (sourced from Woodwork Craft Supplies, UK) rather than Linden. This followed a requirement to maintain a consistent diameter between the rubber and wooden samples, such that the effects of root stiffness alone could be measured, and the consequent difficulty in sourcing Linden wood of appropriate sizes. Beech dowels and Viton rubber could both be sourced with a 3.0mm diameter, which provided a reasonable scale for modelling roots (*Preti and Diadrossich, 2009*). To model the effects of different root diameters, and to provide consistency with the uprooting tests, lengths of 1.6mm diameter Viton rubber were also considered (see Figure 5.3).

The properties of the Viton O-ring rubber are outlined in Chapter 3. The properties of the Beech dowels were measured in the laboratory using a three point bend test, in which 100mm lengths of Beech were placed across two supports, spaced at 50mm, and subjected to a transverse point load at the centre (see Figure 5.4 (a)). This force was supplied by an Instron 5966 loading frame, with a 1kN ± 0.2 mN load cell, under strain control at a displacement rate of 1mm/minute. The consequent forces and cross-head displacements were measured (see Figure 5.4 (b)). The tests were continued until past the point of failure, allowing the maximum bending moment, M_{max}; maximum shear force, V_{max}, and; Bending modulus, E_B to be calculated through Equations 5.1, 5.2 and 5.3, respectively:

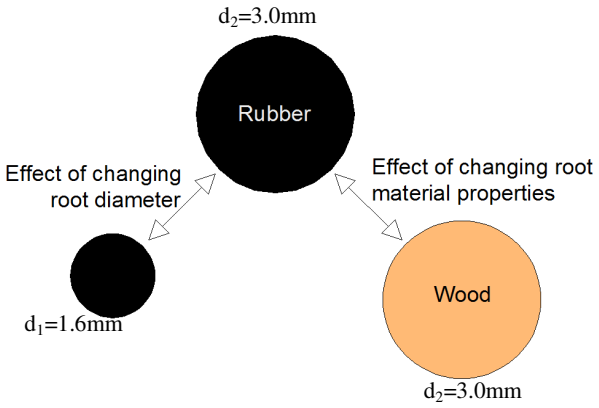

Figure 5.3: Variation in root diameter and material properties.

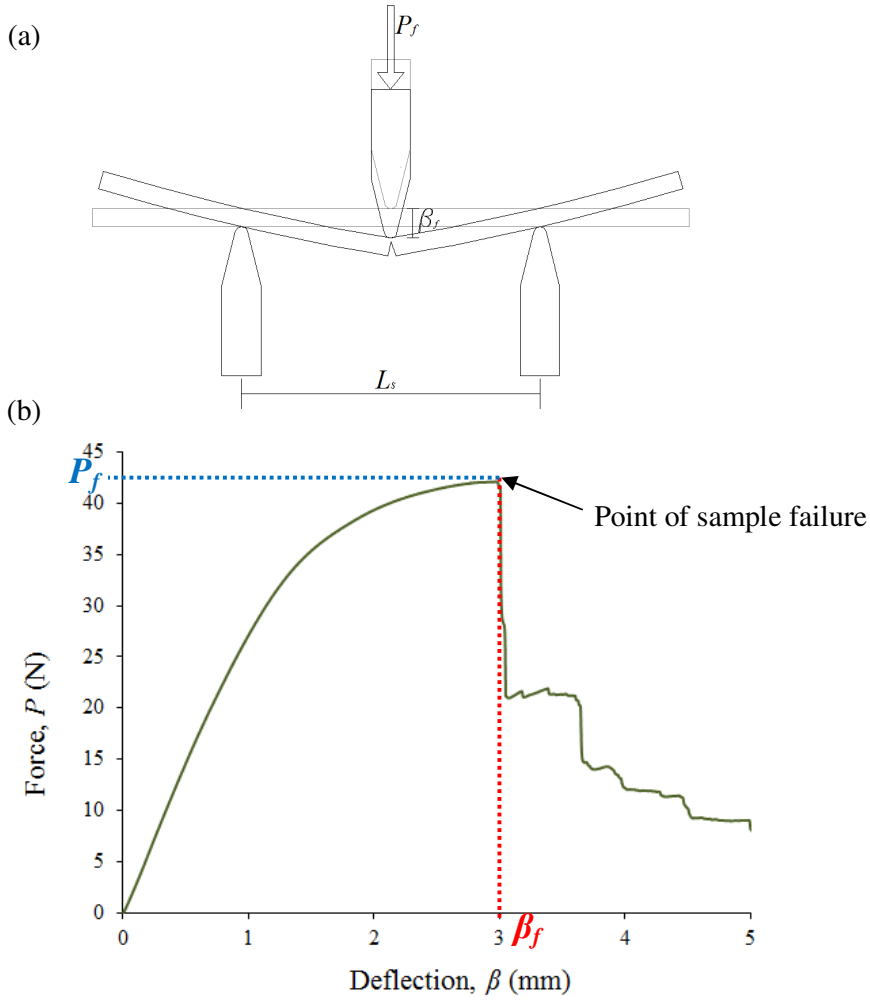

Figure 5.4: Typical output of three point bend tests on Beech wood samples, (a) schematic of test set up and loading, L_s = 50mm, (b) Typical force-deflection curve for Beech wood.

$$M_{\max} = \frac{P_f \cdot L_s}{4} \quad \text{Eq 5.1}$$

$$V_{\max} = \frac{P_f}{2} \quad \text{Eq 5.2}$$

$$E_B = \frac{P_f \cdot L_s^{\,3}}{48 \cdot I_s \cdot \beta_f} \quad \text{Eq 5.3}$$

$$I_s = \frac{\pi}{64} \cdot D_s^{\,4} \quad \text{Eq 5.3 (a)}$$

Where; $\boldsymbol{M_{max}}$ is the maximum bending moment; $\boldsymbol{P_f}$ is the load applied to the centre of the sample at failure; $\boldsymbol{L_s}$ is the length of the sample (between the supports); $\boldsymbol{V_{max}}$ is the maximum shear force; $\boldsymbol{E_B}$ is the Young's modulus of the sample; $\boldsymbol{I_s}$ is the second moment of area of the sample; $\boldsymbol{\beta_f}$ is the deflection at failure, and; $\boldsymbol{D_s}$ is the diameter of the sample.

The maximum bending moment and shear force were recorded to be 525Nmm and 21N, respectively, and indicate the maximum capacity of the root analogues when subjected to lateral loading. The Bending modulus was calculated to be 9003 MPa.

5.2.2 Root preparation

A variety of tap root systems, with varying material properties, diameters and lengths were considered in the full section-centre and cross section-front shear box tests. Both test series employed roots with a length of 150mm (composed of 3.0mm diameter wood and rubber, and 1.6mm diameter rubber root analogues) and 100mm (1.6mm diameter rubber analogues only). The latter of these is comparable to the tap root analogues used in the uprooting tests. Additionally, the full section-centre shear box experiments employed roots with a length of 65mm (1.6mm diameter rubber analogues), in order to model roots with poor anchorage into the stable soil mass. These root architectures are shown in Figure 5.5.

The half and full root analogues were created as described in Chapter 3 (Section 3.4.2), but with the addition of a 10 x 10 mm disk at their top (see Figures 5.5 and 5.6). This provided surface anchorage, preventing the upper root from pulling into the soil during lateral loading (*Sonnenberg, 2008*). Such a feature is provided in nature by both (i) the lateral branching present at the soil surface and (ii) the aboveground portion of the plant (*Sonnenberg, 2008*). The disks were fabricated from 2.5mm thick sheets of cardboard and were glued to the top of the root using a cyanoacrylate adhesive.

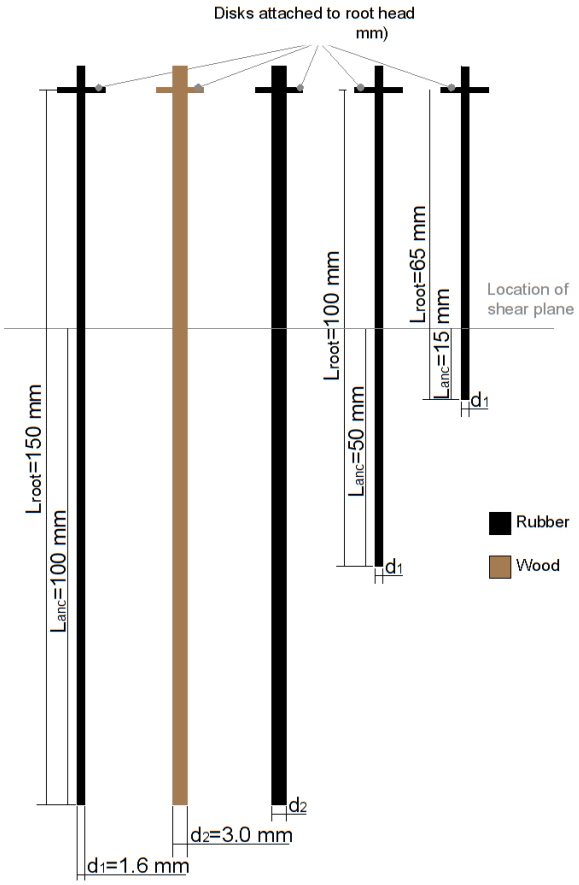

Figure 5.5: Root architecture considered in shear box testing.

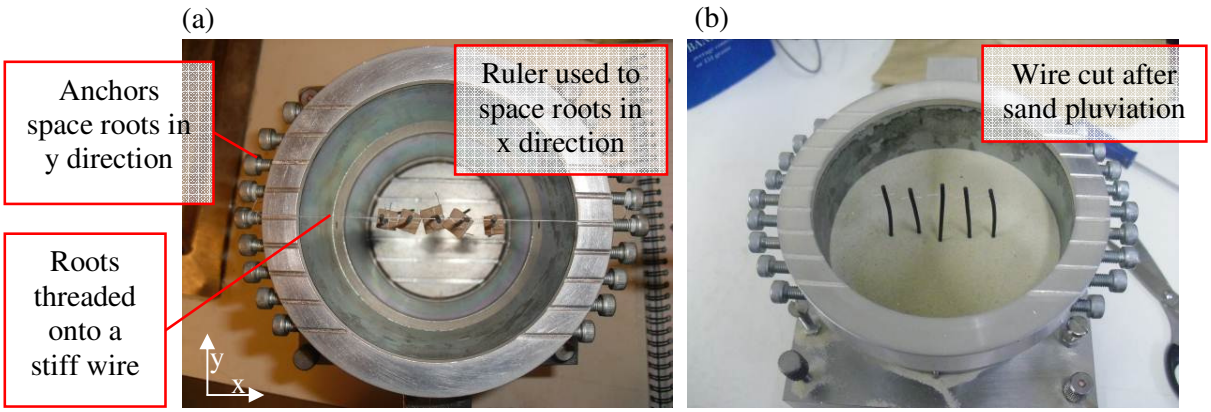

Figure 5.6: Sample set up in full section-centre tests. (a) locating the root analogues, (b) sand pluviated around root analogues.

As with the cross section-front uprooting tests, each half root analogue was located at the edge of the cross sectional apparatus (i.e. flush with the Perspex viewing panel), using silicon grease to hold it in place. The full root analogues, on the other hand, were threaded onto a stiff wire and suspended in

the centre of the traditional apparatus, as shown in Figure 5.6 (a). The ends of the wires were fastened to anchors, which were provided around the rim of the upper shear box. The anchors allowed the root (or line of roots) on each wire to be specifically positioned in the y direction. The root spacing in the x direction was specified using a ruler. The sand was then pluviated around the root analogues, after which the wires were cut (see Figure 5.6 (b)). This method of sample set up worked very well, particularly when working with wooden root analogues. With rubber root analogues, however, it was limited to accurately controlling the root distribution at the height of the wires only. Below this point, the root spacing was influenced by the desire of the rubber to bend.

5.2.2.1 Root number and distribution

The cross section-front shear box tests considered single tap root analogues only, as demonstrated in Figure 5.7, while the full section-centre tests considered soil root systems with varying: (i) number of roots, or RAR, and (ii) root distribution, as shown in Figure 5.8. The number of root analogues in each of the full section-centre experiments was carefully selected in order to represent RAR values

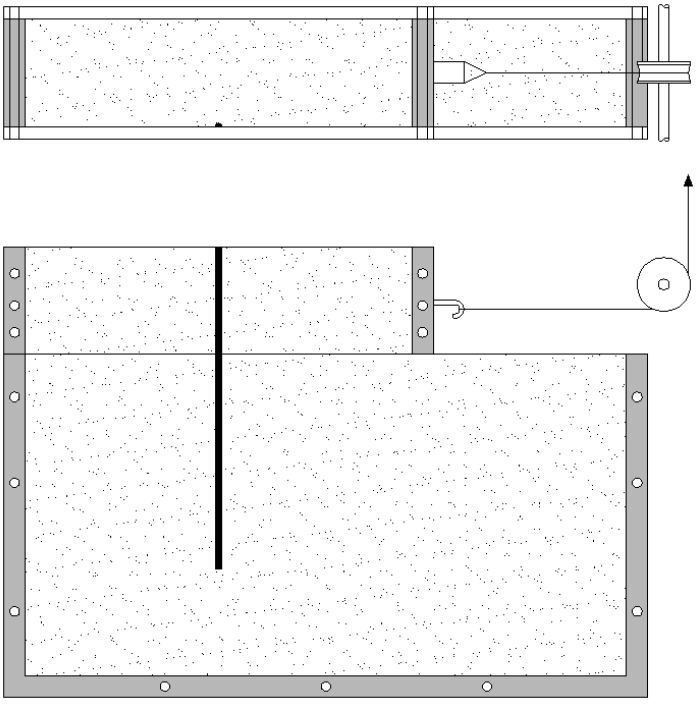

Figure 5.7: Plan and side-elevation schematic of soil root system considered in the cross section-front shear box test series. Root length varies between 150mm and 100mm, root diameter varies between 3.0mm and 1.6mm, and root material properties vary from Viton rubber to Beech wood.

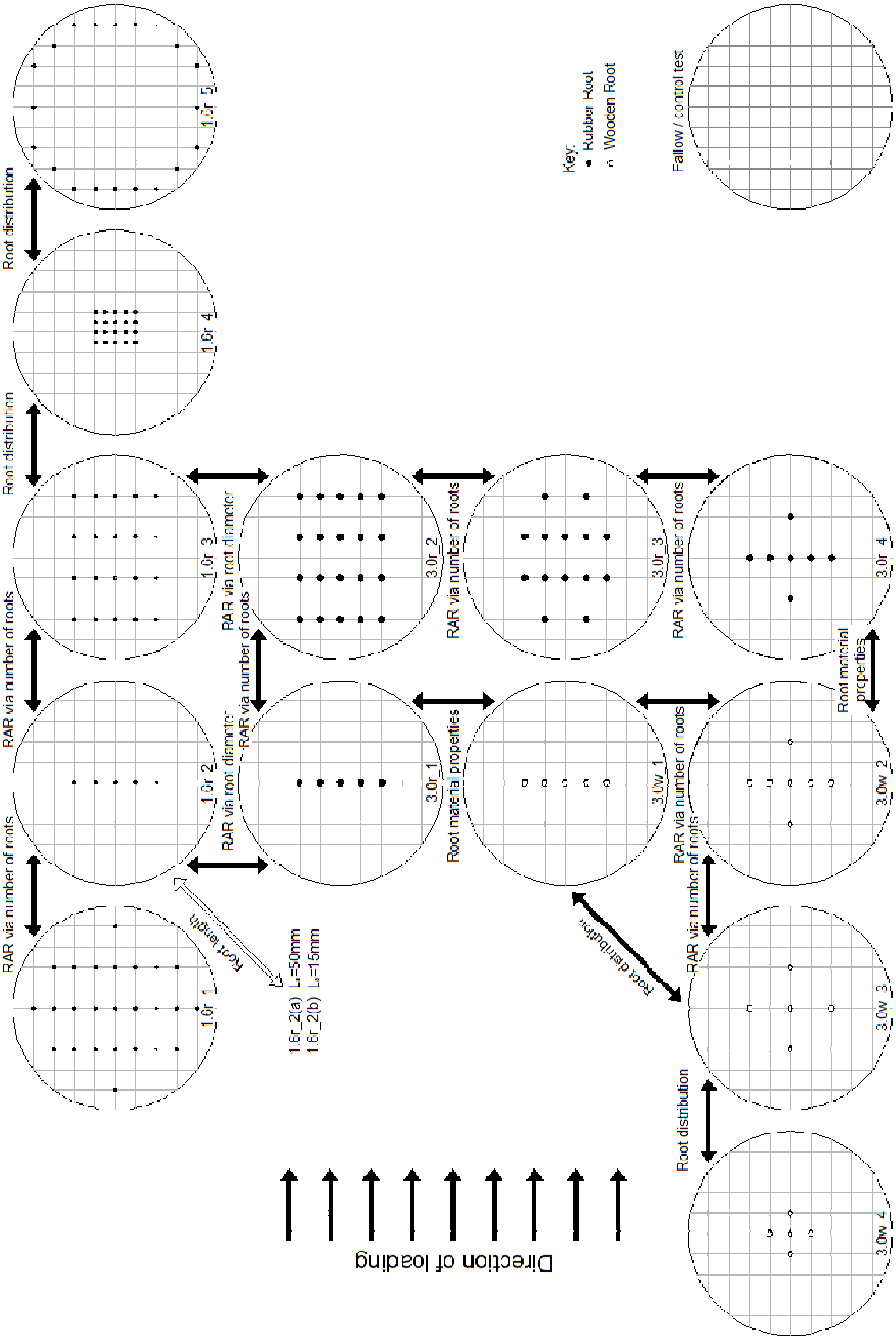

Figure 5.8: Root set up considered in the full section-centre shear box experiments, showing variations in root distribution, number of roots, root material properties and root length. Diagram also indicates the labelling that was used for each shear box test. All roots have a length of 150mm unless otherwise stated

that are expected in the field. Moreover, the root spacing was engineered such as to minimise any 'group effects' and thus allow the later employment of foundation design techniques to predict the shear box experiments. Some control tests were also carried out in order to assess group (test 1.6r_4) and edge effects (test 1.6r_5), see Figure 5.8, as were fallow tests. Each test was repeated 3 times.

Table 5.1 displays a selection of RAR values that were measured through a number of studies and consider different plant species and different depths from the soil's surface. Highlighted in red are the values of RAR that were measured at a depth of 0.05m, which is the depth of the slip plane in the laboratory shear box tests of this study. These values suggest that, at a depth of 0.05m, the root area ratio can be expected to fall between 0.23% and 0.9%, regardless of plant type. This table shows no clear link between plant type (i.e. grass, herb, tree or shrub) and expected RAR. The respective largest and smallest recorded RAR values are 1% at a depth of 0.5m and 0.03% at a depth of 0.2m. Table 5.2 relates the number of root analogues used in the full section-centre test series (see Figure 5.8) to the consequent RAR values that are present at the slip planes (where RAR is calculated using Equation 2.21). As demonstrated, the majority of these values fit within the range that was measured for real roots, either at or slightly out-with a depth of 0.05m. The use of 14 or 20 x 3.0mm diameter roots, however, provides RAR values that are slightly higher than would be expected in reality. The selection of these root numbers, however, allowed the impact of changing RAR through root diameter and number of roots to be further scrutinised (see Figure 5.8).

It is generally agreed that a centre to centre pile spacing of $6 \cdot D_{pile}$ in the direction of loading and $3 \cdot D_{pile}$ in the direction perpendicular to loading is sufficient to render group effects insignificant in the lateral loading of piles in sand, where D_{pile} is the pile diameter (*Prakash, 1962; Franke, 1988; Lieng, 1989; Mokwa, 1999*). The root analogues, therefore, were distributed in the shear box with a spacing not less than 20mm in the direction of loading ($12.5 \cdot D_{root}$ and $6.67 \cdot D_{root}$, for 1.6mm and 3.0mm diameter roots, respectively) and 10mm in the direction perpendicular to loading ($6.25 \cdot D_{root}$ and $3.33 \cdot D_{root}$, for 1.6mm and 3.0mm diameter roots, respectively). The flexibility of the rubber root analogues, however, made it difficult to guarantee that they sat vertically in the shear box as the sand was packed around them (see Figure 5.6). It is therefore likely that, in a number of tests, the specified spacing was reduced to below $3 \cdot D_{pile}$ or $6 \cdot D_{pile}$ at some point along the root's length. To assess the impact of group effects, 20 x 1.6mm diameter rubber root analogues and 5 x 3.0mm diameter wooden root analogues were tested with respective spacing's of 5mm and 10mm in both directions (see Figure 5.8). Finally, as a number of the root distributions considered roots that were located relatively close

to the edge of the shear box, a distribution with 20 x 1.6mm diameter roots located around the perimeter of the shear box was considered to investigate edge effects within the apparatus.

Table 5.1: Root Area Ratio (RAR) measurements for different plants at different depths

Depth, m	*RAR (%)*	*Species*	*Plant Type*	*Study*	*Year*
0.05	0.3-0.5	*Vetiver grass*	Grass	Jasper-Focks and Algera	2006
0.05	0.66	*Lygeum spartum*	Grass	De Beats	2008
0.05	0.23	*Limonium supinum*	Herb	De Beats	2008
0.05	0.81	*Retama sphaerocarpa*	Tree/Shrub	De Beats	2008
0.05	0.4-0.9	*Spanish broom*	Tree/Shrub	Preti and Giadrossich	2009
0.15	0.48	*Atriplex halimus*	Tree/Shrub	De Beats	2008
0.15	0.33	*Salsola genistoides*	Tree/Shrub	De Beats	2008
0.2	0.03-0.07	*Vetiveria zizanioides*	Grass	Mickovski and Van Beek	2009
0.5	1.00	*White oak*	Tree/Shrub	Danjon *et al.*	2008
Between 0-1	0.07-0.24	*Norway spruce*	Tree/Shrub	Bischetti *et al.*	2009
Between 0-1	0.09-0.36	*European Beech*	Tree/Shrub	Bischetti *et al.*	2009
Between 0-1	0.07-0.15	*European Larch*	Tree/Shrub	Bischetti *et al.*	2009
Average between 0-1	0.15	*Sweet chestnut*	Tree/Shrub	Bischetti *et al.*	2009

Red text indicates RAR values that correspond to the slip plane location in the laboratory shear box tests

Table 5.2: RAR considered in full section-centre laboratory shear box tests

Root diameter, mm	**Number of roots Root Area Ratio (RAR) %**				
	5	**7**	**14**	**20**	**25**
1.6	0.128	--	--	0.512	0.640
3.0	0.450	0.630	1.260	1.800	---

Green text indicates tests with higher RAR than the species shown in Table 5.1.

5.2.3 Soil material properties and preparation

The soil was selected and prepared as described in Sections 3.2.3 and 3.2.4.

5.3 Experimental set up

An Instron 5544 (Instron, High Wycombe, UK), with a 1kN load cell, was used to perform the cross section-front shear box tests. The load cell was accurate to 0.2 mN. The prepared shear boxes were placed in a frame, which was bolted in place on the Instron platform (as shown in Figure 5.9) and

accommodated: (i) a runner system, to minimise the separation of the upper and lower boxes due to soil dilation and ensure that the upper box moves in plane (but without constraining the surface of the soil), (ii) a stopper, to prevent the lower box from moving with the upper box, and (iii) a pulley, to transform the vertical Instron displacement to a horizontal translation of the upper frame, via a wire with high tensile stiffness. The Instron was programmed to displace at a rate of 3mm/minute and to continually record the force and cross head displacements. The behaviour of the root and soil was

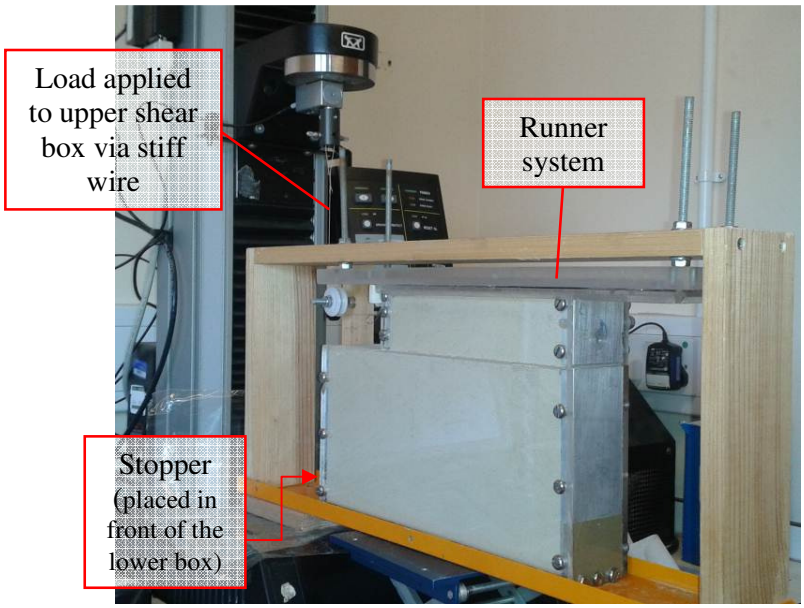

Figure 5.9: Experimental set up used for cross sectional shear box test

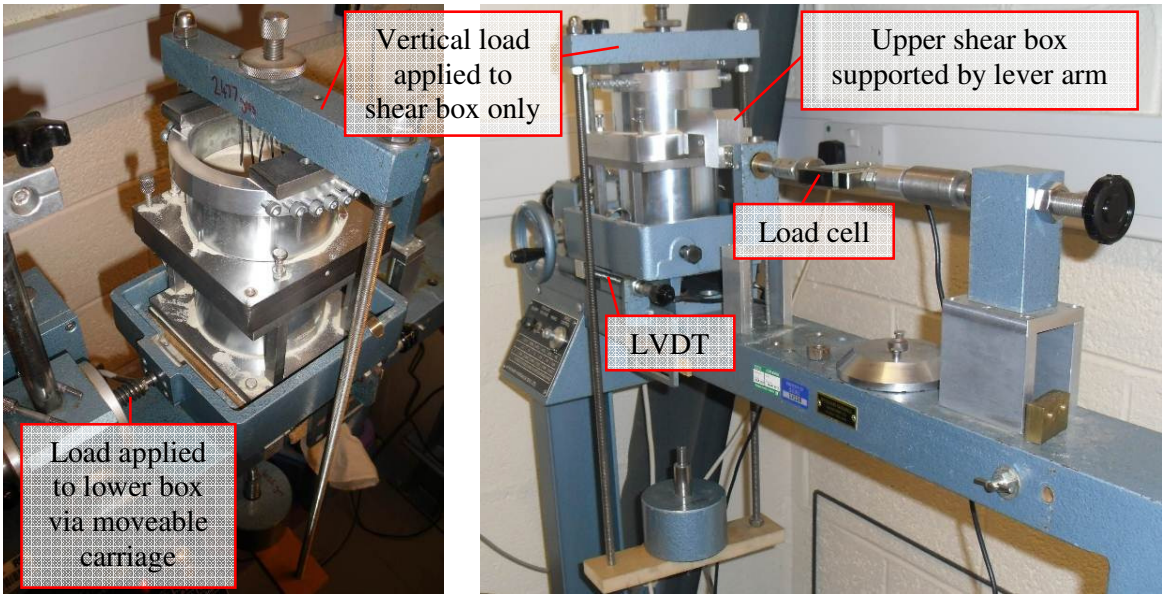

Figure 5.10: Experimental set up used for traditional shear box test

recorded at 10 second intervals using a Nikon D300 camera coupled with a Bowen light diffuser (allowing 0.5mm displacement between images). As with the cross section-front uprooting tests described in Chapter 3, image capture was controlled remotely using a timer. The consequent images had a resolution of 2848 x 4288 pixels and thus had a quality that was far superior to that achieved by Mickovski *et al.* (2005-07).

The full section-centre shear box tests were executed using a standard shear box table (Wykeham Farrance Engineering Ltd, Uk), shown in Figure 5.10. When in place, the lower half of the shear box was clamped in a moveable carriage (which was supported by ball bearings to minimise friction), while the upper half was held in place by a lever arm connected to a load cell. An LVDT was used to trace the displacement of the moveable carriage. A weight of 6.5kg was applied to the rim of the shear box (without contacting the soil) in order to minimise any separation, due to soil dilation, of the upper and lower boxes during testing. The apparatus was programmed to displace the lower shear box at a rate of 2mm/minute. The load cell and LVDT were connected to a computer and, using LabView on a Windows XP platform, were used to record the force and displacement during loading.

In both experimental set ups, the clamps (connecting the upper and lower boxes) remained in place until just before the loading commenced. This ensured minimal sample disruption.

5.4 Results and discussion

5.4.1 Full section-centre

Each of the full section-centre shear box tests was repeated three times, allowing repeatability to be observed. Figure 5.11 shows the repeat force-displacement data that was gathered from four of the fourteen test groups. As demonstrated, each test group has very similar data. This confirms the success of the sample set up technique, and suggests that the reduced control experienced while spacing rubber roots (as a result of rubber flexibility) is not significant. A typical force-displacement curve from each test group only will be considered hereon.

Figure 5.12 compares the force required to shear a variety of root-reinforced soil samples (engineered to experience minimal group effects) to the force required to shear a fallow sample, confirming the benefits of root inclusions. As demonstrated, samples with a small root area ratio (RAR) provide a noticeable increase in soil shear strength and this is improved by increasing RAR and root stiffness, and by reducing root diameter (provided that the RAR remains constant). This additional strength, however, has a complex relationship with RAR and root material properties.

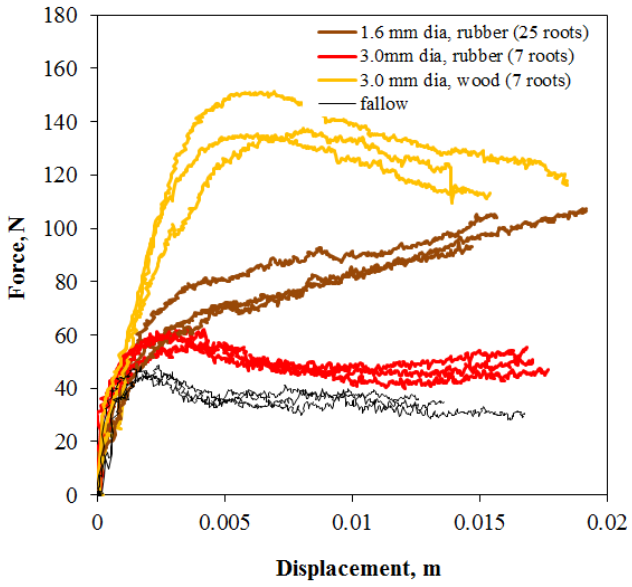

Figure 5.11: Force-displacement data for the repeat tests of four full section-centre test groups, (i) 25 x 1.6 mm diameter rubber, (ii) 7 x 3.0 mm diameter rubber, (iii) 7 x 3.0 mm diameter wood, and (iv) fallow.

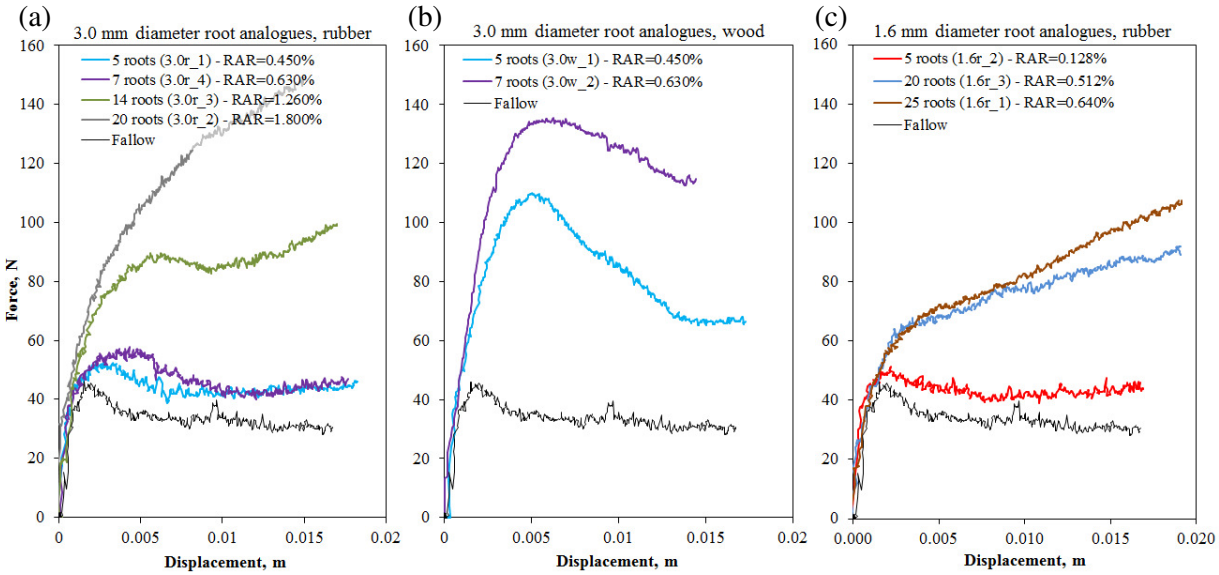

Figure 5.12: Typical force required to displace root reinforced soil samples with RAR values ranging from 0 (fallow) to 1.8%. Each root analogue has a length of 150mm and a diameter of (a) 3.0mm - Viton (b) 3.0mm - Beech (c) 1.6mm - Viton.

Figures 5.12 (a) and (c) suggest that RAR has a significant influence on the additional strength that is provided by rubber root analogues, not only by a change in size but by a change in the force-displacement behaviour. In particular, a small RAR increases the peak and reduces the post peak loss of soil shear strength, while a large RAR provides additional strength that grows as displacement progresses. The force-dispalcement curve generated using a large RAR is therefore quite unlike that of the fallow sample. It is, instead, reminiscent of the force-displacement behaviour that is generated when applying an axial load to Viton rubber. This suggests that, when the RAR is small, the behaviour of the sample is dominated by the material properties of the soil and, when the RAR increases, it is gradually more and more dominated by the tensile properties of the roots. This is typical of fibre reinforced materials (e.g. *Gray and Sotir, 1996*). Figure 5.12 (a) further shows that an intermediate value of RAR creates a sample that is influenced by the material properties of both the root and the soil during shearing (see curve 3.0r_3). In this case, the force-displacement curve shows peak behaviour followed by a steadily increasing shearing force. The RAR of this sample, which utilises 3.0mm diameter rubber root analogues, is 1.26%. This is much larger than the 0.512% value that is required to achieve fibre dominated behaviour when considering 1.6mm diameter rubber root analogues (see curve 1.6r_3). This may imply that it is the number of roots and/or root diameter, rather than the RAR, which initiates the change in force-displacement behaviour.

Root stiffness is also shown to be a significant factor in defining the contribution of root reinforcement to the shear capacity of a soil. Figures 5.12 (a) and (b) illustrate that the additional

shear strength provided by wooden root analogue systems is significantly larger than that provided by equivalent rubber root analogue systems. The wooden roots offer an increase in the peak and residual soil shear strengths, as well as an increase in the displacement required to mobilise peak shear behaviour. The post-peak loss of strength in the wooden root-reinforced samples, however, is much larger than that experienced by the fallow and rubber root-reinforced samples. Interestingly, soil root systems with 7 x 3mm diameter wooden root analogues (3.0w_2) and 25 x 1.6 mm diameter rubber root analogues (1.6r_1) (which vary in root material properties and diameter but share a similar RAR) provide very similar reinforcement towards 0.02m of applied displacement. It is suggested, however, that after 0.02m, the additional strength provided by the rubber root analogues will deliver superior reinforcement. This could suggest that optimum reinforcement may be achieved through combining woody and flexible root systems within a soil mass. However, when comparing the curves of 7 x 3mm diameter wooden root analogues (3.0w_2) and 7 x 3mm rubber root analogues (3.0r_4) (both of which have an identical RAR, root diameter and root distribution), the wooden root analogues provide an unequivocally improved addition to shear resistance, regardless of applied displacement. This confirms the importance of considering the number, diameter and distribution of roots rather than the RAR alone. By combining stiff and flexible roots, the benefits of increased stiffness and strength at small displacement (provided by the stiffer roots) may be coupled with hardening behaviour at larger displacements, maximising the shear strength contribution of the roots over pre- and post-failure stages.

Figure 5.13 shows the force required to shear soil samples that are reinforced with 5 x 1.6mm diameter rubber root analogues, anchored to depths of either 15mm, 50mm or 100mm into the stable soil mass (i.e. into the lower shear box). As demonstrated, reducing the anchorage length from 100mm to 50mm has very little impact on the force-displacement behaviour of the root permeated soil sample. Further reducing the anchor length to 15mm, however, provides a significant loss in the reinforcing capacity of the root analogues. While their initial capacity is akin to that of the longer roots, they provide no, or insignificant, reinforcement when the soil reaches a critical state (this occurs at a displacement of approximately 0.005m, when the fallow force-displacement curve stabilises). It is likely that this is the result of an insufficient contact area between the soil and the length of root that is anchored into the stable soil mass, leading to insufficient friction between the two materials and consequent slippage (insufficient pull-out resistance). When deformations (and therefore any axial forces in the root) are small, this friction is sufficient to lock the lower root in place and thus mobilise a tensile stress at the shear plane, which helps to increase the capacity of the

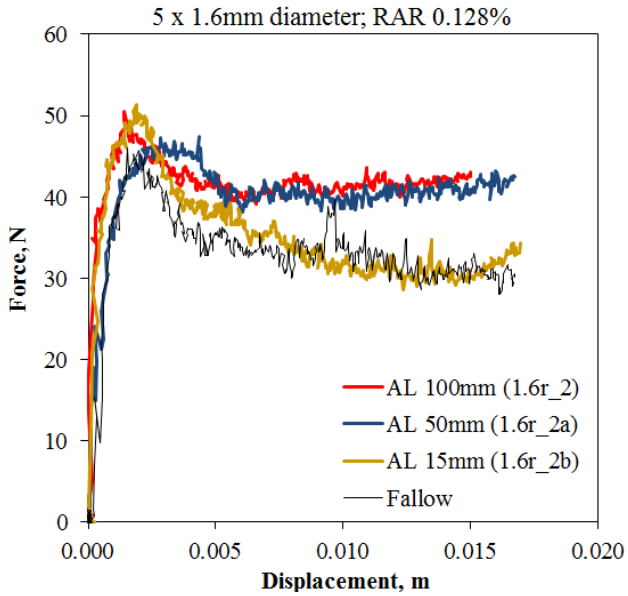

Figure 5.13: Effect of changing root anchor length (AL) to shear force of a root permeated soil sample.

soil system. As deformation continues, however, the tensile stress quickly exceeds the friction that acts between the soil and root and, therefore, causes the lower section of root to pull from the lower soil mass, rather than continuing to stretch and provide reinforcement. This is confirmed by Gray and Sotir (1996), who state that every root has a critical confining stress that needs to be met if it is to remain anchored during shearing. Furthermore, they state that the required critical stress increases as the aspect ratio of the root (length ÷ diameter) reduces.

The impact of altering the distribution of roots across the shear plane, whilst maintaining a constant RAR, is shown in Figure 5.14. As expected, the shear capacity of the soil root system is sensitive to changes in root spacing, with a smaller spacing leading to a smaller capacity. This phenomenon is well understood, is well documented in the context of pile foundation design and informed the selection of root spacing in the experimental set up (see Section 5.2.2.1). In pile design applications, the loss of individual pile efficiency due to pile-soil-pile interaction (shadowing) is accounted for by means of a reduction factor, known as a p-multiplier (p_m). This factor can be calculated at a given spacing, s, through the following equation (*e.g. Mokwa, 1999; Abbas, 2012*);

$$p_m = \frac{\eta_g}{\eta_i \cdot n} \qquad \text{Eq 5.4}$$

Where: $\boldsymbol{p_m}$ is the p-multiplier; $\boldsymbol{\eta_g}$ is the efficiency of the pile group; $\boldsymbol{\eta_i}$ is the efficiency of an isolated pile, and; $\boldsymbol{n}$ is the number of piles in the pile group.

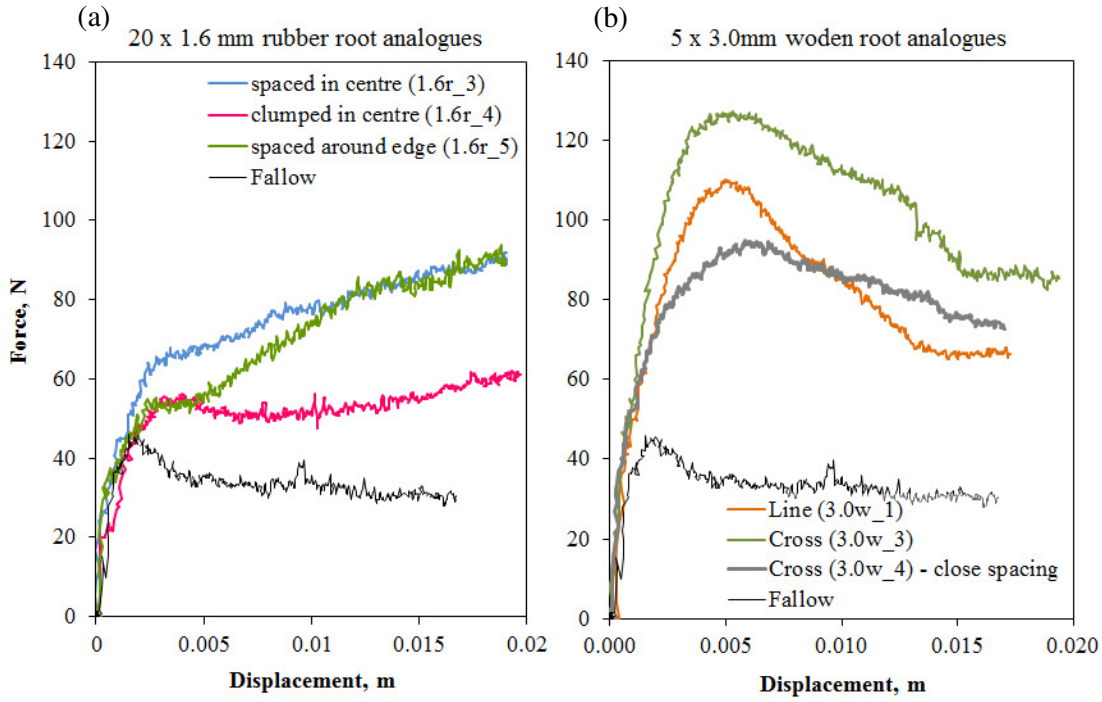

Figure 5.14: Effect of changing root distribution to the shear force of a root permeated soil sample (a) 1.6mm diameter rubber root analogues, (b) 3.0mm diameter wooden root analogues.

If it is assumed that: (i) the efficiency of the pile group, η_g, is equal to $\eta_i \cdot n$ when the roots are spaced in the centre of the shear box (test groups 1.6r_3 and 3.0w_3), and (ii) the applied lateral load is evenly distributed amongst the roots, then Equation 5.4 can be employed to estimate suitable p_m values for the root analogues in tests with closely spaced roots (1.6r_4 and 3.0w_4). Moreover, as root spacing is a known factor, these values can be used in order to estimate a relationship between root spacing and p_m. This, however, requires additional assumptions. That is: (iii) shadowing only takes effect when s falls below $6 \cdot D_{root}$ (*Mokwa, 1999*) and (iv) the relationship between s and p_m is linear. Using this framework, Figure 5.15 shows the s-p_m relationships for the 3.0mm diameter wooden and 1.6mm diameter rubber root analogues, where s is considered as a function of D_{root}. As demonstrated, there is very little difference between these two relationships, indicating that p_m (i.e. root efficiency) is insensitive to changes in material properties. This finding is consistent with pile foundation research (*e.g. Das, 2010*), however, the scale of the relationships are not. Brown *et al.* (1988) suggest that the efficiency of a pile is a function of its location within the group, and provide recommended p_m values, as a function of location, for piles sitting in very dense sand with a spacing/diameter (s/D_{pile}) value of 3. They suggest that the leading row of piles (that sitting farthest from the applied load) have an efficiency of 0.8 and this reduces respectively to 0.4 and 0.3 through

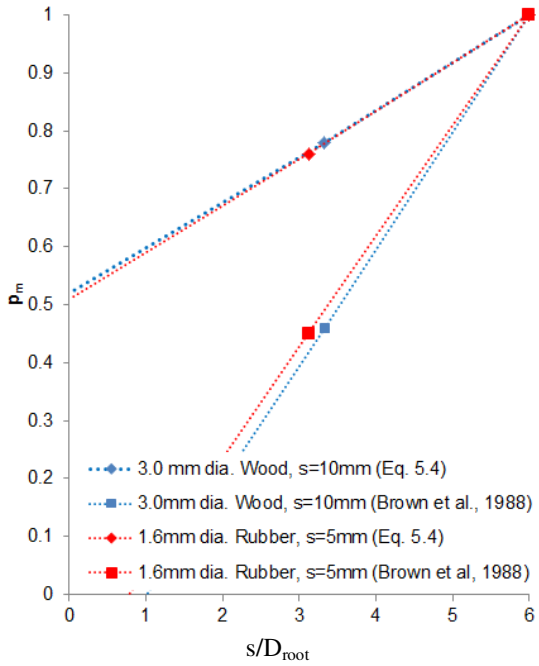

Figure 5.15: Relationship between p-multiplier and root spacing.

rows 2 and 3. Any remaining rows are considered to have a p_m value of 0.3. Considering the root distributions in tests 1.6r_4 and 3.0w_4 (see Figure 5.8), the Brown *et al.* (1988) pile efficiency values and Equation 5.5, overall p_m values of 0.45 (1.6r_4) and 0.46 (3.0w_4) were calculated. Using these values, estimated p_m-s/D_{root} distributions were established, as before.

$$p_{mT} = \frac{p_{m1} \cdot n_1 + p_{m2} \cdot n_2 + p_{m3+} \cdot n_{3+}}{n_T} \qquad \text{Eq 5.5}$$

Where: $\boldsymbol{p_{mT}}$ is the overall p-multiplier; $\boldsymbol{p_{m1}}$ is 0.8; $\boldsymbol{p_{m2}}$ is 0.4; $\boldsymbol{p_{m3+}}$ is 0.3; $\boldsymbol{n_1}$ is the number of roots in row 1; $\boldsymbol{n_2}$ is the number of roots in row 2; $\boldsymbol{n_{3+}}$ is the number of roots in rows 3 through to *i*, where *i* is the final row of roots; $\boldsymbol{n_T}$ is the total number of roots.

Figure 5.15 shows that the Brown *et al.* (1988) technique significantly underestimates the overall efficiency of the root groups. This could be because the scale and material properties of roots are so different from those of piles. Given that the wooden and rubber root analogues bracket the material properties of real roots, however, it is unlikely that changes in root material properties will impact the p_m-s/D_{root} relationship that was estimated using the shear box tests and Equation 5.4. Interestingly, the Brown *et al.* (1988) model suggests that root distribution is the most prevalent factor in defining the relationship between p_m and s/D_{root}. The importance of this factor is confirmed in Figure 5.14 (b), which shows that a group of 5 roots sitting in a line perpendicular to loading provides a lower

additional shear strength than that provided by a group of 5 roots sitting in a cross. This can be attributed to the stronger shape of a cross, providing both a directional and a perpendicular line of reinforcement against the applied loading, and a more even distribution of reinforcement over the shear plane. Mokwa (1999) found that, for a given spacing, a line of piles in the direction of loading will have a superior efficiency against a line of piles in the direction perpendicular to loading. Using the very different distributions provided in test groups 1.6r_4 and 3.0w_4, however, the variation of p_m with s/D_{root} was calculated to be very similar (see Figure 5.15).

In reality, it is unlikely that the spacing between plant roots, which sit in a complex soil root matrix, will be known. Root area ratio, however, is a well-documented parameter (*e.g. Gray and Sotir, 1996*) and is used in existing calculation models to estimate the contribution of a root system to a soil's shear strength (e.g. the fibre bundle model). It was decided, therefore, to establish a means of estimating an approximate representative s/D_{root} value for a rooted soil mass in terms of RAR. To achieve this, it was assumed that plant roots sit evenly spaced across the shear plane and that an average (mean) root diameter can be determined for a root system with a distribution of different root sizes (see Figure 5.16). Using the notation set out in Figure 5.16, the root area ratio can be defined as:

$$RAR = \frac{A_{RS}}{A_s} = \frac{\pi \cdot D_{root}{}^2 \cdot \mathrm{N_x} \cdot \mathrm{N_y}}{4 \cdot N_x \cdot s_x \cdot N_y \cdot s_y} = \frac{\pi \cdot D_{root}{}^2 \cdot}{4 \cdot s_x \cdot s_y} \qquad \text{Eq 5.6}$$

Equation 5.6 can be simplified further if assuming that $s_x = s_y = s$, giving;

$$RAR = \frac{\pi}{4} \cdot \left(\frac{D_{root}}{s} \right)^2 \qquad \text{Eq 5.6 (a)}$$

This equation can then be rearranged in order to estimate an approximate mean s/D_{root} value in terms of RAR;

$$\frac{s}{D_{root}} = \sqrt{\frac{\pi}{4 \cdot RAR}} \qquad \text{Eq 5.6 (b)}$$

Where: $\boldsymbol{RAR}$ is the root area ratio; $\boldsymbol{A_{RS}}$ is the total area of the roots (m^2); $\boldsymbol{A_s}$ is the area of the soil (m^2); $\boldsymbol{D_{root}}$ is the root diameter (m); $\boldsymbol{N_x}$ and $\boldsymbol{N_y}$ are the number of roots in the x and y directions,

respectively; s_x and s_x are the root spacing in the x and y directions, respectively (m); and s is the spacing in both x and y directions (m).

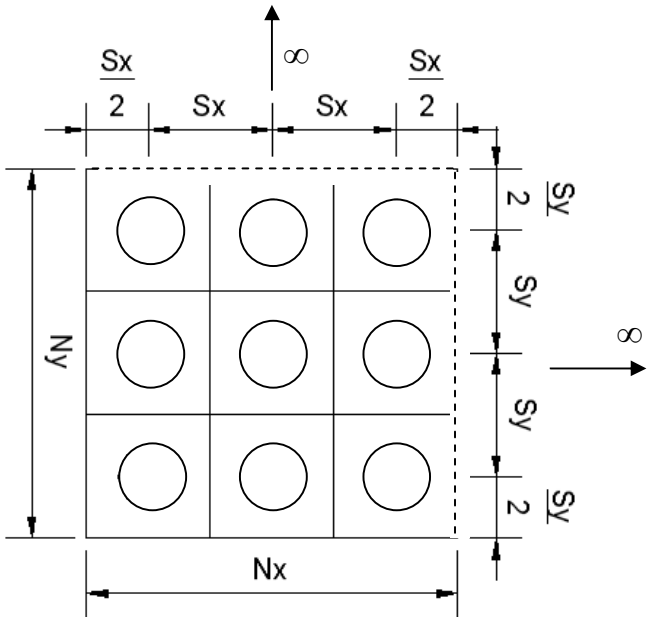

Figure 5.16: Schematic of average root spacing within a soil root matrix. Note: N_x and N_y are the number of roots in the x and y direction, respectively, and s_x and s_y are the spacing between roots in the x and y directions, respectively.

Using Equation 5.6 (b) and test 1.6r_1, which provides the most even distribution of roots across the entire shear plane; an s/D_{root} value of 11.1 was estimated. The actual s/D_{root} values for this test range between 6.25 (in direction perpendicular to loading) and 12.5 (in direction parallel to loading), deeming 11.1 to be a reasonable approximation and confirming the suitability of this model. It should be noted, however, that as 11.1 is closer to 12.5 than 6.25 the estimated s/D_{root} value is slightly biased in the direction of loading. Using Equation 5.6 (b), Figure 5.15 and the capacity of an isolated root, therefore, the capacity of each root within a root group can be estimated.

Figure 5.14 (a) further shows the impact of locating the root analogues near the perimeter of the shear box. Interestingly, this distribution provides reinforcement that is initially akin to a group of roots that are subjected to group effects and is later akin to a group of roots that are working independently. This suggests that edge effects are only significant during the early stages of loading, i.e. during the mobilisation of peak shear.

5.4.1.1 A model to define the contribution of roots to soil shear strength

The full section-centre shear box tests confirmed the ability of plant roots to increase the shear capacity of soil through mechanical interaction. This is generally accounted for in practise through adding a root cohesion factor (c_R') to the Mohr Coloumb failure criterion (see Equation 2.23). Such a term, however, fails to describe the complex nature of the additional shear capacity. It was anticipated, therefore, that this model could be improved by considering both critical and peak state shear and including the effects of soil dilation at low effective stress (ψ), a factor that was shown to be significant in defining the soil root interaction present during uprooting. This adapted model is shown in Equation 5.7 below. Note, when $\phi' = \phi_{cr}'$, $\psi = 0$.

$$\tau_s = \sigma_n' \cdot \tan(\phi' + \psi)\{+ c'\} + c_R' \qquad \text{Eq 5.7}$$

Where: $\boldsymbol{\tau_s}$ is the shear stress of the soil (kPa) ($\boldsymbol{c_R'} = 0$ when considering fallow soil); $\boldsymbol{\sigma_n'}$ is the normal effective stress (kPa); $\boldsymbol{\phi'}$ is the friction angle of the soil (°); $\boldsymbol{\psi}$ is the dilation of the soil at σ (°); $\boldsymbol{c'}$ is the soil's apparent cohesion (kPa), and; $\boldsymbol{c_R'}$ is the additional cohesion provided by the roots (kPa).

Equation 5.7 represents plant roots as some form of stress-independent binding agent that holds the soil together, but this assumption conflicts with the pull out modelling in Chapter 4, which found mechanical soil root interaction to be a purely frictional process. In addition, it is well known that dry sand, such as the silica sand used in this project, resists loading purely through friction. Indeed, sands are only considered cohesive at certain stages during wetting and drying cycles when they are partially saturated, due to the development of negative pore pressures. In design applications, however, this behaviour is seldom relevant and it is therefore the drained strength of sand (frictional response) that is typically considered (*Knappett and Craig, 2012*). This may indicate that a c_R' term would be better suited to implicate the complex hydrological impact of plant roots. It was hypothesised, therefore, that mechanical reinforcement could be better represented through considering an increase in friction, ϖ_R, within the Mohr-Coulomb soil model, as shown in Equation 5.8 below.

$$\tau_{S+R} = \sigma_n' \cdot \tan(\phi' + \psi + \varpi_R)\{+ c'\} \qquad \text{Eq 5.8}$$

Where: $\boldsymbol{\tau_{S+R}}$ is the shear stress of the root reinforced soil (kPa); $\boldsymbol{\sigma_n'}$ is the normal effective stress (kPa); $\boldsymbol{\phi'}$ is the friction angle of the soil (°); $\boldsymbol{\psi}$ is the dilation of the soil at σ (°); $\boldsymbol{\varpi_R}$ is the additional dilation caused by the presence of plant roots (kPa), and; $\boldsymbol{c'}$ is the apparent soil cohesion (kPa).

Having established these equations, a means of accurately estimating soil dilation, ψ, was considered. Figure 3.10 (b) shows the relationship between ϕ'_{pk} and ϕ'_{cr} that was measured from direct shear box tests on fallow soil samples. On the shear plane of the root permeated soil samples that were considered in this project, the normal effective stress (provided by the weight of the soil in the upper shear box) was calculated to be 0.83kPa. Using Figure 3.10 (b) ϕ_{pk}' is shown to equal to 59.1° when ϕ_{cr}' is equal to 0.83kPa. As ϕ_{pk}' is simply the sum of ϕ_{cr}' and ψ, and ϕ_{cr}' is known to be 34.0°, dilation was calculated to be 25.1°.

Having established the properties of the fallow soil (obtaining respective values for σ_n', ϕ' and ψ of 0.83 kPa, 34.0° and 25.1°), the critical and peak shear stress of each root permeated soil sample was calculated. As the reinforcement provided by rubber root analogues continued to increase with increasing displacement, as shown in Figures 5.12 (a) and (c), the critical shear stress of these samples was taken at a displacement of 20mm. This provided a conservative estimate of the maximum reinforcement that the rubber root analogues can provide, given that the response is still hardening at this point. With this information, Equations 5.7 and 5.8 can be rearranged in order to estimate suitable peak and critical values for c_R' and ϖ_R for each of the laboratory shear box tests. These values are shown in Figures 5.19 (a) and (b), respectively.

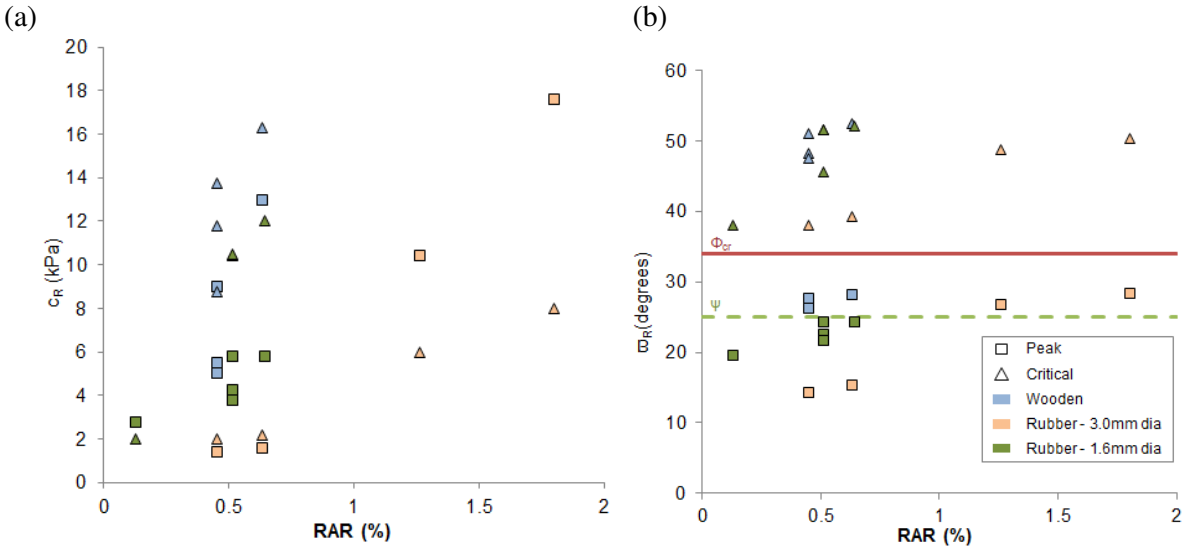

Figure 5.19: Variation of (a) c_R with RAR (Eq. 5.7), and (b) ϖ_R with RAR (Eq. 5.8).

Table 5.3: Root cohesion, calculated from direct shear box tests.

Study	*Year*	*Species*	*Depth of shear plane (m)*	*RAR, %*	c_R *(kPa)*
Comino et al†	2010	*Lotus corniculatus* (grass)	0.1	0.102 ± 0.078	10.2 ± 3.4
Comino et al	2010	*Trifolium pratense* (grass)	0.1	0.033 ± 0.017	7.6 ± 2.8
Comino et al	2010	*Medicago sativa* (grass)	0.1	0.069 ± 0.026	7.8 ± 2.3
Comino et al	2010	*Festuca pratensis* (grass)	0.1	0.059 ± 0.023	8.9 ± 1.9
Comino et al	2010	*Lolium perenne* (grass)	0.1	0.060 ± 0.040	8.6 ± 2.3
Chiaradia et al*	2012	Shrub/tree	0.65	0.05	1.87
Chiaradia et al	2012	Shrub/tree	0.65	0.01	1.45
Chiaradia et al	2012	Shrub/tree	0.65	0.06	1.80

† Roots smaller than 0.1mm were not considered in the calculation of RAR, all roots smaller than 0.7mm.
* Roots smaller than 1mm were excluded from the calculation of RAR.

As shown in Figure 5.19 (a), a positive relationship was established between root area ratio and apparent cohesion, which is confirmed in the literature (e.g: *Wu et al., 1979*). The properties of this relationship, however, depend on the roots material properties, diameter, spacing and anchorage length, with an increase in stiffness and a decrease in diameter resulting in an increased value of cohesion. This figure also shows that root cohesion during peak shear is significant, particularly when considering the wooden root analogues. The key reinforcement provided by stiff roots was shown to occur during the initial stages of shearing (see Figure 5.12 (b)). Table 5.3 shows a selection of root cohesion values (determined at critical state) taken from the literature. These have been back calculated from direct shear box tests of real plant root soil systems being sheared below the depths used in this project. Within these root soil systems, the very fine roots could not be accurately measured and were therefore withheld from the RAR calculations. Despite the differences between these tests and the tests carried out in this Thesis, the c_R' values in Table 5.3 are fairly comparable to the critical c'_R values shown in Figure 5.19. This verifies the suitability of the rubber and wooden root analogues.

Through including a c_R' term in the Mohr-Coulomb failure envelope, it is assumed that the contribution of a root to a soils shear strength is independent of depth (or normal stress). This conflicts with an earlier finding, which stated that the stress confining a root had an impact on its abiltiy to reinforce the soil (see Figure 5.13). Considering the root reinforcement as a ϖ_R term in place of the traditional c_R' term, however, corrects this. Figure 5.19 (b) shows a positive relationship between RAR and root friction. During critical state shear, the root friction is calculated to be as, if

not more, significant than the soil dilation present during peak shear. Moreover, the total friction experienced during peak shear ($\phi_{cs}'+\psi+\varpi_R$) is very similar to that experienced during critical shear ($\phi_{cs}'+\varpi_R$). This could indicate that, while plant roots do not offer a large additional strength during peak shear, they help to maintain the peak frictional properties during shear at larger strains (see Section 5.4.3.2.1).

5.4.2 Cross section-front tests

5.4.2.1 Force-displacement data

The force-displacement curves that were obtained from the cross section-front shear box tests were very variable and did not conclusively confirm that the root analogues were reinforcing the soil, as demonstrated in Figure 5.20. This can be attributed to the extremely small RAR values that were considered (namely, 0.01% and 0.04% for the 1.6mm and 3.0mm diameter root analogues, respectively), resulting in root reinforcement that was less significant than the variability created by friction in the apparatus. As a result, these data cannot be used to verify whether or not the cross section-front tests are modelling the cross section of the full section-centre tests. Given the success of the uprooting tests, however, comparability was assumed.

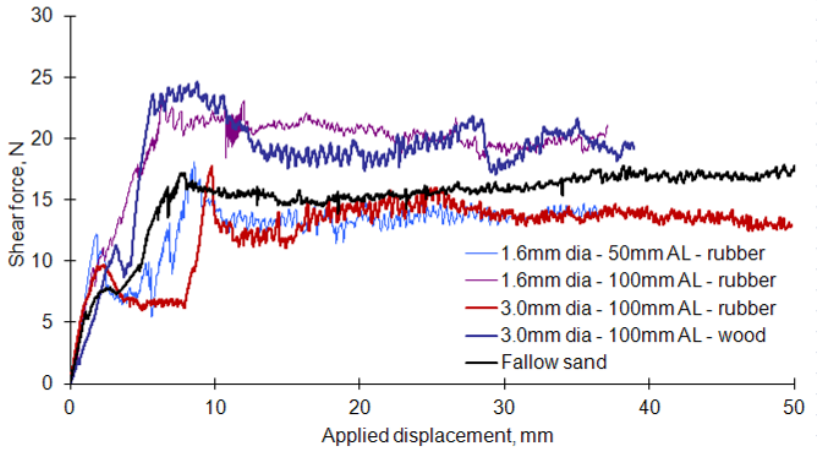

Figure 5.20: Typical force-displacement curves obtained from root reinforced and fallow cross secton-front shear box tests.

5.4.2.2 Digital images

A selection of digital images, taken during shear loading, is presented in Table 5.5. These images were analysed, as described in Section 3.6, with a view to better understand the mechanical

reinforcing process of roots and to generate input data for the development of a predictive tool. Key to this investigation was to measure; (i) the development of axial strain within the flexible root analogues, and (ii) the horizontal displacement of both the root analogues and the soil (for use in the *p-y* calculation model, see Section 2.3.2). This required each digital image series to display sufficient soil and root texture and to have a clear view of the root analogues throughout. As demonstrated in Table 5.4, this is generally the case. The observations of the uprooting images in Table 3.2, however, are also applicable here. These are: (i) rubber root analogues provide a sharp contrast against the silica sand, while wooden root analogues do not; (ii) wooden root analogues are moved out of plane during loading, and; (iii) the later images of all soil root systems succumb to 'wild' sand particles, in this case due to the extreme deformation of the system. As such, the image series of a half wooden root during shear was not suitable for a full analysis, with clear root visibility only present in the first seven images (3.5mm of applied shear displacement).

Table 5.4: Selection of images taken at the start, middle and end of the cross section-front shear box tests.

Test reference:	Image taken at the beginning of the shear box test.	Image taken towards the middle of the shear box test.	Image taken towards the end of the shear box test.
1.6r_half_1	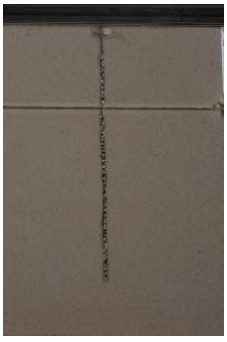		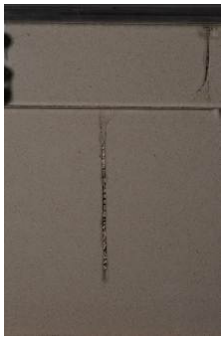
1.6r_half_2			

Test reference:	Image taken at the beginning of the shear box test.	Image taken towards the middle of the shear box test.	Image taken towards the end of the shear box test.
3.0r_half_1			
3.0w_half_1			

Additionally, these images show that there is very little separation of the upper and lower shear boxes in the directions that sit horizontally and vertically perpendicular to the direction of loading. This highlights the success of the runner system, which was put in place to ensure that the upper shear box moved in plane with its lower counterpart.

5.4.2.3 GeoPIV analysis

To measure the displacement of the root and soil during loading, GeoPIV analysis was employed. This technique is fully explained in Section 3.5 (and appropriate input parameters are detailed). The deformation of the soil root system during uprooting, however, is very different to that experienced during shearing. Suitable minimum patch and search zone sizes were therefore reassessed for this analysis. This is shown in Figure 5.21, which displays the horizontal movement of the root and soil (sitting approximately 0.04m from the root) after 25mm of applied displacement, using test group 1.6r_half_1. Figures 5.21 (a) and (b) show the impact of changing the size of the test patch (using a search zone of 30 pixels), highlighting that a patch size as small as 16 pixels will incorporate enough texture to eliminate wild vectors (as with uprooting). Figures 5.21 (c) and (d), on the other hand,

show that the same results can be obtained when the search zone is reduced to 10 pixels. As demonstrated, these findings are true of both the soil and root measurements, despite the very different textures provided.

Additionally, the significance of patch location about the shear plane was determined for the flexible roots. As shown in Table 5.4, this zone is important in the study of soil root interaction, as it houses the key horizontal deformation of the root. The view through the Perspex, however, is somewhat obstructed by the presence of the shear plane and, in the later stages of shearing, by the presence of soil particles between the root analogue and the Perspex. At the top and bottom of the deformation zone, the root develops a bend, with a curvature that increases with increasing shear force. Between these bends, the root is approximately straight. The location of the test patches, therefore, must incorporate the bends within a root in order to successfully estimate its behaviour as it crosses the shear plane. This is confirmed in Figure 5.22, which shows the horizontal deformation of a root, as measured using different patch locations, after 25mm of applied displacement. As demonstrated, excluding as little as half one bend from the GeoPIV analysis results in significant overestimation of the roots inclination as it crosses the shear plane. Including both bends, however, provides a very reasonable estimation of root deformation along the entire length of the root. Incorporating the root

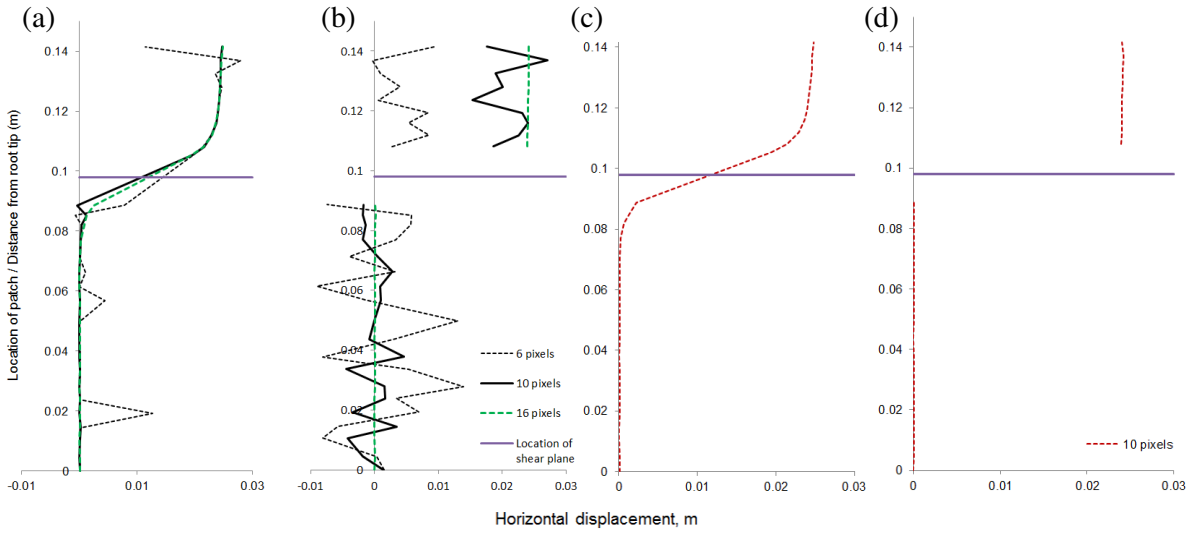

Figure 5.21: Horizontal displacement of the root ((a) and (c)) and the soil ((b) and (d)), measured using different test ((a) and (b)) and search patch ((c) and (d)) sizes. Standard search patch size = 30 pixels and standard test patch size = 24 pixels.

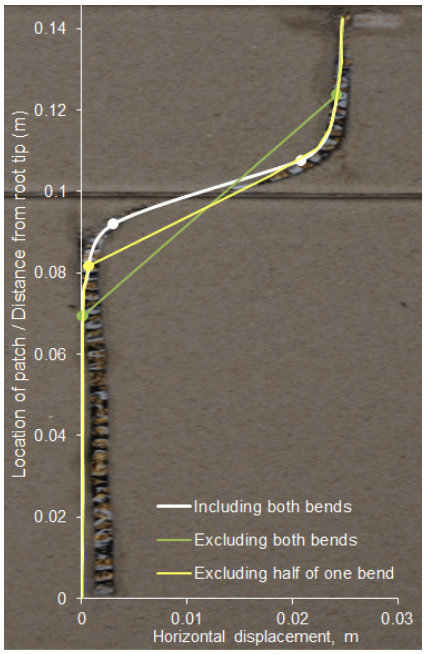

Figure 5.22: Influence of patch spacing about the shear plane on estimation of root deformation at the shear plane.

bends into the GeoPIV analysis may require some trial and error, as they are not present on the initial image, on which the test patches are seeded.

Following this analysis, the subsequent GeoPIV input controls are recommended;

- Test patches must exceed 16 pixels in size and, when placed on the root, must be limited to the root width.
- Search zones can be limited to 10 pixels in size.
- The centre to centre spacing between test patches should not exceed 100 pixels, in order to ensure sufficient deformation detail. Moreover, the patch distribution must include both of the root bends that are present at the top and bottom of the shear deformation zone.

The deformation in each of the cross section-front shear box tests was measured up to an applied displacement of 20mm, incorporating the extent of the full section-centre tests and, thus, peak behaviour. Using Equation 3.2, therefore, the number of images required in each analysis (NI) was calculated to be 40.

5.4.2.3.1 Results and discussion

Figure 5.23 shows the horizontal movement of the rubber root analogues and their surrounding soil, after 20mm of applied displacement, and of the wooden root analogue, after 0.5, 1.5, 2.5 and 3.0mm of applied displacement. While the latter provides a less extensive account of a root's reaction to lateral loading, the failure mechanism of a wooden root is clearly demonstrated and is shown to differ from that of a rubber root analogue.

Figure 5.23 (a) shows that stiff roots rotate about a point (in this case, sitting approximately 20mm from the root tip) and bend across the shear plane (indicated by the discontinuity in the upper and lower measurements) in order to accommodate loading. This is akin to the behaviour of intermediate length pile foundations (see Figure 2.25) and shows that the reinforcement is provided through the ability of the root to resist bending. The rubber root analogues, on the other hand, translate with the soil in the upper shear box and deform significantly about the shear plane, over a length that is dictated by the root's properties (in particular, its stiffness). Indeed, the 3.0mm diameter roots are shown to deform over a length of approximately 0.04m, while the 1.6mm diameter roots deform over a length of approximately 0.03m. Shewbridge and Sitar (*1985*) noted that such an increase in the width of shear zone will increase the friction angle of the soil, endorsing the use of a friction angle based method to describe root reinforcement. Reinforcement, in this case, is provided by the pull out resistance of the lower root (anchored into the stable soil mass) and the consequent development of tensile stress within the length of root crossing the shear plane. This is consistent with the Wu *et al.* (1979) model for flexible roots, as shown in Figure 5.24. Furthermore, the variation in failure mechanism between the two different root types is consistent with the observations made of the full section-centre shear box tests. In particular, the contribution of rubber roots continues to increase with increasing applied displacement (i.e. with increasing tension across the shear plane), while the wooden root analogues show a peak contribution (i.e. mobilisation of root rotation).

Figure 5.23 also shows the horizontal displacement of the soil during shearing (at a distance of approximately 0.04m from the root). As demonstrated, the soil sitting below the shear plane does not move during loading, while the soil sitting above the shear plane translates uniformly along its depth, thus confirming direct shear behaviour. As such, the relative horizontal displacement between the flexible root analogues and the silica sand (termed y), an important parameter in the p-y modelling technique, is very small. Indeed, a significant relative displacement is only present within a small volume of soil directly adjacent to the shear plane.

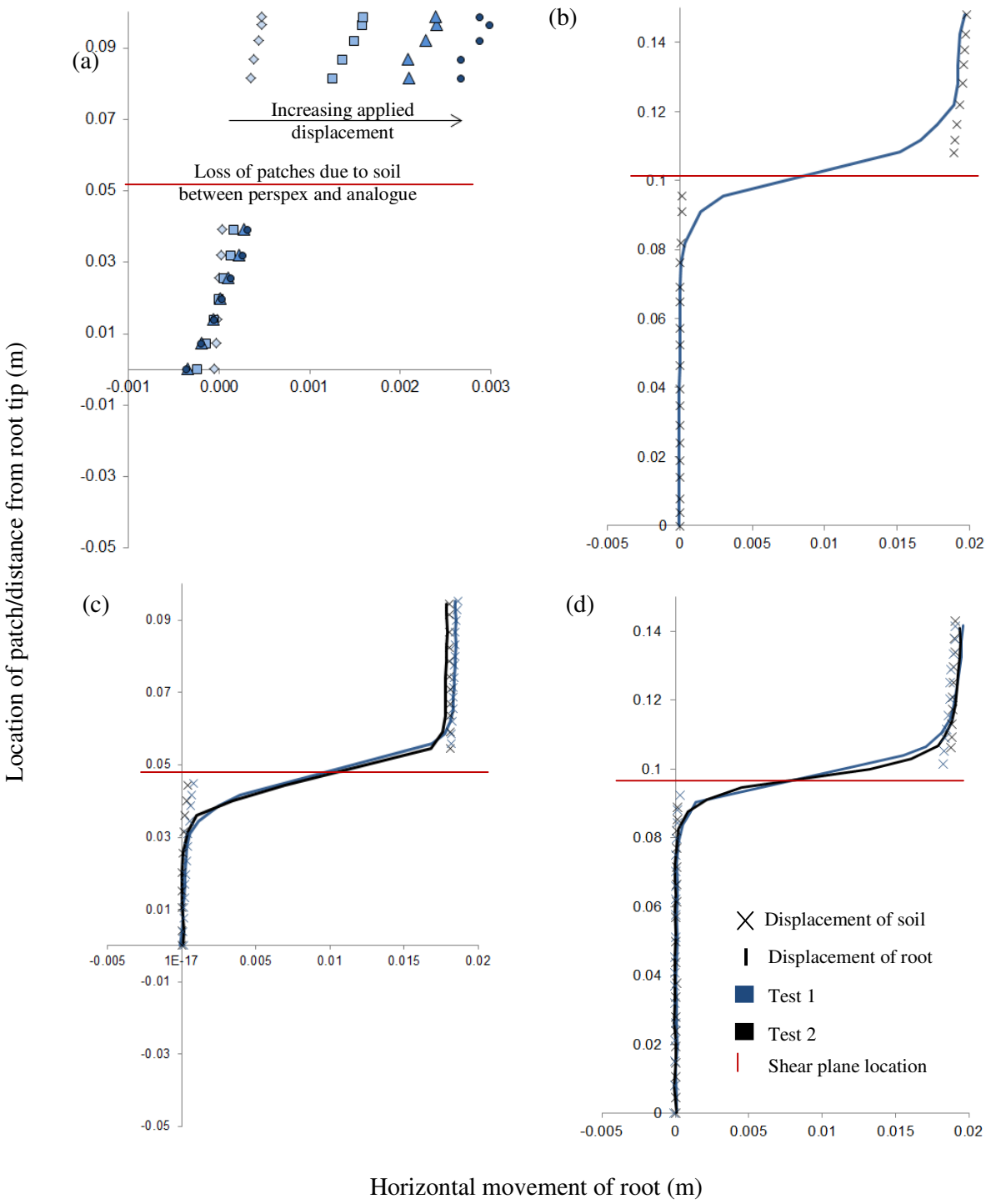

Figure 5.23: Horizontal displacement of the root and soil during shearing (a) Wooden root analogue; (b) Rubber root analogue, 3mm dia, 100mm L_{anc}; (c) Rubber root analogue, 1.6mm dia, 50mm L_{anc}; (d) Rubber root analogue, 1.6mm dia, 100mm L_{anc}.

Using the displacement data that was gathered from the test patches sitting directly above and below the shear plane, the Wu *et al.* (1979) model (see Equation 2.22) was used to estimate the root cohesion (c_R') provided by the rubber root analogues. The development of strain within the roots was calculated using Equation 3.1 and used to estimate the development of tensile strength (T_{root}), a key parameter in the Wu model. These factors are related as shown in Figure 5.25, which displays the data generated from the tensile testing of Viton (see Section 3.2.1.1). Between zero and 50% strain, therefore, T_{root} was calculated through the following equation;

$$T_{root} = 55.47 \cdot \varepsilon \qquad \text{Eq 5.10}$$

Where: $\boldsymbol{T_{root}}$ is the shear strength within the root (kPa), and ε is the strain within the root (%).

The Wu model also considers a parameter α_R to account for the inclination of the root as it crosses the shear plane (θ_R). Using simple geometry, θ_R was calculated in each digital image through employing the equation below;

$$\theta_R = \tan^{-1}\left(\frac{h_p}{v_p}\right) \qquad \text{Eq 5.11}$$

Where: $\boldsymbol{\theta_R}$ is the inclination of the root (°); $\boldsymbol{h_p}$ is the difference in horizontal displacement between two patches (m), and; $\boldsymbol{v_p}$ is the difference in vertical displacement between two patches (m).

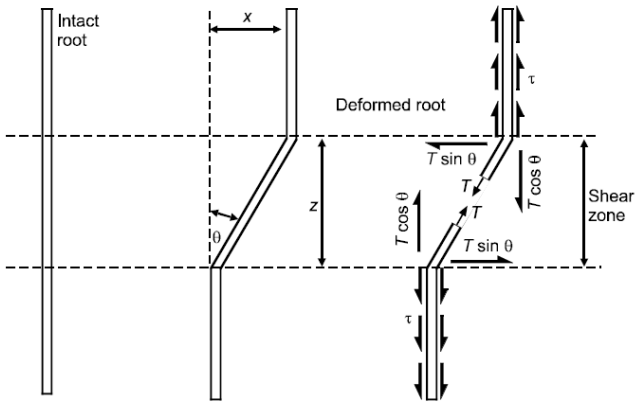

Figure 5.24: Forces acting on a flexible root during applied shear force (Wu *et al.*, 1979).

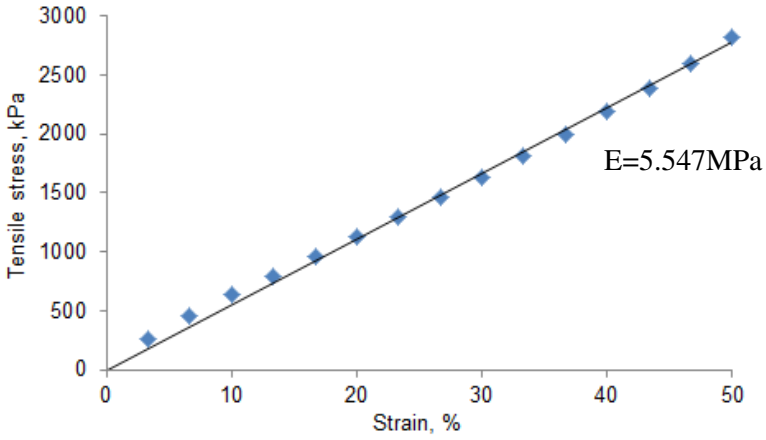

Figure 5.25: Relationship between strain and tensile stress for Viton rubber.

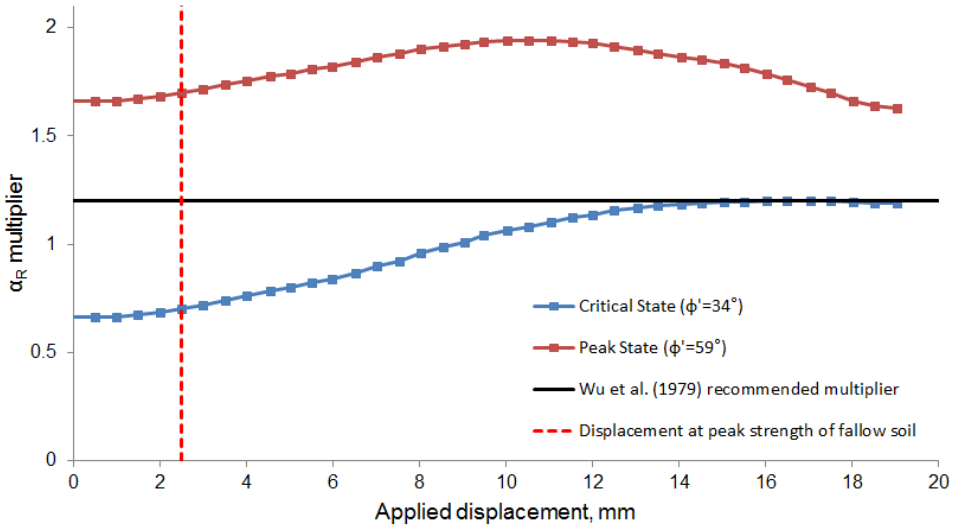

Figure 5.26: Calculation of 'α' multiplier in Wu et al (1979) model, calculated using 1.6mm diameter, 150mm length rubber root analogue. $\alpha_R=(\sin\theta_R+\cos\theta_R\tan\phi')$

Using these data, and the Wu model, the relationship between α_R and applied displacement was calculated. This is shown in Figure 5.26. As demonstrated, the Wu *et al.* (1979) recommended value of α_R = 1.2 provides a suitable estimation when considering the silica sand at critical state. The Wu model was developed to calculate the maximum cohesion provided by roots, and therefore is normally used with values of T_{root} at root failure and ϕ_{cr}'. In the early stages of shearing, where ϕ' = ϕ_{pk}', the Wu model underestimates α_R This stage, however, is followed by a transition between peak and critical state, in which α_R = 1.2 is likely to provide a reasonable approximation (given that α_R = 1.2 sits approximately midway between the peak and critical state curves for approximately 4mm of

applied displacement after peak strength is reached). In order to calculate c_R', therefore, the recommended value of α_R = 1.2 was considered.

Figure 5.27 shows the relationship between apparent root cohesion and applied lateral displacement, as calculated using: (i) the Wu model combined with cross section-front tests, and; (ii) the full section-centre tests. As demonstrated, these calculation techniques are not comparable. The Wu model, as with soil nail design, considers flexible root contribution as a purely axial mechanism, ignoring any bending effects. This provides a conservative account of c_R' in the early stages of shearing, as the root has not yet mobilised a tensile stress and, therefore, is not considered to contribute to the soils shearing capacity in any significant way. The full section-centre tests, however, show that rubber root analogues provide a significant initial increase in mobilised soil strength and, therefore, that the bending resistance of flexible roots may be a significant factor in determining the strength of a root reinforced soil. As the applied displacement is increased and the axial tension within the root begins to dominate its reinforcing mechanism, the two techniques for estimating c_R' remain inconsistent. This may be the result of incompatibility between the full section-centre and cross section-front tests. Figure 5.23 demonstrates that the stiffness of a root impacts it's deformation about the shear plane. Through reducing the cross sectional area and changing the profile of the root analogues for use in the cross section-front shear box tests the deformation of the root about the shear plane, and thus the development of tension throughout loading, may be affected.

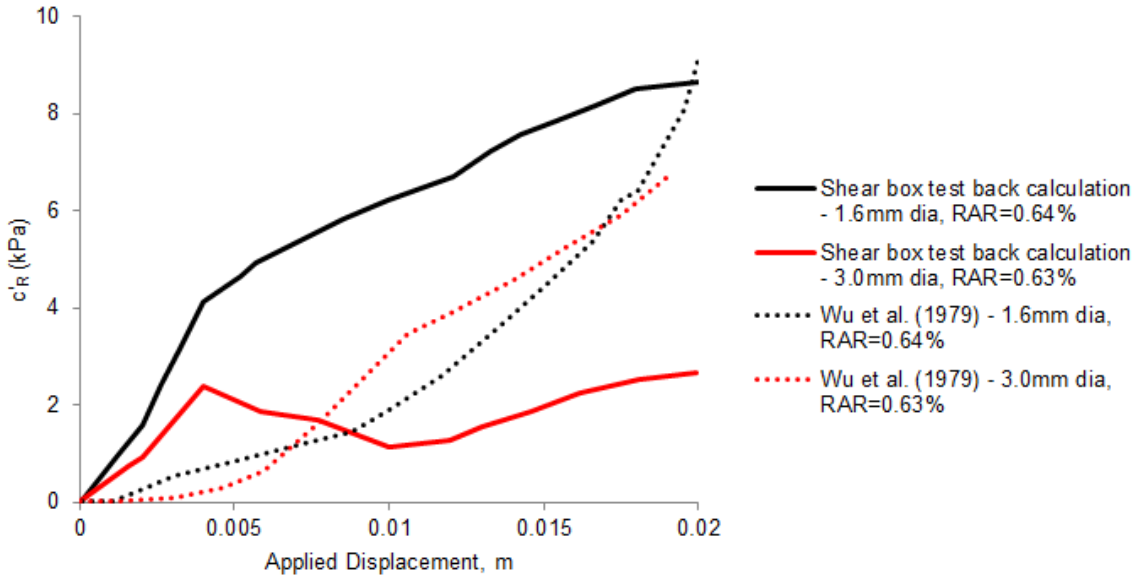

Figure 5.27: Development of root contribution to soil shear strength, modelled using c_R.

Figure 5.13 indicated that anchor length plays a significant role in the ability of a root to strengthen a soil, with reducing length leading to increased slippage and, therefore, reduced reinforcement. To verify this finding, the vertical displacement of the root tips in tests 1.6mm/rubber/half/test1, 1.6mm/rubber/half/test2 and 3.0mm/rubber/half/test1 were measured. These data are presented in Figure 5.28, where root anchor length is described as the length to width ratio of the roots. As expected, there is a definite positive relationship between aspect ratio and pull out resistance. Roots with an aspect ratio of 62.5 remain anchored in the stable soil mass throughout loading, while roots with a smaller aspect ratio began to uproot. The 65mm length roots, sheared in test 1.6r_2b, had an aspect ratio of just 9.4. From Figure 5.28, it can be inferred that these roots had undergone significant uprooting by a displacement of 0.005m, resulting in their loss of reinforcing capacity.

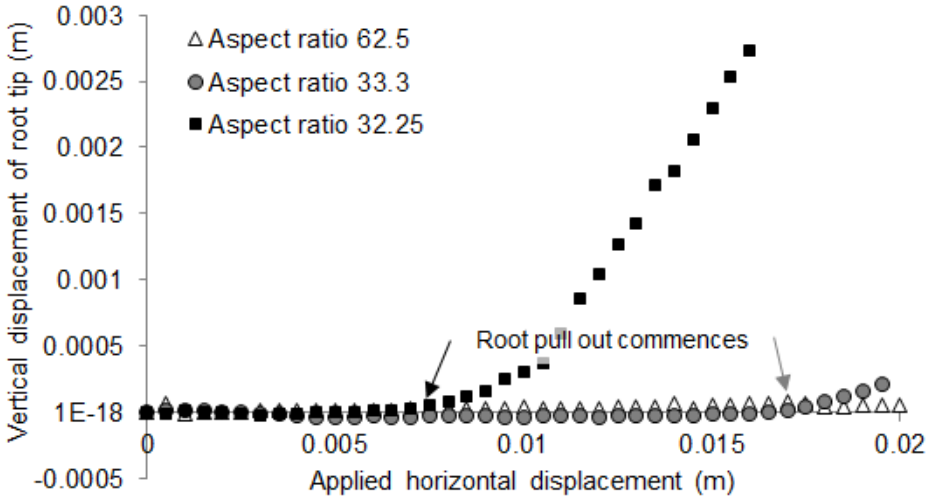

Figure 5.28: Vertical displacement at the root tip during loading. Key: (i) Aspect ratio 62.5, root properties: 1.6mm dia x 100mm L_{anc}; (ii) Aspect ratio 33.3, root properties: 3.0mm dia x 100mm L_{anc}; (iii) Aspect ratio 32.25, root properties: 1.6mm dia x 50mm L_{anc}.

5.5 Summary

A number of full section-centre shear box tests were carried out on root reinforced soil samples in order to gain improved understanding of root contribution to soil shear strength. These tests consider analogue root systems with varying RAR, root diameter, root length and root material properties. Additionally, a selection of shear box tests were carried out in cross section-front form, in order to view the root deformation and failure mechanism during shear loading.

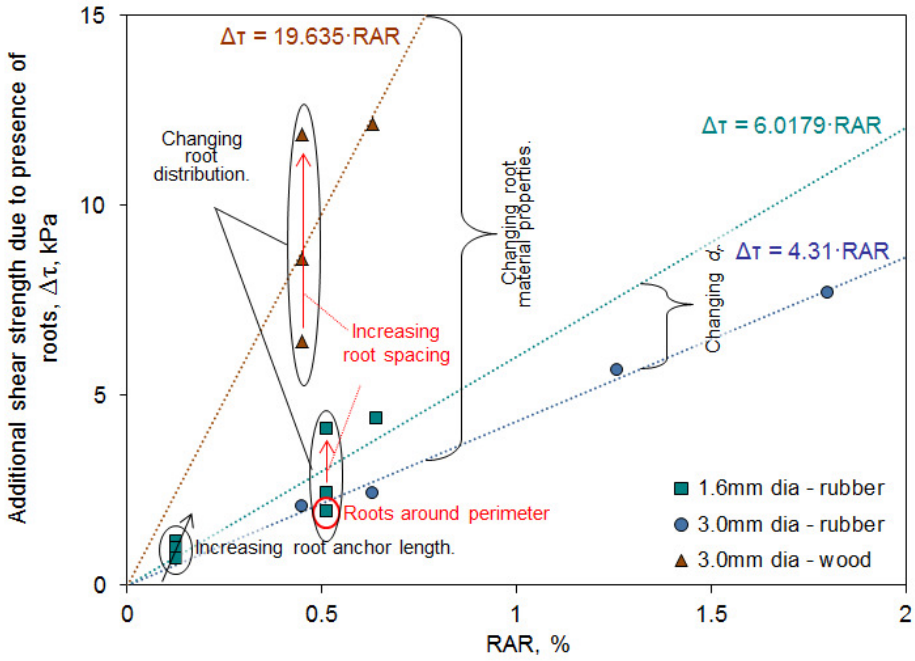

Figure 5.29: Additional shear strength, τ, provided by root inclusions after 4mm of applied displacement (measured using laboratory shear box tests). τ provided as a function of root area ratio, RAR.

Figure 5.29 summarises the key findings of the full section-centre tests, through plotting the additional shear strength provided by each root system after 4mm of applied displacement. As demonstrated;

- Reducing the root diameter, and thus increasing the number of roots required to achieve the same RAR, provides a stronger soil root system. This can be attributed to a larger number of thinner fibres within the soil matrix, reduced root bending and a consequent change in root deformation about the shear plane (which influences the tensile stress development in the root).

- Increasing the bending modulus of the root analogues provides an increase in additional shear strength. This increase is reduced with increasing displacement, as the rubber root analogues provide superior reinforcement during the later stages of shearing. The wooden root analogues reinforce the soil through bending only, while the rubber root analogues reinforce the soil through a combination of bending (early stages of shearing) and tension. Stiff roots, therefore, may help to prevent slope failure initiation, while more flexible roots help the slope to become stable again after slip is initiated.

- For a given RAR, root spacing significantly impacts the additional strength provided by the system. This can be attributed to soil root root interaction, which reduces the efficiency of individual roots when they are spaced closely together. A p-multiplier can be used to estimate the efficiency of each root based on diameter and spacing, see Figure 5.14. As such, if the efficiency of an isolated root is known, the efficiency of a root group can be determined.

- Increasing the length of root that anchors into the stable soil mass reduces the likelihood of root pull out and thus ensures continued reinforcement at large shear displacement.

Cross sectional modelling, combined with GeoPIV analysis, was used to successfully measure the horizontal root displacement during loading. Poor visibility of the wooden root analogues, however, limited their measurements. Given the small relative displacment between the rubber root analogues and their surrounding soil, combined with the complex relationship between root properties and the deformation behaviour about the shear plane, it is possible that the full section-centre and cross section-front shear box tests are not comparable. Moreover, it is possible that they are not suitable for generating displacement data for use in a predictive tool (which uses *p-y* methodology).

The contribution of the roots to the soil shear strength was defined in terms of both root cohesion and by enhanced dilation in the rooted soil material. The root cohesion values were compared to those obtained through combining the data gathered from the cross section-front test with the Wu *et al.* (1979) calculation model. Such a model was shown to not provide a full account of a root's contribution to soil shear strength as a function of shear deformation, highlighting the requirement for a more reliable model.

Chapter 6 Calculating and predicting the contribution of a root to soil shear strength

6.1 Introduction

Predicting the mechanical response of a soil root system to lateral loading is essential in the development of a design tool for assessing the stability of existing or planned vegetated slopes. Current design approaches (*e.g. Chok et al., 2004*) represent soil root interaction as an apparent root cohesion factor (c_R') and incorporate it within standard soil (Mohr-Coulomb) and slope (Factor of safety) strength models. Such approaches provide a simple variation on the well-used, well understood and well trusted stability-based geotechnical methods and are therefore ideal for use within a design office environment. Furthermore, the response of the soil, or c_R' term, can be easily estimated through: (i) back calculation from direct shear box tests, or; (ii) use of the Wu *et al.* (1979) calculation model, as demonstrated in Chapter 5. The assumption that roots provide cohesion within the soil, however, does not provide a particularly accurate account of mechanical soil root interaction (see Section 5.4.1.1). Moreover, the Wu *et al.* (*1979*) model is limited to representing flexible roots (as it excludes any bending capacity of the root), and, therefore, does not always provide an accurate picture of root contribution (see Section 5.4.2.3.1). A means of better quantifying this behaviour, for input into soil and slope strength models, is therefore required.

To estimate the response of a pile foundation to lateral loading (which is a very similar problem), the well-known *p-y* calculation model can be employed, where *p* refers to the reaction per unit length and *y* is the lateral deformation. As with *t-z* modelling (see Chapter 4), this technique uses beam-on-elastic foundation theory. In this case, however, a different loading condition and therefore a different pile soil response is considered. Given the success of using *t-z* theory to predict uprooting, it was hypothesised that *p-y* theory, combined with numerical modelling, could be applied to the root reinforced shear box tests (described in Chapter 5) in order to provide a useful predictive tool.

6.1.1 Method

A finite element model that utilises *p-y* theory was developed and used to predict the shear box tests in Chapter 5. This model was designed in line with the uprooting model in Chapter 4, comprising a beam (root) supported by a series of discrete springs (soil). In this case, however, the stiffness of the

springs is defined by the lateral soil resistance acting locally at the soil root interface during shearing. This can be calculated using existing design codes (e.g. API RP 2A-WSD (2000), DNV (1992) and Reese *et al.* (1974)), which utilise the physical properties of the soil and root, or empirically, based on PIV observations from cross section-front shear box tests (as conducted for pull-out in Chapter 3). The output of the shear box testing (in particular, inconsistency between cross section-front and full section-centre tests, poor views of half wooden root analogues and lack of significant relative displacements), however, creates problems for the empirical PIV method.

This chapter reports on the development of a numerical predictive tool for determining the root contribution to the shear behaviour of rooted soil and on the process required to establish root, soil and soil root interaction properties.

6.2 Design of numerical model

Figure 6.1 presents the finite element model (FEM) that was designed to predict lateral soil root interaction, using Abaqus/CAE 6.8-3. As demonstrated, it comprises a series of element-spring sets, which combine to form a vertical beam that is horizontally supported by springs. Each of these springs connects the centre of an element to a moveable (above the shear plane) or fixed (below the shear plane) point that sits at a horizontal distance away from the root, and represents the free-field soil. The moveable points are used to accommodate the applied lateral shear displacements. When loaded, the model resists uprooting through a roller connection at its tip. This connection provides vertical support, whilst allowing horizontal movement and rotation, and is used assuming complete root anchorage throughout loading. In reality, this assumption will not always hold true (see Section 5.4.2). The model, however, is designed to assess the suitability of the *p-y* modelling technique and, therefore, considers horizontal interaction as an isolated mechanism. Through considering the vertical support as a series of *t-z* springs, rather than a roller connection, it is hypothesised that root slippage in the axial direction (if any) can subsequently be accounted for. The root and soil properties required to define the model are highlighted in Figure 6.1.

The benefits of this model equal those of the proposed uprooting model, which are described in Section 4.2. Additionally, it improves upon the commonly used Wu *et al.* (1979) c_R' model through:

- Providing output in terms of the additional force required to shear soil around an individual root, rather than a root cohesion value.

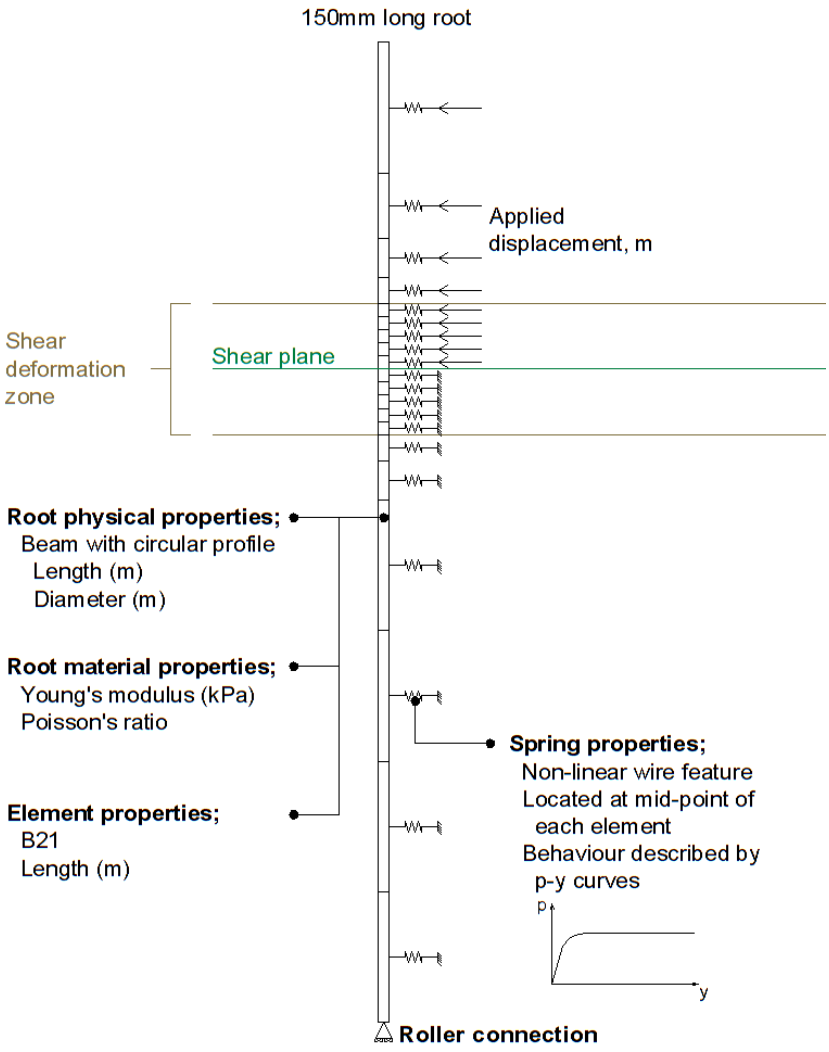

Figure 6.1: Schematic of proposed finite element model, which represents soil root systems undergoing shear loading using Abaqus CAE.

- Accounting for shear plane depth, root length, tortuosity and any changes in sectional properties along the root length, all of which impact the reinforcing potential of a root.

- Accounting for the spacing of roots (or RAR) on the soil root interaction, via 'p-multipliers' which scale *p-y* curves.

- Possessing the potential to consider every root shearing mechanism (i.e. bending, stretching, slipping and breaking) and thus having the capacity to represent the behaviour of all roots, regardless of stiffness (not just flexible ones). Note: slipping is only accounted for when the roller connection is replaced by a *t-z* spring at each element.

6.3 Defining the root

The roots are defined as described in Section 4.3. The properties of Beech (genus *Fagus*) wood are outlined in Section 5.2.1.

6.4 Defining the p-y springs

The stiffness of each *p-y* spring is defined by the local relationship between lateral soil reaction (*p*) and relative soil root displacement (*y*), where locality is defined by spring location and element length. As shown in Figure 6.1, the proposed distribution of element-spring sets is more complex than that considered in the uprooting models. This follows the realisation that flexible roots deform significantly within a smaller zone of soil about the shear plane, while wooden roots deform very little. As each element-spring set models the average behaviour of the soil root system along its length, larger elements at the shear plane may distort the behaviour of flexible roots. As such, the elements are concentrated within the deformation zone, which (following a study of the cross section-front shear box tests in which the deformation zone was measured, see Chapter 5) is considered to have a 20mm depth (see Figure 5.22). In this zone, elements have a length of 2mm, while outside this zone, they increase in size to 20mm, through lengths of 4mm, 6mm and 10mm (see Figure 6.1). The variation in element size, rather than simply considering smaller element-spring sets throughout, was designed to minimise the model preparation and analysis times and thus ensure model efficiency. This section reports on the development of suitable *p-y* spring sets, calculated through applying standard design codes to the proposed element-spring system (i.e. Figure 6.1).

6.4.1 Design codes in piling engineering

Reese and Van Impe (2011) report a calculation model that estimates *p-y* springs for piles sitting in drained sand. This model was originally derived in 1974 (*Reese et al., 1974*) using the data gathered from full scale tests on fully instrumented piles (in particular, the well-known Mustang Island Test) and is considered to provide a reasonable representation of lateral pile-soil interaction (*Brødbæk et al., 2009*). Moreover, it forms the basis on which commonly used design codes, such as API and DNV, were formed. It is therefore used to define the *p-y* springs in this project.

The non-linear *p-y* relationship proposed by Reese *et al.* (1974) is presented in Figure 6.2. As demonstrated, it comprises four distinct stages. In the initial stage, when relative displacements are

small ($y < y_k$), p increases linearly with y. This is followed by a parabolic relationship that remains until y is equal to y_m. In the third stage ($y_m < y < y_u$), linear behaviour is resumed. This, however, is bound by an upper limit that is characterised by p_u (the maximum soil response) (stage four). For a given situation, these curves can be scaled by defining: (i) the data points k, m and u, and (ii) the parabolic relationship of stage 2. Figure 6.2 also shows that the Reese *et al.* (1974) *p-y* model predicts a positive relationship between increasing spring stiffness and depth from the soil surface. This relationship, however, may be affected by soil dilation (ψ) at shallow depths, such as those present during soil root interaction (generally within a 1m depth, see Chapter 4).

The ultimate response of a soil to (relative) pile movement is characterised by the minimum load that is required to induce a critical failure mechanism. This is likely to be a wedge mechanism at shallow

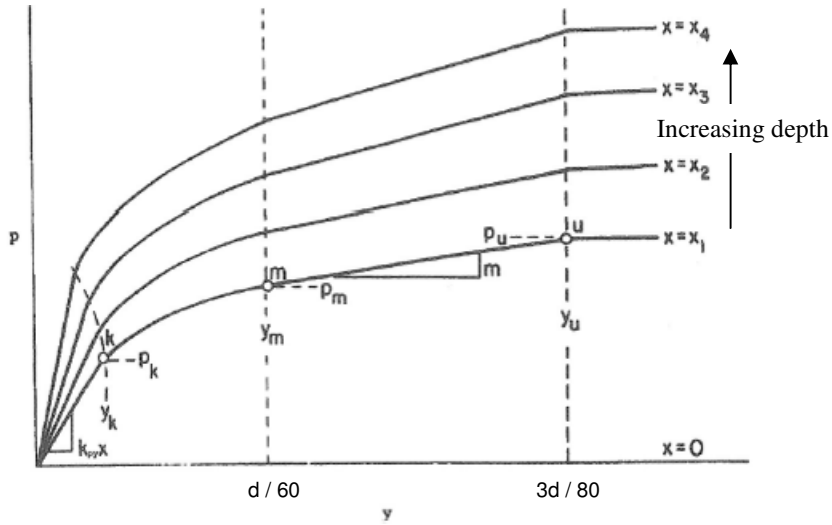

Figure 6.2: *p-y* curves for piles sitting in drained sand (*Reese and Van Impe, 2011*)

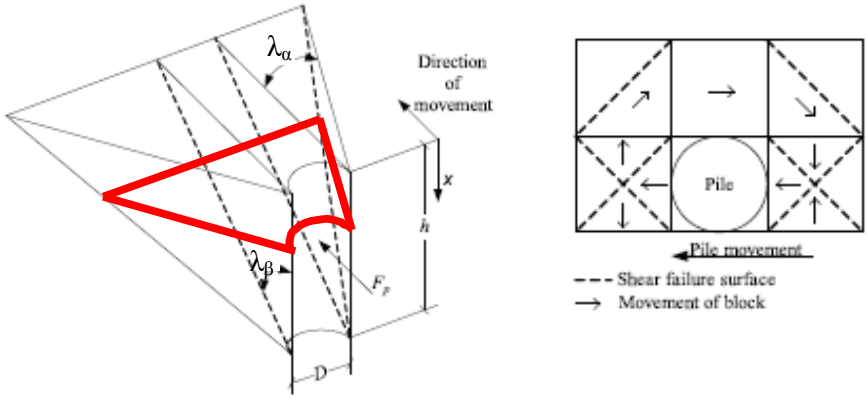

Figure 6.3: Soil failure mechanisms at (a) shallow depths, and (b) deep depths (*Brødbæk et al., 2009 after Reese et al., 1974*).

depths and a flow mechanism at deep depths (*Brødbæk et al., 2009*), as shown in Figure 6.3. During wedge failure, an unstable mass of soil is pushed upwards, along connecting shear planes that sit in front of the pile. For ease of calculation, these planes are assumed to form a sharp edged wedge, which is a simplification of the curved wedges that have been observed in the field (*Møller and Christiansen., 2011*). The geometry of the wedge is defined using two angles, λ_α and λ_β (see Figure 6.3 (a)), which are defined as shown below;

$$\lambda_\alpha = \phi'/2 \; ; \quad \lambda_\beta = 45 + \phi'/2$$

Where: ϕ' is the friction angle of the soil.

Considering the forces that act on an arbitrary horizontal slice of the wedge (highlighted in red in Figure 6.3 (a)), sitting at a depth of *x*, the ultimate soil resistance to wedge failure is calculated. This is shown in the following equation (*Reese et al., 1974*);

$$p_{us} = \gamma_s \cdot x \cdot \left[\begin{array}{l} \dfrac{K \cdot x \cdot \tan(\phi') \cdot \sin(\lambda_\beta)}{\tan(\lambda_\beta - \phi') \cdot \cos(\lambda_\alpha)} + \dfrac{\tan(\lambda_\beta)}{\tan(\lambda_\beta - \phi')} \cdot \left(D_{pile} + x \cdot \tan(\lambda_\beta) \cdot \tan(\lambda_\alpha)\right) + \\ Kx \cdot \tan(\lambda_\beta) \cdot \left(\tan(\phi') \cdot \sin(\lambda_\beta) - \tan(\lambda_\alpha)\right) - K_a \cdot D_{pile} \end{array} \right] \qquad \text{Eq 6.1}$$

$$K_a = \tan^2\left(45 - \phi/2\right) \qquad \text{Eq 6.1 (a)}$$

Where: $\boldsymbol{p_{us}}$ is the ultimate soil resistance at shallow depths (kN/m); $\boldsymbol{\gamma_s}$ is the unit weight of the soil (kN/m^3); $\boldsymbol{x}$ is the depth from the soil surface (m); $\boldsymbol{K}$ is the coefficient of lateral earth pressure, normally taken as 1-sinϕ, but assumed to be 0.4 here; $\boldsymbol{K_a}$ is the active lateral earth pressure, and; $\boldsymbol{D_{pile}}$ is the diameter of the pile (m).

At deeper depths, it is easier for the soil to flow horizontally around the pile than to push upwards in a wedge. The ultimate capacity of the soil against a flow mechanism, again at an arbitrary depth of *x*, is described through Equation 6.2, below;

$$p_{ud} = K_a \cdot D_{pile} \cdot \gamma_s \cdot x \cdot \left(\tan^8(\lambda_\beta) - 1\right) + K \cdot D_{pilr} \cdot \gamma_s \cdot x \cdot \tan(\phi') \cdot \tan^4(\lambda_\beta) \qquad \text{Eq 6.2}$$

Where: $\boldsymbol{p_{ud}}$ is the ultimate soil resistance at deep depths (kN/m)

At any given depth, the ultimate resistance of the soil to failure, and thus the ultimate soil response p_u, is the most critical of these two mechanisms, i.e. the lesser of;

$$p_u = A'_s \cdot p_{us} \qquad \text{Eq 6.3 (a)}$$

$$p_u = A'_s \cdot p_{ud} \qquad \text{Eq 6.3 (b)}$$

Where: $\boldsymbol{p_u}$ is the ultimate soil resistance (kN/m), and; $\boldsymbol{A'_s}$ is a constant, defined as a function of $\boldsymbol{x/D_{pile}}$ using Figure 6.4 (a) ($\boldsymbol{x}$ is the depth from the soil surface and $\boldsymbol{D_{pile}}$ is the pile diameter).

The critical depth at which wedge mechanisms end and flow mechanisms begin is defined by the point at which p_{us} is equal to p_{ud}. It should be noted that A'_s is a constant that was introduced into the modelling technique in order to force the *p-y* curves to fit the data gathered from the Mustang Island test (*Reese et al., 1974*). This 'force' approach was continued into the method proposed for defining the remaining *p* and *y* terms through a second constant, known as B_s, which is further described below (see Figure 6.4 (b)).

Having established the ultimate soil response, the value of *p* at point m (see Figure 6.2) can be estimated, as shown below;

$$p_{pm} = B_s \cdot p_u \qquad \text{Eq 6.4}$$

Where: $\boldsymbol{p_{pm}}$ is the soil resistance at $y=y_m$ (kN/m), and; $\boldsymbol{B_s}$ is a constant, defined as a function of $\boldsymbol{x/D_{pile}}$ using Figure 6.4 (b).

The key *y* data on the *p-y* curves can then be calculated through the following equations;

$$y_k = \left(\frac{C}{k_{py} \cdot x} \right)^{n_a / n_a - 1} \qquad \text{Eq 6.5}$$

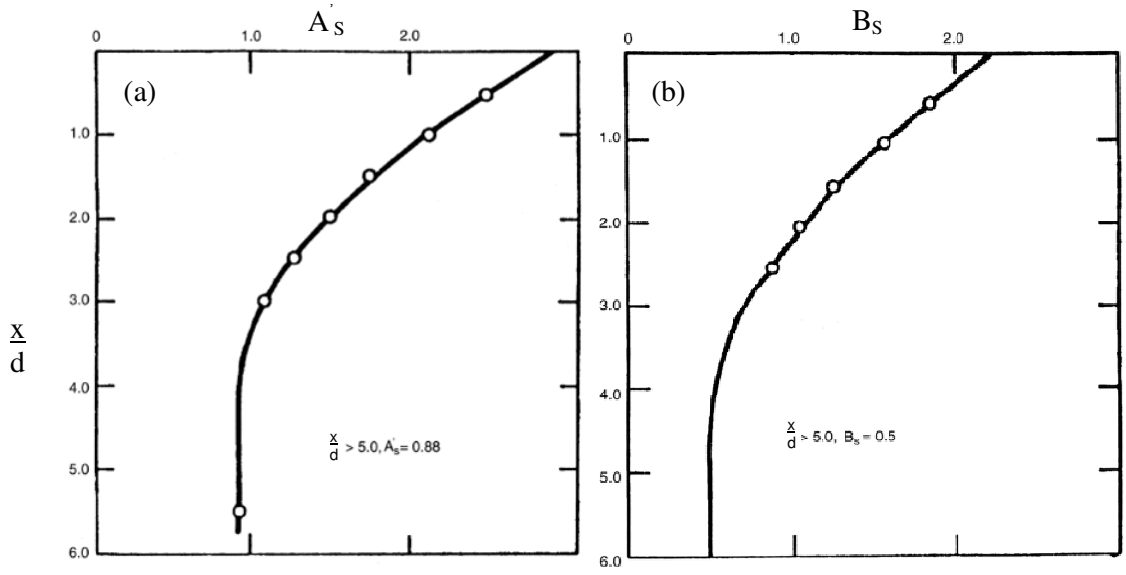

Figure 6.4: Non-dimensional constants used to define: (a) ultimate soil response, p_u, and (b) soil response p_m. Coefficients suitable to assess static loading only.

$$C = \frac{p_{pm}}{y_m^{1/n_a}} \quad \text{Eq 6.5 (b)}$$

$$n_a = \frac{p_{pm}}{m \cdot y_m} \quad \text{Eq 6.5 (c)}$$

$$y_m = \frac{D_{pile}}{60} \quad \text{Eq 6.6}$$

$$y_u = \frac{3 \cdot D_{pile}}{80} \quad \text{Eq 6.7}$$

Where: $\boldsymbol{y_k}$, $\boldsymbol{y_m}$ and $\boldsymbol{y_u}$ are the key relative soil displacements (m); $\boldsymbol{C}$ and $\boldsymbol{n_a}$ are constants; $\boldsymbol{k_{py}}$ is defined using Figure 6.5, and; $\boldsymbol{m}$ is the gradient of the curve between $\boldsymbol{y_m}$ and $\boldsymbol{y_u}$.

Following this, the value of p at point k can be calculated as a function of y_k and some basic soil properties, as shown below;

$$p_k = k \cdot x \cdot y_k \quad \text{Eq 6.8}$$

Where: $\boldsymbol{p_k}$ is the soil response at a relative soil displacement of $\boldsymbol{y_k}$ (kN/m); $\boldsymbol{k}$ is the initial modulus of subgrade reaction, and can be taken from Table 6.1.

Finally, having established the key data points (k, m and u) on the p-y curve, a parabolic function that joins points k and m can be established, using Equation 6.9. The remaining points are joined using straight lines.

$$p = C \cdot y^{1/n} \quad \text{Eq 6.9}$$

Where: $\boldsymbol{p}$ is the soil response (kN/m); $\boldsymbol{C}$ is a constant calculated through Equation 6.5 (b), and; $\boldsymbol{y}$ is the relative displacement between the pile and soil.

The Mustang Island test considered steel piles with a diameter of 0.61m and a length of 21m (L/d ratio = 34.4) (*Brødbæk et al., 2009*). The Reese *et al.* (1974) modelling technique is therefore based on slender piles with a smooth surface, which marries well with the root analogues used in this project. The root analogues, however, cover a range of slenderness between 50 (3mm diameter, 150 mm length) and 94 (1.6mm diameter, 150 mm length), which is notably higher. The author could not find any significant attempt, however, to verify the proposed p-y model against piles of different scales and materials. There may still, therefore, be outstanding questions regarding its ability to universally model the lateral behaviour of pile foundations.

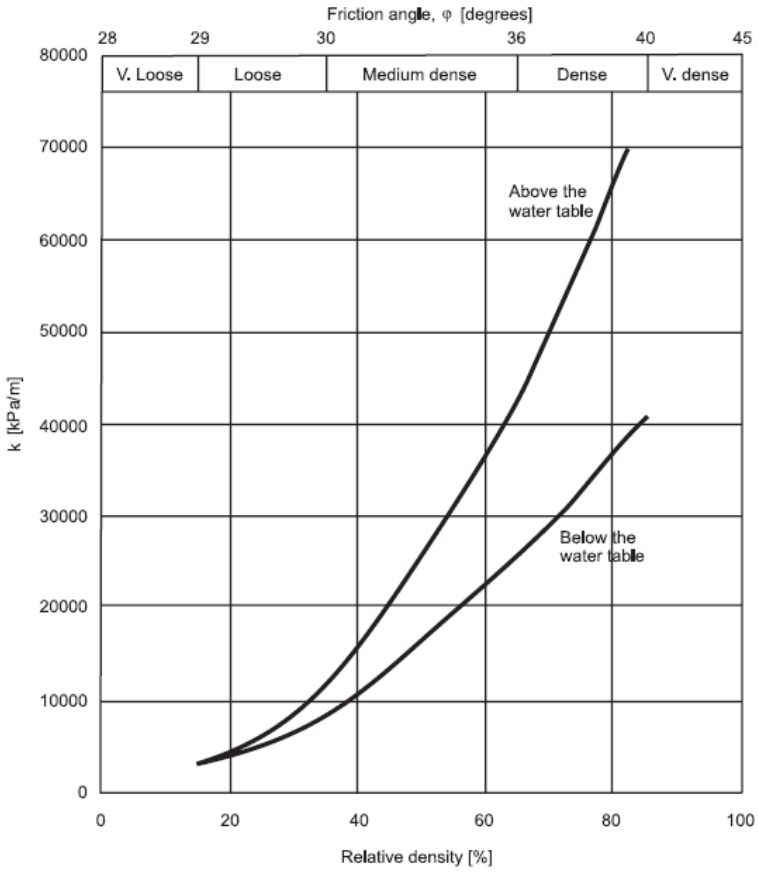

Figure 6.5: Curves used to find suitable values of k_{py} in sands (Reese *et al.*, 1974).

Table 6.1: Initial modulus of subgrade reaction, k (kN/m^3), Reese *et al.* (1974)

Relative density	Loose	Medium	Dense
Unsubmerged	6800	24400	61000
Submerged	5400	16300	34000

6.4.2 Application of *p-y* curves to root analogues

Figure 6.6 shows the variation with depth of p_{us}, p_{ud} and p_u for the (a) 1.6mm diameter and (b) 3.0mm diameter root analogues, using a soil strength of (i) $\phi' = 34.0^{\circ}$, (ii) $\phi' = 59.1^{\circ}$. It should be noted that the proposed calculation model does not account for changes in root material properties and, therefore, these curves (along with the consequent *p-y* curves) are assumed to be applicable to both the rubber and wooden root analogues. It is also assumed for simplicity that the x/D_{root} ratio at which

the soil transitions from wedge to flow failure is unaffected by the low confining stress. Considering first the distribution of soil response when $\phi' = 34.0^{\circ}$, Figures 6.6 (ai) and (bi) show that root diameter has a clear impact on the critical depth at which wedge failure becomes more difficult to achieve than flow failure. In particular, the 1.6mm diameter roots have a critical depth of 0.027m, while the 3.0mm diameter roots have a critical depth of 0.051m. This indicates that, as the diameter of a root increases (along with its flexural stiffness and surface area), wedge failure becomes a more prominent mechanism.

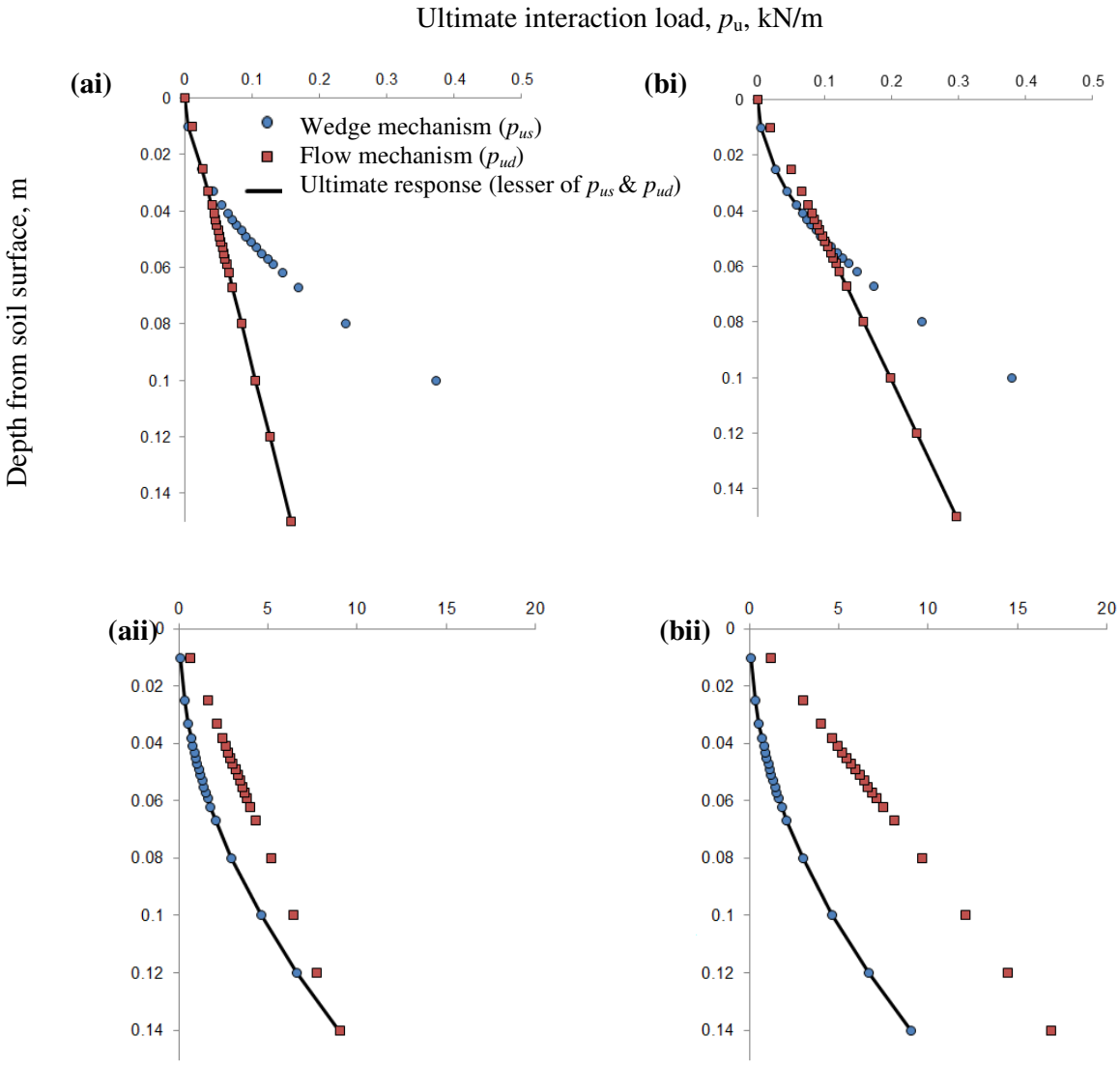

Figure 6.6: Distribution of soil response with depth assuming (ai) D_{root}=1.6mm, no dilation, (bi) D_{root}=3.0mm, no dilation, (aii) D_{root}=1.6mm, dilation, (bii) D_{root}=3.0mm, dilation

Additionally, it is apparent that the 3.0mm diameter roots are encouraging a larger overall soil response (see Figures 6.6 (ai) and (bi)). This corresponds favourably with the laboratory shear box tests, which revealed that soil samples reinforced with larger diameter roots provide a greater shearing resistance than those reinforced with the same number of smaller diameter roots (see Figure 5.12). The effect of increasing soil strength, through considering dilation, also has a significant impact on the predicted response of the system; see Figures 6.6 (aii) and (bii). In this instance, a critical depth is not reached along the length of the 3.0 mm diameter root and is only reached at the tip of the 1.6mm diameter root (i.e. only shallow soil response is considered). Moreover, the scale of soil response is increased.

Using the x-p_u distributions highlighted in Figure 6.6, along with the remaining data that were calculated to describe point's k, m and u at each spring location, p-y curves were constructed. As an example, Figure 6.7 shows such curves when considering a 3.0mm diameter root only. It is assumed that the y/D_{root} ratios for points m and k are also unaltered by the low confining stress levels for simplicity. These curves reach a maximum soil response (p_u) after a very small value of relative root displacement (approx. 0.11mm). This is reduced further when considering a 1.6mm diameter root (approx. 0.06mm) and suggests that the overall soil response is governed by the value of p_u, rather than the initial non-linear behaviour of the spring. The values of y_u and y_m are calculated as a function of root diameter only and, therefore, remain constant with varying soil properties and spring locations (see Equations 6.6 and 6.7). The initial portion of the curve (between the origin and y_m), however, is calculated as a function of the gradient between points m and u, which increase in magnitude with increasing soil strength. Consequently, when dilation is included in the soil model, the value of y_k (and p_k) exceeds the value of y_u (and p_u). The p-y curves in Figures 6.7 (b) and (c) have therefore been adapted from those proposed by Reese *et al.* (1974), through excluding both the k data point and the parabolic segment.

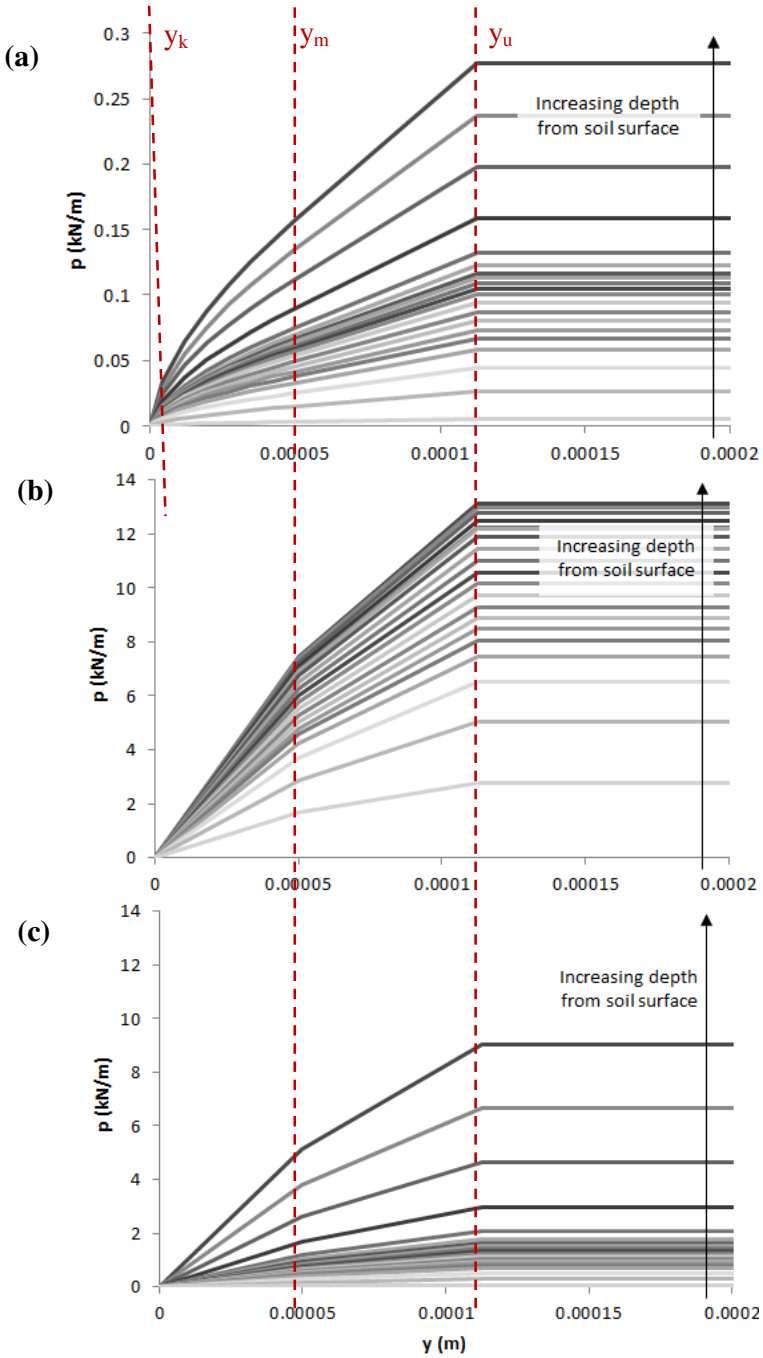

Figure 6.7: *p-y* springs for 3.0mm diameter root interacting with soil, considering (a) no dilation, (b) dilation, and (c) dilation, but with total soil strength capped at 60˚. Note: depth increases from soil surface as described in Section 6.4 and Figure 6.1.

6.4.3 *p-y* curves for input into numerical model

The *p-y* curves presented in Figure 6.7 represent the soil response at each spring location as a force per metre depth. To represent the total soil response (force) in the p-y spring, acting along the length of each element, therefore, they need to be scaled by element length (Equation 6.10);

$$p_e = L_e \cdot p \qquad \text{Eq 6.10}$$

Where: $\boldsymbol{p_e}$ is the total soil response acting along the length of an element (kN); $\boldsymbol{L_e}$ is the element length, and; $\boldsymbol{p}$ is the soil response measured as a force per metre depth (kN/m).

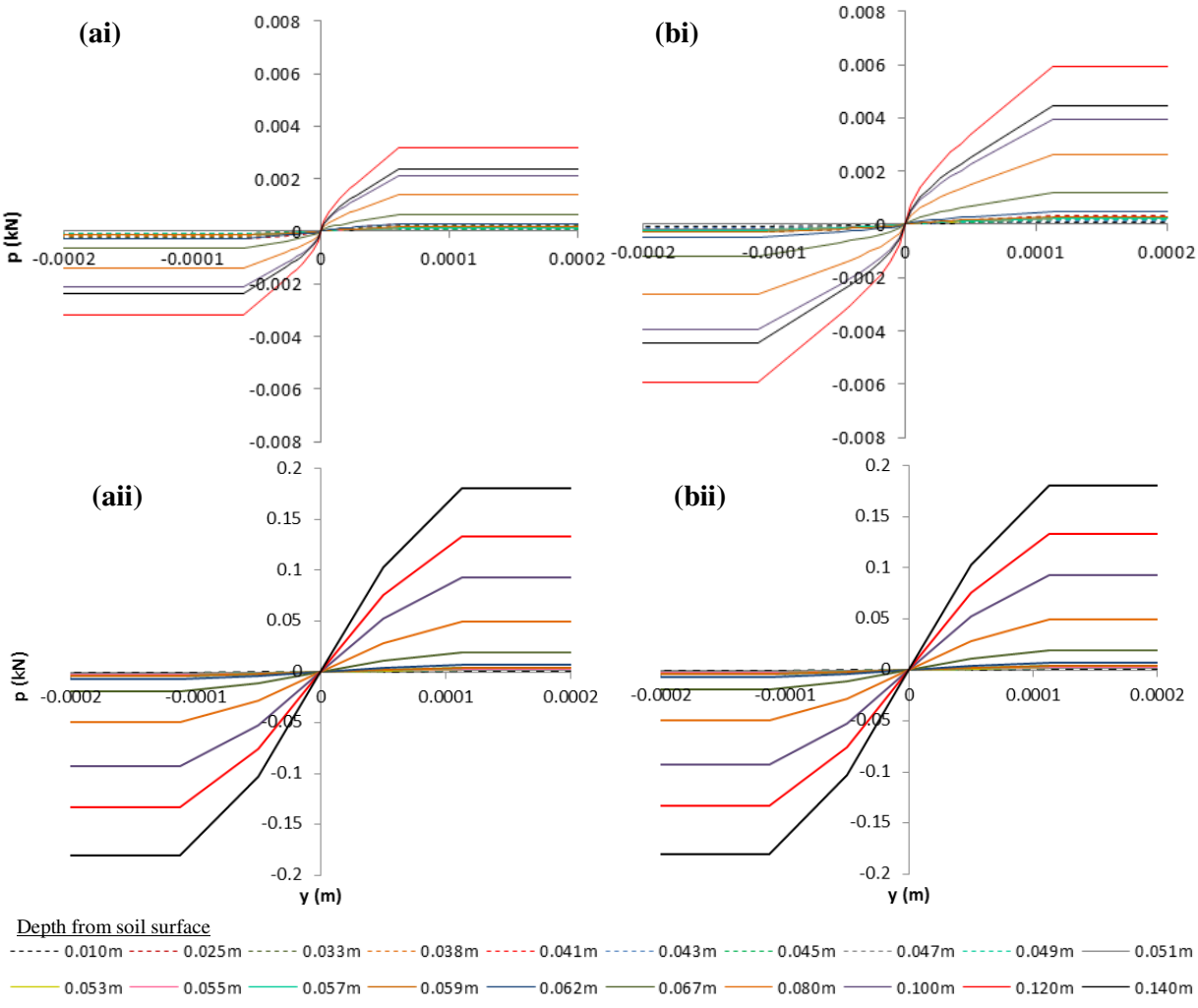

Figure 6.8: *p-y* springs for input into Abaqus/CAE (ai) diameter = 1.6mm, ϕ = 34.0˚, (bi) diameter = 3.0mm, ϕ = 34.0˚, (aii) diameter = 1.6mm, ϕ = 59.1°, (bii) diameter = 3.0mm, ϕ = 59.1°.

Additionally, they need to be extrapolated into the negative *p-y* quadrant so that they can model the response of the soil to both negative and positive relative movements. As soil response is related to the scale of relative movement, and is independent of its direction, the springs have an identical response to both compressive and tensile forces.

The final curves, which were used to define the horizontal wire connectors in the Abaqus/CAE soil root model, are presented in Figure 6.8. In this figure, it is apparent that the difference in spring stiffness with increasing root diameter is much more prominent when the effects of dilation are excluded from the calculations. This is because when the soil strength (or value of ϕ') becomes large, the soil response is governed by wedge failure, which is much less affected by root diameter (as demonstrated in Figure 6.6).

6.5 Numerical modelling of shearbox tests

Figure 6.9 shows the proposed root shearing model within the Abaqus CAE interface, highlighting its key properties. As demonstrated, the selection of features and basic construction technique are very similar to those of the uprooting model (see Figure 5.28). The springs (or wire connectors), however, are now orientated horizontally, rather than vertically, and are connected between the root and a *dummy* beam, where each node on the root has a corresponding dummy beam that sits at a horizontal distance of 0.005m from the root, and is able to move past the root without coming into contact. The purpose of these beams is to provide Abaqus with a series of solid objects that can be displaced to represent the free-field soil movement and to which the free end of the wire connectors (*p-y* springs) can be attached and loaded. Their properties are therefore somewhat immaterial, and have been specified as length = 0.005m, diameter = 0.005m, Young's modulus = 10^{12} kPa and Poisson's ratio = 0. Like the root, these features are created in the *part* module using 2D, deformable wire features. Their material properties are defined in the *property* module, and the *assembly* and *mesh* modules are used to transfer them to the model assembly as *independent instances* and to create a mesh, using B21 elements.

The *p-y* springs are modelled using *disjoint* wire connectors and their stiffness's are defined by the curves outlined in Figure 6.8. To ensure that they act horizontally, each spring is assigned a local orientation with the axial connector in the horizontal direction.

In the *step* and *load* modules, 10 analysis steps are created. A *displacement* boundary condition progressing from 0 to 20mm is applied to the dummy beams sitting above the shear plane, while a displacement of 0 is applied to the dummy beams sitting below the shear plane (as shown in Table 6.2). The beams, therefore, simulate the direct shearing behaviour of the free-field soil mass in the shearbox tests, while the springs simulate the behaviour of the near-field soil sitting adjacent to the root. Additionally, the base of the root is subjected to a displacement boundary condition of zero in the vertical direction.

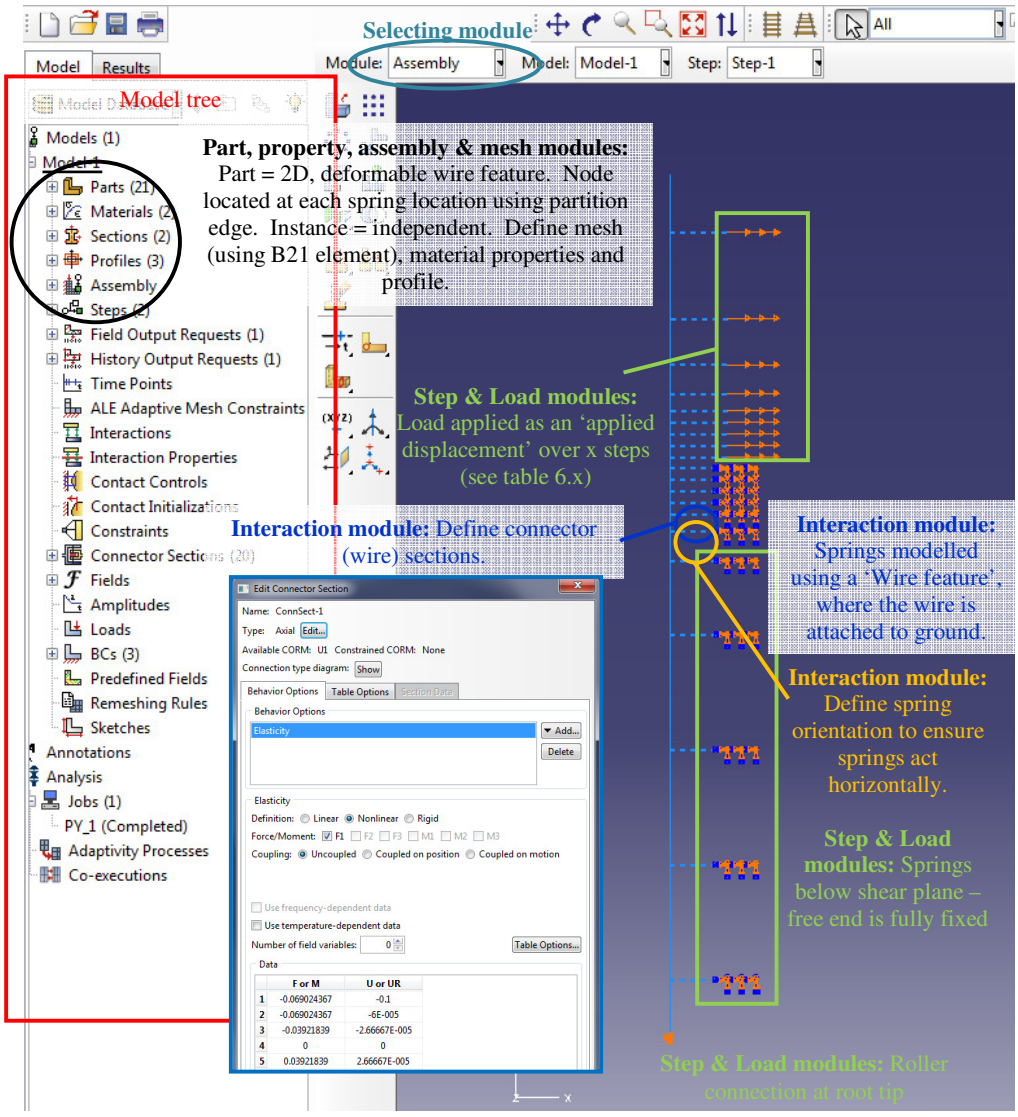

Figure 6.9: Overview of Abaqus/CAE input for modelling an analogue tap root in sand. Figure explains the Abaqus modules that were used to construct each aspect of the model.

Table 6.2: Loading steps input into Abaqus/CAE shearing model

Step		1	2	3	4	5	6	7	8	9	10
Applied displacement, mm	*Above shear plane (horizontal loading)*	0	1	2	3	4	5	7	10	15	20
	Below shear plane (horizontal loading)	0	0	0	0	0	0	0	0	0	0
	Root tip (vertical loading)	0	0	0	0	0	0	0	0	0	0

6.5.1 Initial results and discussion, including effect of strength assumptions

At any point during shearing, the force above the shear plane (applied) should be equal in magnitude, but opposite in direction, to that below (resisting). In the numerical modelling, therefore, the net force across all of the *p-y* springs should always be equal to zero. This was true of each numerical simulation. As *p-y* springs model the behaviour of the root-adjacent soil, then the magnitude of the resisting (or applied) force across each spring set (above or below the shear plane) corresponds to the additional shear resistance provided to the soil by the presence of the root, F_{root}. This can be calculated as shown in Equation 6.11.

$$F_{root} = \sum_{s=1}^{n} F_s \qquad \text{Eq 6.11}$$

Where: $\boldsymbol{F_{root}}$ is the additional resistive force above or below the shear plane (kN); $\boldsymbol{F_s}$ is the force in spring s (kN), and; $\boldsymbol{s}$ is the spring number, which starts at 1 (at the top or tip of the root) and continues to $\boldsymbol{n}$ (at the shear plane).

Root contribution can also be measured experimentally using the force-displacement output of laboratory shear box tests, as shown in Equation 6.12. The predicted (or theoretical) relationship between root contribution and applied displacement could therefore be verified against the laboratory test data (see Chapter 5).

$$F_{root} = \frac{F_{rooted} - F_{fallow}}{N} \qquad \text{Eq 6.12}$$

Where: $\boldsymbol{F_{rooted}}$ is the force required to shear a root reinforced soil sample (kN); $\boldsymbol{F_{fallow}}$ is the force required to shear the fallow soil (kN), and; $\boldsymbol{N}$ is the number of roots (of identical dimensions and material properties) in the rooted soil sample.

For the 1.6 mm diameter rubber root analogues, Figures 6.10 (a) and (b), respectively, compare (i) the theoretical and experimental F_{root} - displacement data and (ii) the theoretical root and soil deformation

behaviour (predicted using soil strengths of ϕ' = 34.0° and ϕ' = 59.1°). As demonstrated, the definition of soil strength (or *p-y* spring capacity) has a significant impact on the output of the numerical modelling. This is because, for a given root material, it defines the ease with which the root can deform relative to the soil (i.e. the number of springs that activate) and the maximum possible soil response (i.e. the lesser of the sum of p_u in all springs sitting either above or below the shear plane).

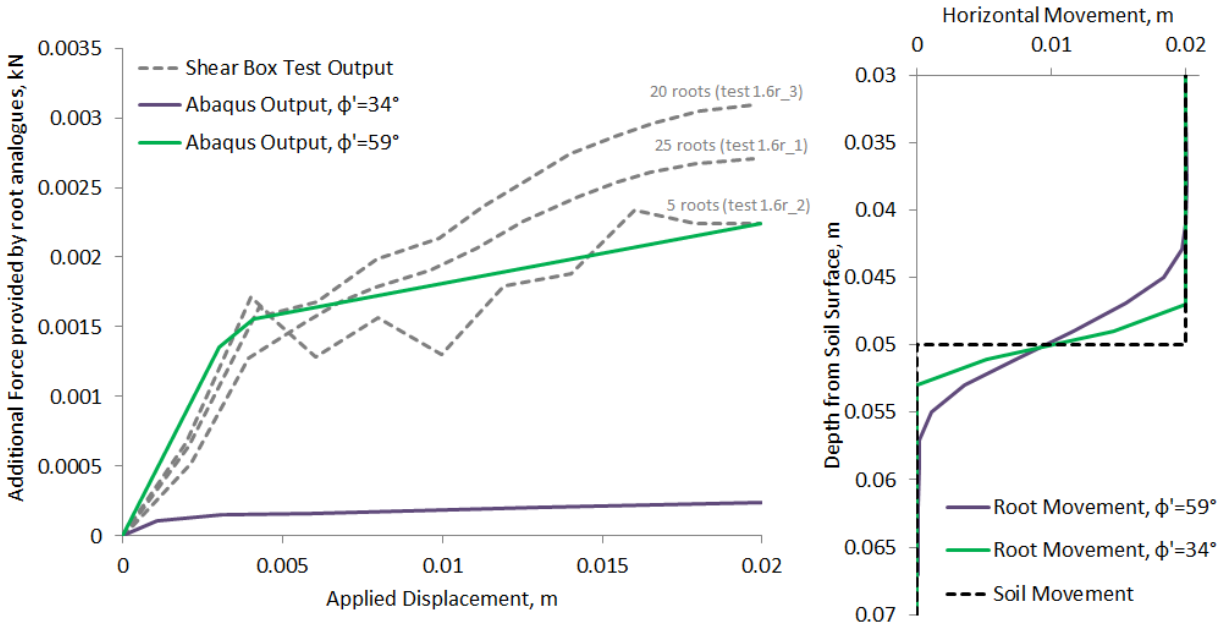

Figure 6.10: (a) Comparison of measured and predicted F_{root} – displacement curves, (b) predicted horizontal displacement of the root and soil about the shear plane. 1.6 mm diameter rubber root analogues.

In Figure 6.10 (b), the weakest soil model (ϕ' = 34.0°) is shown to provide a poor resistance to root deformation. As a result, the output of the numerical simulation does not emulate the experimentally measured reinforcing potential (see Figure 6.10 (a)). The stronger soil model (ϕ' = 59.1°), on the other hand, is shown to provide a high resistance to root movement. This allows the root to stretch significantly within a localised area across the shear plane, develop a large tensile stress and thus provide superior reinforcing potential (Figure 6.10 (a)). In terms of practical applications, these models demonstrate that increasing soil strength will improve both the shear strength of the soil and the extra root contribution to that strength. This is a key finding as current c_R'-based models assume that c_R' is based only on root properties (T_{root} and *RAR*), and not both soil and root properties. c_R' is therefore not independent of soil type, and may explain the reduced scatter in Figure 5.19 when the root contribution is defined within a *friction angle* rather than *cohesion* framework. It should be cautioned, however, that increasing soil strength hinders root growth (strength, scale) and increases

the likelihood of reinforcement failure through root breakage. A balance, therefore, must be made between getting the most out of mechanical root reinforcement and providing an environment in which plants can thrive (which will ultimately further improve reinforcement). Furthermore, these models highlight the importance of correctly representing the soil properties. An incorrect soil definition can significantly under- or over-estimate the contribution of a root to a soils strength.

Having established the impact of soil properties, the theoretical and experimental F_{root}-displacement behaviour was compared. In Figure 6.10 (a), it is demonstrated that when a soil strength of $\phi' = 34.0°$ is used to define the *p-y* springs; the numerical model significantly underestimates the contribution of a single root. This is akin to the output of the uprooting model, which required the inclusion of dilation at low effective stress to accurately represent the behaviour of the soil and, therefore, the soil root interaction (see Chapter 4). Including the effects of dilation (ϕ'=59.1°), however, appears to provide *p-y* springs that can be incorporated into the numerical model and used to successfully predict the contribution of a root to soil shear strength (see Figure 6.10 (a)).

Having demonstrated that $\phi' = 34.0°$ is an unsuitable soil model, Figure 6.11 shows the theoretical and experimental F_{root}-displacement curves and the theoretical root deformation behaviour of the 3.0mm diameter rubber and wooden root analogues, using $\phi' = 59.1°$. As demonstrated, the proposed predictive tool continues to provide a reasonable account of a root's contribution to soil shear strength, particularly when considering flexible roots. It should be noted, however, that when a small number of flexible roots is considered in the laboratory shear box tests, the sample experiences peak shear behaviour followed by a rapid decrease in strength. This behaviour is not reflected in the numerical modelling and may indicate a variation in reinforcing mechanism, due to changes in RAR, that is not accounted for in the proposed calculation model (Figure 6.11 (a)). As such, when a soil sample with a small number of roots is considered (such as a soil reinforced by a non-established plant), the numerical model may over-estimate root contribution. If this behaviour was better understood, it is possible that a representative non-linear multiplier could be introduced to scale the *p-y* curves and account for the consequent change in soil root interaction.

Overestimation is also evident when considering wooden root analogues (Figure 6.11 (b)). Figure 6.11 (c) shows that the theoretically derived deformation of a wooden root analgue below the shear plane is very small. This contrasts with the experimentally observed root movements, presented in Table 5.4, which show the root to displace along its entire length (rotating about a point sitting below

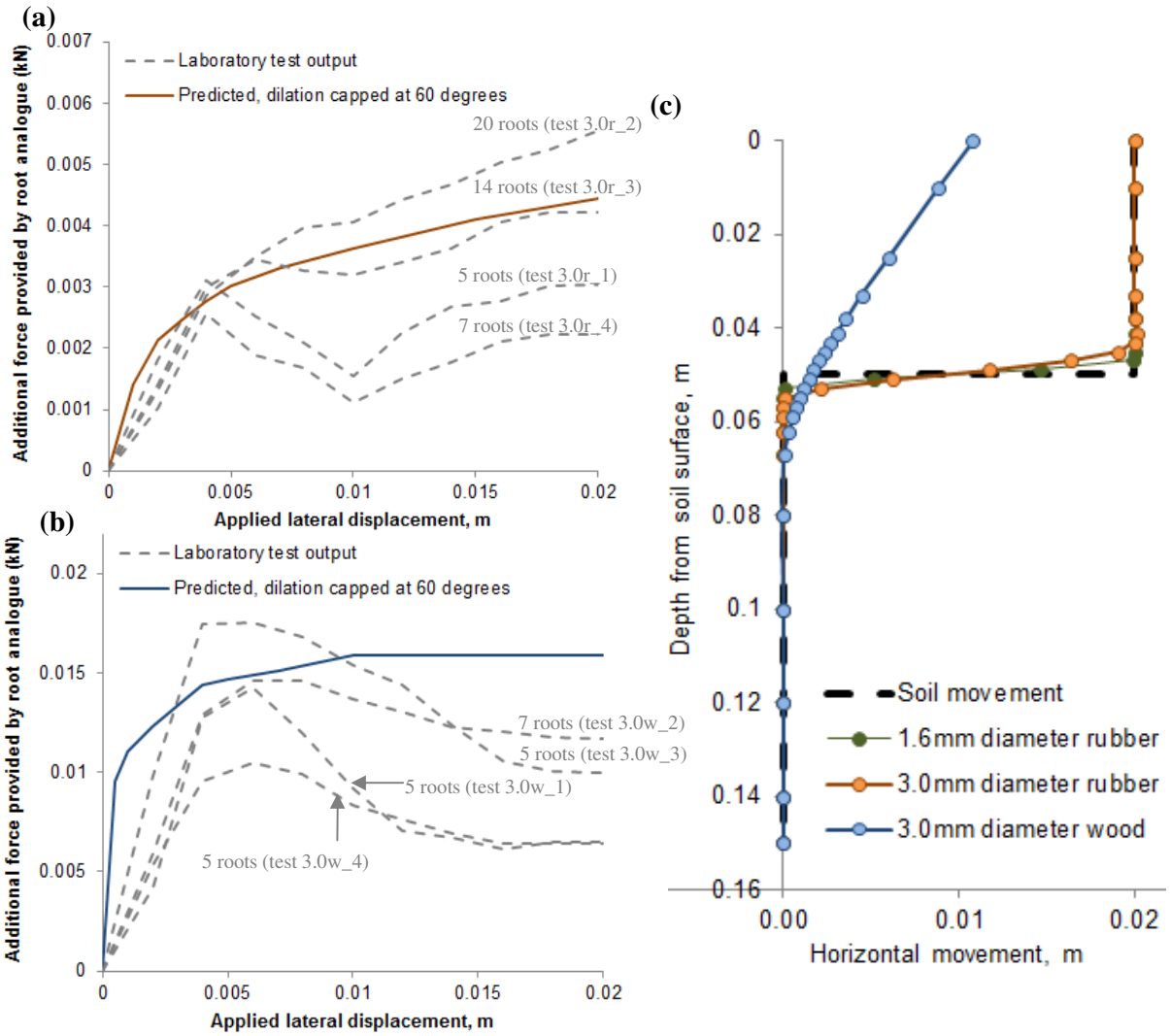

Figure 6.11: Predicted response of 3.0mm diameter root analogues. (a) F_{root}-displacement data for rubber root analogue, (b) F_{root}-displacement data for wooden root analogue, and (c) deformation of root and soil during loading. All tests consider a soil model of $\phi = 59.1°$.

the shear plane and bending slightly across the shear plane) during loading. This could indicate that the soil root interaction below the shear plane is weaker in reality than the strength predicted by Reese *et al.* (1974), which could in turn explain the discrepency between the theoretical and experimental force-displacement curves (see Figure 6.11 (b)). In particular, Table 5.4 shows that, in the early stages of shearing, the root resists loading through bending (as is predicted through numerical modelling). At a critical point, the bending behaviour translates to the root tip causing the entire root to rotate about a point (which sits below the shear plane in this case). This relieves a degree of bending within the root and causes a sudden reduction in the force required to shear the system (see Figure 6.11 (b)). The theoretical response, however, fails to account for root rotation because the maximum root contribution above the shear plane (i.e. the maximum force in each

spring) is reached before the bending translates down the root (Figure 6.11 (c)). As a result, the soil above the shear plane continues to displace with no impact on root deformation (after 10mm of applied displacement) rather than initiating rotation. This mimics a flow failure and is evident on the force-displacement curve as a constant force with increasing applied displacement. A similar behaviour is also evident when considering the experimentally derived force-displacement curves, which could indicate that a flow mechanism was present during the laboratory shear box tests after the root had rotated to a certain degree. As the numerical modelling does not account for root rotation, it does not predict peak behaviour and, as a result, over estimates the later stages of shearing.

6.5.2 Scaling the output of the numerical model to represent root groups

The numerical simulations can be used to predict the contribution of a single root only to the shear strength of a soil. Through considering the effects of root interaction due to shadowing (as discussed in Section 5.4.1), however, the output can be scaled in order to predict the contribution of a root group. This is shown in Equation 6.13, below:

$$F_{root-group} = F_{root} \cdot N \cdot p_m \qquad \text{Eq 6.13}$$

Where: $\boldsymbol{F_{root\text{-}group}}$ is the additional shear force provided by a group of roots (kN); $\boldsymbol{F_{root}}$ is the additional shear force provided by a single root (kN); $\boldsymbol{N}$ is the number of roots, and; $\boldsymbol{p_m}$ is the p multiplier (to account for any group effects), which can be taken from Figure 5.14.

In design applications, however, it is more likely that the RAR, rather than the number of roots, will be known. In this case, *n* in Equation 6.13 can be estimated as;

$$N = \frac{RAR \cdot A_{fs}}{\pi \cdot \frac{D_{av}{}^2}{4}} \qquad \text{Eq 6.13 (a)}$$

Where: $\boldsymbol{RAR}$ is the root area ratio; $\boldsymbol{A_{fs}}$ is the plan area of the soil slip plane / failure surface (m^2), and; $\boldsymbol{D_{av}}$ is the average root diameter (m).

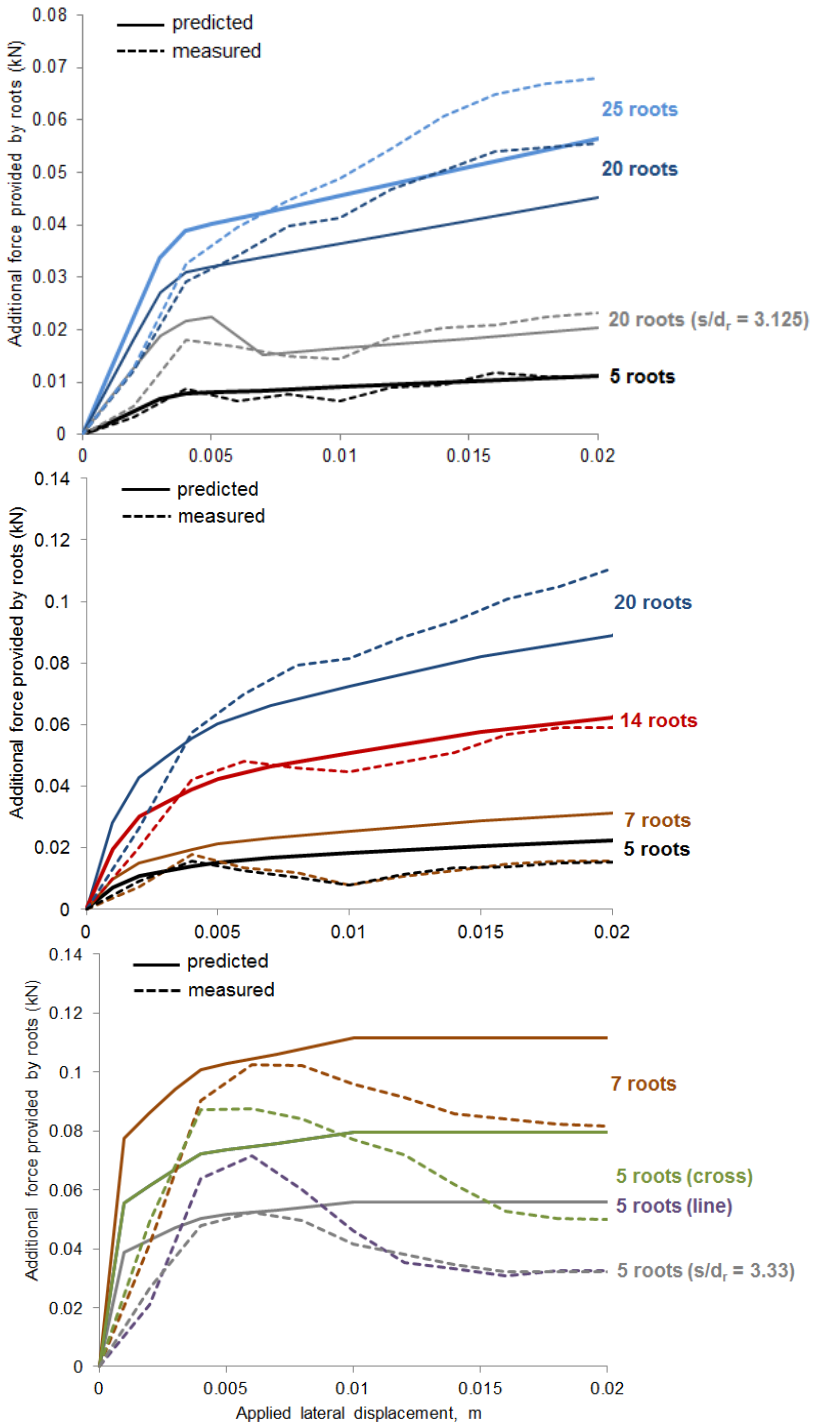

Figure 6.12: predicted and measured F_{root}-displacement data (scaled to model root groups) of: (a) 1.6mm diameter rubber root analogues, (b) 3.0mm diameter rubber root analogues, and (c) 3.0mm diameter wooden root analogues.

Figure 6.12 shows the theoretical and experimental estimations of root contribution, using a variety of root properties and groupings (see Figure 5.8). As demonstrated, the proposed modelling technique provides a lower bound estimate of root contribution when considering flexible roots (with the exception of groups of 5 or 7 3.0mm diameter roots). This is favourable in design applications as it ensures that root reinforced soil structures are likely to be slightly stronger than anticipated. The modelling technique, however, does not currently account for the subtle changes in force-displacement behaviour that occur as a result of changes in RAR (or number of roots). Moreover, it significantly overestimates the contribution of the Beech dowel groups (Figure 6.12 (c)). This indicates scope for improvement, perhaps through: (i) reassessing the soil strength model such that the soil below the shear plane allows for more root movement, (ii) improving the definition of root material properties, and/or (iii) allowing the root to slip vertically (i.e. including *t-z* springs).

It should also be noted from Figure 6.12 that the *p-y* model presented herein provides a complete resistance – soil slip relationship, including information on the root contribution below ultimate conditions. This is a significant improvement in fidelity compared to current c'_R-based models which model only strength increase. While the latter is adequate for use in stability calculations (where only strength properties are required), the *p-y* model is expected to be much more useful in defining the overall continuum properties of rooted soil in finite element models, where both stiffness and strength should be modelled.

6.5.3 Incorporating uprooting into shear simulations

The current numerical model does not allow the root to slip vertically (as it is restrained at its tip, see Figure 6.9). Slippage from the stable soil mass, however, was observed after large displacements (greater than 20mm, see Table 5.4) in the cross section-front shear box tests that considered roots of 100mm and 150mm length and was assumed to take place after small displacements (less than 20mm, see Figure 5.13) in the full section-centre tests that considered roots of 65mm length. A numerical model that combines *p-y* and *t-z* methodology (and therefore allows slippage) was therefore constructed and is presented in Figure 6.13, along with a corresponding *p-y* only model. As demonstrated, the combined model represents vertical (or axial) restraint through a series of discrete *t-z* springs, rather than a roller connection at the root tip (as is considered in the *p-y* only model). This improved representation of axial restraint forms the only difference between the models. The properties of the *t-z* springs are calculated as described in Section 4.5.1, while the remaining

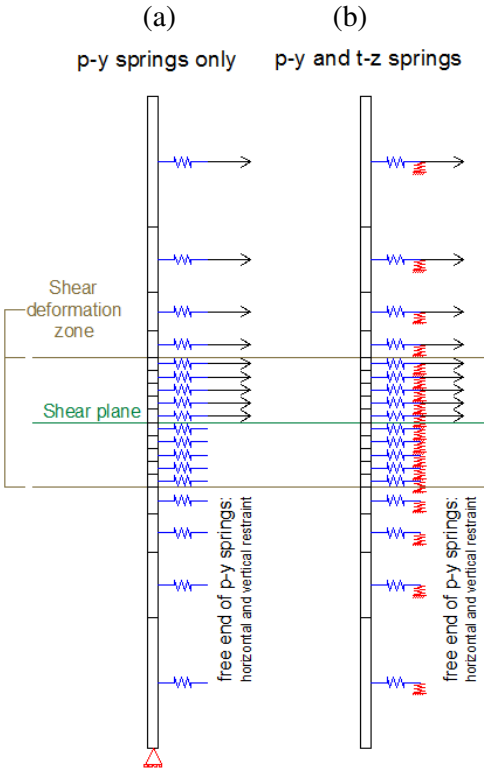

Figure 6.13: Overview of the scope of numerical models representing 100mm long rubber root analogues. (a) *p-y* only model, (b) combined *p-y* and *t-z* model.

properties are defined as described in Section 6.4. The models were otherwise constructed in Abaqus/CAE as described in Figure 6.9 and Table 6.2. The root length considered is 100mm, which provides 50mm of anchorage into the stable soil mass (when considering a shear-plane depth of 50mm) and is consistent with the uprooting tests described in Chapter 3.

Figure 6.14 presents the output of these numerical models. As demonstrated, despite a radical change in the representation of vertical restraint, both the combined *p-y* and *t-z* model and the *p-y* only model predict an identical root contribution. The reason for this is somewhat unclear. During loading, the root deformation about the shear plane is significant, which indicates the development of significant axial loading. In the *p*-y only models, the axial load should translate to the root tip, where it is supported by a vertical restraint. In the combined *p-y* and *t-z* model, it should translate to the *t-z* springs, which should extend (or compress) to allow root extension and/or slippage. In the *p-y* only model, however, the tension developed within the stretch of root crossing the shear plane does not appear to translate to the root tip. This is demonstrated in Figure 6.15, which shows the vertical resisting force in the roller connection (*p-y* only model) after 20mm of applied displacement. As demonstrated, this force is not only extremely small but appears to decrease with increasing deformation past a critical point. As increasing the displacement of the upper soil mass leads to

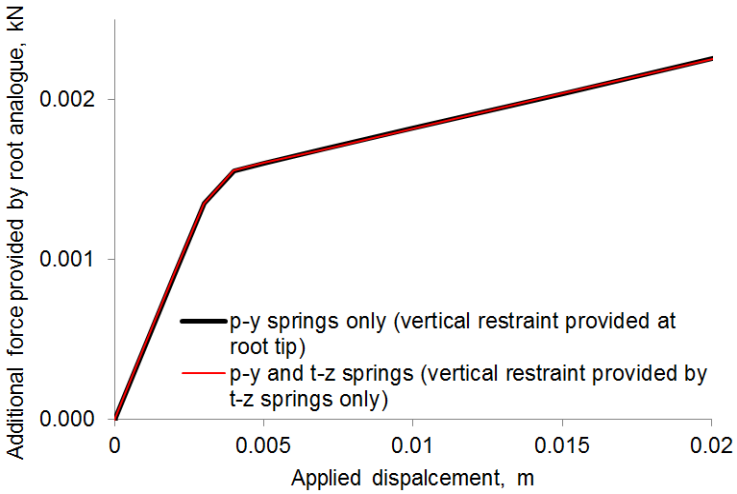

Figure 6.14: Predicted contribution of a single root to soil shear resistance, calculated using both a p-y only model and a combined *p-y* and *t-z* model.

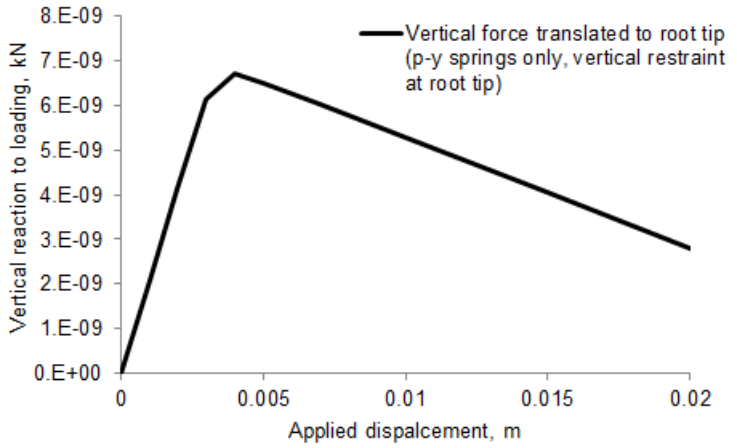

Figure 6.15: Predicted vertical force at root tip (calculated using *p-y* only model) after 20mm of applied displacement.

increasing root deformation and, therefore, increasing tensile force within the root, it is expected that the root will pull out of the soil with increasing displacement. This is confirmed by the cross section-front physical-model, which showed progressive pull out during loading (see Section 5.4.2.2). A possible explanation for the unusual output of the numerical modelling is that the *p-y* springs are absorbing the axial loading within the root, leaving only very small (or negligible) loads to be taken either to the roller connection or to the *t-z* springs. This could also explain why a difference in output is not observed between the *p-y* only and *p-y/t-z* models.

In an attempt to better understand this output, a series of additional root models were constructed and analysed, as shown in Figure 6.16. These models share the same root, element, spring and loading properties as the combined *p*-*y* and *t*-*z* model, but have been slightly altered in order to establish the impact of different model aspects. Model A considers *p*-y springs only, providing no vertical support to the root but maintaining vertical support to the free end of the *p*-*y* springs. Model B considers both *p*-*y* and *t*-*z* springs, but with no vertical support to the free end of the *p*-*y* springs (allowing them to translate vertically with the root, if required). Model C also considers both *p*-*y* and *t*-*z* springs, but with a global *t*-*z* spring at the root tip (as opposed to a series of springs along the root's length). The stiffness of this global *t*-*z* spring is simply the resultant global root pull-out load-displacement curve from a *t*-z pull-out analysis. Finally, model D considers *t*-*z* springs only. In this case, the horizontal (or shear) loading is applied to the root itself. Given that the relative displacement between a flexible root and the soil is approximately zero along the majority of the root (see Figure 5.22), such a loading condition is considered to be a fair representation of soil root displacement (between soil and flexible roots only). The contribution of each root element to the soil shear strength, *p*, is measured as:

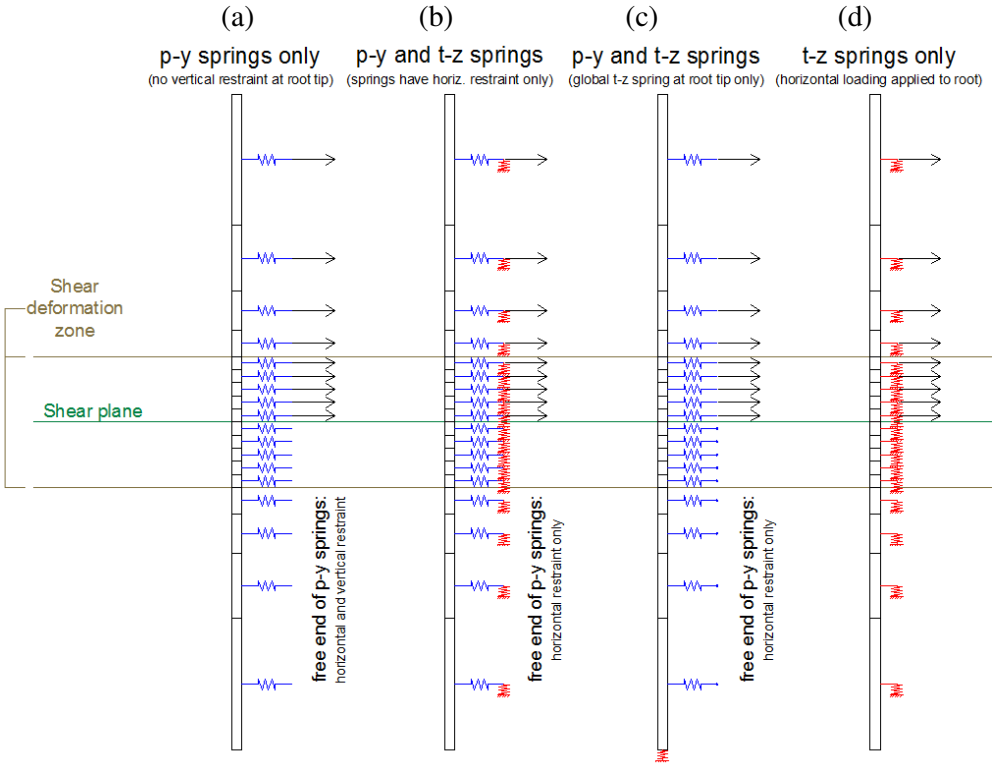

Figure 6.16: Altering root model in order to analyse the impact of different model aspects (a) *p*-*y* only model, with no vertical restraint (b) combined *p*-*y* and *t*-*z* model, free end of the springs subject to horizontal restraint only, (c) combined *p*-*y* and *t*-*z* model, global *t*-*z* spring considered at root tip, and (d) *t*-*z* only model (loading applied to root itself).

$$p = t \cdot \cos(UR3) \qquad \text{Eq 6.14}$$

Where: ***UR3*** is the rotation of the root elements to the horizontal

Figure 6.17 shows the output of these numerical simulations. As demonstrated, vertically restraining the root within a *p-y* model has a significant impact on its response to lateral loading. The form of vertical restraint (be it a series of *t-z* springs (Model B), a global *t-z* spring (Model C) or a roller connection (Original Model)), however, is shown to be unimportant. This is likely to be the result of the extremely small force that is translated to the root tip during loading (see Figure 6.15).

When vertical restraint is removed from the system altogether (Model A), the root undergoes significant and extremely unrealistic vertical displacements (Figure 6.18). In particular, the model suggests that the root will be driven approximately 300m into the stable soil mass as a result of an applied horizontal displacement of 0.005m. This implies that it is easier for the root to move along the vertical rather than the horizontal axis, which is not the case in reality. The reason for such a large displacement is not clear and would benefit from further analysis. Despite such a large vertical displacement, however, the horizontal response of the root is very similar to the remaining *p-y* models. The large displacements, however, would suggest that the springs are stretched to full capacity and, therefore, this is an unlikely outcome.

Having studied the effects of modelling soil root interaction through either *p-y* springs alone or both *p-y* and *t-z* springs, the impact of modelling soil root interaction through *t-z* springs alone was studied (model D). As demonstrated in Figure 6.17, such a model predicts a root contribution that is significantly smaller than expected.

The initial results of the *p-y* based numerical model are promising, showing that when sufficient anchorage into the stable soil mass is considered, the model can predict root response with sufficient accuracy. The subtle complexities of the lateral deformation process, however, are not yet fully understood and this has hindered the development of the model. Further research in this area would be beneficial.

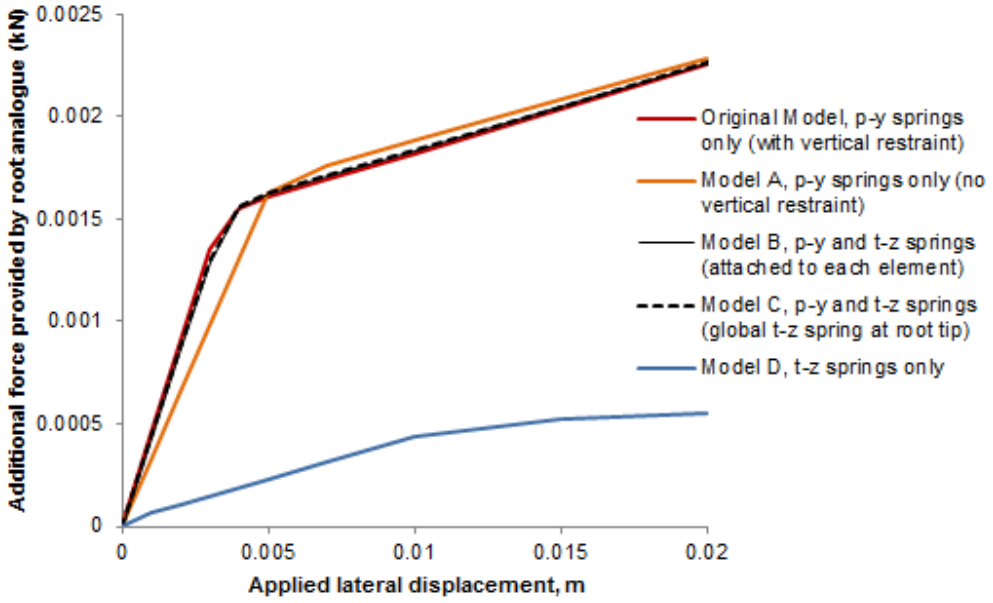

Figure 6.17: Comparison of numerical simulations using models A, B, C and D.

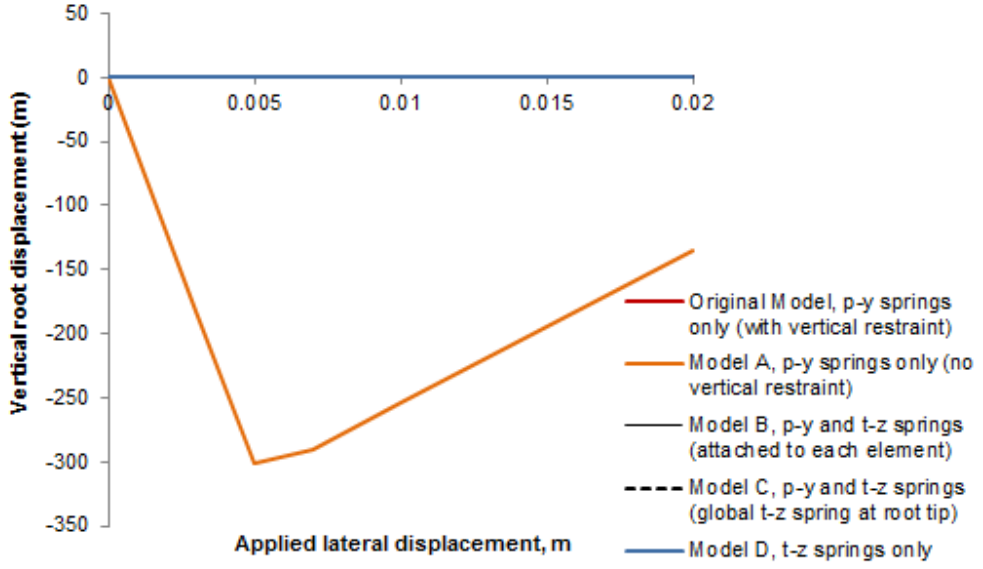

Figure 6.18: Vertical root movement at root tip, using models A, B, C and D.

6.6 Defining p-y springs from PIV observations (Rubber roots only)

As with axial loading, the beam-on-Winkler foundation theory can be applied to measured pile displacement (or strain) data in order estimate soil-pile interaction during lateral loading. Indeed, the response of the soil to pile deformation is always proportional to the intensity of load that presents within the pile, regardless of the loading condition. Under lateral loading, the key mechanisms (or responses) that develop within a pile are: deflection, rotation (or sloping), bending, shearing and lateral resistance (or load intensity). By equilibrium, the load intensity must be equal (but opposite) to the response of the soil, *p*. These mechanisms are explained in Figure 6.19, and can be calculated, if the flexural stiffness of the pile (*EI*) is known, through Equations 6.15 to 6.18.

$$\chi = \frac{dh_d}{dx} \qquad \text{Eq 6.15}$$

$$M_{pile} = (EI)_{pile} \cdot \frac{d^2 h_d}{dx^2} \qquad \text{Eq 6.16}$$

$$V_{pile} = (EI)_{pile} \cdot \frac{d^3 h_d}{dx^3} \qquad \text{Eq 6.17}$$

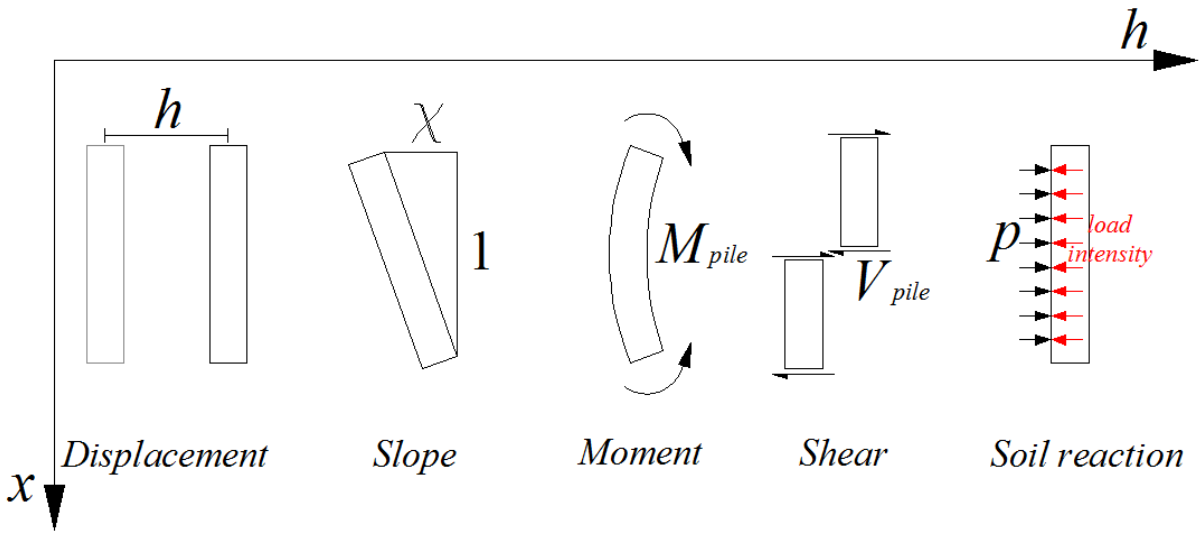

Figure 6.19: Design forces within a root during shear loading (*Adapted from Basu et al., 2008*).

$$p = (EI)_{pile} \cdot \frac{d^4 h_d}{dx^4} \qquad \text{Eq 6.18}$$

Where: χ is the slope of the pile; x is the location along the pile (measured from the pile tip, m); h_d is the horizontal displacement of the pile (m); M_{pile} is the bending moment within the pile (kNm); E_{pile} is the Young's modulus of the pile (kPa); I_{pile} is the pile's second moment of area (m^4); V_{pile} is the shear force within the pile (kN), and; p is the lateral soil pressure per unit length (load intensity, kN/m).

If the distribution of p along the length of a pile is calculated at various stages throughout loading, then the relationship between p and y can be established at any point x along the piles length, where;

$$y = h_{soil} - h_d \qquad \text{Eq 6.19}$$

Where: y is the relative soil root displacement (m), and: h_{soil} is the horizontal displacement of the soil (m).

This process is explained in Figure 6.20 and was used in this project to quantify the p-y behaviour of soil root systems. It should be noted that when calculating y the horizontal soil movement (h_{soil}) needs to be measured at a distance (taken as greater than $6 \cdot D_{pile}$ in this Thesis) from the pile, in order to represent the global soil behaviour (rather than the pile adjacent soil behaviour). If loading is applied to the top of the pile only (rather than through soil shearing failure), then the global soil movement will be equal to zero and y will be equal to h_d.

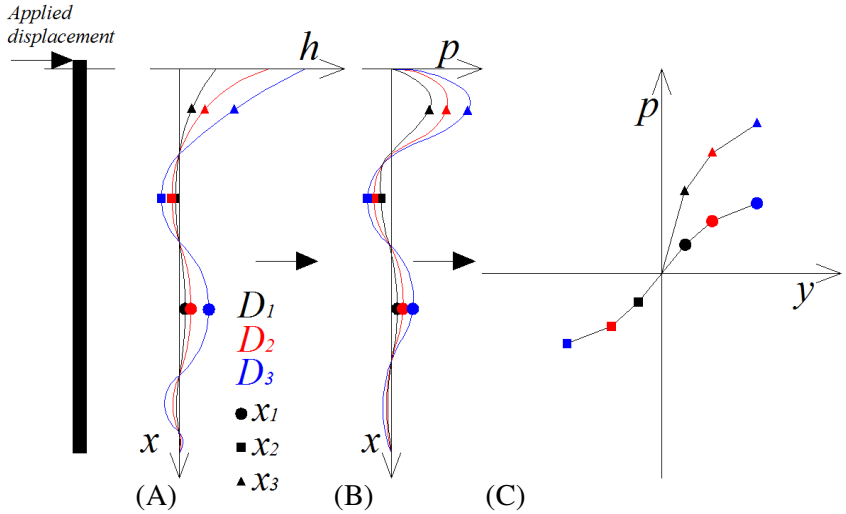

Figure 6.20: Determination of p-y curves using the horizontal root displacement (h), location on root (x), load intensity (p) and relative root-pile movement (y). (A) h_d-x relatioinship is measured during testing, (B) Equation 6.18 is employed to estimate p-x relationship, (C) Data from (A) and (B) are rearranged along with observed soil movement to establish p-y curves at various points, x, along the root length. Note: h_d data is converted to y data through subtracting soil moevement.

Having established a means of quantifying the magnitude of p per metre depth at various points, x, along a pile's length, the total soil response (p_e) to the deformation of a particular element (or stretch of pile) can be obtained. This is achieved through scaling each p-y spring by the length of its corresponding element, using Equation 6.10.

Assuming that roots can be modelled in the same way as piles, these equations were applied to the horizontal root displacement (or h_d-x) data that was measured in Chapter 5 (from GeoPIV analysis of cross section-front models). As with the cross section-front uprooting tests, however, only the flexible root analogues could be clearly viewed (and measured) during shear loading (see Figure 5.22). This is problematic in the development of p-y springs as these roots displace very little relative to the soil (i.e. y stays very small), except within the small shear deformation zone. As the theoretical p-y springs require y values as small as 0.0001m to achieve ultimate p behaviour, however, it was considered that the deformation zone (20mm stretch surrounding the shear plane) would present sufficient data for experimentally determining suitable p-y curves.

6.6.1 Application to laboratory shear box tests

The process of applying the beam-on-Winkler foundation theory to the measured root displacement data (from the cross section-front laboratory shear box tests) is the same as that described in Section 4.4.2.1. That is, the displacement data can be represented using a polynomial equation and used directly in Equations 6.18 (a) and 6.19 in order to establish p-y curves for the half-root analogues or, following a number of assumptions, can be used to establish p-y curves for the full-root analogues. The required assumptions are: (i) the soil root interaction within a cross section-front test equates to half of the soil root interaction within a full section-centre test, and; (ii) any friction that may be present between the Viton and Perspex surfaces is negligible. Equation 6.18 can therefore be adapted in order to estimate the distribution of soil reaction along a full root, p_{full}, using the displacement data gathered from the deformation of a half root, see below;

$$p_{full} = 2 \cdot \left[E \cdot I_{r,half} \cdot \frac{d^4 h_d}{dx^4} \right] \qquad \text{Eq 6.20}$$

Where: $\boldsymbol{P_{full}}$ is the soil response of a full root analogue (kN/m); $\boldsymbol{E}$ is the Young's modulus of a full root analogue (kPa); $\boldsymbol{I_{r,half}}$ is the second moment of area of a half root; $\boldsymbol{h_d}$ is the horizontal displacement of a half root (m), and; $\boldsymbol{x}$ is the position along the root (m).

6.6.1.1 Fitting a polynomial equation to the h-x data

A polynomial equation in the following form was selected to represent the measured *h*-*x* data:

$$h_d = e \cdot x^5 + f \cdot x^6 + g \cdot x^7 + h \cdot x^8 + i \cdot x^9 + j \cdot x^{10} + k \cdot x^{11} + l \cdot x^{12} \qquad \text{Eq 6.21}$$

Where: $\boldsymbol{e}, \boldsymbol{f}, \boldsymbol{g}, \boldsymbol{h}, \boldsymbol{i}, \boldsymbol{j}, \boldsymbol{k}, \boldsymbol{l}$ are constants

Its origin was set at the root tip, where slope, bending moment, shear force and soil reaction are expected to remain zero throughout loading. As such, x^1, x^2, x^3 and x^4 terms were excluded from the equation. Suitable constants (*e* through to *l*) for each set of h_d-*x* data were obtained through use of Gaussian elimination and back substitution, as described fully in Section 4.4.2.1. It should be noted that it is extremely important that the predicted h_d-*x* curves match the measured h_d-*x* curves as closely as possible, as they have to be differentiated four times in order to calculate *p*. Any errors, therefore, will be magnified. Figure 6.21 shows the success of Equation 6.21 at predicting the measured *x*-h_d data at various stages throughout loading.

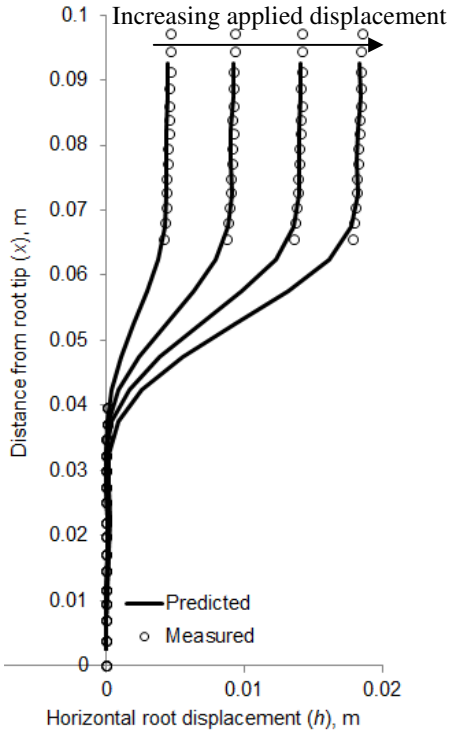

Figure 6.21: Comparison of predicted and measured h_d-*x* data.

6.6.1.2 Improving calcultion efficiency

As with the determination of *t*-z springs, the efficiency of determining *p*-*y* springs was improved through creating a MatLab .m file. This file scripts the calculation process outlined in Section 6.6 and requires input in the form of; (i) GeoPIV analysis output files (i.e. h_d-x and h_{soil}-x data, see Chapter 5),

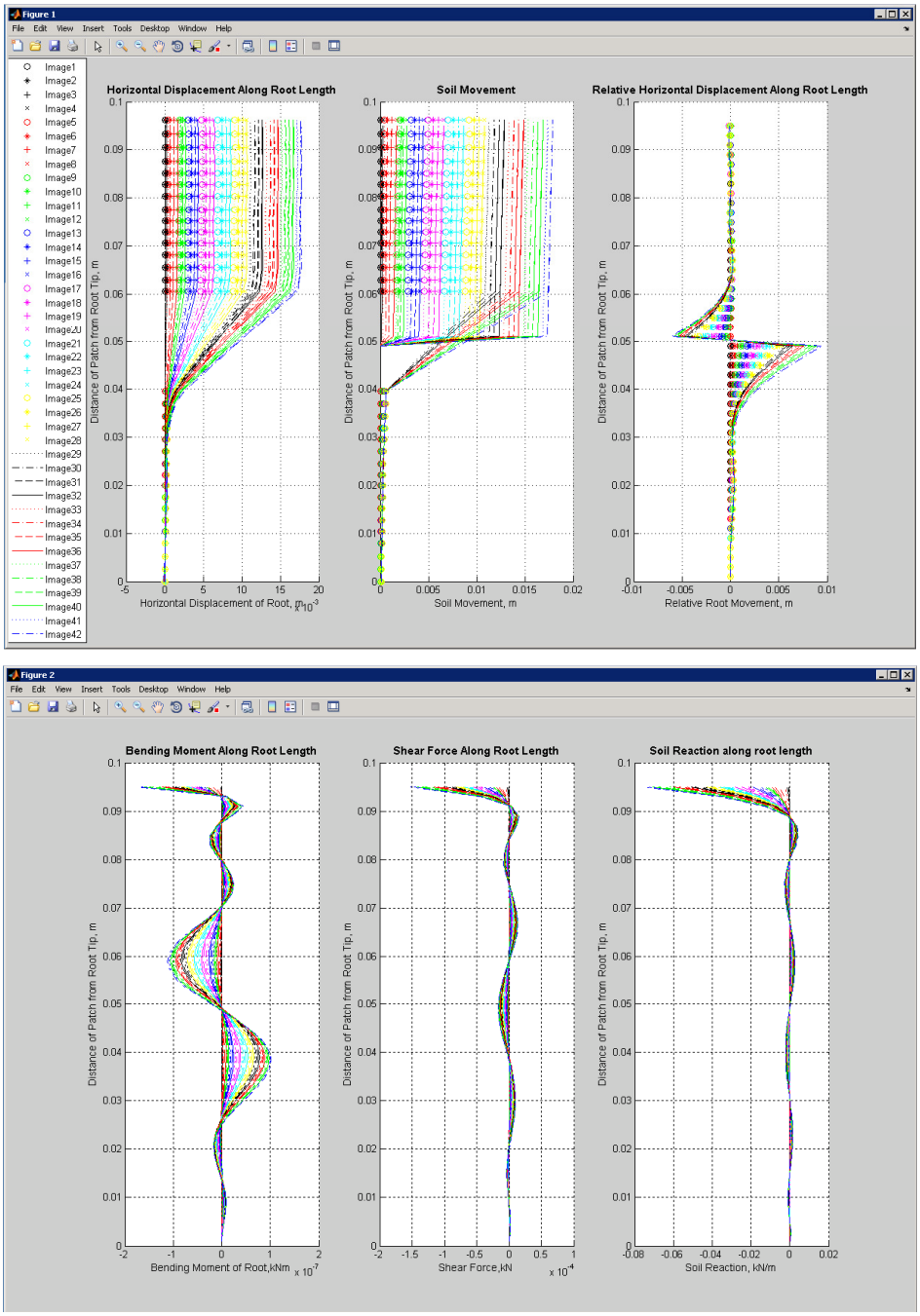

Figure 6.22: Bending, shearing and soil reaction provided by PYCurve.

(ii) a conversion factor (to convert GeoPIV output from pixels to m), (iii) the number of springs sitting above the shear plane, (iv) basic root and soil properties, and (v) the desired spring spacing. The file is named PYCurve and its script is presented in Appendix B.

Prior to running PYCurve in MatLAB, the *input information* section of the code should be completed. Following this, the text 'PYCurve' should be entered into the MatLab command line and the file 'GeoPIV_launcher' should be selected from the consequent pop up window. The PYCode will then run through all the calculations and present the data for each *p-y* spring, as well as plots of *p-y*, *x-p*, *x-*V_{root}, *x-*M_{root} and *x-*h_d behaviour, as shown in Figure 6.22. In order to run PYCurve, the following files are required: consolidate8.m, GeoPIV_launcher.txt and all GeoPIV output files.

6.6.2 *p-y* curves

Figure 6.23 shows the expected distribution of soil reaction, deflection, slope and bending moment along the length of a pile after the application of a lateral force to its head. When compared to the calculated behaviour of the length of root analogue below the shear plane (between 0m and 0.05m in Figure 6.22), and thus below the point of lateral loading, the curves are very similar. This suggests that the first principle modelling technique is successful. Due to the ability of the rubber root analogue to flex, however, the relative displacement (y) along the length of the root is small, other than at the shear plane location. At this point, however, the soil reaction is very small. Considering a 20mm stretch of root across the shear plane Figure 6.24 shows *p-y* curves for a 3.0mm rubber root analogue being sheared in sand, as calculated from using the experimental data. As demonstrated, the scale of these curves is significantly reduced (by a factor of 10,000) from those calculated using first principles (see Figure 6.8). This could be the result of a possible disproportional loss of flexural stiffness when halving the rubber root analogues. Moreover, these curves do not reach peak behaviour within the 0.01m of applied displacement considered in this plot. This suggests that it could be worth considering a more gentle initial stiffness in the theoretical *p-y* springs. Below the shear plane, the stiffness of the springs reduces as the depth from the soil surface is reduced. This is not the case above the shear plane. In general, the stiffness of the springs increase with reducing depth from the soil surface above the shear plane. It is possible that this is the result of soil dilation at low effective stress, something that was considered in the development of theoretical *p-y* springs.

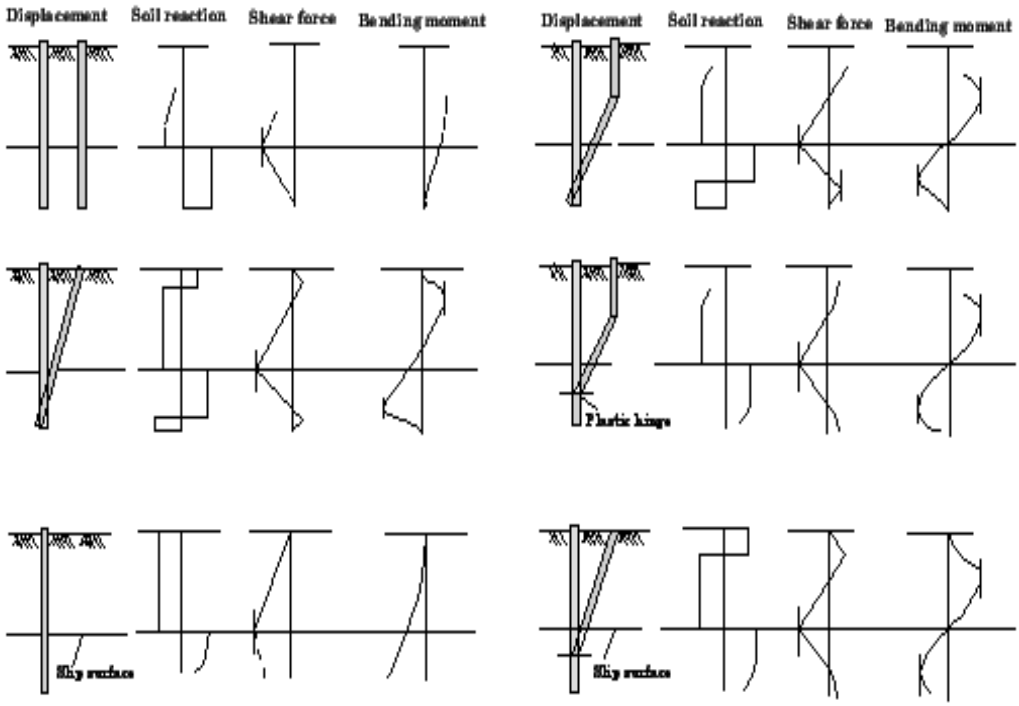

Figure 6.23: Expected distribution of pile loading, soil reaction, pile deflection, pile slope and pile bending moment on application of a lateral load (*Viggiani, 1982*).

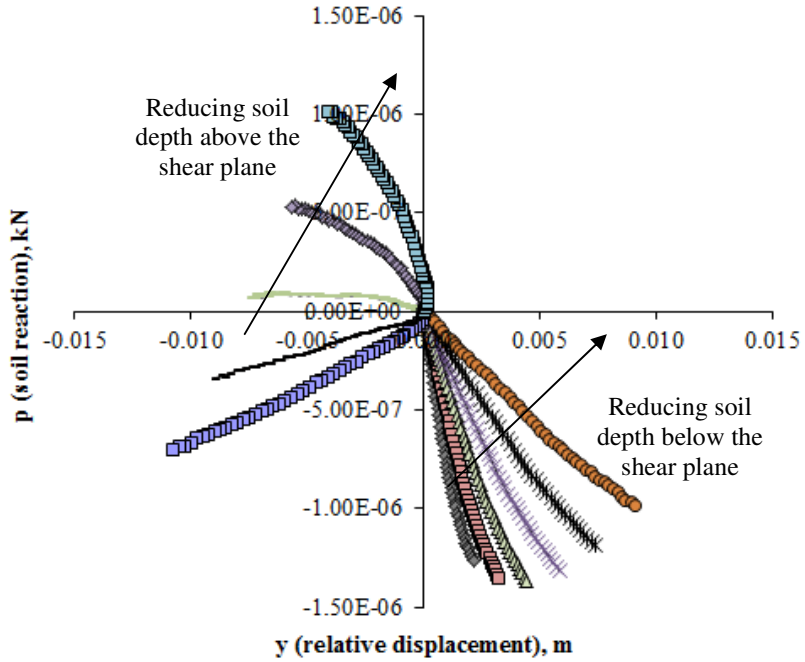

Figure 6.24: Typical *p-y* curves about the shear plane for a half root analogue being shearing in sand. Springs are located at 2mm distances from each other.

Due to the problems with deriving the *p-y* behaviour (curves do not reach peak behaviour; *p* values are too small), they were not considered in the numerical modelling phase of the project. The theoretical springs worked very well at modelling soil root interaction and, therefore, it is apparent that the springs from PIV would not provide adequate stiffness for modelling the soil conditions. The use of the theoretical springs would also be much more useful for application to other cases or in design, as it requires basic soil and root properties and geometric information, rather than requiring PIV observation. Nevertheless, it is dissapointing that the derivation of *p-y* curves was not able to provide additional validation of the suitability of the proposed theoretical curves, to supplement the validation through the shearbox tests.

6.6.3 Discussions and conclusions

A numerical modelling technique, which uses theoretically derived soil root interaction properties, was developed in Abaqus CAE in order to predict a root's contribution to soil shear strength. It is based on the *p-y* calculation model that was proposed by Reese *et al.* (1974) and is, to date, well-used and well-trusted within the geotechnical engineering community for application to the lateral loading of piles.

The proposed predictive tool was shown to successfully estimate the additional shearing resistance provided by roots, of varying diameter and material properties, if the roots were sufficiently anchored into the stable soil mass; that is, when the lateral reaction between the root and soil governs the overall behaviour of the system. The development of resistance with soil shear displacement could be determined in addition to the additional ultimate contribution of the root, which is a significant improvement on existing strength-only based models. The model also demonstrated that a root's mechanical contribution to soil strength is dependent on both root and soil properties, as previously demonstrated in Chapter 5.

When considering a combined *p-y* and *t-z* model, however, the tool was not successful. The combined axial and lateral behaviour is complex and the predictive tool appeared to disregard axial behaviour, using the *p-y* springs to absorb any impending root slippage.

The predictive tool could be improved through:

1. A better understanding of a soil's mechanical properties at low effective stress (i.e. dilation).

   The definition of the properties of the soil mass at low confining stress was shown to be extremely influential to the output of the numerical modelling and therefore it is important that its behaviour is understood for the development of suitable *p-y* relationships.

2. A better understanding of combined axial and lateral interaction.

   A technique for combining axial and lateral soil root interaction, both of which can be independently modelled successfully, needs to be developed.

Nevertheless, the tool shows substantial promise, and it would be straightforward to extend the method to mildly tortuous roots (different initial geometry of root (beam elements), account for the soil passing through layered soils (or zones of very different material properties, through change in *p-y* properties), incorporate variable diameter and material properties along the length of the root (change of element properties), and account for the above ground loading of vegetation (apply a load condition at the root head).

Chapter 7 Conclusions and recommendations for future work

Predicting root reinforcement has significant applications in developing bioengineering techniques and improving the management of agricultural land, forests and naturally vegetated slopes. Existing predictive tools are not consistently reliable, and they generally do not model pre-failure behaviour of root reinforced soil (e.g Wu *et al.*, 1979). There is a need for improved predictive tools to model root reinforcement and increase confidence in, and practical application of, bioengineering techniques (*Sonnenberg, 2008; Schwarz et al., 2009*). This Thesis reports experiments that were performed to develop and test a numerical root reinforcement model based on the *t*-z and *p*-y pile analysis techniques, which simplify the soil inclusion system to a beam-column supported by a series of springs (which model the soil inclusion interaction; *e.g. Reese and Van Impe, 2011*). Pile design analysis techniques were chosen as they are well known to the engineer and model both the axial and bending capacity of inclusions. This modelling approach incorporates the bending capacity of roots, which is commonly neglected in the study of soil root interaction (root reinforcement is usually considered a purely tensile mechanism; e.g. Wu *et al.,* 1979). It was hypothesised that this may be one of the reasons for the shortcomings of existing predictive tools, as woody roots may have significant bending capacity.

7.1 Experimental measurement of root reinforcement during shear and pull-out

The experimental work comprised root pull out and direct shear box tests, on a number of root reinforced soil systems. Tap root analogues, made of Linden wood, Beech wood and Viton rubber, were incorporated into silica sand samples. These simplified root systems provided a bridge between the biological properties of roots and the inert properties of pile foundations (allowing the applicability of pile design techniques to be studied). Moreover, they allowed isolated properties (such as length, stiffness, diameter and spacing) to be considered in a study of root reinforcing capacity. These materials have been used in the past as analogues for plant roots (*Mickovski et al., 2007; Sonnenberg,* 2008). Both full section-centre tests, where the roots were located in the centre of the soil sample, and novel cross section-front tests, where the roots were placed at the edge of the soil sample, were carried out. The latter of these allowed the root soil system to be observed during loading.

The root pull out tests were carried out by S. B Mickovski, formerly of the James Hutton Institute. Their output was re-analysed in this Thesis, with a focus on measuring root displacement during loading and assessing the requirements of a predictive tool that is to quantify axial soil root interaction. For consistency, the direct shear box tests were designed in line with the root pull out tests, considering the same soil and root properties, and sample set up. Again, these tests were analysed with a view to measure displacement fields and assess the requirements of a predictive tool. In addition, a series of full section-centre direct shear box tests was carried out using a variety of root soil systems to investigate a roots contribution to soil shear strength. These tests considered the effects of different RAR, root diameter, root length and root material properties. Their repeatability showed that the effects of root inclusions within a soil are consistent and measurable. The key findings are summarised in Section 5.5. Of significant interest was the finding that soil root interaction is a purely frictional process (see Chapter 4). This conflicts with the commonly used root cohesion factor to describe root contribution, which considers the root as some form of adhesive that binds the soil together. An improvement on this is therefore to use a stress related parameter, such as dilation. Such a suggestion is also made by Diambra *et al.* (2010).

The cross section-front tests were shown to be comparable to the full section-centre tests and were successful at visualising a vertical transect through the soil root system during loading. By capturing the soil root deformation process in a series of digital images, the root movement could be measured during loading (using GeoPIV analysis). This data was later used in the development of the predictive *t*-z and *p*-*y* numerical models. While the root movement could be visualised throughout each test, however, it could not always be estimated accurately using PIV. This is because sand particles became dislodged between the root and the Perspex, ruining the clarity of the root in the digital images, and was particularly problematic when considering the stiffer root analogues. Despite considerable care and control during the experimental set up, this could not be resolved, making the digital images of wooden root analogues unsuitable for further analysis. As a result, much of the development of the predictive tools concentrated on flexible rubber roots only. A future study in this area might consider refining this testing technique, or designing a new technique, such as to better visualise stiff root analogues during loading.

7.2 Numerical modelling of root reinforcement using pile analysis techniques

Two numerical models were designed, in line with the *t-z* and *p-y* pile analysis techniques, to predict the response of a root system to axial and lateral loading. The properties of the *t-z* and *p-y* springs were calculated empirically, using the measurements gained from the GeoPIV analyses of cross section-front laboratory tests, and theoretically, using standard pile design codes (API RP 2A-WSD, 2000 for pull out, and Reese *et al.*, 1974 for direct shear). In the shallow layers of soil that were considered in this study (maximum depth of 0.15m), dilation was shown to significantly influence mechanical soil root interaction. This is consistent with Bolton (1986) and was accounted for in the development of theoretical *t-z* and *p-y* springs.

The axial (or *t-z*) numerical model simulates the uprooting process. Given that the root was considered to sit vertically in the soil and the load was applied axially, this model simulates a very simple deformation process in which the root stretches and displaces in the axial direction only. Likewise, the response of the soil (or *t*-z springs) is purely axial. Constructing the numerical model and understanding its output was therefore a simple process, and the results were very promising when considering the empirically derived *t-z* curves for rubber roots. In particular, the *t-z* numerical model provided an accurate account of the force required to pull a rubber root analogue from either wet or dry sand, as follows: In dry sand, the numerically predicted pull out force displacement curve followed the shape of the experimentally measured curve, but underestimated the peak pull out force by around 20%. This is considerably more accurate than the Ennos (1993) uprooting model, which was shown to underestimate the peak pull out force by around 40% (if dilation is considered in the soil properties), overestimate the critical state pull out and fail to indicate the relationship between applied displacement and pull out capacity (as shown in Figure 4.31). In wet sand, pull out behaviour is more complex. The full section-centre test results revealed two distinct shapes of pull out force displacement curve. The first (and least prominent) showed a loss of soil root interaction after the peak pull out force was reached, as in dry sand, while the second showed continued interaction. The cross section-front tests, however, exclusively showed a loss of interaction. The ability of the numerical modelling technique to simulate uprooting in wet sand was therefore limited to modelling uprooting where a loss of interaction had incurred (as the *t-z* springs were developed solely using the cross section-front tests). In the case of lost interaction, the predicted pull out force displacement curves compared well to the experimental curves, possessing the same shape and scale. Following

these results, the robustness of the modelling technique was tested in order to better understand, and possibly enhance, its limits. This was achieved through carrying out a parametric study that looked into the effects of element size/spring spacing, root material properties, spring definition and loading. It found that spring spacing had an insignificant impact on the model output, but root stiffness, spring definition and loading steps were all crucial. (Note: a change in the applied loading steps does not alter the output of the numerical model, but impacts the available data. Data that is too sparse does not show the full root pull out behaviour and opens the door to poor data interpretation.)

It should be noted that, as there was no laboratory test data suitable for measuring the displacement of stiff roots during pull out loading, the development of empirical *t-z* springs to represent the interaction between wooden root analogues and silica sand could not be generated. Moreover, the standard API (*API RP 2A-WSD, 2000*) design codes were not suitable for modelling soil root interaction, as the simplifications made for pile foundations are not transferrable to plant roots. In particular, API design codes do not consider pile material properties or exact soil properties in their calculation of *t-z* springs. This infers that pile properties do not influence axial pile behaviour, a reasonable assumption given the relatively small range of stiffness's of pile foundation materials. This is not true, however, of plant roots. In this testing programme, for example, the rubber (flexible) tap root analogues displayed a significantly slower mobilisation of peak pull out force and a stretching-uprooting cycle that was not observed in the wooden tap root analogues. Adding lateral branches to the tap root system further showed that wooden (stiff) root analogues offer far superior resistance to uprooting. Moreover, during the development of empirical *t*-z springs for rubber root analogues (based on the cross section-front laboratory tests) the intricacies of soil behaviour at low effective stress were shown to be significant, indicating that exact (rather than approximate) soil properties are required. As a result, the *t-z* numerical model could not be verified for stiff roots. It is hypothesised, however, that as the *t-z* analysis technique was originally developed for stiff pile inclusions, it will be suitable for this application.

The lateral (or *p-y*) numerical model simulates the response of a soil root system to the loading caused by mass soil movements above a known failure plane. This process is much more complex than uprooting, subjecting the root to bending as well as axial loading. As a result, the *p*-y numerical model was not as successful as the *t*-z numerical model. The initial output, where axial interaction was accounted for by a vertical restraint at the root tip (assuming strong anchorage of the lower root throughout the loading process) and *p-y* springs were developed theoretically using Reese *et al.*

(1974) calculation model, was promising. The scale and general shape of the shear force-applied displacement curves compared favourably with those obtained from laboratory tests. In particular, the predicted additional shear force provided by a rubber tap root analogue (with respect to applied displacement) fitted well within the range of output observed within the experimental data (considering laboratory tests where the roots were sufficiently anchored into the mass of soil below the shear plane only). The predicted response of wooden root analogues was less accurate, showing a much slower mobilisation of peak shear contribution than was experimentally measured and no post-peak loss of contribution (as observed in the experimental data). The numerical models, therefore, require improvement in order to better predict the experimental output (wooden root analogues) and model roots with poor anchorage (rubber and wooden root analogues). In an attempt to do this, the fixed vertical restraint was replaced with a series of *t-z* springs. This revealed some problems with the model. In particular, the *p-y* springs appeared to be taking the axial as well as the horizontal loads that develop in the root, making the *t-z* springs redundant. Removing all vertical restraint, however, resulted in the root undergoing enormous vertical displacement. Further work, and detailed analysis of the software function, is therefore required to better understand the subtle complexities of the numerical modelling technique and fully develop this promising predictive tool.

It should be noted that no empirical *p-y* springs were used in the development of the *p-y* numerical model. The images of wooden root analogues could not be used to measure root displacement, as already described. The images of rubber root analogues could be used, but the deformation of the root resulted in very small to no relative displacement between the root and soil (critical data that forms the *y* axis of the *p-y* curves). This meant that empirical *p-y* springs with appropriate properties could not be parameterised.

The results of the numerical models suggest that, provided suitable springs can be established, the *t-z* and *p-y* modelling techniques are applicable to the study of soil root interaction and can be used to predict a roots response to mechanical loading more accurately than existing root analysis tools. The Wu *et al.* (1979) model, for example, is widely criticised for overestimating root contribution as a result of incorporating a number of inappropriate assumptions, such as assuming that every root mobilises its full tensile strength at the same time (*e.g. Shewbridge and Sitar, 1990; Pollen et al., 2004; Pollen, 2007*). As one of the most established predictive models available, a large quantity of research has been carried out in an attempt to develop it into a more accurate tool (*e.g.* Waldren and Dakessian (1981) introduced two new parameters to account for root slippage and root breakage).

This Thesis, however, challenges the fundamentals of such a model, which considers root contribution as a root cohesion factor (calculated using RAR and the tensile capacity of plant roots), by proposing an alternative modelling technique that responds to the findings of extensive laboratory testing. These findings contradict the existing calculation models, such as that proposed by Wu *et al.* (1979) and the FBM, by suggesting that soil root interaction is a frictional process in which root bending plays a significant role. Further research is, however, required in order to develop the numerical models and verify their advantage over existing models.

While above ground loading was not considered in this study, it can be accounted for in the proposed numerical models by adding a load to the top of the root. This allows the full effects of vegetation (above and below ground) to be modelled.

7.3 Recommendations for future work

This Thesis aimed to develop a numerical modelling technique that can be used to predict the response of a root system to mechanical loading more accurately than the existing predictive tools. Specific areas for future study are described in relation to specific sections of the thesis:

Improved quantification of root and soil deformations: In Chapters 3 and 5, cross section-front modelling was used to capture soil root deformation during loading. Soil, however, became dislodged between the root and viewing panel when stiff wooden roots were tested. An alternative testing technique, such as using a soil with a smaller particle size (e.g. silica sand) could eliminate this problem and could allow the development of empirically derived *t-z* and *p-y* curves. Alternative techniques such as X-ray microtomography might be used with 3-D volume correlation techniques if appropriate equipment is available.

Improved t-z and p-y curves: In Chapter 4, empirical *t-z* curves were used to develop the *t-z* numerical model. While the output was beneficial, it would be of greater value in practise to establish theoretical *t-z* curves for root soil interaction. This could be achieved through developing empirical *t-z* curves for a range of root stiffness's and soil types, and analysing the results to look for trends. It would be beneficial to run the same exercise to improve the theoretical *p-y* curves for plant roots. (Note: theoretical *p-y* curves for pile foundations were shown to transfer to the study of soil root interaction, provided dilation at low effective stress was included. Empirical *p-y* curves, which could

not be generated with the data available in this project, would help to optimise these for this application.)

Improved p-y modelling: In Chapter 6, a *p-y* numerical model was developed, but had several shortcomings. The reason for these is unknown to the author, but is thought to be the result of subtle complexities in the deformation process and its simulation. Further analysis of this, and development of the model, would be of great benefit to the study of soil root interaction.

Application of the model to slope stabilisation by roots: One of the key driving forces behind the development of improved predictive tools was to encourage the use of bioengineering for slope stability applications. Use of the proposed numerical models in a slope stability context would be beneficial in measuring their effectiveness. For example, the *p-y* numerical models could be used to quantify the increase in soil dilatancy as a result of root inclusions. This information could then be used to construct a 2- or 3-D slope model with adjusted soil properties (using a readily available FE package such as Plaxis). The results could be compared to laboratory test data and the output of existing predictive tools.

Improved experimental database: Further experiments are also needed using real plant roots and a wider range of soil types and conditions. Real roots are more complex geometrically and variable in material properties than the analogue roots used in this study (*Mickovski et al., 2007; Sonnenberg, 2008*). Similarly there are a wide range of soil types and conditions that require consideration to properly validate this modelling approach. This would also help in the development of appropriate theoretical *p-y* and *t-z* curves.

References

Abbas J. M (2012) '*Lateral response of pile groups.*' International Journal of Civil Engineering and Building Materials. **2(3)**:101-106.

Abe K, Ziemer R.R (1991) '*Effect of tree roots on a shear zone: modelling reinforced shear stress.'* Canadian Journal of Forest Research **21:** 1012-1019.

Abernethy B, Rutherford I.D (2001) '*The distribution and strength of riparian tree roots in relation to riverbank reinforcement.'* Hydrological Processes **15:** 63-79.

Ali F (2010) '*Use of vegetation for slope protection: Root mechanical properties of some tropical plants.'* International Journal of Physical Sciences **5(5)**: 496-506.

American Water Works Association (2002) '*PVC Pipe –Design and Installation.*' AWWA Manual M23, Second Ed.

Ang E.C (2005) '*Numerical investigation of load transfer mechanism in slopes reinforced with piles.'* Doctor of Philosophy. University of Missouri-Columbia.

API 2A-WSD (2000) '*Recommended practise for planning, designing and constructing fixed offshore platforms – working stress design*' 21st Edition, December 2000, Errata and Supplement 1, December 2002.

Aryal K.P (2006) '*Slope stability evaluations by limit equilibrium and finite element methods.'* Doctor of Philosophy, Norwegian University of Science and Technology.

Ashour M, Norris G, Elfass S (2008) '*Analysis of laterally loaded long or intermediate drilled shafts of small or large diameter in layered soil.*' Prepared for California Dept. of Transportation by the Dept. of Civil and Environmental Engineering, University of Nevada, Reno. Report No. CA04-0252.

Ausilio E, Conte E, Dente G (2001) '*Stability analysis of slopes reinforced with piles.'* Computers and Geotechnics **28:** 591-611.

References

Bailey P.H, Currey J.D, Fitter A.H (2002) '*The role of root system architecture and root hairs in promoting anchorage against uprooting forces in Allium cepa and root mutants of Arabidopsis thaliana.'* Journal of Experimental Botany **53(367):** 333-340.

Basu D, Salgado R, Prezzi M (2008) '*Analysis of laterally loaded piles in multi-layered soil deposits.*' JTRP Technical report. Project No. C-36-36LL. Purdue University.

Bengough A.G (2003) '*Root growth and function in relation to soil structure, composition and strength.*' Ecological studies. **168:** 151-172

Bengough A.G, Croser C, Pritchard J (1997) '*A biophysical analysis of root growth under mechanical stress.'* Plant and Soil **189**: 155-164.

Bischetti G. B, Chiaradia E. A, Epis T, Morlotti M (2009) '*Root cohesion of forest species in the Italian Alps.*' Plant and Soil. **324(1)**:71-89.

Bischetti G. B, Chiaradia E. A, Simonato T, Speziali B, Vitali B, Vullo P, Zocco A (2005) '*Root Strength and Root Area Ratio of Forest Species in Lombardy (Northern Italy).*' Plant and Soil **278**:11-22.

Bolton M. D (1986) '*The strength and dilatancy of sands.*'Geotechnique **36(1)**: 65-78.

Bowls J. E (1996) '*Foundation analysis and design.*' 5th Edition. ISBN-10: 0071188444.

Bransby M.F, Knappett J.A, Brown M.J, Hudasecsek P (2011) '*The vertical capacity of grillage foundations.*' Geotechnique.

Briggs K (2010) '*Charing embankment: Climate change impacts on embankment hydrology.'* Paper submitted for Cooling Prize 2010.

Brødbæk K.T, Møller M, Sørensen S.P.H, Augusteen A.H (2009) '*Review of p-y relationships in cohesionless soil.*' DCE Technical Report No. 57, Department of Civil Engineering, Aalborg University, Denmark.

Brown D. A, Morrison C, Reese L. C (1988) '*Lateral load behaviour of pile groups in sand.*' ASCE Journal of Geotechnical Engineering **114(11)**:1261-1276.

BSEN 1997-2:2007 (2007) '*Eurocode 7 – Geotechnical Design – Part 2: Ground Investigation and Testing.*' British Standards/Eurocodes.

Buma J, Dehn, M (1998) '*A method for predicting the impact of climate change on slope stability*'. Engineering Geology **35**: 190-196.

Burylo M, Rey F, Roumet C, Buisson E, Dutoit T (2009) '*Linking plant morphological traits to uprooting resistance in eroded marly lands (Southern Alps, France).'* Plant Soil **324:** 31-42.

Chen C.S (2004) '*Failure of a soil nailed slope.*' 15th South East Asian Geotechnical Society Conference, 22-26 November 2006, Bangkok, Thailand.

Cheng Y.M, Lansivaara T, Wei W.B (2007) '*Two dimensional slope stability analysis by limit equilibrium and strength reduction methods.'* Computers and Geotechnics **34**: 137-150.

Chiaradia E. A, Bischetti G. B, Vergani C (2012) '*Incorporating the effect of root systems of forest species into spatially distributed models of shallow landslides.*' International Journal of Forest, Soil and Erosion **2(3)**:107-118.

Chok Y.H, Kaggwa W.S, Jaksa M.B, Griffiths D.V (2004) '*Modelling the effects of vegetation on the stability of slopes.'* Proceedings, 9th Australia New Zealand Conference on Geomechanics, Aukland.

Clark L.J, Whalley W.R, Barraclough P.B (2003) '*How do roots penetrate a strong soil?.'* Plant and Soil **255**: 93-104.

Clouterre (1991) '*French national research project Clouterre – Recommendations Clouterre (English translation 1993).'* Federal Highway Administration, US Department of Transportation, Washington D.C, USA, Report No. FHWA-SA-93-026. pp 321.

Collison A.J.C, Anderson M.G, Llyod D.M (1995) '*Impact of vegetation on slope stability in a humid tropical environment: A modelling approach.'* Proc. Inst. Civil Engineers Wat., Marit. & Energy **112**: 168-175

Comino E, Druetta A (2009) '*In situ shear tests of soil samples with grass roots in Alpine environment.'* American Journal of Environmental Sciences **5(4):** 474-485.

Comino E, Marengo P, Rolli V (2010) '*Root reinforcement effect of different grass species: A comparison between experimental and models results.*' Soil and Tillage Research **110(1)**: 60-68.

Coppin N.J, Richards I.G (2007) '*Use of vegetation in civil engineering.*' CIRIA. London: Butterworths Construction Industry Research and Information Association. 2007.

Craig R F (2004) '*Soil Mechanics*' 7th Edition, published Chapman and Hall. ISBN:9780415327039

Danjon F, Barker D.H, Drexhage M, Stokes A (2008) '*Using three dimensional plant root architecture in models of shallow-slope stability.'* Annals of Botany **101**: 1281-1293.

Das B. M (2010) '*Geotechnical Engineering Handbook.*' J Ross Pub. Inc.

Davoudi M. H (2011) '*Influence of willow root density on shear resistance parameters in fine grain soils using in situ direct shear tests.*' Research Journal of Environmental Sciences **5(2)**: 157-170.

De Beats S, Poesen J, Knapen A, Barbera GG, Navarro J.A (2007) '*Root characteristics of representative Mediterranean plant species and their erosion-reducing potential during concentrated run-off.'* Plant Soil **294**: 169-183.

De Beats S, Poesen J, Reubens B, Wemas K, De Baerdemaeker J, Muys B (2008) '*Root tensile strength and root distribution of typical Mediterranean plant species and their contribution to soil shear strength.'* Plant Soil **305**: 207-226.

De Micco V, Aronne G, Joseleay JP, Ruel K (2008) '*Xylem development and cell wall changes of soy bean seedlings grown in space.*' Annals of Botany **101**: 661-669.

Degenhardt B, Gimmler H (2000) '*Cell wall adaptations to multiple environmental stresses in maize roots.*' Journal of Experimental Bottany **51**:595-603

Der-Guey, Wen-Tsung, Shin-Hwei (2011) '*Estimating the effect of shear strength increment due to root on the stability of Makino Bamboo forest slopeland.*' J. Geo. Eng. **6**: 73-88.

Diambra A, Ibraim E, Muir Wood D, Russell A R (2010) '*Fibre reinforced sand: Experiments and modelling.*' Geotextiles and Geomembranes **28**:238-250.

DNV (1992) '*Foundations*' Classification Note 30.4. Det Norske Varitas. February 1992.

Downie H, Holden N, Otten W, Spiers A. J, Valentine T. A, Dupuy L. X (2012) '*Transparent soil for imaging the rhizosphere.*' PLoS ONE **7(9)**:e4426.

Dupuy L, Fourcaud T and Stokes A (2007) '*A numerical investigation into factors affecting the anchorage of roots in tension.'* Journal of Soil Science **56**: 319-327.

Dupuy L, Fourcaud T, Stokes A (2005) '*A numerical investigation into the influence of soil type and root architecture on tree anchorage.*' Plant and Soil. **278(1-2)**:119-134.

Ennos A.R (1993) '*The scaling of root anchorage.'* Journal of Theoretical Biology **161**: 61-75.

Fan C.C, Chen Y.W (2010) '*The effect of root architecture on the shearing resistance of root-permeated soils.'* Ecological Engineering **36:**813-826.

Fioravante V (2002) '*On the shaft friction modelling of non-displacement piles in sand.*' Soils and Foundations **42(2)**: 22-33.

Fitter A.H (1986) '*The topology and geometry of plant root systems: Influence of watering rate on root system topology in Trifolium pratense.'* Annals of Botany **58**: 91-101.

Fitter A.H, Stickland T.R (1991) '*Architectural analysis of plant root systems: Influence of nutrient supply on architecture in contrasting plant species.'* New Phytologist **118**: 383-389.

Fleming W.G.F, Weltman A.J, Randolph M.F, Elson W.K (2009). Piling Engineering. 3rd Edition. Taylor and Francis, UK.

Fogiel M (2004) '*The biology problem solver.'* Printed in the United States of America by Research and Education Association. Piscataway, New Jersey 08854. ISBN: 0-87891-514-1.

Fourcaud T, Ji J.N, Zhang Z.Q, Stokes A (2007) '*Understanding the impact of root morphology on overturning mechanisms: A modelling approach.'* Annals of Botany. 1-14. doi:10.1093/aob/mcm245.

Franke E (1988) '*Group action between vertical piles under horizontal loads.*' W. F. Van Impe ed. A. A. Balkema, Rotterdam, The Netherlands, 83-93.

Garnier J (2002) '*Size effects in shear interfaces.*' Proc. Constitutive and Centrifuge modelling: two extremes, Springman ed, Swers and Zeitlinger Lisse, 5-19.

Genet M, Stokes A, salin F, Mickovski S, Fourcaud T, Dumail J.F, van Beek R (2005) '*The influence of cellulose content on tensile strength in tree roots.'* Plant Soil **278(1-2)**: 1-9.

Geotechnical Engineering Office (2008) '*Guide to soil nail design and construction.*' Geoguide 7. Prepared by Geotechnical Engineering Office, Civil Engineering and Development Dept., the Government of Hong Kong, Special Administrative Region.

Graf F, Frei M, Böll A (2009) '*Effects of vegetation on the angle of internal friction of a moraine.*' For. Snow. Lansdsc. Res. **82 (1)**: 61-77.

Gray D.H, Sotir R.B (1996) '*Biotechnical and soil engineering slope stabilisation: A practical guide for erosion control.'* John Wiley and Sons, Inc. ISBN: 0-471-04978-6

Greenway D.R (1987) '*Vegetation and Slope Stability.'* Slope Stability. New York: John Wiley and Sons Ltd; 1987. 187-230.

Greenwood J.R, Norris J.E and Wint J (2004) '*Assessing the contribution of vegetation to slope stability.'* Geotechnical Engineering **157**: 199-207.

Gregory P.J (2006) '*Plant roots: Growth, activity and interaction with soils.'* Blackwell Publishing. ISBN-10-4051-1906-3.

Gunaratne M (2006) '*The foundation engineering handbook.'* Published CRC Press, Taylor and Francis Group. ISBN: 13:978-0-8493-1159-8.

Hamza O, Bengough A.G, Bransby M.F, Davies M.C.R, Hallett P.D (2006) '*Biomechanics of plant roots: Estimating localised deformation with particle image velocimetry.'* Biosystems Engineering **94(1)**: 119-132.

Hinsinger P., Bengough A.G.**,** Vetterlein D, Young I.M (2009) '*Rhizosphere: biophysics, biogeochemistry and ecological relevance'*. Plant and Soil **321**: 117-152.

James A. M, Lord M. P (1992) '*Macmillans chemical and physical data.*' Publisher London Macmillan, 1992. ISBN: 033351167097803335116 71.

Jasper-Focks D. J, Algera A (2006) '*Vetiver grass for river bank protection.*' Sourced from www.vetiver.org.

Jeffrey J, Brown M.J, Knappett J, Ball J, Caucis K (2015) Modelling of continuous helical displacement pile performance, Part: Physical testing. Canadian Geotechnical Journal. Submitted for consideration.

Jeong S, Kim B, Won J, Lee J (2003) '*Uncoupled analysis of stabilizing piles in weathered slopes.'* Computers and Geotechnics **30(8):** 671-682.

Jewell R.A, Wroth C.P (1987) '*Direct shear tests on reinforced sand.'* Geotechnique **37(1):** 53-68.

Johnson P.E (2002) '*Soil Nailing for Slopes.'* Transport research Laboratory. 2002.

Jones C.P.D (1990) '*In-situ techniques for reinforced soil.'* Proceedings of the International Reinforced Soil Conference, Glasgow. 277-282.

Karam G.N (2005) '*Biomechanical model of the xylem vessels in vascular plants.*' Annals of Botany **95**: 1179-1186.

Kassif G, Kopelovitz A (1968) '*Strength properties of soil root systems.'* Department of Technion Research and Development Foundation, Ltd. Technion, Israel Institute of Technology, Haifa, Israel.

Khare M. G, Gandhi S. R (2001) '*Behaviour of coated piles under dragload.*' Soil Mechanics and Geotechnical Engineering, 13th Asian Regional Conference, 321-324.

Kleidon A. (2004) *'Global Datasets of Rooting Zone Depth Inferred from Inverse Models.'* Journal of Climate **17**: 2714-2722.

Knappett J. A, Craig R. F (2012) '*Craigs soil mechanics.*' 8th Edition. Published by E & FN Spon.

Kramer S.L, Heavey E.J (1988) '*Lateral load analysis of nonlinear piles.'* Journal of Geotechnical Engineering **144(9):** 1045-1049.

Kretschmann D.E (2010) '*Wood handbook: Wood as an engineering material.*' Chapter 5. General Technical Report FPL-GTR-190. Madison, WI: U.S. Department of Agriculture, Forest Service, Forest Products

Kuriakose S. L, van Beek L. P. H (2011) '*Plant root strength and slope stability.*' Encyclopedia of Earth Sciences Series 2011: 622 -627.

Lambe T. W (1969) '*Soil mechanics.*' Published by John Wiley and Sons.

Lawrence C.J, Rickson R.J, Clark J.R (1996) '*The effect of grass roots on the shear strength of colluvial soils in Nepal.'* In: Advances in Hillslope Processes, Anderson M.G and Brooks S.M (EDs). John Wiley and Sons, USA. ISBN: 0-471-96774-2. Pp. 857-868.

Liao J.C, Lin S.S (2003) *'An analytical model for deflection of laterally loaded piles.'* Journal of Marine Science and Technology **11(3):** 149-154.

Lieng J. T (1989) '*A model for group behaviour of laterally loaded piles.*' Offshore Technology Conference, Houston, TX, 377-394.

Lijima M, Higuchi T, Barlow P.W, Bengough A.G (2003) '*Root cap removal increases root penetration resistance in maize (Zea mays L.).'* Journal of Experimental Botany. **54**: 2105-2109.

Loades K.W, Bengough A.G, Bransby M.F, Hallett P.D (2009) '*Planting density influence on fibrous root reinforcement of soils.'* Ecological Engineering. In Press. Doi: 10.1016/j.ecoleng. 2009.02.005.

Lopez-Bucio J, Cruz-Ramirez A, Herrera-Estrella L (2003) '*The role of nutrient availability in regulating root architecture.'* Current Opinion in Plant Biology **6**: 280-287.

Lynch J.P, Neilsen K.L, Davis R.D, Jablokow A.G (1997) '*SimRoot: Modelling and visualization of root systems.'* Plant and Soil **188:** 139-151.

Maffian S, Huat B.B.K, Ghiasi V (2009) '*Evaluation on root theories and root strength properties in slope stability.'* European Journal of Scientific Research **30(4)**: 594-607.

Materechera S.A, Dexter A.R, Alston A.M (1991) '*Penetration of very strong soils by seedlings of different plant species.'* Plant and Soil **135**: 31-41.

McNear Jr. D. H (2013) '*The Rhizosphere – Roots, soil and everything in between.*' Nature Education Knowledge **4(3):** 1.

McPhee K (2005) '*Variation for seedling root architecture in the core collection of pea gerplasm.´* Crop Sci. **45**: 1758-1763.

Mickovski S. B, Bransby M. F, Bengough A. G, Davies M. C. R, Hallett P. D (2010) '*Resistance of simple plant root systems to uplift loads.*' Can. Geotech. J **47**:78-95.

Mickovski S.B, Bengough A.G, Bransby M.F, Davies M.C.R, Hallett P.D, Sonnenberg R (2007) '*Material stiffness, branching pattern and soil matric potential affect the pull out resistance of model root systems.'* European Journal of Science **58**: 1471-1481.

Mickovski S.B, Sonnenberg R, Bransby M.F, Davies M.C.R, Lauder K (2007i) '*Shear reinforcement of soil by vegetation*' Proceedings of the 14th European Conference on Soil Mechanics and Geotechnical Enigneering. Madrid. Millpress Science. Rotterdam. 1491-1496.

Mickovski S.B, Ennos A.R (2003) '*Model and whole-plant studies on the anchorage capabilities of bulbs.'* Plant and Soil **255**: 641-652.

Mickovski S.B, Stokes A, ven Beek R, Ghestem M, Fourcaud T (2011) '*Simulation of direct shear tests on rooted and non-rooted soil using finite element analysis.*' Ecological Engineering **37**: 1523-1532.

Mickovski S.B, van Beek L.P.H (2009) '*Root morphology effects on soil reinforcement and slope stability of young vetifer (Vetiveria zizanioides) plants grown in semi-arid climate.'* Plant Soil **324**: 43-56.

Mickovski S.B, Hallett P.D, Bransby M.F, Davies M.C.R, Sonnenberg R, Bengough A.G (2009) '*Mechanical Reinforcement of Soil by Willow Roots: Impacts of Root Properties and Root Failure Mechanism.*' Soil Sci. Soc. Am. J. **73**:1276-1285

Mitsch M.P, Clemance S.P (1985) '*The uplift capacity of helical anchors in sand: Uplift behaviour of anchor foundations in soil.*' Proc. ASCE, New York, N.Y, 26-47.

Mittal S, Biswas AK (2006) '*River bank erosion control by soil nailing*.' Geotechnical and Geological Engineering **24**:1821-1833.

Mokwa R.L (1999) '*Investigation of the resistance of pile caps to lateral loading.*' Doctor of Philosophy. Virginia Tech.

Møller I. F, Christiansen T. H (2011) '*Laterally loaded monopole in dry and saturated sand – static and cyclic loading: Experimental and numerical studies.'* Master project. Aalborg University Esbjerg.

Mulatya J.M, Wilson J, Ong C.K, Deans J.D, Sprent J.I (2002) *'Root architecture of provenances, seedlings and cuttings of Melia volkensii: Implications for crop yield in dryland agroforestry.'* Agroforestry Systems **56**: 65-72.

Newson T.A, Smith F.W, Brunning P, Gallagher S (2003) '*An experimental study of inflatable offshore anchors.*' Proceedings of the Thirteenth (2003) International Offshore and Polar Engineering Conference, Honolulu, Hawaii, USA, May 25-30.

Nicoll B.C, Berthier S, Achim A, Gouskou K, Danjon F, van Beek L.P.H (2006) '*The architecture of Picea sitchensis structural root systemsm on horizontal and sloping terrain.'* Tree Structure and Function **20(6)**: 701-712.

Norris J.E (2005) '*Root reinforcement by hawthorn and oak roots on a highway cut-slope in southern England.'* Plant and Soil **278(1)**: 43-53.

Norris J.E, Greenwood J.R (2006) '*Assessing the role of vegetation on soil slopes in urban areas.'* Geological Society of London. IAEG2006 Paper Number 744.

Norris J.E, Stokes A, Mickovski S.B, Cammeraat E, van Beek R, Nicoll B.C, Achim A (2008) '*Slope Stability and Erosion Control: Ecotechnological Solutions.'* Published by Springer. ISBN: 978-4020-6675-7(HB).

O'Brien A.S (2007) '*Rehabilitation of urban railway embankments: Research, analysis and stabilisation.'* Millpress Science. Rotterdam. 125-143.

O'Loughlin C.L, Ziemer R.R (1982) '*The importance of root strength and deterioration rates upon edaphic stability in steepland forests.'* Proceedings of I.U.F.R.O Workshop. 2-3 August, Oregon State University. Corvallis.

Operstein V, Frydman S (2000) '*The influence of vegetation on soil strength.'* Ground Improvement **4**: 81-89.

Oriens C.M, Ardón M, Mohammad B.A (2002) '*Vascular architecture and patchy nutrient availability generate within-plant heterogeneity in plant traits important to herbivores.'* American Journal of Botany **89(2)**: 270-278.

Patra C.R, Basudhar P.K (2005) '*Optimum design of nailed soil slopes.'* Geotechnical and Geological Engineering **23:** 273-296.

Pedley MJ (1990) '*The performance of soil reinforcement in bending and shear*.' Doctor of Philosophy, University of Oxford.

Perry J.G, Pedley M, Reid M (2003) '*Infrastructure embankments – Condition appraisal and remedial treatemnet.'* CIRIA. London.

Phanikanth V.S, Choudhury D, Rami Reddy G (2010) '*Behaviuor of fixed head single pile in cohesionless soil under lateral loads.'* EJGE **15:** 1243-1262.

Phear A, Dew D, Ozsoy B, Wharmby N.J, Judge J (2005) '*Soil nailing – Best practice guidance.'* C637. CIRIA. London.

Pollen N (2007) '*Temporal and spatial variability in root reinforcement of streambanks: Accounting for soil shear strength and moisture.'* Catena. **69(3):** 197-205.

Pollen N, Simon A, Collison A.J.C (2004) '*Advances in assessing the mechanical and hydrological effects of riparian vegetation on streambank stability.'* In: Bennett S, Simon A (Eds.), Riparian Vegetation and Fluvial Geomorphology. Water Science and Applications **8:** 125-139.

Poulos H.G (1995) '*Design of reinforcing piles to increase slope stability.'* Canadian Geotechnical Journal **32(5):** 808-818.

Powrie W (2004) '*Soil Mechanics: Concepts and Applications.'* 2nd. Ed, ISBN 041531156X

Prakash S (1962) '*Behaviour of pile groups subjected to lateral loads.* Doctor of Philosophy, University of Illinois, Urbana, Il.

Pratt R.B, Jocobsen A.L, Ewers F.W, Davis S.D (2007) '*Relationships between xylem transport, biomechanics and storage in stems and roots of nine Rhamnaceae species of the California chaparral.*' New Phytologist **174**: 787-798.

Preti F, Giadrossich F (2009) '*Root reinforcement and bioengineering stabilisation by Spanish broom'.* Hydrol. Earth Syst. Science **13**: 1713-1726.

Read J, Stokes A (2006) '*Plant biomechanics in an ecological context.'* American Journal of Botany **93(10)**: 1546-1565.

Reese L. C, Cox W. R, Koop F.D (1974) '*Analysis of laterally loaded piles in sand.*' Proceedings, VI Annual Offshore Technology Conference, Houston Texas, 2(OTC 2080) pp. 473-485.

Reese L.C, Van Impe W.F (2011) '*Single piles and pile groups under lateral loading.*' 3rd Edition. CRC Press.

Reubens B, Poesen J, Danjon F, Geudens G, Muys B (2007) '*The role of fine and coarse roots in shallow slope stability and soil erosion control with a focus on root system architecture: A review.'* Trees J. **21**: 385-402.

Saleeba J.A, Ly P.K.C, Prodhan A, Alomari O.K, McGee P.A (2009) '*Genetics of root architecture.'* International Symposium "Root Research and Applications" RootRAO, 2-4 September 2009, Boku – Vienna, Austria.

Schenk H.J, Jackson R.B (2002) '*The global biogeography of roots.'* Ecological Monographs **72(3):** 311-328.

Schlenker W, Roberts M (2008) '*Estimating the impact of global climate change on crop yields: The importance of non-linear temperature effects.'* National Bureau of Economic Research. Working Paper 13799. http://www.nber.org/papers/w13799.

Schmidt, Roering, Stock, Dietrich, Montgomery, Schaub (2001) '*The variability of root cohesion as an influence on shallow landslide susceptibility in the Oregon Coast Range.*' Can. Geotech. J **38**: 995-1024.

Schuppener B (2001) '*The design of slope backups using plants.'* Geotechnik **24(3):** 175-185.Schwartz M. Cohen D, Or D (2010) '*Mechanical interactions during pullout and failure of root bundles.*' Journal of Geophysical research: Earth Surface. **115(F4)**.

Schwarz M, Lehman P, Or D (2010) '*Quantifying lateral root reinforcement in steep slopes – from a bundle of roots to tree stands.'* Earth Surface Processes and Landforms **35**: 354-367.

Schwarz M, Preti F, Giadrossich F, Lehmann P, Or D (2009) '*Quantifying the role of vegetation in slope stability: A case study in Tuscany (Italy).'* Ecological Engineering-1529. In press.

Scott J.M, Loveridge F, O'Brien A.S (2007) '*Influence of climate and vegetation on railway embankments.'* Millpress Science. Rotterdam. Proceedings of the 14th European Conferenec on Soil Mechanics and Geotechnical Engineering. Madrid. 659-664.

Shewbridge S.E, Sittar N (1985) '*The influence of fiber properties on the deformation characteristics of fiber soil composites.*' University of California Geotechnical Report No UCB/GT/85-02, 100p.

Shrewbridge S.E, Sitar N (1990) '*Deformation based model for reinforced sand in direct shear.'* Journal of Geotechnical Engineering **116(GT7):** 1153-1157.

Silva J.S, Rego F.C, Martins-Loução M.A (2003) '*Root distribution of Mediterranean woody plants. Introducing a new empirical model.'* Plant biosystems **137(1)**: 63-72.

Simon A, Collison A.J.C (2002) '*Quantifying the mechanical and hydrological effects of riparian vegetation on streambank stability.'* Earth Surface Processes and Landforms **27**: 527-546.

Skene K.R (1998) '*Cluster roots: model experimental tools for key biological problems.'* Journal of Experimental Botany **52**: 479-485.

Sonnenberg R (2008) *'Centrifuge modelling of root reinforced slopes.'* Doctor of Philosophy, University of Dundee.

Sonnenberg R, Bransby M.F, Hallett P.D, Bengough A.G, Mickovski S.B, Davies M.C.R (2010) '*Centrifuge modelling of vegetation reinforcement of soil slopes.'* Can Geotech. J. **47:**1415-1430.

Steele D.P, Mac Neil D.J, Barker D.H, McMahon W (2004) '*The use of live willow poles for stabilizing highway slopes.'* TRL619, TRL Ltd, Crowthorne, England.

Steffan OKH, Contreras LF, Terbrugge PJ, Venter J (2008) '*A risk evaluation for pit slope design.*' American Rock Mechanics Assossiation. 42nd US Rock Mechanics Symposium and 2nd Canada Rock Symposium. San Francisco, June 29-July 2.

Stocker M.F, Korber G.W, Gassler G, Gudehus G (1979) '*Soil Nailing.'* In: Proceedings of the International Conference on Soil Reinforcement. Paris. Pp 469-474.

Stokes A, Atger C, Bengough A.G, Fourcaud T, Sidle R.C (2009) '*Desireable plant root traits for protecting natural and engineered slopes against landslides.'* Plant Soil **324**: 1-30.

Stokes A, Ball J, Fitter A.H, Brain P, Coutts M.P (1996) '*An experimental investigation of the resistance of model root systems to uprooting.'* Annals Bot **78**: 415-421.

Sun H.L, Li S.C, Xiong W.L, Yang Z.R, Cui B.S, Tao-Yang (2007) '*Influence of slope on root system anchorage of Pinus yunnanensis.'* Ecological Engineering **32(1):** 60-67.

Take W.A (2002) '*The influence of seasonal moisture cycles on clay slopes.'* Doctor of Philosophy. University of Cambridge.

Tan YC and Chow CM (2004) '*Slope stabilisation using soil nails: Design assumptions and construction realities.*' G & P Geotechnics SDN. BHD.

Tarantino A, Mongiovi L, McDougall J.R (2002) '*Analysis of hydrological effects of vegetation on slope stability.*' Unsaturated soils. 749-754.

Tardieu F (1994) '*Growth and functioning of roots and of root systems subjected to soil compaction. Towards a system with multiple signalling?'* Soil and Tillage Research **30(2-4)**: 217-243.

Tei K (1993) '*A study of soil nailing in sand.'* Doctor of Philosophy. University of Oxford.

Teodoru I.B (2009) '*Beams on elastic foundation, the simplified continuum approach.*' Publication of the Polytechnic Institute of Jassy. Construction Architecture Section.

Thomas R.E and Pollen-Bankhead N (2010) '*Modelling root reinforcement with a fibre-bundle model and Monte Carlo simulation.'* Ecological Engineering **36**: 47-61.

Tobias S (1994) '*Shear strength of the soil system: In situ shear tests.'* Proceeding of the 1st International Congress of the European Society for Soil Conservation, Conserving Soil Resources, (ICCSR '94), Wallingford, United Kingdom. Pp 405-412.

Tomlinson M, Woodward J (2007) '*Pile Design and Construction Practice, Fifth Edition*' CRC Press.

Tsakaldimi M, Tsitsoni T, Ganatsas P, Zagas T (2009) '*A comparison of root architecture and shoot morphology between naturally regenerated and container-grown seedlings of Quercus ilex.'* Plant Soil **324**: 103-113.

van Beek L.P.H, Wint J, Cammeraat L.H, Edwards J.P (2005) '*Observation and simulation of root reinforcement on abandoned Mediterranean slopes.'* Plant and Soil **278**: 55-74.

Viggiani, C (1981) '*Ultimate Lateral Load on Piles Used to Stabilize Landslides*.' Proceedings of The 10th International Conference on Soil Mechanics and Foundation Engineering. **3:** 555-560 Stockholm

Waldren L.J, Dakessian S (1981) '*Soil reinforcement by roots: Calculation of increased soil shear resistance from root properties.'* Soil Science **132(6)**: 427-435.

Waldron L.J (1977) *'Shear resistance of root-permeated homogenous and stratified soil.'* Soil Science Society of America Journal **41(5)**: 843-849.

Walk T.C, van Erp E, Lynch J.P (2004) '*Modelling applicability of fractal analysis to efficiency of soil exploration by roots.'* Annals of Botany **94:** 119-128.

Wei W.B, Cheng Y.M (2010) '*Soil nailed slope by strength reduction and limit equilibrium methods.'* **37(5)**: 602-618.

White D.J (2002) '*An investigation into the behaviour of pressed in piles.'* Doctor of Philosophy. University of Cambridge

White D.J, Take W.A (2002) '*GeoPIV: Particle Image Velocimetry (PIV) Software for use in Geotechnical Testing.'* Cambridge University Engineering Department. Technical Report. CUED/D-SOILS/TR322.

White D.J, Take W.A, Bolton M.D (2003) '*Soil deformation measurement using particle image velovimetry (PIV) and photogrammetry.'* Geotechnique **53(7):** 619-631.

Wilson D.W (1998) '*Soil-pile superstructure interaction in liquefying sand and soft clay.'* PhD Dissertation, University of California at Davis, Dept. of Civil and Environmental Engineering, College of Engineering. Centre for Geotechnical Modelling.

Windsor-Collins A.G, Atherton M.A, Collins M.W, Cutler D.F (2008) '*Section properties of palm petioles, Part 1: The influence of section shape on the flexural and torsional properties of selected palm petioles.'* Brunel University.

Wu T.H (2007) '*Root reinforcement: Analysis and experiments.'* Eco and Ground Bioengineering: the Use of Vegetation to Improve Slope Stability **103:** 21-30.

Wu T.H, McKinnell W.O, Swanston D.N (1979) '*Strength of tree roots and landslides on Prince-Of-Wales-Island. Alaska.'* Canadian Geotechnical Journal **16(1):** 19-33.

Wu T.H, Watson A (1998) '*In situ shear tests of soil blocks with roots.'* Canadian Geotechnical Journal **35**: 579-590.

Yen C.P (1987) '*Tree root patterns and erosion control.'* In: Jantawat, S (Ed), Proceedings of the International Workshop on Soil Erosion and its Countermeasurements. Soil and Water Conservation Society of Thailand, Bangkok. 92-111.

Yu H.S, Salago R, Sloan S.W, Kim J.M (1998) *'Limit analysis versus limit equilibrium analysis for slope stability'*. Journal of geotechnical and geoenvironmental engineering. Vol 124.

Zhang L.L, Fredlund D.G, Zhang L.M, Tang W.H (2004) '*Numerical study of soil conditions under which matric suction can be maintained.*' Canadian Geotech. **41(4):**569-582.

Zhang H, Zhu Y, Chen H (2013) '*Root growth model: A novel approach to numerical function optimization and simulation of plant root system.*' Soft Computing. DOI: 10.1007/s00500-013-1073-z.

Zornberg J.G (2004) '*Discrete framework for limit equilibrium analysis of fibre-reinforced soil.'* Geotechnique **54(1)**: 72-73.

Appendices

Appendix A – Full Excerpt of TZCurve.m

```
function TZCurve
% USE FOR:      Quantifying soil root interaction during uprooting.
% CALCULATES:   Interface shear force (t) along the length of a root as a
%               function of its vertical displacement (z)
% REQUIRES:     > The output of a GeoPIV analysis that measures the
%                 vertical displacement of a root during uprooting.
%                   - Requires a column of patches along the length
%                     of the root, the first of which sits at root tip.
%               > Conversion factor to convert GeoPIV output (pixels) to
%                 metres. Input in section 1 'FACTOR'.
% ASSUMPTIONS:  > The friction between root and Perspex is only present if
%                 soil is dry.
%               > 4 degree polynomial can be used to represent the
%                 relationship between vertical displacement and patch
%                 location. [Note: Accuracy of this relationship defines
%                 the success of the calculations-Please check it's
suitability].
% LIMITATIONS:  > TZCurve does not account for multiple roots, tuorosity,
%                 branching or changing diameter along root length.


%%   SECTION 1
%    INPUT INFORMATION
%
%       Root properties;
        diameter=0.0016;   %Diameter of the root; UNITS = m
        PoiRat=0.4895; %Poissons ratio of root; no units
        Erhalf=5652; %Youngs modulus of a half root, UNITS =kPa
        Erfull=5001; %Youngs modulus of a half root, UNITS =kPa
%
%       Soil properties;
        Soil=0; %(0=dry soil; 1=wet soil)
%
%       Data Conversion;
        FACTOR=5.227E-05;  %(1 pixel =[x]FACTOR mm)

%%  SECTION 2
%   COLLECTING AND ORGANISING DATA;

        data=consolidate8;
        X=data(:,:,1);
        X(:,1)=[];%deleting first column of matrix (numbering of patches)
        X=FACTOR*X;
        Y=data(:,:,2);
        Y(:,1)=[];
        Y=FACTOR*Y;
        S=size(Y);
        nr=S(1,1); %number of rows/number of patches used
        nc=S(1,2); %number of columns/number of images
```

```
        %Distance between each patch
        for i=2:nr
            for j=1:nc
                distance(i,j)=sqrt((X(i,j)-X(i-1,j))^2+(Y(i,j)-Y(i-1,j))^2);
            end
        end

        % initial length of root segment
        for i=1:nc
            length(:,i)=sum(distance(:,i));
        end

        %Distance of each patch from the root tip (in image 1) (x);
        PatchPosition(:,1)=cumsum(distance(:,1));

        %Calculating the Vertical Displacement (z) of Each Patch
        for i=1:nr
            for j=1:nc
                VerticalDisplacement(i,j)=-(Y(i,j)-Y(i,1));
            end
        end

%%  SECTION 3;
%   FITTING A POLYNOMIAL EQUATION TO "x-z" DATA;

% - The aim of this step is to generate a 4 degree polynomial equation,
%   excluding the x^1 term (as t = 0 at root tip, where EA*dy/dx = t)
%   i.e. create an equation in the form: c0 + c2x^2 + c3x^3 + c4x^4.
% - This is achieved through using gaussian elimination to evaluate A'Ac=A'y,
%   where;  A=[a1,x1^2,x1^3,x1^4;
%              a2,x2^2,x2^3,x2^4;
%              ..............;
%              an,xn^2,xn^3,xn^4],
%           y=VerticalDisplacement, and
%           c is the matrix of coefficients, which we are trying to find.

        d=4;  %number of coefficients required

        g=size(VerticalDisplacement);
        n=g(1,1);
        hcol=g(1,2);

        %Generating data for matrix A
        for i=1:n
                a(i,1)=1;
        end
        for i=1:n
                ce(i,1)=PatchPosition(i,1)^2;
        end
        for i=1:n
                de(i,1)=PatchPosition(i,1)^3;
        end
        for i=1:n
                e(i,1)=PatchPosition(i,1)^4;
        end
```

```
        for g=1:hcol
            A=[a(:,1),ce(:,1),de(:,1),e(:,1)];
            y=VerticalDisplacement(:,g);
            coeff(:,g)=A\y; % \ performs gaussian elimination and back
substitution in order to obtain values for each of the coefficients.
        end

        %Calculate z(estimated) data.
        %Require X DATA (X Data = spring/patch locations)
        SpringSpacing=0.02 %metres
        FirstSpring=0.01; %from tip of root
        N=length(1,1)/SpringSpacing;
        NumberOfSprings=floor(N); %rounding N to the nearest lower integer.
        for i=1:NumberOfSprings
            XDataA(:,i)=FirstSpring+(SpringSpacing*(i-1));
        end
        XData=XDataA';

        for i=1:hcol  % number of columns in 'coeff' matrix.
            for j=1:NumberOfSprings

ZData(j,i)=coeff(1,i)+(coeff(2,i)*XData(j,1)^2)+(coeff(3,i)*XData(j,1)^3)+(coe
ff(4,i)*XData(j,1)^4);
            end
        end

%% SECTION 4:
%  CALCULATING AXIAL STRAIN
%  Differentiate best fit equation;
%  equation =  c0 + c2x^2 + c3x^3  + c4x^4
%  dy/dx    =  0  + 2c2x  + 3c3x^2 + 4c4x^3

        DifferentiationCoefficients1=[0 2 3 4];  %If equation changes, this
vector will have to be altered.
        for i=1:hcol
            for j=1:d
                Diff(j,i)=(coeff(j,i))*(DifferentiationCoefficients1(1,j));
%<<Altering diff coeffs to match dy/dx equation.
            end
        end

        for i=1:NumberOfSprings
            for j=1:hcol

Strain(i,j)=((Diff(2,j)*ZData(i,j))+(Diff(3,j)*ZData(i,j)^2)+(Diff(4,j)*ZData(
i,j)^3));  %<<putting new coeffs and x^n terms in equation to find strain.
            end
        end

%% SECTION 5:
%  CALCULATING VERTICAL FORCE IN THE ROOT.
%
%  Accounting for change in roots cross sectional area as the root
%  stretches.
%       NOTE:
```

```
%       PoiRat=StrainT/StrainL
%       So, deltad= PoiRat x StrainL x diameter
%       Where; StrainL=Longintudinal Strain; StrainT = Transverse Strain;
deltad
%       = change in diameter due to root stretching

        StrainL=Strain;
        for i=1:NumberOfSprings
            for j=1:hcol
                deltad(i,j)=PoiRat*diameter*StrainL(i,j);
                ChangingDiameter(i,j)=diameter-deltad(i,j);
                area(i,j)=((pi()/8)*ChangingDiameter(i,j)^2); %<<Consider full
cross section of root (circular rather than semi circular)
             end
        end

        AreaFull=area;
        AreaHalf=0.5*area;

%  Accounting for Root-Perspex friction (for a Viton rubber root);

            VD=ZData*1000; %Convert vertical displacement from m to mm as
friction model uses mm.
            for i=1:NumberOfSprings;
                for j=1:hcol;
                    Friction(i,j)=(1/(0.1/SpringSpacing))*((-5.37E-
09*VD(i,j)^2)+((4.45E-08)*VD(i,j))+5.03E-05);
                end
            end

            if isequal(Soil,0);
                fr(:,:)=Friction(:,:);
            else
                fr(i,j)=0;
            end

% Fhalf=Ehalf*Ahalf*Strain
        for i=1:NumberOfSprings;
            for j=1:hcol;
                Fhalf(i,j)=(Erhalf*AreaHalf(i,j)*Strain(i,j));
            end
        end

% Ffull=Efull*Afull*Strain-2*fr
        for i=1:NumberOfSprings;
            for j=1:hcol;
                Ffull(i,j)=((Erfull*AreaFull(i,j)*Strain(i,j))-
(2*fr(i,j))+2*fr(1,j));
            end
        end

% By equilibrium, the vertical shear resistance in the soil must equal
% the vertical force in the root.
        thalf=Fhalf'; %flipping columns and rows for plotting...
        tfull=Ffull';
```

```
%% SECTION 6:
%  PLOTS

    %PLOT BEST FIT DISPLACEMENT, STRAIN, FORCE AND SHEAR

a=char('ok','*k','+k','xk','.k','bo','b*','b+','bx','b.','ro','r*','r+','rx','r.','go','g*','g+','gx','g.','mo','m*','m+','mx','m.','co','c*','c+','cx','c.');
    b=char('--k','-.k','-k',':k','--k','b--','b-.','b-','b:','b--','r--','r-.','r-','r:','r--','g--','g-.','g-','g:','g--','m--','m-.','m-','m:','m--','c--','c-.','c-','c:','c--','--k','-.k','-k',':k','g--','g-.','g-','g:','r--','r-.','r-','r--','b--','b-.','b-','b:','m--','m-.','m-','m:','c--','c-.','c-','c:');
    c=char('-ok','-+k','-xk','--ok','--+k','--xk',':ok',':+k',':xk','-.ok','-.+k','-.xk','-or','-+r','-xr','--or','--+r','--xr',':or',':+r',':xr','-.or','-.+r','-.xr','-ob','-+b','-xb','--ob','--+b','--xb',':ob',':+b',':xb','-.ob','-.+b','-.xb');
    figure(1)
    subplot(1,3,1);
    hold on
    scale=1;
    for i=1:hcol
        plot(VerticalDisplacement(:,i),PatchPosition(:,1),a(i,:))
    end
    for i=1:hcol
        plot(ZData(:,i),XData(:,1),b(i,:))
    end
    xlabel('Vertical displacement, z (m)','FontSize',14,'FontName','Zapf Chancery');
    ylabel('Distance of patch from root tip, x (m)','FontSize',14,'FontName','Zapf Chancery');
    title('Check: Best fit "x-z" polynomial','FontSize',14,'FontName','Zapf Chancery');
    grid;
    subplot(1,3,2);
    hold on
    scale =1;
    for i=1:hcol
        plot(Fhalf(:,i),XData(:,1),c(i,:))
    end
    xlabel('Vertical shear force, t (kN)','FontSize',14,'FontName','Zapf Chancery');
    ylabel('Distance of patch from root tip, x (m)','FontSize',14,'FontName','Zapf Chancery');
    title('Distribution of t - Half root','FontSize',14,'FontName','Zapf Chancery')
    grid;
    subplot(1,3,3);
    hold on
    scale =1;
    for i=1:hcol
        plot(Ffull(:,i),XData(:,1),c(i,:))
    end
    xlabel('Vertical shear force, t (kN)','FontSize',14,'FontName','Zapf Chancery');
```

```
    ylabel('Distance of patch from root tip, x
(m)','FontSize',14,'FontName','Zapf Chancery');
    title('Distribution of t - Full root','FontSize',14,'FontName','Zapf
Chancery')
    grid;

%PLOT T-Z CURVES
    Z=ZData';
    PatchNumber=[1:nc]';
    figure (2)
    clf
    subplot(2,1,1);
    hold on
    scale=1;
    for i=1:NumberOfSprings
            plot(Z(:,i),thalf(:,i),c(i,:))
    end
    legend('Patch-1','Patch-2','Patch-3','Patch-4','Patch-5','Patch-6','Patch-
7','Patch-8','Patch-9','Patch-10','Patch-11','Patch-12','Patch-13','Patch-
14','Patch-15','Patch-16','Patch-17','Patch-18','Patch-19','Patch-20','Patch-
21')
    xlabel('z-vertical displacement, m','FontSize',14,'FontName','Zapf
Chancery');
    ylabel('thalf-vertical shear force, kN','FontSize',14,'FontName','Zapf
Chancery');
    title('t-z Curve: Half root','FontSize',14,'FontName','Zapf Chancery')
    grid;
    subplot(2,1,2);
    hold on
    scale=1;
    for i=1:NumberOfSprings
            plot(Z(:,i),tfull(:,i),c(i,:))
    end
    legend('Patch-1','Patch-2','Patch-3','Patch-4','Patch-5','Patch-6','Patch-
7','Patch-8','Patch-9','Patch-10','Patch-11','Patch-12','Patch-13','Patch-
14','Patch-15','Patch-16','Patch-17','Patch-18','Patch-19','Patch-20','Patch-
21')
    xlabel('z-vertical displacement, m','FontSize',14,'FontName','Zapf
Chancery');
    ylabel('tfull-vertical shear force, kN','FontSize',14,'FontName','Zapf
Chancery');
    title('t-z Curve: Full root','FontSize',14,'FontName','Zapf Chancery')
    grid;

    %PRINT T-Z Curves
%   t-z curves: Half root
    for SpringNumberHalf=1:NumberOfSprings
        SpringNumberHalf
        TZ=[thalf(:,SpringNumberHalf),Z(:,SpringNumberHalf)]
    end
%   t-z curves: Full root
    for SpringNumberFull=1:NumberOfSprings
        SpringNumberFull
        TZ=[tfull(:,SpringNumberFull),Z(:,SpringNumberFull)]
    end
```

Appendix B – Full Excerpt of PYCurve.m

```
function PYCurve

% USE FOR:      Quantifying soil root interaction during transverse loading.
% CALCULATES:   Soil reaction (P) along the length of a root as a function
%               of the relative displacement (y) between the root and the
%               soil during shear loading
% REQUIRES:     > PIV analysis of a series of digital images taken during
%                 a CS shear box test
%                   - Patch locations: (1) a column of patches along the
length
%                     of the root.  First sits at root tip. [Calculations
%                     require axis to sit at the root tip]. (2) a column of
%                     patches sitting in the soil.  Each patch should
%                     correspond to a patch on the root, with the same
%                     y value but a displaced x value.  This displacement
%                     should be sufficient such that any interaction
%                     between soil and root is negligible.
%               > Conversion factor to convert PIV output (pixels) to
%                 metres. Input in section 1 'FACTOR'.
%               > consolodate8.m file to run
% ASSUMPTIONS:  > Cross sectional shear box tests represent the cross
%                 section of a traditional shear box test - the
%                 calculated py values can therefore be multiplied by 2
%                 to represent a full root during shearing
%               > 12 degree polynomial can be used to represent the
%                 relationship between horizontal root displacement and
%                 patch location. [Note: Accuracy of this relationship defines
%                 the success of the calculations].
%               > Shear plane sits at the mid point between the patch
%                 immediately above it and the patch immediately below it.
% LIMITATIONS:  > PYCurve does not account for multiple roots, tuorosity,
%                 branching or changing diameter along root length.
% When prompted, select 'geoPIV_launcher'...


%% SECTION 1:
%INPUT INFORMATION;
        Dia=0.0016; % Diameter of the root; UNITS = m
        YoungMod=5105; % Youngs modulus (E value); UNITS = kN/m2

        FACTOR=0.000051; %i.e 1 pixel = 0.00004 metres

        Patches=15; %Number of patches sitting above the shear plane.
        SpringSpacing=0.002;

% Useful material properties:
%       MATERIAL            YOUNGS MOD (kN/m2)      UNIT WEIGHT (kN/m3)
%       Viton Rubber        5105                    9.3163175
%       Rubber (General)    1e4-10e4
%       Balsa Wood          113e4-600e4             0-2.941995
%       Willow (<5yrs)      440e4-1010e4            0-3.2361945
%
% NB:  Conversion factor between kg/m3 & kN/m3 is : 0.00980665
```

```
%
%% SECTION 2:
% COLLECTING & ORGABISING DATA;
    %X & Y Data used for finding curvature k, bending moment M & shear force
V.
    data=consolidate8;
    X=data(:,:,1);
    X(:,1)=[];  %deleting first column of matrix (numbering of patches)
    X=FACTOR*X;
    Y=data(:,:,2);
    Y(:,1)=[];
    Y=FACTOR*Y;
    S=size(Y);
    nr=S(1,1); %number of rows/number of patches used
    nc=S(1,2); %number of columns/number of images

    NumPatchesOnRoot=nr/2;

    %Angle of root to the vertical plane [Assuming the root has zero or
    %negligeable tourosity & taking the first image only].
    X1=X(1,1);
    X2=X(NumPatchesOnRoot,1);
    Y1=Y(1,1);
    Y2=Y(NumPatchesOnRoot,1);

    angle=atand((X2-X1)/(Y2-Y1))

    % Length of root considered in analysis (i.e. length of root in image
    % 1);
    for i=2:NumPatchesOnRoot
        distance(i,1)=sqrt((X(i,1)-X(i-1,1))^2+(Y(i,1)-Y(i-1,1))^2);
    end
    length(:,1)=sum(distance(:,1)); %Length of root;
    cumdist(:,1)=cumsum(distance(:,1)); %Distance of each patch from the root
tip;

    %Calculate distance of shear plane [SP] from root tip (root tip = bottom
of root)
        %[Calculation assumes that the SP sits at the midpoint between its
        %two closest patches (i.e the patch just above and the patch just
        %below - the accuracy of this assumption depends on the patch
        %location during the PIV analysis)];
    PatchesBelowSP=NumPatchesOnRoot-Patches;
    DistToSP(:,1)=(cumdist(PatchesBelowSP,1)+cumdist(PatchesBelowSP+1,1))/2;

    %Calculate horizontal displacement, H, of root (between 1st image & image
n);
    %Displacements used for k,M,V & p;
    for i=1:nc
        for j=1:NumPatchesOnRoot
            H(j,i)=(X(j,i)-X(j,1));
        end
    end

%% SECTION 3:
```

```
%CALCULATE A RELATIONSHIP BETWEEN THE HORIZONTAL DISPLACEMENT OF EACH PATCH &
%ITS LOCATION ON THE ROOT (USED TO FIND k, M, V & p);
    % - The aim of this step is to generate a polynomial equation,
    %   excluding x^2, x^3 & x^4 terms(as M, V & p should = 0 at root tip,
    %   where EI*d^2y/dx^2=M, EI*d^3y/dx^3=V & EI*d^4y/dx^4=p), i.e. create
    %   an equation in the form:
c1x^5+c2x^6+c3x^7+c4x^8+c5x^9+c6x^10+c7x^11+c8x^12.
    %   [NB: Additional terms c0 and cx have been excluded from the analysis -
    %   this is because a better best fit is obtained without these terms].
    % - This is achieved through using gaussian elimination to evaluate
    %   A'Ac=A'y, where;
    %           A=[x1^5,x1^6,x1^7,x1^8,x1^9,x1^10,x1^11,x1^12;
    %              x2^5,x2^6,x2^7,x2^8,x2^9,x2^10,x2^11,x2^12;
    %              ........................................;
    %              xn^5,xn^6,xn^7,xn^8,xn^9,xn^10,xn^11,xn^12;],
    %           y=H, &
    %           c=a matrix of coefficients, which we are trying to find.
    %
    HMatrixSize=size(H);
    hrow=HMatrixSize(1,1);  %number of rows/patches
    hcol=HMatrixSize(1,2);  %number of columns/images+1
    %
    d=8;  % number of coeffs required
    %
    %Generating data for 'A' matrix
    c=zeros(hrow,hcol);
    for i=1:hrow
        for j=1:hcol
            c(i,j)=cumdist(i,1)^5;
        end
    end
    de=zeros(hrow,hcol);
    for i=1:hrow
        for j=1:hcol
            de(i,j)=cumdist(i,1)^6;
        end
    end
    e=zeros(hrow,hcol);
    for i=1:hrow
        for j=1:hcol
            e(i,j)=cumdist(i,1)^7;
        end
    end
    f=zeros(hrow,hcol);
    for i=1:hrow
        for j=1:hcol
            f(i,j)=cumdist(i,1)^8;
        end
    end
    ge=zeros(hrow,hcol);
    for i=1:hrow
        for j=1:hcol
            ge(i,j)=cumdist(i,1)^9;
        end
    end
    h=zeros(hrow,hcol);
    for i=1:hrow
```

```
        for j=1:hcol
            h(i,j)=cumdist(i,1)^10;
        end
    end
    ai=zeros(hrow,hcol);
    for i=1:hrow
        for j=1:hcol
            ai(i,j)=cumdist(i,1)^11;
        end
    end
    aj=zeros(hrow,hcol);
    for i=1:hrow
        for j=1:hcol
            aj(i,j)=cumdist(i,1)^12;
        end
    end
    coeff=zeros(d,hcol);
    for g=1:hcol
        A=[c(:,g),de(:,g),e(:,g),f(:,g),ge(:,g),h(:,g),ai(:,g),aj(:,g)];
        y=H(:,g);
        coeff(:,g)=A\y; % '\' performs gaussian elimination & back
substitution in order to obtain values for each of the coefficients.
    end
    %
    %Calculate Y(estimated) using the new found coefficients.
    %Requires X DATA

    FirstSpring=SpringSpacing/2; %from tip of root
    N=length(1,1)/SpringSpacing;
    NumberOfSprings=floor(N); %rounding N to the nearest lower integer.
    NumberOfSprings
    for i=1:NumberOfSprings
        dat(:,i)=FirstSpring+(SpringSpacing*(i-1));
    end
    XData=dat';
    Ydata=zeros(21,hcol-1);
    for i=1:hcol  % number of columns in 'coeff' matrix.
        for j=1:NumberOfSprings

YData(j,i)=(coeff(1,i)*XData(j,1)^5)+(coeff(2,i)*XData(j,1)^6)+(coeff(3,i)*XDa
ta(j,1)^7)+(coeff(4,i)*XData(j,1)^8)+(coeff(5,i)*XData(j,1)^9)+(coeff(6,i)*XDa
ta(j,1)^10)+(coeff(7,i)*XData(j,1)^11)+(coeff(8,i)*XData(j,1)^12);
        end
    end

%% CALCULATION CHECK:  COMPARISON BETWEEN MEASURED AND CALCULATED
DISPLACEMENTS
    %Generate YData for comparison of estimated data against actual data
    %(calculation the same as above, but using cumdist instead of XData)
    for i=1:hcol
        for j=1:hrow

Compare(j,i)=(coeff(1,i)*cumdist(j,1)^5)+(coeff(2,i)*cumdist(j,1)^6)+(coeff(3,
i)*cumdist(j,1)^7)+(coeff(4,i)*cumdist(j,1)^8)+(coeff(5,i)*cumdist(j,1)^9)+(co
eff(6,i)*cumdist(j,1)^10)+(coeff(7,i)*cumdist(j,1)^11)+(coeff(8,i)*cumdist(j,1
)^12);
```

```
        end
    end

%% SECTION 4:
%CALCULATING CURVATURE & BENDING MOMENT
    % DOUBLE DIFFERENTIATE BEST FIT CURVE TO FIND APPROXIMATIONS OF k & M.
    % Steps of differentiation are shown below:
    % Best fit curve y = c2x^5   + c3x^6   + c4x^7   + c5x^8   + c6x^9   +
c7x^10 +  c8x^11   + c9x^12;
    % (dy/dx) =          5c2x^4  + 6c3x^5  + 7c4x^6  + 8c5x^7  + 9c6x^8  +
10c7x^9 + 11c8x^10 + 12c9x^11; <<This equation shows the slope/rotation of
pile section
    % (d^2y/dx^2) =      20c2x^3 + 30c3x^4 + 42c4x^5 + 56c5x^6 + 72c6x^7 +
90c7x^8 + 110c8x^9 + 132c9x^10;

    DoubleDiffCoeffs=[20 30 42 56 72 90 110 132]; %<<Factors from equation
d^2x/dx^2.  These will have to be multiplied by constants c,de,e,f,ge&h,
below;

    for i=1:hcol
        for j=1:d
            CurvatureCoeffs(j,i,1)=(coeff(j,i))*(DoubleDiffCoeffs(1,j)); %Best
fit (figure 1) coefficients x coefficients of d^2y/dx^2.
        end
    end
    % Below; New coefficients are multiplied by values
    % of X^n (as required by the d^2x/dx^2 equation) to find k.

    for dist=1:NumberOfSprings
        for eq=1:hcol
            k(dist,eq,1)= (CurvatureCoeffs(1,eq)*XData(dist,1)^3) +
(CurvatureCoeffs(2,eq)*XData(dist,1)^4) +
(CurvatureCoeffs(3,eq)*XData(dist,1)^5)+(CurvatureCoeffs(4,eq)*XData(dist,1)^6
) + (CurvatureCoeffs(5,eq)*XData(dist,1)^7) +
(CurvatureCoeffs(6,eq)*XData(dist,1)^8)+
(CurvatureCoeffs(7,eq)*XData(dist,1)^9)+
(CurvatureCoeffs(8,eq)*XData(dist,1)^10);
        end
    end

    % M is calculated by multiplying k by stiffness of the root, EI.
    % Below; Bending stiffness of root (calcualtions use root properties
    % specified in section 1 of the code).
    r=Dia/2; % << radius of the root
    Icc=((pi()*r^4)/8)+r*Dia*r^2;  % <<I value for a semi-circular cross
section
    If=(pi()*Dia^4)/64; %<< I value for a circular cross section
    EIcs=YoungMod*Icc;
    EIf=YoungMod*If;
    % Bending moment;
    BMcs=EIcs*k;  %<< Bending moment for a cross sectional root
    BMf=EIf*k  %<< Bending moment for a full root
    % Calculating I;
    % CROSS SECTION         EQUATION - Unit weight*...
    % Circular              [pi*r^4]/4        <<r=radius
    % Semi-circular         [pi*r^4]/8
```

```
    % Rectangular           [bh^3]/12         <<b=breadth, h=height
    %
%% SECTION 5:
%CALCULATING SHEAR FORCE
%DIFFERENTIATE BM TO FIND V.
    % From before; (d^2y/dx^2) =  20c2x^3 + 30c3x^4  + 42c4x^5  + 56c5x^6  +
72c6x^7  + 90c7x^8  + 110c8x^9 + 132c9x^10 ;
    % so,          (d^3y/dx^3) =  60c2x^2 + 120c3x^3 + 210c4x^4 + 336c5x^5 +
504c6x^6 + 720c7x^7 + 990c8x^8 + 1320c9x^9;
    %
    TripleDiffCoeffs=[60 120 210 336 504 720 990 1320];
    %
    for i=1:hcol
        for j=1:d
            ShearCoeffs(j,i)=(coeff(j,i))*(TripleDiffCoeffs(1,j));  %Best fit
(figure 1) coefficients x coefficients of d^3y/dx^3.
        end
    end
    %
    for dist=1:NumberOfSprings
        for eq=1:hcol
            SHEAR(dist,eq,1)=(ShearCoeffs(1,eq)*XData(dist,1)^2) +
(ShearCoeffs(2,eq)*XData(dist,1)^3) +
(ShearCoeffs(3,eq)*XData(dist,1)^4)+(ShearCoeffs(4,eq)*XData(dist,1)^5) +
(ShearCoeffs(5,eq)*XData(dist,1)^6) +
(ShearCoeffs(6,eq)*XData(dist,1)^7)+(ShearCoeffs(7,eq)*XData(dist,1)^8) +
(ShearCoeffs(8,eq)*XData(dist,1)^9);
        end
    end
    Vcs=EIcs*SHEAR  %<< Shear force along length of cross sectional root
    Vf=EIf*SHEAR %<< Shear force along length of full root

%% SECTION 6:
%CALCULATING SOIL REACTION

    % From before; (d^3y/dx^3) = 60c2x^2 + 120c3x^3 + 210c4x^4 + 336c5x^5  +
504c6x^6  + 720c7x^7 + 990c8x^8 + 1320c9x^9;
    %      so, (d^4y/dx^4)     = 120c2x  + 360c3x^2 + 840c4x^3 + 1680c5x^4 +
3024c6x^5 + 5040c7x^6+ 7920c8x^7 + 11880c9x^8;

    QuadrupleDiffCoeffs=[120 360 840 1680 3024 5040 7920 11880];

    for i=1:hcol
        for j=1:d
            SoilReactionCoeffs(j,i)=(coeff(j,i))*(QuadrupleDiffCoeffs(1,j));
%Best fit (figure 1) coefficients x coefficients of d^4y/dx^3.
        end
    end

    for dist=1:NumberOfSprings
        for eq=1:hcol
            SoilReac(dist,eq,1)=(SoilReactionCoeffs(1,eq)*XData(dist,1)) +
(SoilReactionCoeffs(2,eq)*XData(dist,1)^2) +
(SoilReactionCoeffs(3,eq)*XData(dist,1)^3)+(SoilReactionCoeffs(4,eq)*XData(dis
t,1)^4) + (SoilReactionCoeffs(5,eq)*XData(dist,1)^5) +
(SoilReactionCoeffs(6,eq)*XData(dist,1)^6)+
```

```
(SoilReactionCoeffs(7,eq)*XData(dist,1)^7) +
(SoilReactionCoeffs(8,eq)*XData(dist,1)^8);
        end
    end
    pcs=EIcs*SoilReac   %<<Soil reaction along cross sectional root
    pf=EIf*SoilReac  %<<Soil reaction along full root.

%% SECTION 7
%FIND RELATIVE ROOT MOVEMENT...
    %Find horizontal displacement in soil;
    XSoil=X;
    XSoil(1:NumPatchesOnRoot,:)=[];  %Deleting root data
    YSoil=Y;
    YSoil(1:NumPatchesOnRoot,:)=[];  %Deleting root data
    for i=1:hcol
        HSoil(:,i)=XSoil(:,i)-XSoil(:,1);  %Finding horizontal soil movement
between image n & the initial image.
    end
    %
    for i=2:NumPatchesOnRoot
            distanceS(i,1)=sqrt(((XSoil(i,1)-XSoil(i-1,1))^2)+((YSoil(i,1)-
YSoil(i-1,1))^2));
    end
    Slength(:,1)=sum(distanceS(:,1));
    cumdistS(:,1)=cumsum(distanceS(:,1));

    cumdistA=cumdistS;
    cumdistA(1:PatchesBelowSP,:)=[];  %deleting patches below the shear plane;
    cumdistB=cumdistS;
    cumdistB(PatchesBelowSP+1:NumPatchesOnRoot,:)=[];  %deleting patches
sitting above the shear plane;
    %
    AboveSP=HSoil;
    AboveSP(1:PatchesBelowSP,:)=[];  %Horizontal soil movement - deleting
patches below the shear plane;
    BelowSP=HSoil;
    BelowSP(PatchesBelowSP+1:NumPatchesOnRoot,:)=[];  %Horizontal soil
movement - deleting patched above the shear plane;
    %
    MatrixSizeAbove=size(AboveSP);
    ARow=MatrixSizeAbove(1,1);
    ACol=MatrixSizeAbove(1,2);
    MatrixSizeBelow=size(BelowSP);
    BRow=MatrixSizeBelow(1,1);
    BCol=MatrixSizeBelow(1,2);
    %
    %Best fit equation for data above shear plane, equation in the form:
    % y = a + bx

    d=2;
    a=zeros(ARow,ACol);
    for i=1:ARow
        for j=1:ACol
            a(i,j)=1;
        end
    end
```

```
    b=zeros(ARow,ACol);
    for i=1:ARow
        for j=1:ACol
            b(i,j)=cumdistA(i,1);
        end
    end
    coeffA=zeros(d,ACol);
    for g=1:ACol
        A=[a(:,g),b(:,g)];
        y=AboveSP(:,g);
        coeffA(:,g)=A\y;
    end
    % XData as before
    YDataA=zeros(NumberOfSprings,ACol-1);
    for i=1:ACol
        for j=1:NumberOfSprings
            YDataA(j,i)=coeffA(1,i)+coeffA(2,i)*XData(j,1);
        end
    end

    %
    for i=1:NumberOfSprings
        for j=1:nc
            if XData(i,1)>DistToSP(:,1);
                BestFit(i,j)=YDataA(i,j);
            else BestFit(i,j)=0;
            end
        end
    end

    for i=1:NumberOfSprings
        for j=1:nc
            if XData(i,1)>DistToSP(:,1)
                RelativeY(i,j)=YData(i,j)-YDataA(i,j);
            else RelativeY(i,j)=YData(i,j);
            end
        end
    end
    RelativeRootMovementY=RelativeY';
    SoilReactioncs=pcs';
    SoilReactionf=pf';
    %
%% PLOTS

%Plotting Horizontal Displacement, Bending Moment, Shear Force & Soil
%Reaction;

w=char('ok','k*','k+','kx','ro','r*','r+','rx','go','g*','g+','gx','bo','b*','
b+','bx','mo','m*','m+','mx','co','c*','c+','cx','yo','y*','y+','yx','k:','k-
.','k--','k-','r:','r-.','r--','r-','g:','g-.','g--','g-','b:','b-.','b--','b-
','m:','m-.','m--','m-','c:','c-.','c--','c-','y:','y-.','y--','y-
','ok','k*','k+','kx','ro','r*','r+','rx','go','g*','g+','gx','bo','b*','b+','
bx','mo','m*','m+','mx','co','c*','c+','cx','yo','y*','y+','yx','k:','k-.','k-
-','k-','r:','r-.','r--','r-','g:','g-.','g--','g-','b:','b-.','b--','b-
','m:','m-.','m--','m-','c:','c-.','c--','c-','y:','y-.','y--','y-');
```

```
    v=char('k:','k-.','k--','k-','r:','r-.','r--','r-','g:','g-.','g--','g-
','b:','b-.','b--','b-','m:','m-.','m--','m-','c:','c-.','c--','c-','y:','y-
.','y--','y-','k:','k-.','k--','k-','r:','r-.','r--','r-','g:','g-.','g--','g-
','b:','b-.','b--','b-','m:','m-.','m--','m-','c:','c-.','c--','c-','y:','y-
.','y--','y-','k:','k-.','k--','k-','r:','r-.','r--','r-','g:','g-.','g--','g-
','b:','b-.','b--','b-','m:','m-.','m--','m-','c:','c-.','c--','c-','y:','y-
.','y--','y-','k:','k-.','k--','k-','r:','r-.','r--','r-','g:','g-.','g--','g-
','b:','b-.','b--','b-','m:','m-.','m--','m-','c:','c-.','c--','c-','y:','y-
.','y--','y-');

LegendText=char('Image1','Image2','Image3','Image4','Image5','Image6','Image7'
,'Image8','Image9','Image10','Image11','Image12','Image13','Image14','Image15'
,'Image16','Image17','Image18','Image19','Image20','Image21','Image22','Image2
3','Image24','Image25','Image26','Image27','Image28','Image29','Image30','Imag
e31','Image32','Image33','Image34','Image35','Image36','Image37','Image38','Im
age39','Image40','Image41','Image42','Image43','Image44','Image45','Image46','
Image47','Image48','Image49','Image50','Image51','Image52','Image53','Image54'
,'Image55','Image56','Image57','Image58','Image59','Image60','Image61','Image6
2','Image63','Image64','Image65','Image66','Image67','Image68','Image69','Imag
e70','Image71','Image72','Image73','Image74','Image75','Image76','Image77','Im
age78','Image79','Image80','Image81','Image82');
    LegendText2=char('Patch-1','Patch-2','Patch-3','Patch-4','Patch-5','Patch-
6','Patch-7','Patch-8','Patch-9','Patch-10','Patch-11','Patch-12','Patch-
13','Patch-14','Patch-15','Patch-16','Patch-17','Patch-18','Patch-19','Patch-
20','Patch-21','Patch-22','Patch-23','Patch-24','Patch-25','Patch-26','Patch-
27','Patch-28','Patch-29','Patch-30','Patch-31','Patch-32','Patch-33');


figure(1);
subplot(1,3,1);
    scale=1;
    hold on;
    for j=1:nc
        plot(H(:,j),cumdist(:,1),w(j,:))
        legend(LegendText,'Location','SouthWest')
    end
    for j=1:nc
        plot(Compare(:,j),cumdist(:,1),v(j,:))
    end
    grid;
    xlabel('Horizontal Displacement of Root, m','FontSize',12,'FontName','Zapf
Chancery')
    ylabel('Distance of Patch from Root Tip, m','FontSize',12,'FontName','Zapf
Chancery')
    title('Horizontal Displacement Along Root
Length','FontSize',14,'FontWeight','bold','FontName','Zapf Chancery')
subplot(1,3,2);
    hold on
    scale=1;
    for j=1:nc
        plot(BestFit(:,j),XData(:,1),v(j,:))
        legend(LegendText,'Location','SouthWest')
    end
    for j=1:nc
        plot(HSoil(:,j),cumdist(:,1),w(j,:))
    end
```

```
    grid;
    xlabel('Soil Movement, m','FontSize',12,'FontName','Zapf Chancery')
    ylabel('Distance of Patch from Root Tip, m','FontSize',12,'FontName','Zapf
Chancery')
    title('Soil Movement','FontSize',14,'FontWeight','bold','FontName','Zapf
Chancery')
subplot(1,3,3);
    hold on
    scale=1;
    for j=1:nc
        plot(RelativeY(:,j),XData(:,1),w(j,:))
    end
    grid;
    xlabel('Relative Root Movement, m','FontSize',12,'FontName','Zapf
Chancery')
    ylabel('Distance of Patch from Root Tip, m','FontSize',12,'FontName','Zapf
Chancery')
    title('Relative Horizontal Displacement Along Root
Length','FontSize',14,'FontWeight','bold','FontName','Zapf Chancery')


figure(2);
subplot(1,3,1);
    scale=1;
    hold on;
    for j=1:nc
        plot(BMf(:,j),XData(:,1),v(j,:))
    end
    grid;
    xlabel('Bending Moment of Root,kNm','FontSize',12,'FontName','Zapf
Chancery')
    ylabel('Distance of Patch from Root Tip, m','FontSize',12,'FontName','Zapf
Chancery')
    title('Bending Moment Along Root
Length','FontSize',14,'FontWeight','bold','FontName','Zapf Chancery')
subplot(1,3,2);
    scale=1;
    hold on;
    for j=1:nc
        plot(Vf(:,j),XData(:,1),v(j,:))
    end
    grid;
    xlabel('Shear Force,kN','FontSize',12,'FontName','Zapf Chancery')
    ylabel('Distance of Patch from Root Tip, m','FontSize',12,'FontName','Zapf
Chancery')
    title('Shear Force Along Root
Length','FontSize',14,'FontWeight','bold','FontName','Zapf Chancery')
subplot(1,3,3);
    hold on
    scale=1;
    for j=1:nc
        plot(pf(:,j),XData(:,1),v(j,:))
    end
    grid;
    xlabel('Soil Reaction, kN/m','FontSize',12,'FontName','Zapf Chancery')
```

```
    ylabel('Distance of Patch from Root Tip, m','FontSize',12,'FontName','Zapf
Chancery')
    title('Soil Reaction along root
length','FontSize',14,'FontWeight','bold','FontName','Zapf Chancery')


% Plotting P-Y Curve, relative soil displacement & soil reaction.



figure(3)
    w=char('o--b','b--*','b--+','b--x','r--o','r--*','r--+','r--x','k--o','k--
*','k--+','k--x','m--o','m--*','m--+','m--x','b--o','b--*','b--+','b--x','k--
o','k--*','k--+','k--x','y--o','y--*','y--+','y--x','k:','k-.','k--','k-
','r:','r-.','r--','r-','g:','g-.','g--','g-','b:','b-.','b--','b-','m:','m-
.','m--','m-','c:','c-.','c--','c-','y:','y-.','y--','y-');
    hold on
    scale = 1;
    for i=1:NumberOfSprings
            plot(-RelativeRootMovementY(:,i),-SoilReactionf(:,i),w(i,:))
            legend(LegendText2,'Location','SouthWest')
    end
    grid;
    xlabel('Relative Root Movement, m','FontSize',14,'FontName','Zapf
Chancery')
    ylabel('Soil Reaction, kN/m','FontSize',14,'FontName','Zapf Chancery')
    title('P-Y Curve','FontSize',16,'FontWeight','bold','FontName','Zapf
Chancery')

%PYSprings
    for SpringNumber=1:NumberOfSprings
        SpringNumber

PY=[SoilReactionf(:,SpringNumber),RelativeRootMovementY(:,SpringNumber)]
    end
```